CLIMATE CHANGE ASSESSMENT FOR THE SOUTHEASTERN UNITED STATES

A Dissertation
Presented to
The Academic Faculty

by

Feng Zhang

In Partial Fulfillment
of the Requirements for the Degree
Doctor of Philosophy in the
School of Civil and Environmental Engineering

Georgia Institute of Technology
December 2011

CLIMATE CHANGE ASSESSMENT FOR THE SOUTHEASTERN UNITED STATES

Approved by:

Dr. Aris Georgakakos, Advisor
School of Civil and Environmental Engineering
Georgia Institute of Technology

Dr. Terry Sturm
School of Civil and Environmental Engineering
Georgia Institute of Technology

Dr. Jian Luo
School of Civil and Environmental Engineering
Georgia Institute of Technology

Dr. Huaming Yao
School of Civil and Environmental Engineering
Georgia Institute of Technology

Dr. Jiawen Yang
School of City and Regional Planning
Georgia Institute of Technology

Date Approved: August 11, 2011

ACKNOWLEDGEMENTS

This thesis would not have been possible without the support and advice of my advisor, Dr. Aris P. Georgakakos. I am very appreciative of his generosity with his time, advice, patience, and references, to name a few of his contributions. By working closely with Dr. Georgakakos, I learned so many things which are very important for me to become a good researcher. His encouragement and enthusiasm are very important for the completion of this thesis.

The good advice and help of Dr. Huaming Yao has been invaluable on both an academic and a personal level, for which I am extremely grateful. I would also like to thank Dr. Terry Sturm, Dr. Jian Luo, and Dr. Jiawen Yang for their invaluable advices on this study.

I would like to thank my colleagues and friends in the Georgia Water Resources Institute: Mr. Chia-Jeng Chen, Mr. Dongha Kim, Mr. Martin Kistenmacher, Mr. Christian V. Braneon, Mr. Jeffrey Regan, Mr. Frederick M. Kimaite, Mr. Ke Yu, Ms. Xi Chen, and Ms. Denise Taylor. I will never forget the time and fun we enjoyed and shared together as a wonderful team.

I wish to thank my father Zhang Zhifa, my mother Wang Ruilian, and my sister Zhang Li. My parents gave me everything: they bore me, raised me, supported me, taught me, and loved me. I also thank Ms. Greta Reed for her taking care of me during my studying in Atlanta.

The most special thanks belong to my wife Wang Ren for her understanding about my leaving during all these years, and for her selfless love, support all along, encouragement and company.

This thesis research was funded in part by the National Oceanic and Atmospheric Administration, Office of Global Programs, Climate Prediction Program for the Americas (CPPA; NOAA contract No. NA06OAR4310073), the Georgia Department of Natural Resources, Environmental Protection Division (Georgia EPD contract No. 761-70091), and the State Water Institute Program (104B) administered by USGS. I am grateful to all sponsors. However, the ideas and opinions presented herein do not necessarily reflect those of the sponsoring organizations.

TABLE OF CONTENTS

LIST OF TABLES

LIST OF FIGURES

SUMMARY

Water resource planning and management practices in the southeastern United States may be vulnerable to climate change. This vulnerability has not been quantified, and decision makers, although generally concerned, are unable to appreciate the extent of the possible impact of climate change nor formulate and adopt mitigating management strategies. Thus, this dissertation aims to fulfill this need by generating decision worthy data and information using an integrated climate change assessment framework.

To begin this work, we develop a new joint variable spatial downscaling technique for statistically downscaling gridded climatic variables to generate high-resolution, gridded datasets for regional watershed modeling and assessment. The approach differs from previous statistical downscaling methods in that multiple climatic variables are downscaled simultaneously and consistently to produce realistic climate projections. In the bias correction step, JVSD uses a differencing process to create stationary joint cumulative frequency statistics of the variables being downscaled. The functional relationship between these statistics and those of the historical observation period is subsequently used to remove GCM bias. The original variables are recovered through summation of bias corrected differenced sequences. In the spatial disaggregation step, JVSD uses a historical analogue approach, with historical analogues identified simultaneously for all atmospheric fields and over all areas of the basin under study.

In the second component of the integrated assessment framework, we develop a data-driven, downward hydrological watershed model for transforming the climate variables obtained from the downscaling procedures to hydrological variables. The watershed model includes several water balance elements with nonlinear storage-release functions. The release functions and parameters are data driven and estimated using a recursive identification methodology suitable for multiple, inter-linked modeling components. The model evolves from larger spatial/temporal scales down to smaller spatial/temporal scales with increasing model structure complexity. For ungauged or poorly-gauged watersheds, we developed and applied regionalization hydrologic models based on stepwise regressions to relate the parameters of the hydrological models to observed watershed responses at specific scales.

Finally, we present the climate change assessment results for six river basins in the southeastern United States. The historical (baseline) assessment is based on climatic data for the period 1901 through 2009. The future assessment consists of running the assessment models under all IPCC A1B and A2 climate scenarios for the period from 2000 through 2099. The climate assessment includes temperature, precipitation, and potential evapotranspiration; the hydrology assessment includes primary hydrologic variables (i.e., soil moisture, evapotranspiration, and runoff) for each watershed.

CHAPTER 1

INTRODUCTION

Water resource planning and management practices in the southeastern United States may be vulnerable to climate change. This vulnerability has not been quantified, and decision makers, although generally concerned, are unable to appreciate the extent of the possible impact of climate change nor formulate and adopt mitigating management strategies. This dissertation aims to fill this need by generating decision-worthy data and information using the integrated climate change assessment framework depicted on **Figure 1.1**. This framework includes three inter-linked components pertaining to climate, hydrology, and water resources, providing the technical basis for answering a range of questions.

The climate component establishes ways to downscale global circulation model (GCM) scenarios to finer (and more hydrologically relevant) spatial and temporal scales. The downscaling process is designed to generate data that *(1)* capture key climatic features including mean and variability trends, spatial and temporal correlations, and other interdependencies between atmospheric variables that drive hydrological processes; *(2)* are adequately characterized with respect to their uncertainty; and *(3)* are smooth across different temporal scales (e.g., annual, monthly, and daily).

The hydrology component describes the watershed response to alternative atmospheric forcing by simulating all relevant hydrologic processes such as evapotranspiration, infiltration, soil moisture storage, and runoff, among others. The development of hydrologic models entails several issues including *(1)* whether to use the physical-based or conceptual models; *(2)* what hydrological processes to include; *(3)* how to identify and estimate model parameters in gauged and un-gauged watersheds; and *(4)* how to characterize the additional uncertainties that hydrologic models introduce into the assessment.

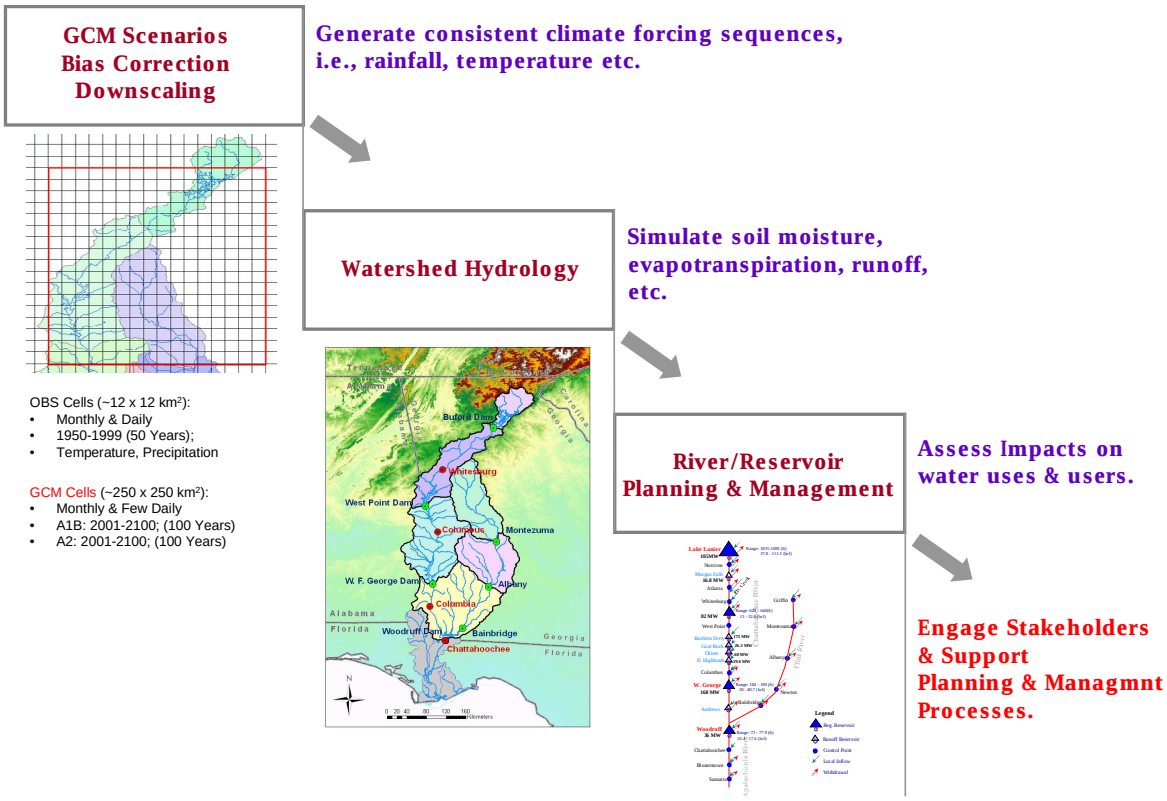

Figure 1.1: Integrated Modeling Framework (Source: Georgakakos et al., 2010).

The river and reservoir planning and management component aims to assess the water resources impacts of alternative hydrologic (and corresponding GCM) scenarios. Among others, such impacts pertain to water supply for domestic, industrial, and irrigation use; energy generation; navigation; and environmental and ecosystem preservation.

The assessment is carried out for the Apalachicola-Chattahoochee-Flint (ACF) and other southeast US river basins, and seeks to identify and assess effective mitigation strategies.

The research contributions of this study include *(1)* new methods for consistent temperature-precipitation downscaling; *(2)* guidelines for hydrologic watershed model identification and parameter calibration and regionalization; and *(3)* hydrologic and water resources assessment results for the southeast US using integrated climate-hydrology-water resources models.

The dissertation includes seven chapters, including this introduction. **Chapter 2** reviews the existing literature on climate change scenarios, climate downscaling methods including dynamic and statistical approaches, watershed hydrologic modeling methods and their parameter estimation methods, and hydrological regionalization approaches. Chapter 2 also describes the historical climate, hydrology, and water uses for six major river basins studied in this dissertation: the Apalachicola-Chattahoochee-Flint (ACF); the Alabama-Coosa-Tallapoosa (ACT); the Oconee-Ocmulgee-Altamaha (OOA) basin; the Ochlocknee-Suwannee-Satilla-St. Marys (OSSS), the Savannah-Ogeechee (SO); and the Tennessee (TN).

Chapter 3 presents a new statistical method, named Joint Variable Spatial Downscaling (JVSD), for downscaling gridded climatic variables. It is developed to generate high resolution gridded datasets for regional watershed modeling and assessments. The proposed approach differs from previous statistical downscaling methods in that multiple climatic variables are downscaled simultaneously and consistently to produce realistic climate projections.

Chapter 4 describes a lumped conceptual watershed model developed for hydrologic impact assessment in this study. The watershed model includes several water balance elements with nonlinear storage-release functions at monthly and daily time resolution. The function forms and parameters of the model are data driven, and they are estimated using a recursive identification methodology suitable for multiple, inter-linked modeling components. The watershed models are calibrated and employed to characterize the hydrologic responses under the historical and future climate scenarios.

Chapter 5 discussed the methodology for developing hydrological regionalization relationships. The approach is applied to 53 Georgia catchments where long-term and monthly unimpaired flow observations are available. The catchment parameters are related to eleven soil characteristics extracted from the Soil Survey

Geographic (SSURGO) Database, and thirteen land use variables obtained from the Georgia Gap Analysis Project (University of Georgia).

Chapter 6 presents the climate changes assessment results for the six case study river basins. The historical (baseline) assessment is based on climatic data for the period 1901 through 2009 (109 years). The future assessment consists of running the assessment models under all A1B and A2 climate scenarios for the period from 2000 through 2099 (100 years). The climate assessment includes the assessments of temperature, precipitation and potential evapotranspiration. The hydrology assessment includes the assessments of primary hydrologic variables (i.e., soil moisture, evapotranspiration, and runoff) for each watershed. The water resources assessment uses the Apalachicola-Chattahoochee-Flint Decision Support System (ACF DSS), developed at the Georgia Water Resources Institute (Georgakakos and Yao, 1999), to quantify the water use implications and potential mitigation measures.

Finally, conclusions and further research recommendations are presented in **Chapter 7**.

CHAPTER 2

LITERATURE REVIEW

2.1 Climate Change Scenarios

2.1.1 GHG Emission Scenarios

The Intergovernmental Panel on Climate Change (IPCC) was set up jointly by the World Meteorological Organization and the United Nations Environment Program to promote the scientific understanding of climate change causes and impacts (IPCC, 2007). To date, IPCC has produced four assessment reports (in 1990, 1995, 2001 and 2007) which are referenced widely by scientists in a broad range of disciplines.

The IPCC reports are based on the results and findings of many climate research programs and experiments. One such program is the World Climate Research Program (WCRP) Coupled Model Intercomparison Project Phase Three (CMIP3), carried out under the Program for Climate Model Diagnosis and Intercomparison (PCMDI; Meehl et al., 2007). This program produced an array of climate change computational experiments under past, projected, or idealized greenhouse gas (GHG) emission scenarios, three of which are used in this study.

The first experiment, 20CM3, represents the 20th century historical emission scenarios, and serves as a baseline case illustrating the way in which climate models simulate the historical climate. The 20CM3 experiments are baselines for the climate change studies. The other two experiments pertain to projected climate changes in the 21st century and are a subset of the IPCC Special Report on Emission Scenarios (SRES; Nakicenovic and Swart, 2000). These experiments are the SRESA1B and SRESA2, respectively based on medium and high emission scenarios. The SRESA1B experiments are initialized with conditions from the 20CM3 experiments and they continue to run to 2100 under the assumption that the GHG emission will peak at the mid-century and

decline thereafter. The SRESA2 experiments are also initialized with conditions from the 20CM3 experiments and run to 2100 under the assumption that the GHG emission will continue to increase throughout the century. After 2100, they hold concentrations fixed and continue the simulation to 2200.

2.1.2 Global Circulation Models

Many researchers have demonstrated the physical science basis, impact, adaptation, and vulnerability of our changing climate and environment. Some have also addressed water resources impacts under climate changes (Lettenmaier and Rind, 1992; Stamm et al., 1994; Conway, 1998; Wood et al., 2004; Maurer, 2007; Georgakakos et al., 2011; Zhang and Georgakakos, 2011b). All impact assessment studies are driven by general circulation model (GCM) scenarios.

General circulation models (GCMs) are scientific tools used to assess the future global climate response associated with various greenhouse gas emission scenarios (IPCC WGI, 2007). The GCMs represent (through a large system of partial differential equations) the coupled atmospheric and oceanic processes currently understood to govern the Earth's climate. Climate scenarios are generated by the numerical integration of the underlying equations over space and time. Table 2.1 lists 13 different GCMs, selected scenarios from which (corresponding to emission scenarios 20CM3, SRESA2, and SRESA1B) are utilized in this study. In this table, under atmospheric resolution, T is the horizontal resolution and L is the vertical resolution in numbers of vertical layers. Oceanic resolution is provided in degrees (T: horizontal resolution) and numbers of vertical layers (L: vertical resolution).

The purposes of developing GCMs are initially to obtain the future global climate responses forced with concentrations of greenhouse gases and other constituents derived from various emissions scenarios (IPCC WGI, 2007). In general, GCMs were designed to run on global scales at relatively low spatial resolutions (~100x100 km^2 to ~250x250

km^2). However, the observational grids usually have much higher spatial resolution (ex., ~12x12 km^2). Therefore, before any regional climate change assessment by using GCMs, their outputs should be transformed from low spatial resolutions to high spatial resolutions. Such transformations can be performed by using climate downscaling techniques to be discussed in the next section.

Table 2.1: Summary of GCMs Used in This Study (Source: Georgakakos et al., 2010).

Model	Contributor	Atm. Resolution	Ocean Resolution
BCCR-BCM2.0, Norway	Bjerknes Centre for Climate Research	T63L31	1.5 x1.5^o, L31
CGCM3.1(T63), Canada	Canadian Centre for Climate Modeling and Analysis	T63L31	1.4^{o}x0.9^o, L29
CNRM-CM3, France	Centre National de Recherches Meteorologiques	T63L45	2.0^{o}x1.2^o
CSIRO-Mk3.5, Australia	CSIRO, Australia	T63L18	1.875^{o}x0.84^o
ECHAM5/MPI-OM, Germany	Max Planck Institute for Meteorology	T63L31	1.5^{o}x1.5^o, L40
GFDL-CM2.1, USA	Geophysical Fluid Dynamics Laboratory, NOAA	2.5^{o}x2.5^o	1^{o}x1^o
GISS-AOM, USA	NASA Goddard Institute for Space Studies	4^{o}x3^o, 12L	4^{o}x3^o, L16
MIROC3.2(hires), Japan	CCSR/NIES/FRCGC, Japan	T105L56	0.28^{o}x0.19^o, L47
CCSM3, USA	National Center for Atmospheric Research (NCAR),	T85L26	1.125^{o}x(0.27^o -1.0^o)
PCM, USA	NCAR, NSF, DOE, NASA, NOAA	T42L26	1.125^{o}x0.469^o, L40
UKMO-HadCM3, UK	Hadley Centre for Climate Prediction and Research	2.75^{o}x2.75^o	1.25^{o}x1.25^o
MIUB ECHO-G, Germany/Korea	Meteorological Institute of the University of Bonn	T30L19	T42
INM-CM3.0, Russia	Institute for Numerical Mathematics	N.A.	N.A.

2.2 Climate Scenario Downscaling Methods

GCM outputs are usually inadequate to capture the spatial variability at regional or local scales necessary for hydrological applications. Xu (1999) shows that predicting runoff directly from GCM outputs is over-simplified and ignores the lateral transfer of water between grid cells within the land phase. This conclusion is corroborated by the large uncertainties arising from using different models driven by the same scenarios (Tebaldi, 2005; Mitchell and Hulme, 1999; Mujumdar and Ghosh, 2008). The purpose of downscaling procedures to be discussed is to construct climate scenarios at more application-relevant spatial (and temporal) scales.

Existing downscaling techniques can be organized into two main categories, dynamic downscaling and statistical downscaling. Fowler and Blenkinsop (2007), Wilby and Wigley (1997), and Xu (1999) thoroughly reviewed most existing downscaling techniques of both types.

2.2.1 Dynamic Downscaling Methods

For dynamic downscaling, regional climate models (RCMs) are used to model the target region at finer scales bounded by larger GCM nodes (Miller et al., 1999; Xue et al., 2007). A high-resolution RCM is nested in a low-resolution grid initialized by a GCM simulation. In each selected time period, the GCM provides lateral boundary conditions for the nested RCM, such as radiation forcing, pressure levels, air temperature, air humidity, aerosol forcing, soil conditions, and etc. The time-dependent boundary conditions are then assimilated into the RCM fields to drive the continuous simulation. The subscale climatic features are physically simulated to enhance the simulations of atmosphere and land surface dynamics, such as complex topographical features, land cover inhomogeneity, and spatial distributions of aerosol, among others. There are usually no feedback mechanisms from the nested RCM simulations, which imply that the GCM sub-GCM grid forcing is not included in the GCM simulations.

The results of RCMs depend on the validity and skill of the overriding GCM. The systematic errors and biases in GCM outputs are passing down to RCMs and therefore any downscaled climatic variables inherit these errors and biases from global scale simulations. Typical GCM outputs have biases of temperature about 2-3 degrees and precipitation about 50%-60% (Mearns et al., 2003). Mearns et al. (2003) outlined the advantages and disadvantages of using RCMs and provided guidance on the use of their outputs. Generally, RCMs provide high resolution climatic fields spatially and globally consistent with GCM scenarios. However, these results inherit the biases of the driving global models and are computationally expensive.

The North American Regional Climate Change Assessment Program (NARCCAP) is among the most notable dynamic downscaling research efforts and provides valuable online datasets (http://www.narccap.ucar.edu/). This program investigates the uncertainties of regional scale projections of GCM outputs, and generates high resolution scenarios for regional climate impact assessments. Although NARCCAP provides a very important source of dynamically downscaled regional climatic scenarios, there are only a few simulations available up to date. These simulations correspond only to SRES A2 emissions scenario and are generated for selected time horizons (1971-2000; 2041-2070) due to their heavy computational requirements. It takes approximately 36 hours to complete a 30-day simulation using a RCM (e.g., MM5 or WRF) over an area of 90,000 km^2 with 30 x 30 km spatial resolution on a 2.1GHz dual core personal computer. Thus, the currently available results are not sufficient for comprehensive climate change impact assessments, but are used in this study to compare the skill of statistical versus dynamic downscaling methods. Lastly, it is unclear whether the uncertainties surrounding dynamic downscaling methods are not comparable to those of the more computationally efficient statistical downscaling methods.

2.2.2 Statistical Downscaling Methods

Statistical downscaling is based on relationships between low resolution GCM outputs and associated higher resolution observations over the same historical period. These statistical relationships are then used to infer the observations on finer grids at future times when only GCM outputs are available. Statistical downscaling does not depend on GCM boundary conditions and can be used to downscale climatic variables without the full set of climatic fields at the coarse level. Examples of statistical downscaling methods include changing factor methods (Beniston et al., 2003), regression methods (Huth, 1999), weather typing schemes (Vrac, 2007), weather generators (Wilks and Wilby, 1999), bias correction and spatial disaggregation (BCSD; Wood et al., 2004), constructed analogues (Hidalgo et al., 2008), and joint variable spatial downscaling (JVSD; Zhang and Georgakakos, 2011a).

Huth (1999) evaluated the performances of a number of statistical downscaling methods, e.g., canonical correlation analysis (CCA), singular value decomposition (SVD), and multiple regression models. For the regression model, Huth adopt a stepwise model selection process to select statistically significant predictors. He found that the temperature variables yield more accurate results than circulation variables and his results showed that the best predictor is the combination of 500 hecto Pascal (hPa) geo-potential heights and 850 hPa temperatures. He concluded that the global climate models always simulate different climate variables with different skills, thus in order to take the best advantage of the GCM outputs, the downscaling procedure should consider these variables jointly instead of treating them individually.

Vrac et al. (2007) proposed a stochastic weather typing approach to perform precipitation downscaling. They used the mix gamma and generalized Pareto (GP) distributions of precipitation to generate stochastic climatic sequences of small, medium and extreme precipitations. In their procedures, the climate variables (e.g., precipitation) are treated individually when downscaled. However, the regional or local precipitation

distributions can be distorted by other climatic variables (e.g., air temperature). For example, the shift of seasonal trends of temperature may infer that the seasonal precipitation also changes as well. Therefore, the joint distribution, rather than the marginal distribution, of important climatic variables is necessary to be investigated.

Wilks and Wilby (1999) discussed the weather generators and their applications in regional climate downscaling. The stochastic weather models are extended to accommodate the differences between local and area-averaged weather statistics, and they are validated using the observed inter-annual climatic variability as an analog for climate change. Their techniques also treat precipitation separately.

Wood et al. (2004) proposed a two-step statistical downscaling method to address bias correction and spatial disaggregation (BCSD). In the first step, GCM biases are adjusted through a quantile mapping technique individually for temperature and precipitation. The spatial disaggregation step translates adjusted GCM data on climate model resolutions to a basin-relevant resolution (observational resolution) by using interpolated spatial factors. The spatial interpolation method is a modified version of inverse-distance-squared interpolation developed by Shepard (1984). As will be seen, such interpolation tends to generate homogenous factor maps.

BCSD is a very efficient statistical downscaling technique for climate change assessments. One BCSD disadvantage, however, is that it generates more homogenous downscaled fields than the observed fields. This results from the use of cell-by-cell spatial interpolation factors, and marginal, not joint, variable distributions in the quantile mapping process. Furthermore, while the temperature shift-removing procedure enables the bias-correction step without extrapolation, it also makes the assumption that future temperature distributions remain similar to those of the historical run. However, the extreme future temperature distributions (either high or low) are most likely to change outside the historical range.

Li et al. (2010) recently proposed the equidistant cumulative distribution function matching (EDCDFm) method as an improvement to the cumulative distribution function matching (CDFm) method used as part of BCSD (bias correction step). EDCDFm explicitly considers the changes between the baseline and future distributions. It also fits the marginal CDF of precipitation and temperature with a mixed two-parameter gamma distribution and a four-parameter beta distribution respectively. By performing a synthetic experiment at a continental scale (northern Eurasia), they conclude that EDCDFm is superior to the CDFm method in that it reduces the mean bias and RMSE for summer and winter, especially under changing variability. Furthermore, EDCDFm is found to perform better than CDFm in correcting biases of extremes. However, as the original CDFm, EDCDFm is based on the idea of downscaling climatic variables individually. This method only concerns the bias correction step and presents no new spatial downscaling experiments or data.

Hidalgo et al. (2008) and Maurer et al. (2010) proposed and implemented the constructed analogues (CA) and the hybrid bias correction and constructed analogues (BCCA) techniques. The CA method essentially makes no bias corrections, but rather relates model-simulated variables to observed variables, using relationships established during historical periods when observations are available. These relationships are established through multiple regression analysis and are based on daily reanalysis data. Maurer and Hidalgo (2010) further investigated the application of a bias correction step before the CA process is performed and conclude that the BCCA method is consistently better than BCSD in simulating daily stream flows, especially for hydrologic extremes. The CA assumption is that the relationships between large-scale and downscaled fields derived based on historical reanalysis data will also be valid in future climates.

The primary advantage of the statistical downscaling techniques is that they are computationally efficient, and do not require the use of the full GCM climatic fields. Statistical downscaling techniques also bias correct the GCM outputs by comparing the

control (current climate) simulations with aggregated observations at GCM scales. Their disadvantage, however, is that some of their assumptions are only approximately valid.

The performance of downscaling methods varies across seasons, stations, and indices (Fowler and Blenkinsop, 2007). The accuracy of statistical downscaling methods has a geographical and seasonal component (Huth, 1999).

Overall, downscaled sequences must meet several criteria to be useful in regional water resources assessments: First, the downscaled sequences should be consistent with historical observations. Second, the downscaled sequences should capture climatic mean and variability trends. Third, spatial and temporal correlations and interdependencies between the atmospheric fields that largely drive hydrological processes should be represented. Lastly, to ensure that hydrological assessments at different temporal scales (e.g., annually, monthly, and daily) using the same downscaled products are consistent, the smoothness of these products across these time scales should be ensured.

2.3 Watershed Hydrological Models

Watershed models have been developed since the 1940s for applications ranging from streamflow forecasting (e.g., Thornwaite, 1948; Thornwaite and Mather, 1955; Alley, 1985; Xu and Vandwiele, 1995; Georgakakos and Baumer, 1996; and Mohseni and Stefan, 1998), simulation of land hydrological processes (e.g., Liang et al., 1994; Arnold, 2005; Vieux, 2001; Koren et al., 2004; and Carpenter and Georgakakos, 2004), and, most recently, climate change assessments (Lettenmaier and Rind, 1992; Stamm et al., 1994; Conway, 1998; Wood et al., 2004; and Maurer, 2007).

The simulation of the relevant processes of water flux over the delineated watershed area is the basis of almost all hydrologic models. These models can be generally distinguished as conceptual or physically based, depending on the way they represent the hydrological processes, such as rainfall, evapotranspiration, infiltration,

percolation, and runoff. There are also other model types based on input-output relationships such as Unit Hydrograph methods, SCS curve number approach, transfer functions models, time series models (e.g., ARMA), multiple regression models, artificial neural networks (ANNs), and transfer functions methods.

Another categorization of hydrologic models is based on the processes that each model represents. Thus, hydrological models can be distinguished in (1) models that represent water fluxes only, and (2) models that represent both water and energy fluxes. Models in the former category, such as SAC-SMA model (Burnash et al., 1973), only include water balance components, and require less input data and parameters than the latter. An example of water-energy flux model is the Variable Infiltration Capacity (VIC) model developed by Liang et al. (1992; 1994). The VIC model is a macro-scale hydrologic model that solves the coupled water and energy balance equations at sub-daily time steps. It is a physically-based and distributed model requiring input data for precipitation, temperature, wind, soil, vegetation, Aledo, and other parameters.

2.3.1 Physically-based Models

Physically-based models generally represent hydrological systems by small scale hill-slope drainage or channel storage elements. The physically-based models are used in many distributed hydrologic modeling systems such as SWAT (Neitsch et al., 2002), Mike 11 (Havno et al., 1995), tRIBS (Ivanov et al., 2004), VIC (Liang et al., 1994), TOPNET (Bandaragoda et al., 2004), HRCDHM (Carpenter and Georgakakos, 2003), HL_RMS (Koren et al., 2004), and etc. These models include models for rainfall-runoff vertical fluxes and channel routing.

For the rainfall-runoff and vertical flux component, Darcy-like or Richard-like equations are used in many cases to simulate the small scale hill-slope drainage (e.g., Bandaragoda et al., 2004, Stieglitz and Pan, 2006), and kinematic wave equations are used to simulate the surface flow (Vieux, 2001). In the coupled water-energy models, the

water and energy fluxes are considered simultaneously (e.g., Liang et al., 1994, Neitsch et al., 2002, Havno et al., 1995, Ivanov et al., 2004). The infiltration fluxes are also simulated by various dynamic equations such as Richard equations, Green-and-Ampt equations (Green and Ampt, 1911), Philip equations (Philip, 1957), Manley equations (Manley 1977), and others. The estimation of potential and actual evapotranspiration can be obtained either by temperature-based relationships or by radiation-based models, constrained by water/energy balance requirements.

The channel routing component is based on linear or nonlinear reservoir routing, Muskingum routing, Kinematic wave routing, Linearized St. Venant equations, and fully dynamic wave equations. The more complex routing models require more parameters for their successful calibration.

Physically based models depend on aggregating small scale physical models to represent large scale hydrologic processes. Such schemes generally result in a large number of model parameters and pose calibration challenges. Such difficulties can also be demonstrated by looking into the inherent equifinality problem when the model is matched to limited observations (Beven, 1996). The parameter estimation and the issue of over-parameterization will be discussed in the Section 2.3.3.

2.3.2 Conceptual Models

Conceptual models comprise a number of lumped storage elements which involve a limited number of parameters and are relatively easier to calibrate. The basis of most conceptual models is the principle of water balance expressed at various temporal scales (e.g., hourly, daily, weekly, monthly, and yearly). Unlike physically based models, conceptual models do not attempt to simulate every aspect of the underlying hydrologic processes, but rather simulate the relevant aggregate response by using appropriately lumped functions and parameters. These include precipitation partition to effective

precipitation and surface storage retention, soil moisture storage to multiple soil layers, storage-release response, percolation functions, evaportranspiration, and others.

One of the earliest studies on the conceptual hydrologic models is the Stanford watershed model developed by Crawford and Linsley (1966) at Stanford University, which later evolved into the hydrocomp simulation program (HSP). The Stanford model can be viewed as an explicit soil moisture accounting (SMA), and it has 35 parameters in total. Some of the parameters can be fixed according to physical conditions of the watershed or catchment. The SMA-type hydrologic models generate runoff based on storage elements and functions controlling the exchanges of water. Since the original Stanford model, a number of SMA-type models have been developed, some of which are still in use (Fleming, 1975; Singh, 1995). These include HSPF, SSARR, HBV, UBC, VIC, Xiaanjiang, and other models. In the United States, the Stanford model was extended to the Sacramento (SAC) model jointly by the United States National Weather Service (NWS) and the California State Department of Water Resources (Burnash et al., 1973). The SAC-SMA model has 16 parameters and is the basis of the operational NWS River Forecast System (Burnash, 1995). The success of the SAC-SMA models is largely due to their simplicity, efficiency, and predictive accuracy relative to the physically-based models.

Conceptual models have several parameters to fit rainfall-runoff data. It has been shown that increasing the number of parameters in a conceptual model can potentially increase model skill. However, there are also concerns of data over-fitting if the number of parameters becomes too large. Dawdy and O'Donnel (1965) tried to define a generic model structure with 16 parameters. Theirs was one of the early studies on the issue of model parsimony. **Chapter 4** addresses this aspect in more detail using an inductive approach.

2.3.3 Parameter Estimation Methods

Both physically-based and conceptual hydrologic models present parameter estimation challenges. Estimating model parameters has been the topic of many hydrological (Duan et al., 1994; Gupta and Sorooshian, 1998; Yapo et al., 1998; Duan et al., 2007; Wagener et al., 2009; and Apostolopoulos and Georgakakos, 1997).

Parameter calibration can be carried out using the deductive or the inductive approach. The deductive approach first assumes a certain model structure and then estimates the parameters through various optimization methods. The inductive approach does not assume any pre-defined model structure and parameters. Instead, it deciphers the model structure from the available data. The inductive approach begins with the consideration of first order model inter-relationships, functions, and parameters pertaining to the primary watershed hydrologic response. Additional model complexities are progressively introduced as necessary to represent more particular watershed response aspects. Deductive and inductive parameter estimation approaches are reviewed next in more detail.

Duan et al. (1994) proposed a population-evaluation based global optimization method known as the SCE-UA (shuffled complex evolution method developed at the University of Arizona) to calibrate the physically based and conceptual watershed models by using a single-objective function. It has shown to be an effective and efficient method in locating the global optimal model parameters. However, model calibration exercises have shown that a single-objective function is usually not sufficient to represent all model performance aspects.

Gupta and Sorooshian (1998) argued that parameter optimization schemes by using single-objective functions may not solve the model calibration problem fully. Their paper suggests that the inherent multi-objective nature of the hydrologic simulation require more powerful model calibration paradigms to evaluate multiple objectives and to explicitly recognize the role of model errors.

Yapo et al. (1998) extended the SCE-UA method by using the Multi-Objective Complex Evolution (MOCOM-UA) technique to calibrate the Sacramento Soil Moisture Accounting model (SAC-SMA) for the Leaf River watershed. This technique introduces the Pareto ranking instead of the algorithm ranking in its sorting routine. It uses a rank-based selection procedure to select the points closest to the Pareto set. The MOCOM-UA method was also applied to more complex physically based models.

Wagner et al. (2009) worked with distributed hydrological models and showed that it is important to use multiple evaluation metrics when assessing model predictions. They suggested a dynamic calibration process to take advantage of spatial parameter controls on model responses at different times. It was shown that even for a distributed model with so many parameters; there are no 'best' parameters that work for all times and under all scenarios.

Bae and Georgakakos (1992; 1994) developed a calibration procedure in which parameters are first manually initialized (Peck, 1976) and then optimized by an automatic downhill simplex optimization routine. They applied their technique to a modified Sacramento type model for the Upper Des Moines River basin. Among the model parameters, the upper soil free water capacity, tension water capacities, exponent of the percolation function, and fraction of base flow lost to deep groundwater are identified as the most important parameters for continuous river flow simulation during long periods.

The parameter estimation challenges documented in the literature provide evidence that the assumed model parameters are not truly identifiable and always end up fitting data instead of representing real underlying physical processes. Identifying appropriate model parameters is the most difficult step in hydrologic model building. For example, Wagener and Wheater (2006) explicitly explored the impact of model structure errors on the identification of parameters to be regionalized. They concluded that the uncertainty in the locally estimated model parameters is a function of their importance in representing the response of a given catchment. Parameters associated with major

hydrologic processes in a well structured conceptual model are called controlling parameters and regionalize easier than those representing secondary hydrologic processes.

2.3.3 Nonlinear Storage-Release Relationships

A core component of conceptual hydrologic models is the soil moisture storage release function. This function determines the flow contribution from soil layers, and it has linear or non-linear forms. Although linear storage-release forms (e.g., Wood, 1992) have been broadly used, there is increasing interest in developing nonlinear storage-release relationships (e.g., Amorocho, 1963, 1967; Wittenberg, 1999; Mishra et al., 2003; Brutsaert, 2005; and Botter, 2009). The nonlinearity of storage-release relationships can be represented by quadratic and polynomial functions, exponential functions, and power functions.

Amorocho (1963, 1967) investigated the nonlinear watershed response by using higher power function series on a laboratory catchment. It was shown that by incorporating nonlinear functions, the forms and magnitudes of flood events were better represented than those obtained from linear approximation functions such as the unit hydrograph. Amorocho's nonlinear model was calibrated by a trial-and-error method and it was later improved by Helweg et al. (1982). Amorocho's study was also followed by several discussions on the applicability of nonlinear time series on hydrologic prediction.

Wittenberg (1999) developed deterministic nonlinear reservoir algorithms extended for separation of base flow from daily river discharges of 14 stations in the upper Weser and Ilmenau basins in Germany. The nonlinear relationships are estimated from a numerical analysis of the flow recession curves with power function forms. This non-linear reservoir function is found to be a more realistic alternative to the linear reservoir function. By using an inverse nonlinear reservoir routing algorithm, Wittenberg

estimated the recharge flux from groundwater to the river system and used it to estimate the long term water balance changes.

The storage-release functions can also be analyzed by performing flow recession analysis. Horton (1941) was one of the earliest hydrologists who suggested the use of power laws for flow recession curves, followed by Brusaert and Niber (1977). The recession analysis has been based on nonlinear reservoir models representing the subsurface flows (e.g., Brutsaert and Lopez, 1998; Lyon and Troch, 2007; Rupp and Woods, 2008). More recently, Kirchner (2009) working with two small watershed also showed that the storage-release function has a power function form. Gupta et al. (1996), Furey and Gupta (2005; 2007) also showed that peak-discharge and drainage area are related through a power law. Their conclusions are based on two empirical studies with the Goodwin Creek experimental watershed.

In addition to the storage-release function, the infiltration and percolation functions also play key roles in model performance. At small spatial scales, these functions can be fully characterized using, for example, the Green-and-Ampt (Green and Ampt, 1911) or the Richards equations (Richards, 1931). At watershed scales, however, direct application of such approaches is inadequate.

In the Soil and Water Assessment Tool (SWAT) model developed by USDA, the percolation is calculated by the storage routing methodology with a parameter of the drainable volume of water and an exponential form of the function including two routing parameters: the time step and the travel time for percolation. The water percolates from the lowest layer to the vadose zone, which lies between the bottom of the soil column (modeled by hydrologic models) and the top of the aquifer.

In the Sacramento Soil Moisture Accounting (SAC-SMA) model, the percolation function has an exponential form with two parameters. The top and bottom storage layer drainage is expressed in linear form with one coefficient. The Variable Infiltration Capacity model developed by Liang et al. (1992, 1994) has a unique infiltration scheme

by using the variable infiltration curve in an exponential form with three parameters: maximal infiltration capacity, infiltration shape parameter, and the fraction of an area of infiltration deficiency.

In the previous studies, the watershed functions (linear or nonlinear) are based on the assumption that they have a particular form including certain hydrologic state variables (e.g., soil moisture, evaportranspiration, and effective precipitation) and parameters. However, few studies address the question whether such assumptions represent the real hydrologic processes.

Stochastic approaches have also been used in developing conceptual hydrologic models. Both linear stochastic models (e.g., Harms and Campbell 1967, Klemes 1978, Salas and Smith 1981) and nonlinear stochastic models (e.g., Kavvas 2003, Botter 2009) have been investigated. Most of the earlier studies focus on the stochastic nature of rainfall, runoff, lake volumes, and other hydrologic variables. More recent studies pay more attention on the stochastic nature of model structure and functional parameters. For example, the nonlinear stochastic approaches have investigated how different function forms and parameters contribute to model output uncertainty. Botter (2009) developed an analytical stochastic solution for runoff variability by using different nonlinear forms, including concave and convex power and hyperbolic forms. Botter also introduced probabilistic measures for the nonlinear storage-release function, so that runoff can be estimated in a stochastic framework. It is found that different stream flow distributions are directly related to nonlinear features of the storage-runoff relationship.

2.3.4 Data-driven and Inductive Modeling Approach

Most hydrologic modeling approaches preselect the model structure and parameters based on prior model calibration experience. Young (1993, 1998, 1999, and 2003) classified such models as hypothetic-deductive type, which implies that certain structural assumptions are made first, and then the associated parameters are estimated using

various methods. Alternatively, the inductive approach infers the functional model forms and associated parameters directly from data, the aim being to keep the model order and complexity minimal while achieving maximal statistical significance. In other words, the inductive modeling approach seeks to identify the simplest model structure supported by the data.

Yong and Beven (1994) discussed the data-based mechanistic approach in identifying the structure of IHACRES model. There is no need to fix the model structure beforehand, but instead, an analysis of the data itself suggests the appropriate structure forward. The model is identified by using statistical inference techniques on a a generic class of linear transfer function models whose parameters are allowed to change over time.

Bai et al. (2009) proposed a top-down strategy for model evaluation and selection under uncertainty. The watershed model structures with increasing complexity were applied to twelve watersheds with different characteristics in the US. Their model selection process is automated by combining the reliability and shape performance measures in a fuzzy rule system.

Another inductive modeling approach was recently proposed by Kirchner (2009) when studying two headwater catchments of the Severn and Wye rivers at Plynlimon, Wales. Each catchment is represented by a single storage element. The discharge from the single storage is determined by the storage alone and the storage-release function is estimated from an analysis of stream fluctuations. The catchment sensitivity to changes in storage is estimated by identifying times when the precipitation and evapotranspiration are relatively small. In cross validation, the Nash-Sutcliffe (N-S) efficiencies for the two watersheds were found to range from 0.82 to 0.94. This N-S efficiency range is compatible with a 4-parameter model.

Kirchner's modeling scheme can be improved by adding extra components into the model structure (i.e., a second storage element) that would expand the applicability of

such models to larger spatial and temporal scales. Majone et al. (2010) applied the flow sensitivity analysis by using a two storage model, calibrated by particle swarm optimization (PSO) method for four small Alpine catchments in the northeastern part of Italy. Their model generated runoff by adding the discharges from both a non-linear storage (superficial layer) and a linear storage (underground layer). They found that the model can reproduce the observed discharges better and more consistently. However, such extensions complicate the underlying function and parameter identification process.

Teuling et al. (2010) applied Kirchner's daily conceptual model to a Swiss watershed (Rietholzbach). Instead of using multiple storage elements, Teuling splits the runoff function g(Q) to three regions and use a piecewise linear regression to fit the data points falling in these regions. They found that the stream flow recession at the daily time scale shows a marked seasonal cycle due to seasonal changes of evapotranspiration. They also concluded that better results can be obtained when the discharge sensitivity function is calibrated on a monthly time step to avoid the impact of diurnal cycles. However, the seasonal differences in the discharge sensitivity function are physically due to different response characteristics of varies surface/soil layers. For instance, the outflow from lower soil layer may response to the storage changes in a rate much slower than the upper soil layer and the surface layer.

This study uses a watershed model with two or three storages and storage-release and percolation functions derived based on an inductive approach. Model parameters are estimated using a recursive identification methodology suitable for multiple, inter-linked modeling components.

The thesis also introduces a new downward inductive modeling approach to identify model structures and parameters suitable for a certain scale. This approach starts from aggregate spatial and temporal scales and proceeds to introduce more detailed processes and relevant parameters as spatial and temporal resolution increases until no improvements of the modeling performance can be achieved.

The new model is applied here to intermediate scale watersheds (10^2 to 10^4 square miles) at monthly time resolution. However, the modeling concept is applicable to finer spatial and temporal scales, with additional modeling elements used to represent hydrologic process that become important at finer scales. We have tested the model on several small experimental watersheds (10 to 10^2 square miles) in Tifton, Georgia (not shown in this Thesis). The calibrated watershed models are employed to characterize the hydrologic watershed response under the historical and future climate scenarios.

2.4 Hydrologic Regionalization Models

Hydrological measurements (e.g., catchment runoff) are often limited both temporally and spatially. Data deficiencies in ungauged and poor-gauged watersheds pose challenges in the calibration and verification of hydrologic models.

Hydrologic regionalization seeks to transfer information from one catchment to another (Bloschl and Sivapalan, 1995). Early attempts to create regionalization relationships focused on modeling hydrologic catchment behaviors in ungauged or poorly gauged areas. Regionalization is typically performed with watershed hydrologic models and works well with parsimonious models. This outcome is attributed to the parameter uncertainty inflation caused by the more complex models. The following two sections review the literature on regionalization methods and applications.

2.4.1 Regionalization Methods

Early hydrologic model regionalization studies simply use parameters derived from proxy catchments or neighboring catchments (e.g., Klemes, 1986, Mosley, 1981, Vandewiele and Elias, 1995). The assumption under this approach is that the nearby catchments should have same or similar hydrologic behavior. Guo et al. (2001) uses a linear interpolation method to spatially interpolate model parameters within a region.

Vandewiele and Elias (1995) use kriging interpolation instead. Such an assumption, however, is not true for many places where nearby catchments may have very different hydrologic features (Post et al., 1998).

Burn and Boorman (1993) applied a clustering method to estimate the hydrological parameters at ungauged catchments. They classify the catchments into groups according to their flow regime and assign each catchment to a group based on its physical characteristics. Finally, they use similarity relationships to transfer parameters from gauged to ungauged catchments. A similar approach is also tested by Huang et al. (2003) and Marechal and Holman (2005).

Koren et al. (2003) use soil properties to directly derive parameters in the Sacramento Soil Moisture Accounting (SAC-SMA) model. The soil texture data in 11 soil layers are used to derive analytical relationships for the 11 parameters used by SAC-SMA. However, the soil parameters used are from point measurements, while the SAC-SMA model is a conceptual model representing aggregated watershed response. These scale differences create severe challenges for this approach.

The most commonly used regionalization approach is to relate model parameters with catchment characteristic in a statistical manner (e.g., Abdulla and Lettenmaier, 1997, Post et al., 1998, Sefton and Howarth, 1998, Seibert, 1999, Xie et al, 2006, Wagener and Wheater, 2006). Using the same hydrologic model, many catchments are calibrated to derive a set of parameters. The watershed descriptors for the same catchments are also obtained from different sources. The model parameter sets are then regressed on catchment descriptors. Different regression methods have been used for such purpose with reported to be successful while others are not encouraging. In recent studies, the uncertainties of the regionalization models have drawn considerable attentions (e.g., Kling and Gupta, 2009, Wagener and Wheater, 2006).

Kling and Gupta (2009) investigated how the sub-basin scale variability impacts the development of regionalization relationships. They found that the noise in the lumped

parameters diminishes the correlation with catchment properties and concluded that the degree of spatial variability of sub-catchment scale processes must be taken into account.

Wagener and Wheater (2006) explicitly explored the impact of model structure errors on the identification of parameters to be regionalized. They conclude that the uncertainty in the locally estimated model parameters is a function of their importance in representing the response of a given catchment. It can be expected that for a well structured conceptual model, the parameters representing the major hydrologic features (such as storage capacity and lag time) will be regionalized easier than those representing hidden or secondary hydrologic processes.

One recent study by Kokkonen et al. (2002) use a top-down approach to create regionalization models predicting daily flows. The factors controlling parameter variability are identified first and such information is used in smaller sub-regions. They concluded that the interrelationships between model parameters should be retained in the regionalization model instead of deriving quantitative relationships between parameters and catchment descriptors individually.

2.4.2 Regionalization Applications

Regionalization and the prediction of the response of ungauged catchments have been major objectives of the International Association of Hydrological Sciences known as Prediction in Ungauged Basins (PUB). Its applications range from filling missing stream flow data, estimating flooding or low flow frequencies of ungauged catchments, providing guidelines for civil infrastructures in ungauged basins, providing the scientific bases for ecosystem studies in ungauged areas, and several others.

Verification of catchment classification datasets is another application of regionalization models. Marechal and Holman (2005) developed the catchment resources and soil hydrology (CRASH) model and applied it to three catchments in England with parameterized values from the existing national hydrology of soil types (HOST)

classification. The model successfully simulates the daily flows in all three catchments. However, the relationships between HOST classes and the CRASH model are not fully regionalized models. It only verifies the classification of a specific watershed. In order to regionalize the parameters, a single set for each HOST class needs to be derived and verified.

There is also increasing interest in applying regionalization approaches to assess the impact of land use change on catchment hydrology (e.g., Heuvelmans et al., 2004, Hundecha and Bardossy, 2004, Brath et al., 2003). The regionalization models are developed first for historical periods when no significant land use changes are observed. They are then used to model the resulting runoff and other hydrologic variables for different land use scenarios generated in the model area.

Regionalization models are also useful to characterize the response of ungauged watersheds under future climate scenarios. Furthermore, for places where both climate *and* land use changes impacts are to be assessed, parameter regionalization is a necessary component for integrated assessments.

2.5 Climate of the Southeast US

Southeast US includes the states of Alabama, Georgia, Florida, North Carolina, South Carolina and Tennessee. It has a warm, humid, and temperate climate, typical of the tropics and subtropics, with mild winters and hot summers. Most of the precipitation in winter months falls as cold rain from large cyclonic storm systems. During summer months, the climate is hot and humid with rain falling in heavy downpours from localized convective thunderstorms.

2.5.1 Hydro-climatic Conditions

Georgia river basins experience all four seasons, with monthly mean temperature varying from 39°F (4°C) in the winter to 76°F (25°C) in the summer. The average annual precipitation over Georgia is 50 inches (1250 mm). Spatially, annual precipitation varies from 45 inches (1100 mm) in central Georgia to approximately 75 inches (1900 mm) in the northeast corner of the state. Water in Georgia originates mainly as rainfall and occasionally as snow or sleet. Over the long term, approximately 70 percent of Georgia's precipitation becomes evapotranspiration (ET), while the remaining 30 percent becomes runoff and stream flow. These percentages vary seasonally and by watershed location, with ET being higher during summer and at lower latitudes.

Figure 2.1: Photos of upper Chattahoochee River (left) and upper Flint River (right). (Acquired from NWS website: http://www.georgiaencyclopedia.org on June 5, 2011)

Surface water availability is a major concern in Georgia. Georgia's geological conditions play a key role in shaping watershed surface features, including soil type, hydrology, and stream morphology. The rivers and streams emanating from the Blue Ridge Mountains of north Georgia (e.g., the upper Chattahoochee River as shown in **Figure 2.1**) are generally fast-flowing, cold, and clear. In the Piedmont (e.g., middle Chattahoochee and upper Flint Rivers as shown in **Figure 2.1**), rivers are slower because of the flatter, rolling topography. Rivers and streams below the fall line (e.g., Apalachicola and lower Chattahoochee and Flint Rivers) exhibit varying degrees of

aquifer interactions. Lime sinks, sinkholes, and springs are common in this part of the Georgia.

Groundwater is another critical water resource especially in southern Georgia, where agricultural irrigation relies heavily on groundwater pumping. The fall line runs across Georgia and the ACF river basin northeastward from Columbus to Augusta. It separates the Upper Coastal Plain sedimentary rocks to the south from the Piedmont crystalline rocks to the north. This leads to a clear separation of groundwater aquifer systems between the north and south parts of Georgia.

The Valley and Ridge (Paleozoic Rock) Aquifers consist of limestone underlying the valleys. These aquifers are generally very productive. The Piedmont and Blue Ridge Aquifers are crystalline rock aquifers and they consist of bedrock overlain by unconsolidated material called regolith. Groundwater can be obtained from either regolith or fractures in the rock, with high yield.

The Upper Floridian Aquifer, underline most of South Georgia, is confined by clay layers, and it is shallow and productive. In the lower Flint River basin in South Georgia, the aquifer is semi-confined, and it is primarily used for agricultural pumping. The Claiborne and Cretaceous Aquifers in South Georgia consist of sands and gravels deposited on ancient beaches and are not as productive as the Upper Floridian Aquifer.

2.5.2 Precipitation

The mechanisms of Georgia's precipitation vary from season to season. Frontal storms are common during winter, spring, and fall, while convective storms dominate during summer. Hurricane-induced tropical storms are also common during the hurricane season from June to November. Strong El Niño years tend to be wetter than normal,

while La Niña years are drier. Overall, annual precipitation varies by as much as 40 percent of the long term mean.

Figure 2.2 shows the seasonal (DJF, MAM, JJA, and SON) precipitation climatology over Georgia and the ACF basin, based on historical data from 01/1950 to 12/1999. The figures show that the northeastern ACF region (Blue Ridge) receives much more precipitation than the rest of the basin, except during summer and fall when southern Apalachicola in Florida is impacted by tropical cyclones and summer thunderstorms. The Blue Ridge Mountains have the most frequent snowfall in Georgia, although snowfall is less than other regions of the Appalachian Mountains.

We also aggregated the precipitation field (climatology) into different basin areas in Georgia to derive the monthly precipitation climatology by sub-basin. All basins exhibit a similar monthly precipitation pattern with highs in March and July and lows in October. The July high and October low become more pronounced for watersheds in lower latitudes. The Buford watershed, extending in the Blue Ridge Mountains, receives the highest precipitation amounts in all months.

2.5.3 Temperature

Georgia's temperature exhibits temporal and spatial variations due to regional geographic and climatic features. **Figure 2.3** shows the ACF seasonal temperature climatology (DJF, MAM, JJA, and SON) based on the historical data from 01/1950 to 12/1999. Seasonal average temperature variations of 3 to 6 degrees are observed from north to south, with the northeastern region being colder due to its topography.

All sub-basins exhibit similar patterns. The hottest months are July and August with temperatures varying from 22°C to 28°C, while the two coldest months are December and January with temperatures varying from 4°C to 10°C.

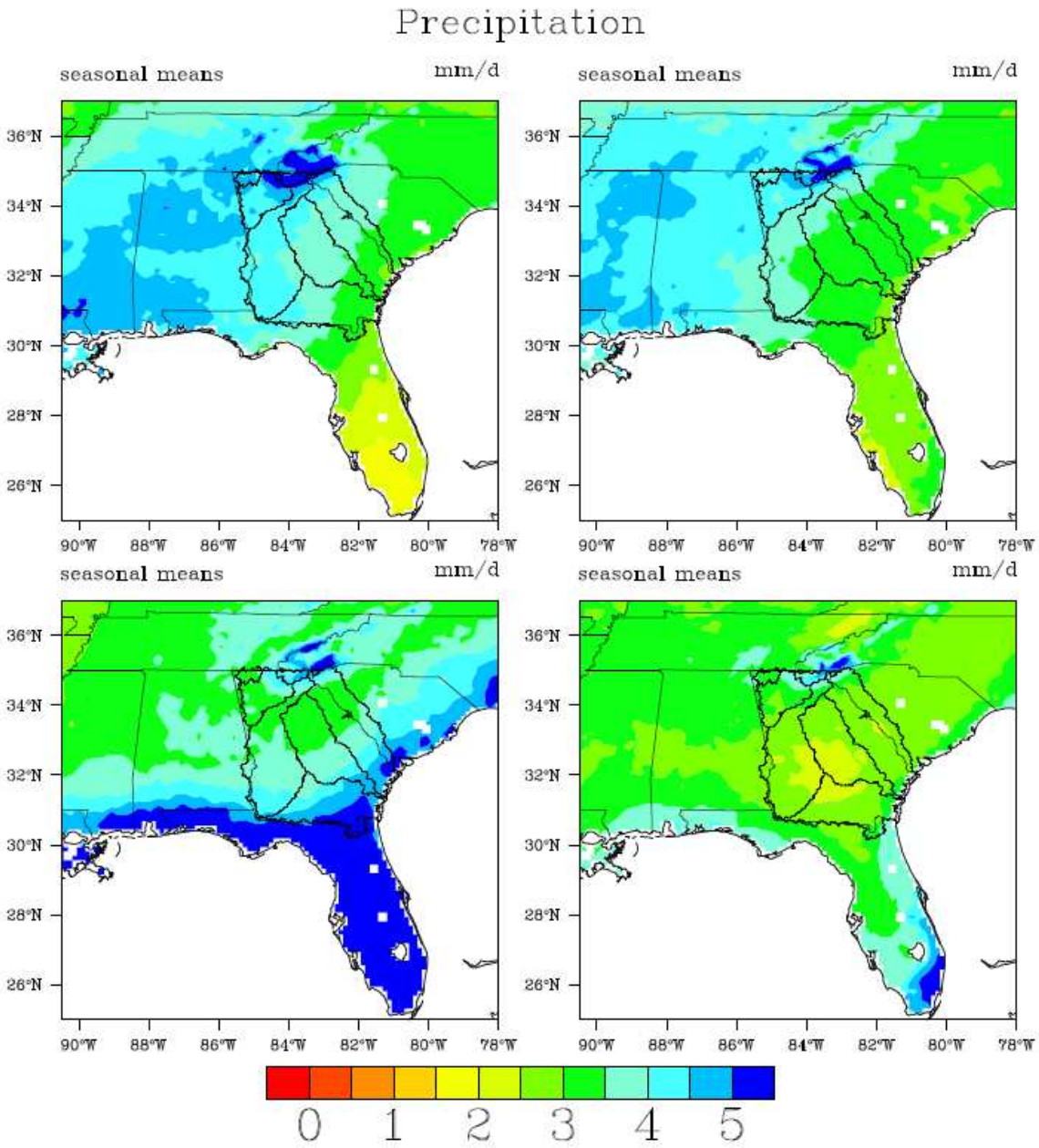

Figure 2.2: Seasonal Precipitation Climatology of the Southeast US: DJF (top left), MAM (top right), JJA (bottom left), and SON (bottom right).

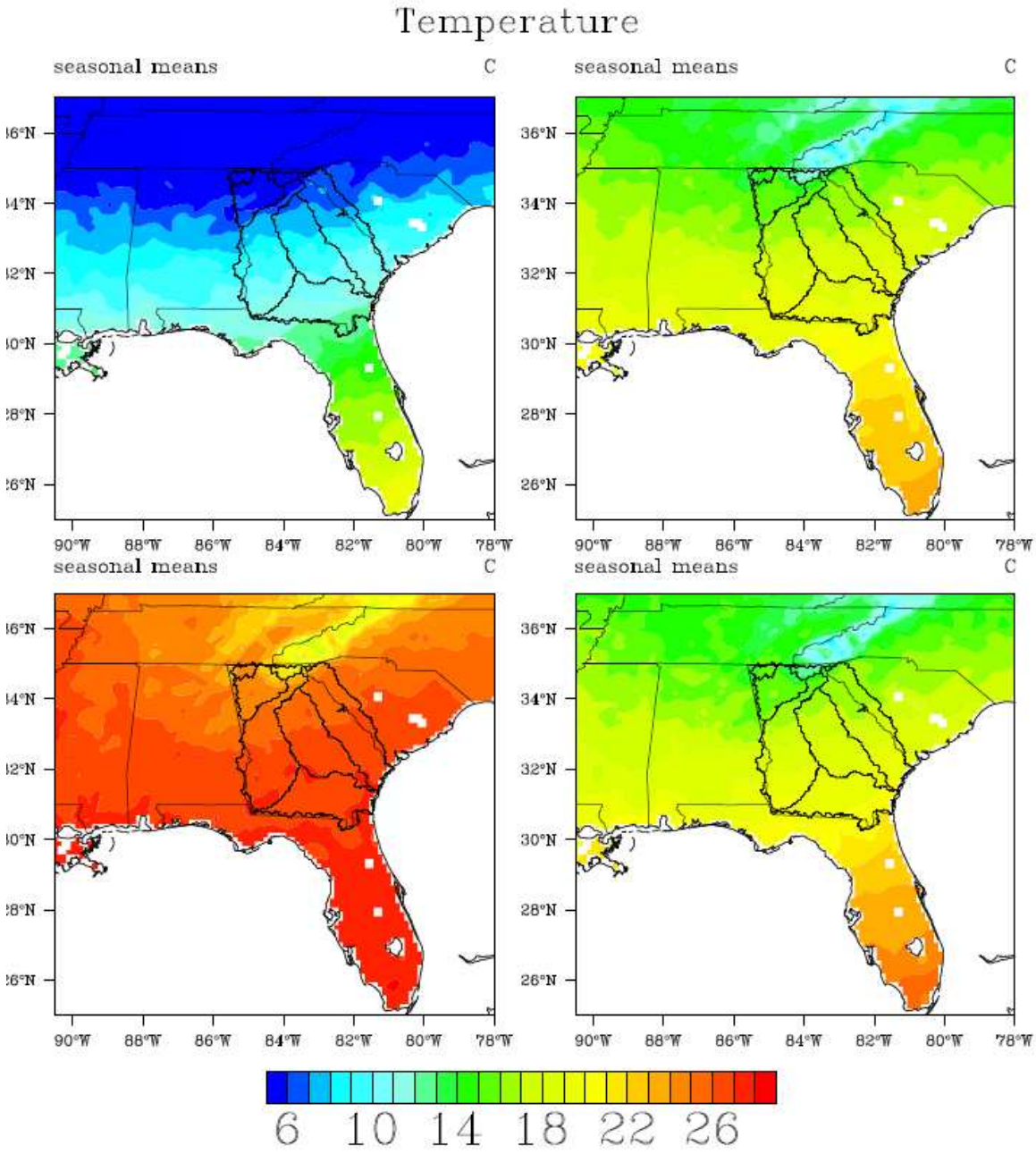

Figure 2.3: Seasonal Ground Air Temperature Climatology of the Southeast US: DJF (top left), MAM (top right), JJA (bottom left), and SON (bottom right).

2.6 Georgia River Basins

2.6.1 Apalachicola-Chattahoochee-Flint (ACF) River Basin

The Apalachicola-Chattahoochee-Flint (ACF) river system (**Figure 2.4**) is shared by three southeast states: Georgia, Alabama, and Florida. It begins from north Georgia and flows into the Gulf of Mexico, near Apalachicola, Florida. The total ACF drainage area is 19,600 square miles.

The Chattahoochee River originates in the Blue Ridge Mountains of the Appalachian Highlands in northeast Georgia, and flows southwesterly for 120 miles and then southerly along the Georgia - Alabama border for another 200 miles. The Chattahoochee drainage basin is 8,770 square miles. The Flint originates south of Atlanta and flows in a southerly direction toward the Coastal Plain where it joins the Chattahoochee River at Lake Seminole. The Flint River drainage basin is 8,460 square miles. The releases from Lake Seminole enter the Apalachicola River which lies in the Coastal Plain over its entire length of 108 miles and flows south across northwest Florida to the Apalachicola Bay. The Apalachicola River drainage basin is 2,370 square miles.

The Chattahoochee flows are highly regulated by a series of federal and private reservoirs. The federal reservoirs operate for multiple purposes, including flood control, water supplying, hydropower, navigation, water quality, recreation, and aquatic life protection, while the private reservoirs are power facilities. The Flint and Apalachicola Rivers are largely unregulated.

Based on the locations of major storage projects and the geography of the basin, this study distinguishes the sub-basins with the following outlets: *(1)* Buford dam, *(2)* Norcross, *(3)* Atlanta, *(4)* Whitesburg, *(5)* West Point dam, *(6)* Columbus, *(7)* W.F.

George dam, *(8)* Columbus, *(9)* Woodruff dam, *(10)* Montezuma, *(11)* Albany, *(12)* Milford, *(13)* Newton, *(14)* Iron City, and *(15)* Bainbridge.

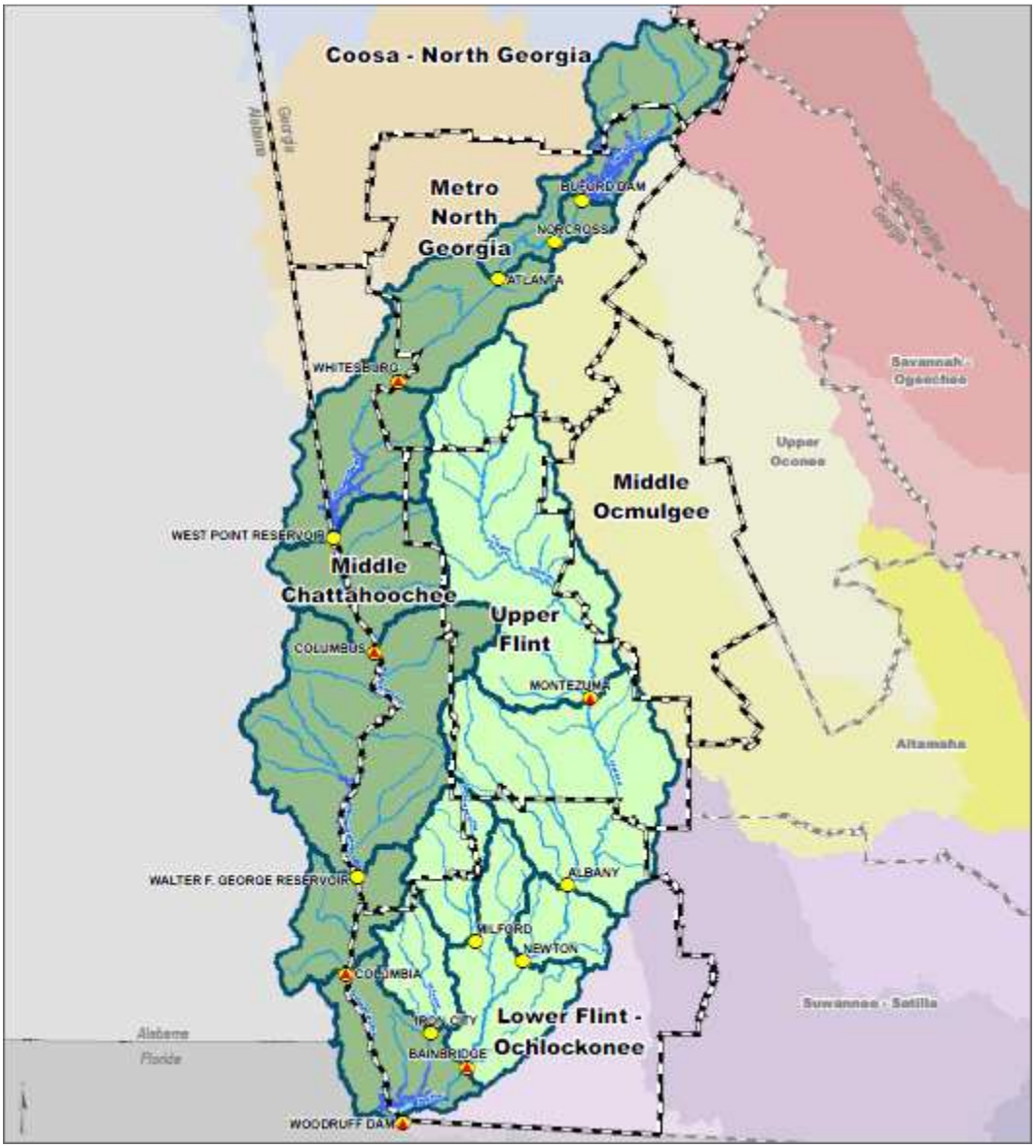

Figure 2.4: The Apalachicola-Chattahoochee-Flint (ACF) River System (Courtesy: Georgia Environmental Protection Division).

2.6.2 Alabama-Coosa-Tallapoosa (ACT) River Basin

The Alabama-Coosa -Tallapoosa (ACT) river system (**Figure 2.5**) is shared by Georgia and Alabama. It begins from north Georgia and continues across the border into Alabama. The total ACF drainage area is 22,500 square miles.

The Alabama River basin has its source in the Blue Ridge Mountains of northwest Georgia. The Tallapoosa River originates west of Atlanta, and flows westerly for about 100 miles before it enters Alabama. The Tallapoosa drainage basin is 4,680 square miles, of which 720 square miles lie in Georgia and 3,690 square miles are in Alabama. The Coosa river is formed by the convergence of the Etowash and Oostanaula rivers and flows into the Gulf of Mexico in southwest Alabama.

The Tallapoosa and Coosa rivers are regulated by several federal and private projects. There are six major hydroelectric projects constructed by the Alabama Power Company (APC) on the Coosa and Tallapoosa Rivers and two US Army Corps of Engineers (USACE) projects, Allatoona and Carters, located above the APC Coosa projects. There are several federal lock and dam facilities on the Alabama River including the Robert F. Henry, Millers Ferry, and Claiborne. The ACT rivers support threatened and endangered aquatic species as well as a significant for fishing industry in Alabama.

Based on the location of major storage projects and the basin geography, this study distinguishes the following ACT sub-basins: *(1)* Tilton, *(2)* Resaca, *(3)* Carters Lake, *(4)* Caters Reregulation Dam, *(5)* Pine Chapel, *(6)* Oostanaula, *(7)* Canton, *(8)* Alatoona Dam, *(9)* Kingston, *(10)* Etowah, and *(11)* Coosa.

Figure 2.5: Alabama, Coosa, and Tallapoosa (ACT) River Basin (Courtesy: Georgia Environmental Protection Division).

2.6.3 Oconee-Ocmulgee-Altamaha (OOA) River Basin

The Oconee-Ocmulgee-Altamaha (OOA) river system (**Figure 2.6**) is located entirely within Georgia. A major continental divide occurring between the Ocmulgee and Flint rivers causes the Altamaha River basin to drain into the Atlantic Ocean. The total OOA drainage area is 14,260 square miles.

The Oconee and Ocmulgee River begins from the foothills of the Appalachians meet the Altamaha River in the Upper Coastal Plain, and flows into the Atlantic Ocean. The Ocmulgee River basin is located in the Piedmont and Coastal Plain physiographic provinces of Central Georgia. The Oconee River basin is located just east of the Ocmulgee River basin and is formed by the confluence of the Middle and North Oconee rivers. Farther downstream of the confluence, the tributary joins the Altamaha River. The Altamaha River basin is the largest watershed in Georgia draining into the Atlantic Ocean. The Altamaha River is part of the large Floridian aquifer which becomes shallower near the fall line. In the lower Altamaha River basin, the majority of domestic water supply comes from groundwater.

The Oconee River and Ocmulgee River are regulated by several hydropower reservoirs (Lake Jackson, Lake Oconee, and Lake Sinclair) operated by Georgia Power. The Altamaha River is unregulated, having no federal or private power storage reservoirs in its drainage basin.

This study distinguishes the following OOA sub-basins: *(1)* Jackson, *(2)* Macon, *(3)* Lumber City, *(4)* Athens, *(5)* Penfield, *(6)* Milledgeville, *(7)* Dublin, *(8)* Mount Vernon, *(9)* Baxley, *(10)* Reidsville, and *(11)* Doctortown.

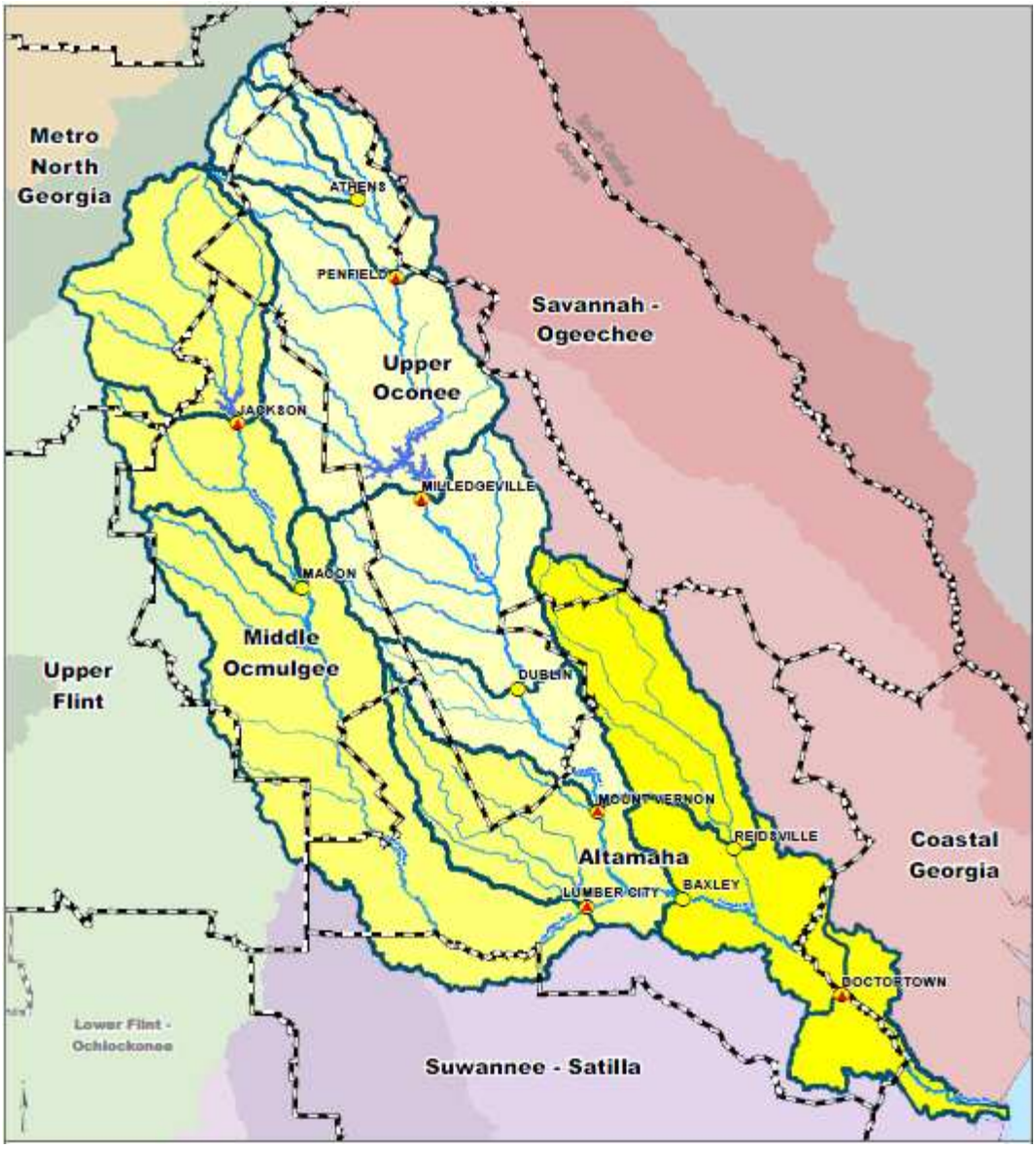

Figure 2.6: Oconee-Ocmulgee-Altamaha (OOA) River Basin (Courtesy: Georgia Environmental Protection Division).

2.6.4 Savannah-Ogeechee (SO) River Basin

The Savannah-Ogeechee (SO) river system (**Figure 2.7**) is shared by Georgia, South Carolina and a small portion of North Carolina. It is located in northern and eastern Georgia, originating in the Blue Ridge Mountains. The total SO drainage area is 10,580 square miles.

The Savannah River begins at Lake Hartwell, in Hart County, at the confluence of the Seneca and Tugaloo rivers and flows easterly toward Savannah into the Atlantic Ocean. Above the junction of the Seneca and Tugaloo rivers, the major headwater streams of the Seneca River are the Keowee River and the Twelve Mile Creek. The Ogeechee River begins in the southeastern edge of the Piedmont physiographic region and flows 245 miles in a southeasterly direction to the Atlantic Ocean.

The SO is one of the most complex and highly-regulated basins in Georgia. The Savannah River upstream of Augusta is highly regulated by three large multipurpose USACE reservoirs (Hartwell, Richard B. Russell, and Thurmond), and a number of private reservoirs owned by Georgia Power and Duke Energy. The Corps New Savannah Bluff Lock and Dam and the South Carolina Electric and Gas Stevens Creek project are located downstream of Augusta, both of which are essentially run-of-river projects.

This study distinguishes the following SO sub-basins: *(1)* Lake Keowee, *(2)* Hartwell Reservoir, *(3)* Russell Reservoir, *(4)* Bell, *(5)* Thurmond Reservoir, *(6)* Augusta, *(7)* Millhaven, *(8)* Burtons Ferry, *(9)* Clyo, (10) Eden, *(11)* Claxton, *(12)* Kings Ferry, and *(13)* Savannah.

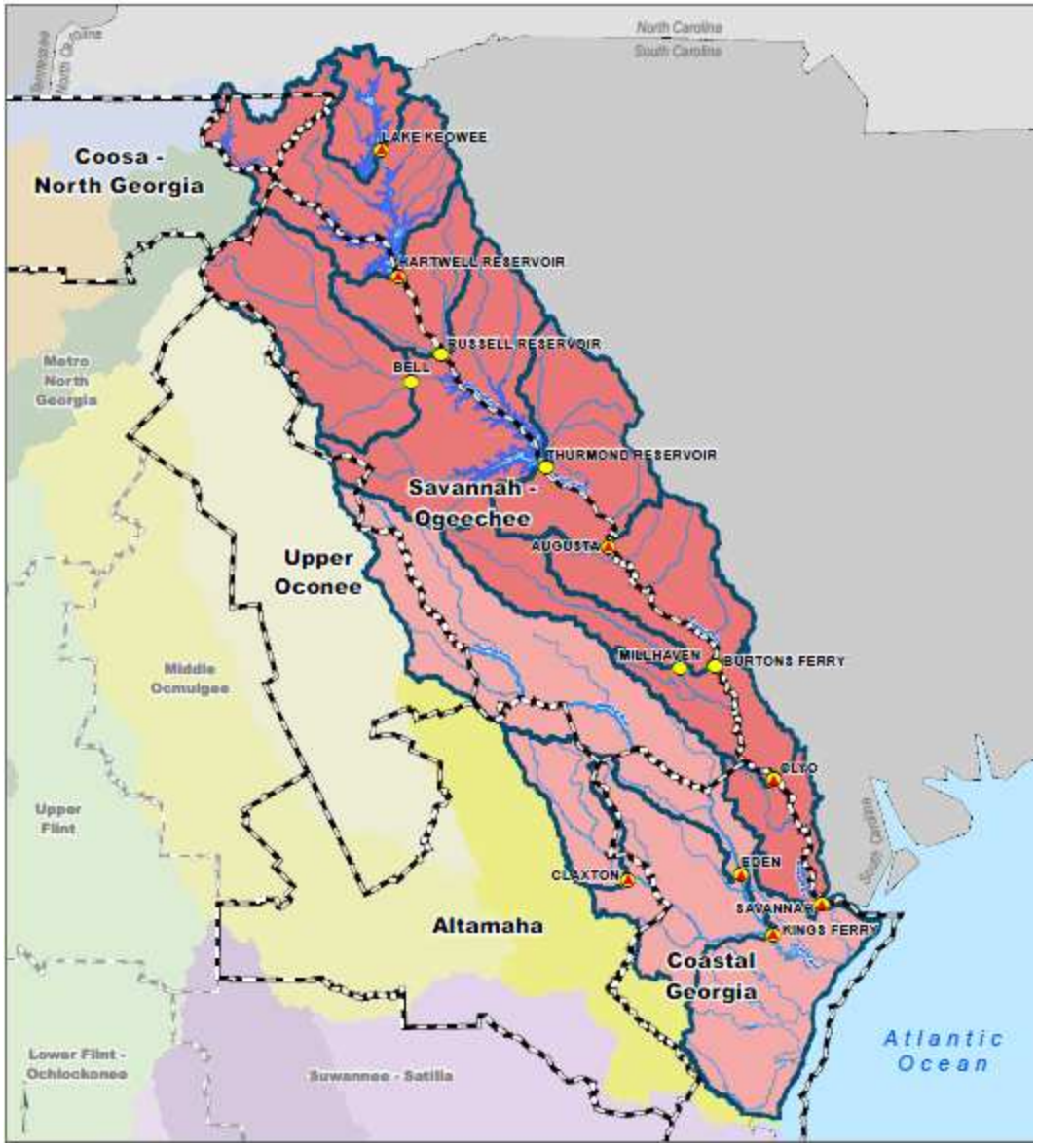

Figure 2.7: The Savannah-Ogeechee (SO) River System (Courtesy: Georgia Environmental Protection Division).

2.6.5 Ochlocknee-Suwannee-Satilla-St. Mary's (OSSS) River Basin

The Ochlocknee-Suwannee-Satilla-St. Mary's (OSSS) river system (**Figure 2.8**) is located in southern Georgia across the border with Florida. The total OSSS drainage area is 10,450 square miles.

The Ochlocknee River begins approximately 19 miles southeast of Albany; the Suwannee River begins approximately 9 miles south of Waycross; the Satilla River begins approximately 25 miles east of Tifton; and the St. Mary's River begins approximately 14 miles east of Lake City. The Ochlochnee River and Suwannee Rivers flow into the Gulf of Mexico, and the Satilla River and St. Mary's Rivers flow into the Atlantic Ocean. The OSSS basin is unregulated, having no federal or private power storage reservoirs.

This study distinguishes the following OSSS sub-basins: *(1)* Quincy, *(2)* Concord, *(3)* Thomasville, *(4)* Quitman, *(5)* Bemiss, *(6)* Alapaha, *(7)* Jennings, *(8)* Statenville, *(9)* Waycross, *(10)* Fargo, *(11)* Offerman, *(12)* Atkinson, *(13)* Gross, and *(14)* Macclenny.

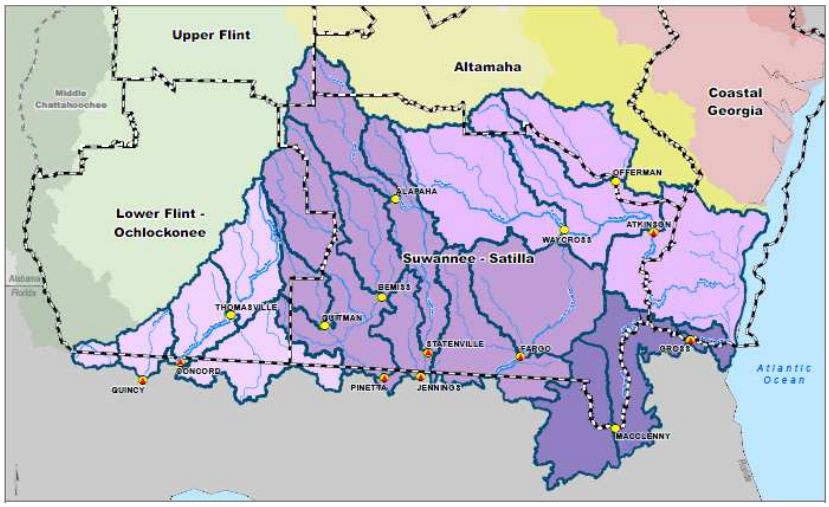

Figure 2.8: The Ochlocknee-Suwannee-Satilla-St. Mary's (OSSS) River System (Courtesy: Georgia Environmental Protection Division).

2.6.6 Tennessee (TN) River Basin in Georgia

The Tennessee (TN) river basin (**Figure 2.9**) in Georgia is located in north of Georgia across the border with North Carolina. The total TN drainage area is 2100 square miles.

The Little Tennessee River begins in Georgia and drains north into North Carolina. The Toccoa-Nottley-Hiwassee begins in Georgia and drains northwest into Tennessee and North Carolina. The South Chickamauga-Lookout Creek basin begins in Georgia and Alabama and drains north into Tennessee. These three rivers are regulated by three reservoirs respectively for the purpose of flood control and hydropower.

This study distinguishes the following TN sub-basins: *(1)* New England, *(2)* Chickamauga, *(3)* Copperhill, *(4)* Blue Ridge Reservoir, *(5)* Nottely Dam, *(6)* Chatuge Dam, and *(7)* Little Tennessee.

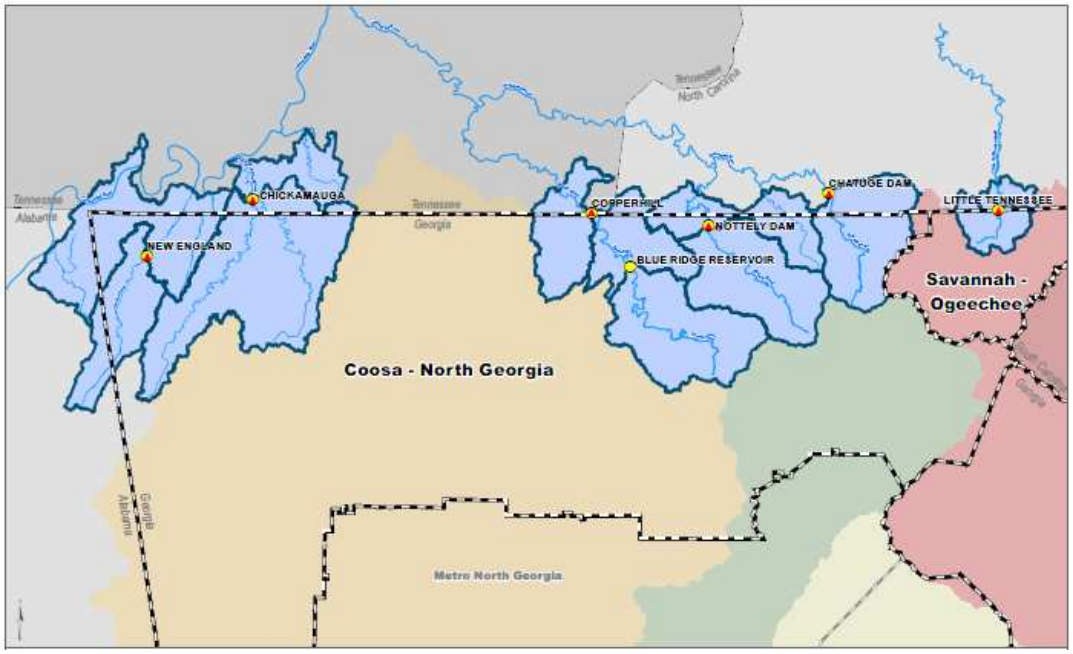

Figure 2.9: The Tennessee (TN) River System (Courtesy: Georgia Environmental Protection Division).

CHAPTER 3

JOINT VARIABLE SPATIAL DOWNSCALING

In this chapter, we develop a new statistical technique for downscaling gridded climatic variables, joint variable spatial downscaling (JVSD), to generate high resolution gridded datasets for regional watershed modeling and assessments. The proposed approach differs from previous statistical downscaling methods in that multiple climatic variables are downscaled simultaneously and consistently to produce realistic climate projections.

In the bias correction step, JVSD uses a differencing process to create stationary joint cumulative frequency statistics of the variables being downscaled. The functional relationship between these statistics and those of the historical observation period is subsequently used to remove GCM bias. The original variables are recovered through summation of bias corrected differenced sequences.

In the spatial disaggregation step, JVSD uses a historical analogue approach, with historical analogues identified simultaneously for all atmospheric fields and over all areas of the basin under study. Analysis and comparisons are performed for 20th Century Climate in Coupled Models (20C3M), broadly available for most GCMs.

The results show that the proposed downscaling method is able to reproduce the sub-grid climatic features as well as their temporal/spatial variability in the historical periods. Comparisons are also performed for precipitation and temperature with other statistical and dynamic downscaling methods over the southeastern US and show that JVSD performs favorably. The downscaled sequences are used to assess the implications of GCM scenarios for the Southeast US river basins as part of a comprehensive climate change impact assessment.

3.1 JVSD Flowchart

JVSD aims to produce high resolution gridded hydrological datasets suitable for regional watershed modeling and assessments. The method is applicable to multiple atmospheric fields, but it is presented here for precipitation and temperature, as these two variables represent the principle atmospheric forcing that drives watershed response. JVSD conceptually follows the general approach introduced by Wood et al., 2004 (Bias Correction and Spatial Downscaling—BCSD), with several new features.

First, instead of removing and replacing the variable long term trends before and after the bias correction step, JVSD uses a differencing process to create stationary time series and joint frequency distributions (for temperature and precipitation) between GCM control and future runs. Bias correction is then based on quantile-to-quantile mapping of these stationary frequency distributions. The bias corrected sequences are recovered by inverting the differenced series.

For spatial disaggregation, JVSD also uses the historical analogue approach. However, historical analogues are identified simultaneously for all atmospheric fields being downscaled, and for all GCM cells that cover the assessment region. This feature ensures the temporal and spatial coherence of the downscaled climatic fields. Finally, a technique to expand the range of the historical analogues is implemented to handle future data values that fall outside the historical range.

Overall, downscaled sequences must meet several criteria to be useful in regional water resources assessments:

- First, the downscaled sequences should be consistent with historical observations.
- Second, the downscaled sequences should capture climatic mean and variability trends.
- Third, spatial and temporal correlations and interdependencies between the atmospheric fields that largely drive hydrological processes should be represented.

- Lastly, to ensure that hydrological assessments at different temporal scales (e.g., annually, monthly, and daily) using the same downscaled products are consistent, the smoothness of these products across these time scales should be ensured.
- These criteria formed the guiding principles for a new statistical downscaling method discussed next.

JVSD is implemented as shown in **Figure 3.1** as a two step process: bias correction and spatial downscaling.

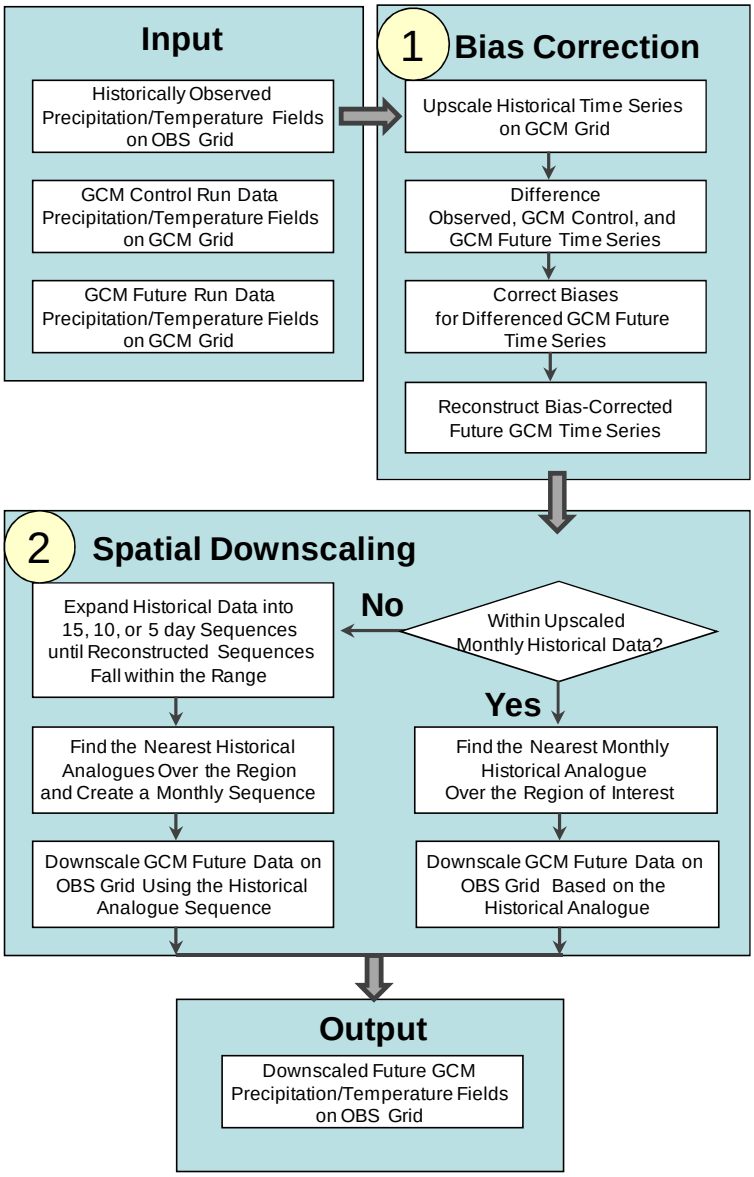

Figure 3.1: Joint Variable Spatial Downscaling Method Flow Chart.

3.2 Bias Correction

GCM outputs contain significant biases that must be corrected before any meaningful assessment can be carried out. **Figure 3.2** compares the frequency distributions of GCM simulated (CGCM3.1, run1) temperature and precipitation versus observed values aggregated over the same ACF cells for the historical period 1950-1999. Biases exist not only in the mean of these distributions but throughout the distributional range, and they are uneven at different quantiles.

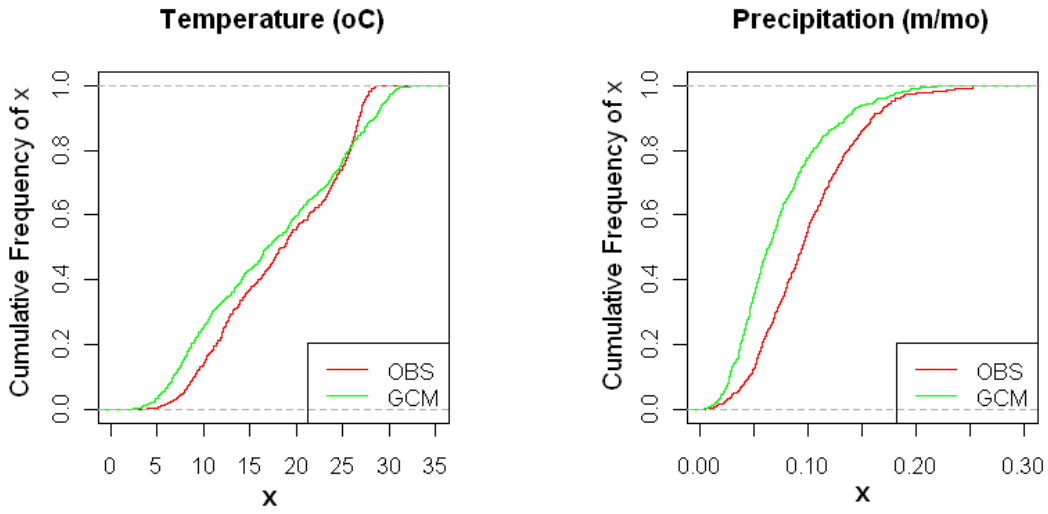

Figure 3.2: Typical Cumulative Frequency Curves of GCM Simulated and Observed Variables.

The JVSD bias correction process is presented using the following notation:

- TS1 and TS2: Monthly precipitation and temperature time series of GCM *future* runs on individual GCM grids:

$$TS1: \quad P\_GCM_t \quad (t = 1,2,\cdots, NF_{month})$$

$$TS2: \quad T\_GCM_t \quad (t = 1,2,\cdots, NF_{month})$$

where, NF_{month} is the length of the monthly time series.

- TS3 and TS4: Monthly precipitation and temperature time series of GCM *control* runs on individual GCM grids. GCM control runs correspond to a historical (control) time period, such as the entire 20th Century or some portion of it.

$$TS3: \quad P\_\mathrm{CON}_{t} \quad (t = 1,2,\cdots,\mathrm{NC}_{month})$$

$$TS4: \quad T\_\mathrm{CON}_{t} \quad (t = 1,2,\cdots,\mathrm{NC}_{month})$$

  where, NC_{month} is the length of the monthly time series.

- DTS5 and DTS6: Daily *observed* precipitation and temperature time series on individual observational scale grids:

$$DTS5: \quad P\_\mathrm{OBS}_{td} \quad (td = 1,2,\cdots,\mathrm{NO}_{day})$$

$$DTS6: \quad T\_\mathrm{OBS}_{td} \quad (td = 1,2,\cdots,\mathrm{NO}_{day})$$

  where NO_{day} is the length of the daily observed time series.

3.2.1 Step 1: Historical Dataset Upscaling

DTS5 and DTS6 are aggregated into two new monthly sequences TS5 and TS6 over the GCM spatial resolution grids. The aggregation process can be represented as shown below:

$$TS5: \quad P\_\mathrm{OBS}_{t} = \Delta_{P}^{d_t}\left(P\_\mathrm{OBS}_{td}\right)_{t} \quad (t = 1,2,\cdots,\mathrm{NC}_{month}) \tag{3.1a}$$

$$TS6: \quad T\_\mathrm{OBS}_{t} = \Delta_{P}^{d_t}\left(T\_\mathrm{OBS}_{td}\right)_{t} \quad (t = 1,2,\cdots,\mathrm{NC}_{month}) \tag{3.1b}$$

where

d_t is the number of days in month t;

P is the number of observational cells falling into a GCM cell;

Δ_{P}^{d} is the upscaling operator in space and time.

The upscaling operator Δ_P^d first performs spatial upscaling over each GCM cell and then performs temporal upscaling to monthly time scales. The *spatial* upscaling operator, $\Delta_P(TS_i; i \in A_P)$, corresponding to a GCM cell P which includes A_P observational cells, is defined by:

$$\Delta_P(TS_i; i \in A_P) = \frac{\sum_{i \in A_P}(TS_i)}{P} \tag{3.2}$$

Other spatial aggregation schemes such as spatial interpolation and kriging (Drignei, 2009) may also be used in this step. The concept of spatial upscaling of observational fields is illustrated in **Figure 3.3**.

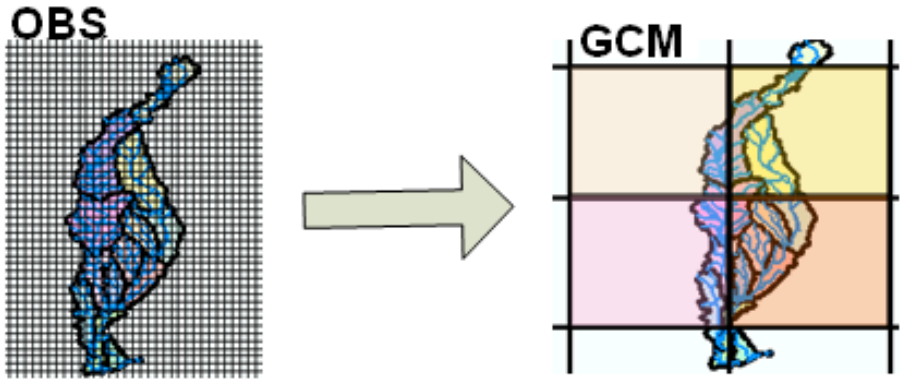

Figure 3.3: Schematic of Spatial Upscaling, From Observational Scale Grids (OBS) to GCM Scale Grids (GCM); Also Shown are the Main Sub-basins of the ACF River Basin.

The *temporal* upscaling operator, $\Delta^{d_t}(TS)_t$, for a month t with d_t days is defined by:

$$\Delta^{d_t}(TS)_t = \frac{\sum_{i=1}^{d_t} TS_i}{d_t} \tag{3.3}$$

3.2.2 Step 2: Time Series Differencing

Differencing aims to remove seasonalities and deterministic trends, and create stationary time series. Differencing can be applied at various lags and orders. For example, a 12-month differencing process applied to the monthly time series (*TS1*, *TS2*, *TS3*, *TS4*, *TS5*, and *TS6*) on each GCM cell can be expressed as shown below:

$$TS1': \quad SP\_GCM_t = \nabla_{12}(P\_GCM_t) \quad (t = 1,2,\cdots,NF_{month})$$

$$TS2': \quad ST\_GCM_t = \nabla_{12}(T\_GCM_t) \quad (t = 1,2,\cdots,NF_{month})$$

$$TS3': \quad SP\_CON_t = \nabla_{12}(P\_CON_t) \quad (t = 1,2,\cdots,NC_{month})$$

$$TS4': \quad ST\_CON_t = \nabla_{12}(T\_CON_t) \quad (t = 1,2,\cdots,NC_{month})$$

$$TS5': \quad SP\_OBS_t = \nabla_{12}(P\_OBS_t) \quad (t = 1,2,\cdots,NC_{month})$$

$$TS6': \quad ST\_OBS_t = \nabla_{12}(T\_OBS_t) \quad (t = 1,2,\cdots,NC_{month})$$

where, the differencing operator ∇_D with lag D is defined as

$$\nabla_D(TS_t) = TS_t - TS_{t-D} \tag{3.4}$$

For D = 12 months, the operator simply subtracts the series values one year apart. If trends persist, higher order differencing may also be used.

The effect of 12-month differencing of GCM temperature and precipitation outputs is shown on **Figure 3.4**. The top plots of this figure show contour lines of the joint empirical temperature-precipitation cumulative frequency curve of the control (CON) and future runs (from the Canadian GCM—CGCM3.1/ run1). Future runs are divided into the first 50-year period (FUT1) from 2000 to 2049, and the second 50-year period (FUT2) from 2050 to 2099. Thus, all sample sizes (i.e., CON, FUT1, and FUT2) are 50-year long. These plots support the following observations:

(1) The joint frequency distributions of temperature and precipitation are different in the control and future runs; and

(2) The relationship of the joint frequency distributions (of control versus future data) is appreciably different in the first versus the second 50-year period, indicating that the joint frequency distribution is non-stationary.

These differences and nonstationarities bias the results of all existing downscaling methods that are commonly based on quantile-to-quantile mapping of these or the associated marginal statistics.

On the other hand, the bottom two plots of **Figure 3.4** show the joint cumulative frequency distribution (of temperature and precipitation) after a 12-month differencing of the original sequences. These plots clearly show that the differenced sequences exhibit very good correspondence between control and future runs, for both future periods. Thus, the joint statistics of the 12-month differenced series are stationary and can serve as pivotal quantities for the quantile-to-quantile bias correction process. This result and conclusion has been tested and shown to hold for all 13 GCMs available through IPCC.

To detect the possible existence of higher order nonstationarities, higher order differencing and other lags were also tested, but they did not yield any significant improvements over 12-month, single differencing.

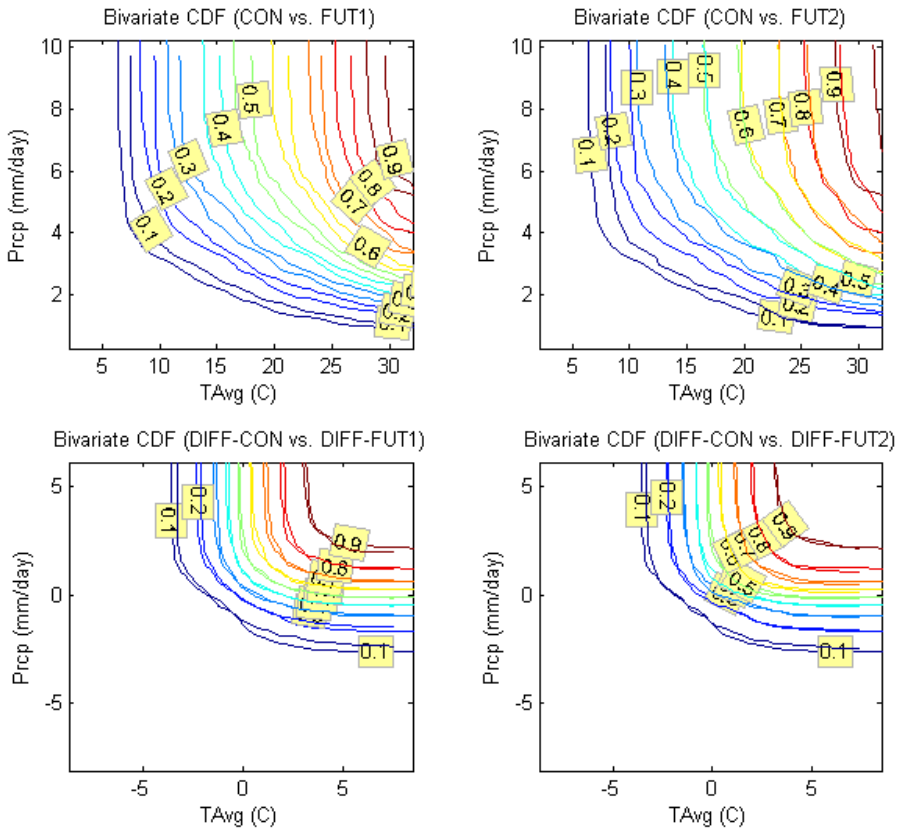

Figure 3.4: Bi-variant Empirical Cumulative Frequency Curves for Original (Top) and Differenced (Bottom) Time Series of Temperature and Precipitation**.**

3.2.3 Step 3: Joint Frequency Mapping

In keeping with the previous discussion, the bias correction process consists of *(1)* creating a differenced series of future temperature and precipitation; *(2)* finding the joint frequency of the contemporaneous differenced data values; *(3)* considering that this joint frequency is the same in the future differenced series as it is in the control differenced series; and *(4)* mapping each joint frequency point of the GCM Control distribution to a corresponding point on the joint frequency distribution of the observed differenced series (OBS). The last step is illustrated in **Figure 3.5**. The schematic shows two corresponding pairs of GCM and OBS joint iso-probability curves, and the nearest

neighbor mapping of a GCM point to a point on the corresponding OBS iso-probability contour in probability space. The nearest neighbor is the one which minimizes the Euclidean distance between the GCM point and all points on the OBS frequency contour.

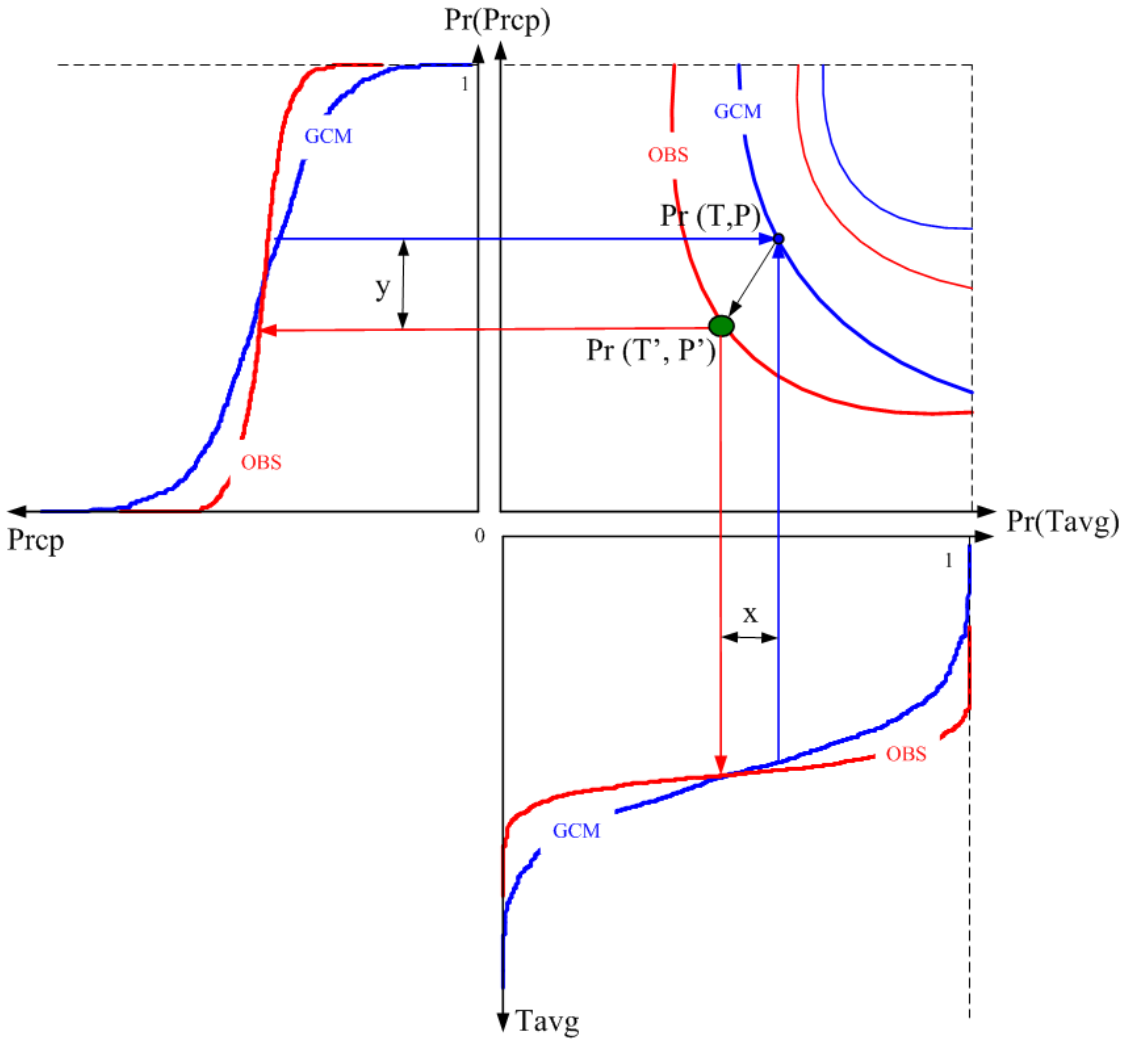

Figure 3.5: Joint Frequency Distribution Mapping in Probability Space. The mapping is that the two points have the same joint CDF values and the Euclidean distance of their marginal CDFs ($\sqrt{x^2 + y^2}$) is minimum.

The cumulative frequency distribution functions in the above procedure are developed empirically for the observational as well as the GCM data. These empirical distributions are used in the joint frequency mapping step directly. No analytical

approximations are derived for this step, although a copula type procedure (Nelsen, 1999) could be employed. Such an analytical approximation would be necessary if the ranges of these distributions are significantly different. However, the frequency distributions are derived herein for the *differenced* data, and it turns out that the extreme values are fairly commensurate. Thus, simple linear extrapolation is used occasionally to identify the bias corrected values.

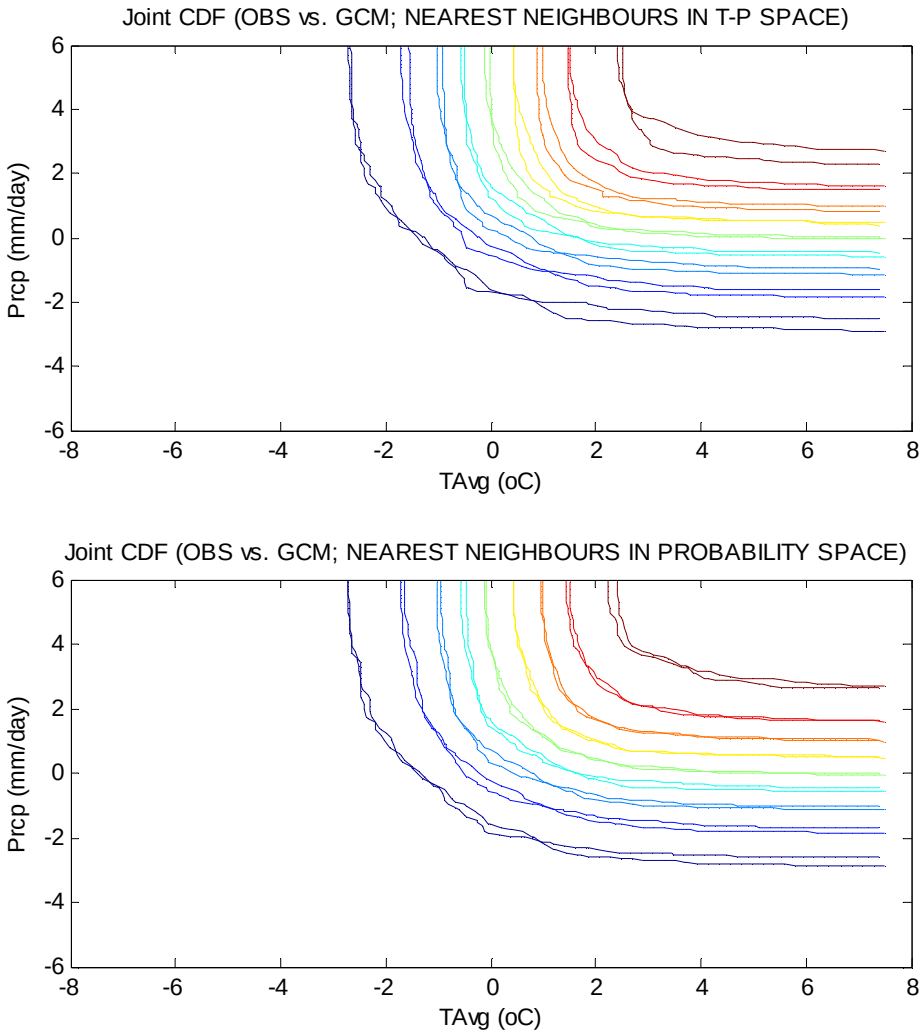

Figure 3.6: Comparison between Two CDF Mapping Approaches for the CSIRO-MK3.5 GCM (Australia). The Top Graph Compares the OBS versus the Mapped GCM Joint

CDFs for the Nearest Neighbor Approach in T-P Space (9 Iso-Probability Contours from 0.1 to 0.9 in 0.1 Increments). The Second Graph Displays the Same Results for the Nearest Neighbor Approach in Probability Space.

The mapping of a point on the GCM joint cumulative distribution function (CDF) onto a point of the OBS joint CDF (of differenced temperature and precipitation values) can be performed in several ways, two of which are examined below. The mapping "goodness" criterion is how well the mapped GCM joint CDF corresponds to the OBS CDF. The first mapping procedure ensures that the mapped points have the same GCM and OBS CDF values, and finds the "nearest neighbors" on the T-P space. The second procedure is implemented as follows: A (T,P) point on the GCM joint CDF is associated with a joint CDF value as well as two marginal CDF values, one for temperature and a second for precipitation. The mapping is then carried out using the nearest neighbor concept in probability space. More specifically, the two points are selected to have the same joint CDF value (on the GCM and OBS CDFs) and the shortest distance between their marginal CDF values (in a Euclidian measure sense).

Figure 3.6 presents a comparison between the two approaches CSIRO-MK3.5 GCM (Australia). The top graph compares the OBS versus the mapped GCM joint CDFs for the first approach by displaying 9 iso-probability contour lines from 0.1 to 0.9 (in 0.1 increments). The second graph displays the same results for the second approach. The figure shows that the second approach represents better the joint CDF than the first approach. This finding is typical of all GCMs. Thus, this study uses the nearest neighbor approach in probability space (second approach).

3.2.4 Step 4: Time Series Reconstruction

The bias corrected monthly temperature and precipitation series for each GCM cell (denoted *TS7* and *TS8*) are obtained by inverting the differencing operation on the bias corrected series:

$$TS7:\ P\_C_t = (\nabla_D)^{-1}(SP\_C_t) = SP\_C_t + SP\_C_{t\text{-}D} \quad (t = 1,2,\cdots,NF_{month}) \tag{3.5a}$$

$$TS8:\ T\_C_t = (\nabla_D)^{-1}(ST\_C_t) = ST\_C_t + ST\_C_{t\text{-}D} \quad (t = 1,2,\cdots,NF_{month}) \tag{3.5b}$$

3.3 Spatial Downscaling

The JVSD spatial downscaling component is based on matching the bias-corrected temperature and precipitation patterns with similar observed patterns (historical analogues) over the assessment region (e.g., the ACF river basin). This process has the following distinguishing features compared to existing methods:

(1) Pattern matching is performed *simultaneously* for temperature and precipitation fields;

(2) Pattern matching is performed *simultaneously* for all GCM cells that cover the region of interest (e.g., the ACF river basin), thus maintaining the climatic coherence and plausibility of the temperature and precipitation fields;

(3) Future temperature and precipitation fields that fall outside the historical range are accommodated by expanding the range of historical analogues as described in the following section.

The spatial downscaling procedure is summarized below.

3.3.1 Step 5: Data Range Adequacy Test

In this step, the monthly temperature and precipitation values of the relevant GCM cells are checked to determine if they fall within the historical observed range of the monthly values. If they fall within the historical range, the downscaling process continues to Step 7; otherwise, the process continues to Step 6.

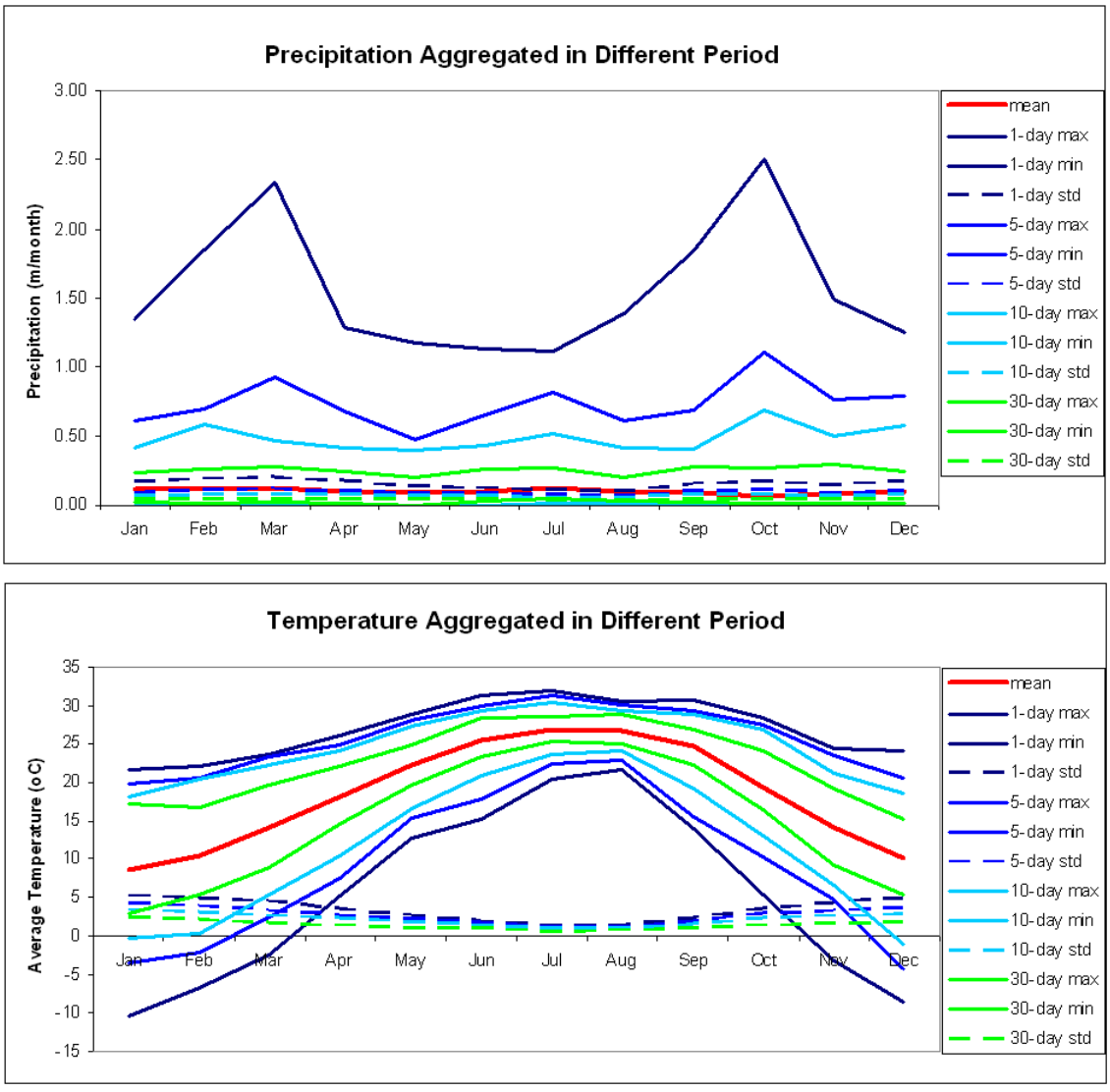

Figure 3.7: Data Range Expansion Example.

3.3.2 Step 6: Historical Analogue Range Expansion

This step is invoked when the future GCM patterns fall outside the historical range, a case particularly relevant to a changing climate. To expand the historical analogue range, upscaling of the historical data in Step 4 is performed for periods smaller than a month, e.g., d = 15, 10, 5, or 1 days. Because these periods entail fewer days than those in a month, their averages are expected to exhibit higher (than monthly) variability and a wider data range. This process aims to identify the largest interval d which generates historical analogues containing the future T and P values. The data range expansion is carried out for the calendar month to be downscaled. However, if this is not sufficient, the data range is expanded to include 15 days from the previous and 15 days from the following months, expected to exhibit a similar climatic behavior.

The process is illustrated in **Figure 3.7**. In the top plot, the maximum and minimum historical monthly precipitation averaged over 30, 10, 5, and 1 days are plotted in solid lines, and the corresponding standard deviations in dashed lines. In the bottom plot, the same quantities are plotted for the historical temperature. These plots show the data range expansion as the averaging interval decreases.

3.3.3 Step 7: Historical Analogue Matching

Next, the nearest point (OBS_P_i, OBS_T_i) in the historical sequences *TS5* and *TS6* to a particular point (GCM_P_i, GCM_T_i) in the future GCM sequences *TS7* and *TS8* is determined by minimizing the Euclidean distance:

$$\mathrm{R}^2 = \sum_{i \in A} \alpha (OBS\_P_i - GCM\_P_i)^2 + \beta (OBS\_T_i - GCM\_T_i)^2 \tag{3.6}$$

where *A* is the set of cells that cover the region (basin) of interest; α and β are weighting coefficients if one wishes to emphasize matching one of the variable over the other; and *i* is the cell index on the GCM grid.

Once the nearest historical analogue point is identified, the T-P values can be spatially downscaled based on the historical T-P values over the observational cells. The downscaled temperature and precipitation sequences are denoted *TS9* and *TS10*:

$$\begin{Bmatrix} TS9 \\ TS10 \end{Bmatrix} : \begin{Bmatrix} P\_\mathrm{DS_t} \\ T\_\mathrm{DS_t} \end{Bmatrix} = NearestHistoricalAnalogue \begin{Bmatrix} P\_OBS_j \\ T\_OBS_j \end{Bmatrix} \quad (\mathrm{t} = 1,2,\cdots,\mathrm{NF_{month}})$$

where *j* is the cell index of the observational (high resolution) grid.

3.3.4 Temporal Downscaling

Daily (or other duration) temperature and precipitation sequences DTS9 and DTS10 can now be constructed by suitable temporal upscaling of the historical analogue fields. If the nearest historical analogue was found from the monthly historical observed fields, then, the downscaled daily sequences are directly extracted from the corresponding month. On the other hand, if the nearest historical analogue required expansion of the historical range (using the process outlined in Step 6), then, the downscaled daily sequences are constructed by assembling several nearest historical analogues the total duration of which equals one month. In the assessments carried out for the ACF river basin, data range expansion was not necessary beyond the 15 day interval.

3.4 Results and Comparisons

The geographic focus of the downscaling study in this chapter is the Apalachicola-Chattahoochee-Flint (ACF) river basin located in the southeast US as shown in chapter 2. The ACF basin begins in north Georgia (mostly within a sub-tropic region) and flows into the Gulf of Mexico, near Apalachicola, Florida. It drains an area of about 19,600 square miles. Based on its hydrological characteristics and the locations of major storage projects, the ACF basin comprises seven watersheds (sub-basins): *(1)* the Chattahoochee headwater reach extending up to and including Lake Lanier and Buford Dam; *(2)* the Chattahoochee reach from Lake Lanier up to and including West Point Lake and Dam; *(3)* the Middle Chattahoochee reach from West Point up to and including Lake Walter F. George and Dam; *(4)* the Lower Chattahoochee reach from Lake W.F. George up to and including Lake Seminole and Jim Woodruff Lock and Dam; *(5)* the Flint headwater reach up to Montezuma; *(6)* the Flint reach from Montezuma up to Albany; and *(7)* the Flint reach from Albany to Bainbridge. **Table 1** lists the characteristics of all ACF sub-basins. More detailed descriptions of ACF basins can be found in a recent technical report (Georgakakos et al., 2010).

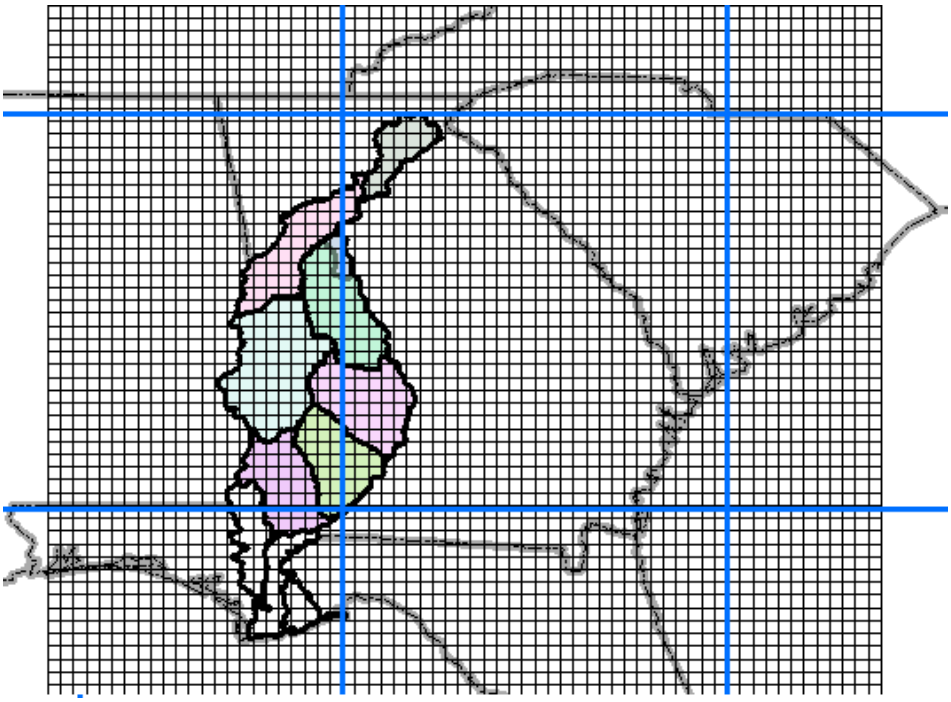

Figure 3.8: Spatial Resolutions of the Canadian GCM3.1 (blue) and Observational Data Sets (black) over the Southeast US.

In this section, JVSD is evaluated by comparison with observed historical data and other statistical and dynamic downscaling methods.

Table 3.1: General Characteristics of the ACF Sub-basins.

ACF Sub-basins	Latitude (Centroid)	Longitude (Centroid)	Area (km^2)	Mean Elevation (m)	Min. Elevation (m)	Max. Elevation (m)
Buford	34°31’	-83°48’	2694	454	320	1250
West Point	33°40’	-84°44’	5189	270	137	455
George	32°20’	-85°01’	4787	143	46	396
Woodruff	31°13’	-84°58’	2141	64	22	167
Montezuma	32°55’	-84°24’	4507	213	85	394
Albany	32°01’	-84°11’	2605	115	53	235
Bainbridge	31°25’	-84°24’	1875	72	23	173

3.4.1 Seasonal Comparison with Observed Data

The climatology maps of precipitation and temperature in the southeast US (the region where the ACF basin is located). The results presented here are from the Canadian model CGCM3.1, run1. Results from all other GCMs and scenarios can be found in the technical report by Georgakakos et al., 2010. Monthly precipitation and temperature data are aggregated by seasons (DJF, MAM, JJA, and SON) for three 50-year periods: *(1)* 01/1950 to 12/1999 using both observation data as well as data from the CMIP pilot project called 20th Century Climate in Coupled Models (20CM3); *(2)* 01/2000 to 12/2049 for the CGCM A1B scenario, and *(3)* 01/2050 to 12/2099 again for the CGCM A1B scenario. The first column is constructed from observed, high resolution data from the 1/8 degree spatial resolution dataset (Maurer et al., 2002) for the period 1950-1999. The second column shows the JVSD results with input from the coarse resolution GCM data from the 20CM3 experiments (1950-1999). The third (2000-2049) and fourth columns (2050-2099) are also generated by JVSD with input from the A1B CGCM3.1 scenario runs.

The important comparison in **Figures 3.9** and **3.10** is between the first two columns (observations versus JVSD). The figures show that JVSD results compare favorably with observed precipitation and temperature data in that they reproduce fairly well the seasonal spatial distributions and coherence. (In generating the JVSD results, the corresponding historical month being downscaled has, of course, been *excluded* from the historical analogue data set.) Furthermore, specifically for the CGCM A1B run shown, the results in columns 3 and 4 indicate:

(1) Temperature exhibits increasing trends over the southeast and the ACF basin for all seasons; Temperature increases are more significant in the 2050 – 2099 time period. The most pronounced temperature increase appears to take place in spring and fall. The A2 scenario results (not shown) are similar but temperature increases are even greater in the second half of the 21st century. This observation holds true for most GCM scenario results and will be quantified further in a later section.

(2) Precipitation exhibits an increasing trend in winter and a mild declining trend in spring and summer.

Similar analysis (not shown) has been carried out using the BCSD method. The BCSD datasets are obtained from the Program for Climate Model Diagnosis and Inter-comparison website (http://gdo-dcp.ucllnl.org/downscaled_cmip3_projections/). Generally, BCSD performs well, showing similar overall trends for seasonal temperature and precipitation as those of the observed data and JVSD. However, the following differences are noted between the two methods:

(1) The BCSD precipitation fields exhibit less spatial variability and milder changes than those of JVSD. The reasons for these differences are that (i) the BCSD downscaled values for nearby cells are calculated based on the same upscaled information (through a variant of the inverse distance weight approach) and (ii) JVSD is based on historical analogues that have been observed over the *entire* region of interest, not separately for individual cells. (More quantitative comparisons of these differences are forthcoming later in this section.)

(2) BCSD predicts that the highest temperature increases will occur during spring and fall as does JVSD. However, summer temperature increases (July and August) are higher under BCSD than under JVSD.

Furthermore, the JVSD seasonal joint temperature and precipitation CDFs were compared with their observed counterparts (Maurer et al., 2002) for each of the seven ACF sub-basins over the historical period 01/1950 - 12/1999 (control period). The results (**Figure 3.11**) show that JVSD represents the joint relationships fairly well over the entire frequency range, with discrepancies appearing at the extreme value regions which are characterized only by a few data points.

The performance of downscaling methods varies across seasons, stations, and indices (Fowler and Blenkinsop, 2007). Many researchers have concluded that the accuracy of statistical downscaling methods has a geographical and seasonal component (Huth, 1999). In addition, the GCM skill in simulating regional climate may vary for different locations and scales. In general, GCMs are more likely to capture the large scale climate features, and the relationships between climate variables are likely to be better simulated in locations where the topographic features are not too different from those assumed in the GCMs.

One of JVSD's strengths is that it can represent the co-variability between temperature and precipitation. In places and seasons where there is no significant dependence between these two variables, the JVSD and BCSD bias correction procedures are equivalent. However, where such dependence exists, JVSD generates more representative downscaled fields. To demonstrate this feature, the joint distributions of temperature and precipitation for the observed as well as the BCSD and JVSD

downscaled data are compared for Buford, Woodruff, and the entire ACF. **Figure 3.12** shows this comparison for Buford and the GFDL GCM. This figure shows that in DJF and SON, both BCSD and JVSD represent the joint temperature-precipitation relationship comparably well, although BCSD exhibits some discrepancies in the joint distribution tails. However, in MAM and JJA, JVSD performs clearly better. The underlying reason for these performance differences is illustrated on **Figure 3.13** which depicts the monthly correlation coefficients between temperature and precipitation for four GCMs and the observations, BCSD downscaled data, and JVSD downscaled data (over the 1950-1999 historical period). The figure shows that in DJF and SON correlations are negligible, while in MAM and JJA correlations are significant. Thus, JVSD is more preferable than BCSD in places and seasons where temperature and precipitation exhibit strong co-variability.

Next, the seasonal coefficient of variation (CV) for each ACF watershed is computed and compared for both the observational and downscaled datasets (from JVSD as well as BCSD). The seasonal watershed CV is the spatial mean of the seasonal coefficient of variation. The seasonal CV at a particular grid cell is defined as the ratio of the standard deviation of the cell seasonal values to the mean seasonal value. Then, the watershed CV is obtained as the spatial mean of all seasonal CVs over all watershed grid cells. **Table 3.2** shows that the JVSD watershed CVs are more representative of the historical CVs than those of BCSD, especially for watershed precipitation. It also shows that BCSD underestimates precipitation variability within each watershed.

Lastly, the spatial inter-grid variability is compared for the same three datasets (i.e., the observations, JVSD, and BCSD). Several descriptive statistics exist to

characterize the spatial patterns of gridded data including the covariance matrix (measurement of spatial dispersion), mean correlation coefficient (measurement of spatial correlation), and Ripley's K and L functions (measurements of spatial homogeneity of point data). Here, this variability is compared using the distribution of the pair-wise correlation between any two grid points within a watershed (Gissila et al., 2004). The temperature field (not shown) exhibits high grid point correlations (greater than 0.99), indicating that the monthly temperatures are highly homogeneous within each watershed. Both JVSD and BCSD reproduce this homogeneity. However, for reasons explained below in relation to precipitation, in geographic areas where the actual temperature field exhibits significant spatial heterogeneity, BCSD would tend to over-estimate the inter-grid cross correlations.

Box-plots of these pair-wise correlation coefficients across the ACF watersheds are shown in **Figure 3.14**.The historical correlation distributions vary between 0.75 and 0.9. The plots show that the JVSD distributions match very closely the historical statistics, while BCSD exhibits a significant bias toward homogeneity.

Furthermore, **Figure 3.15** compares the spatial precipitation correlation between observations, BCSD, and JVSD for four GCMs, various grid cell distances, and months. These are correlations of the actual values of a particular cell pair over the 1950 to 1999 period and month of the year. The graphs clearly show the BCSD spatial correlation bias. For adjacent cells, the BCSD correlation is nearly 1. Even for pairs at 15 to 20 cell distances apart, the spatial correlation continues to be more than 0.9 and exhibits no distinct monthly pattern. In comparison, the spatial correlations of the observations and JVSD values have a clear monthly pattern and are consistent. As already indicated, the

reason for this BCSD behavior is that the factors used to downscale nearby values are calculated based on upscaled information at the same GCM grid cells (using a general inverse distance weighting approach). This process over-estimates the spatial correlation, because the inverse distance weights for nearby cells are very similar.

While this distributional bias is not critical with respect to temperature, misrepresenting the spatial precipitation variability is more of a concern, especially if hydrologic assessments are based on distributed (or quasi-distributed) watershed models. The plots also show that the southern ACF watersheds (i.e., those that are situated below the geologic fall line that runs across Georgia) have larger inter-grid precipitation variability than the two northern watersheds (Buford and West Point). A likely reason for this is that convective events dominate southern watershed precipitation over a longer season.

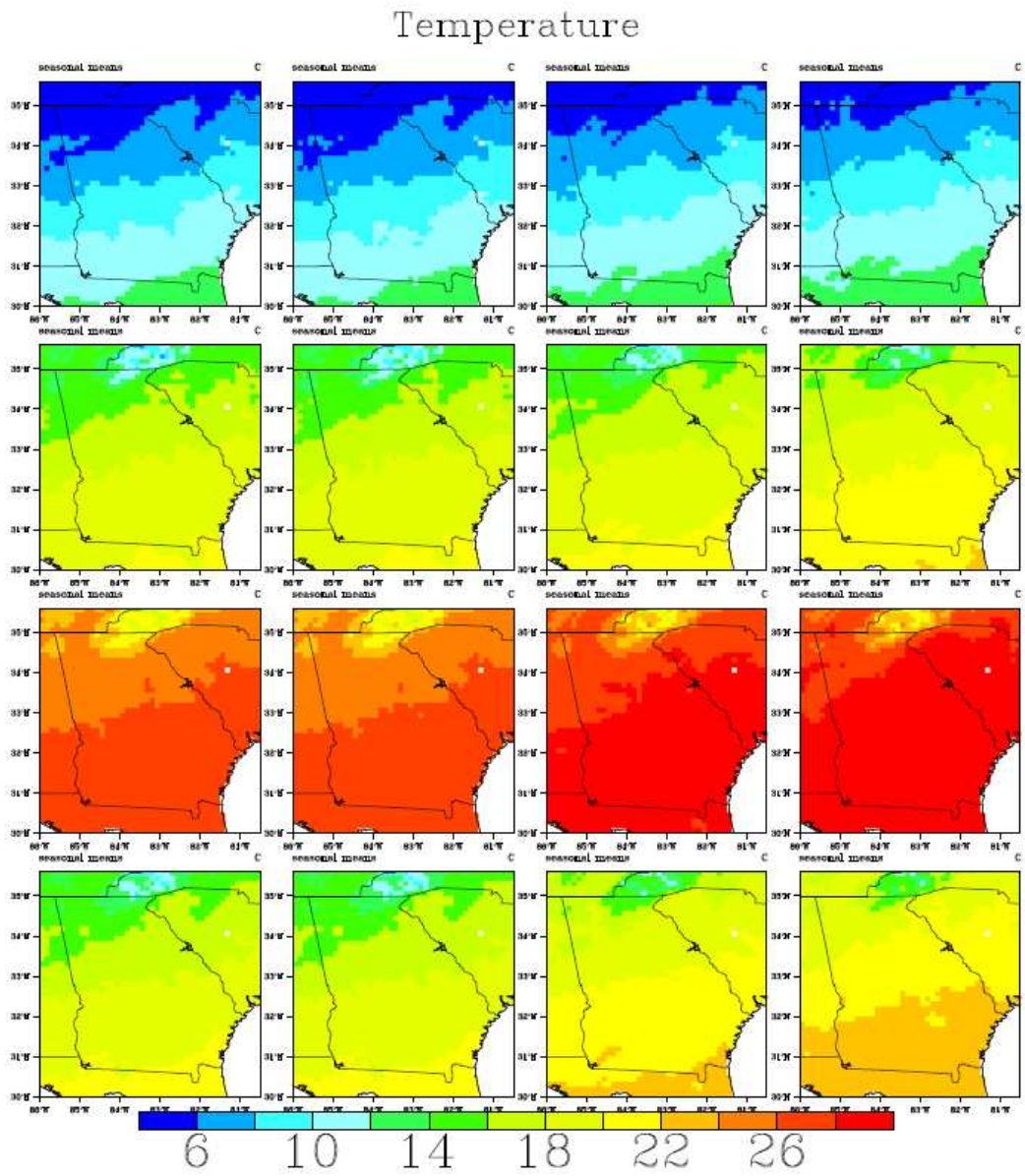

Figure 3.9: Spatial temperature distributions over the ACF basin and the southeast US. Monthly temperature fields are aggregated by season (DJF, MAM, JJA, and SON in rows 1, 2, 3, and 4 respectively). The columns depict observations for the period 01/1950 - 12/1999 (Column 1); JVSD downscaled data using input from the 20CM3 experiment for the period 01/1950 - 12/1999 (Column 2); JVSD downscaled data using input from the CGCM3.1-run1 A1B Scenario for the period 01/2000-12/2049 (Column 3); and JVSD downscaled data using input from the CGCM3.1-run1A1B Scenario for the period 01/2050-12/2099 (Column 4).

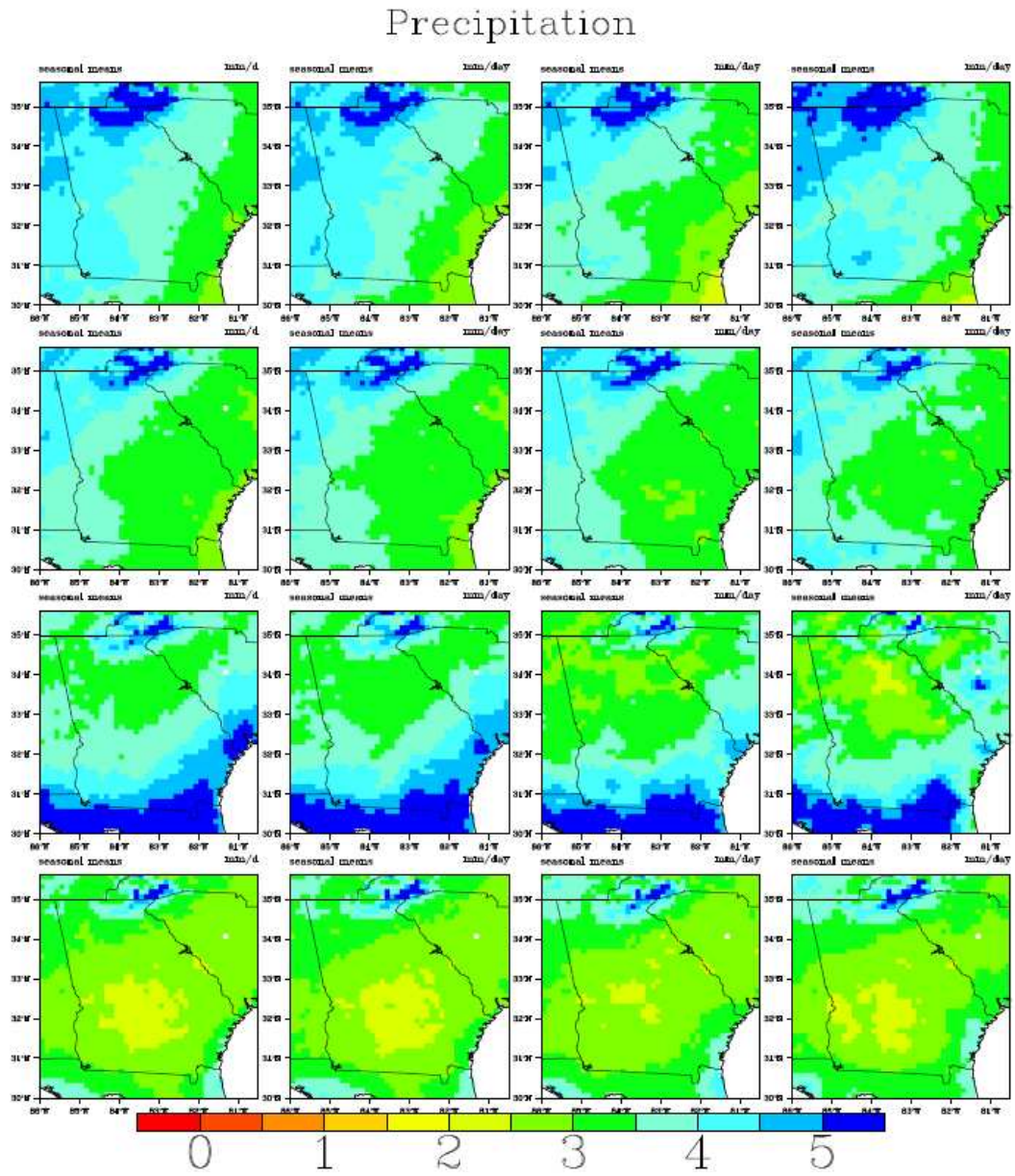

Figure 3.10: Spatial precipitation distributions over the ACF basin and the southeast US. Monthly precipitation fields are aggregated by season (DJF, MAM, JJA, and SON in rows 1, 2, 3, and 4 respectively). The columns depict observations for the period 01/1950 - 12/1999 (Column 1); JVSD downscaled data using input from the 20CM3 experiment for the period 01/1950 - 12/1999 (Column 2); JVSD downscaled data using input from the CGCM3.1-run1A1B Scenario for the period 01/2000-12/2049 (Column 3); and JVSD downscaled data using input from the CGCM3.1-run1 A1B Scenario for the period 01/2050-12/2099 (Column 4).

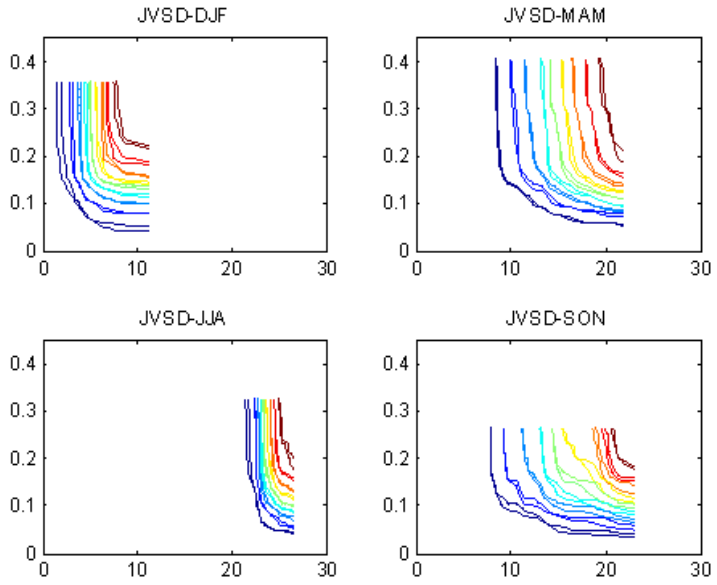

Figure 3.11: An Example of Joint CDFs of Precipitation and Temperature for Each Season Corresponding to OBS and JVSD for ACF Watershed from CGCM3.1 Model.

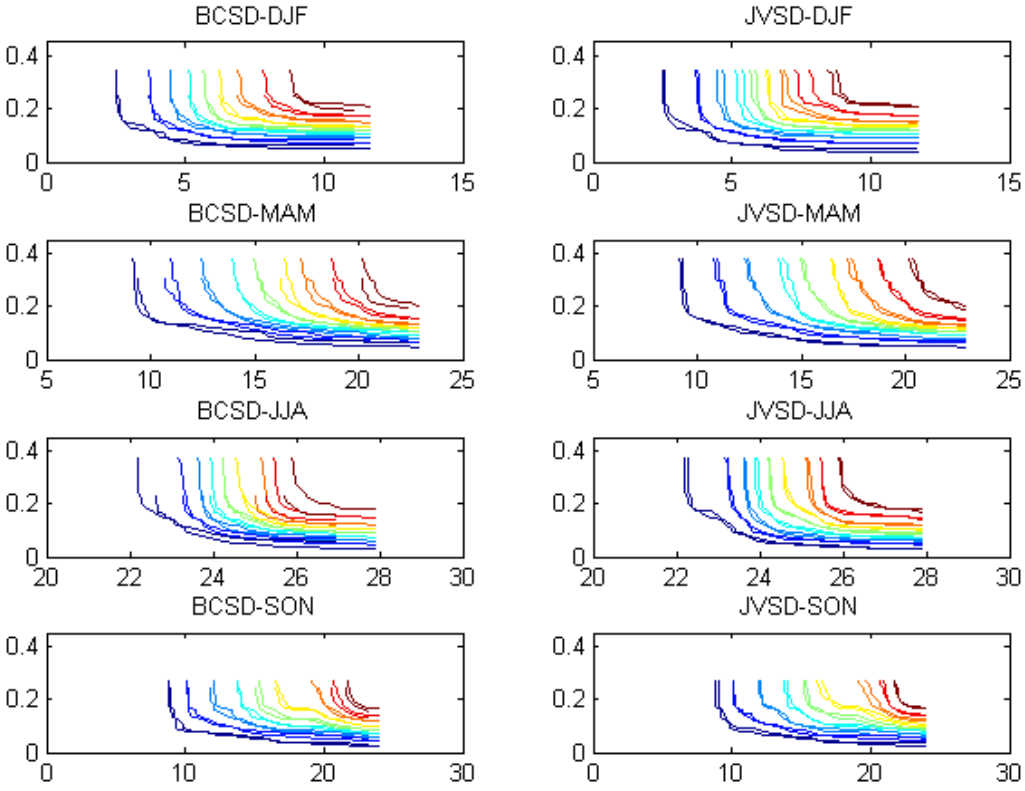

Figure 3.12: Joint CDF between Precipitation and Temperature for Buford Watershed from Observation, BCSD Downscaling (Left Panel), and JVSD (Right Panel).

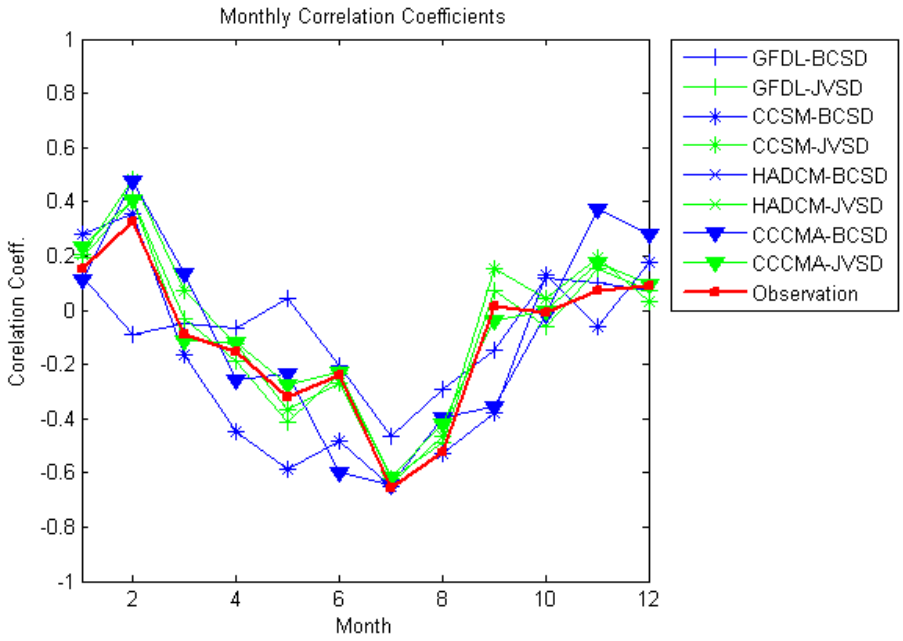

Figure 3.13: Monthly Correlation Coefficients between Precipitation and Temperature for Buford; Observations (red), BCSD (blue), and JVSD (green).

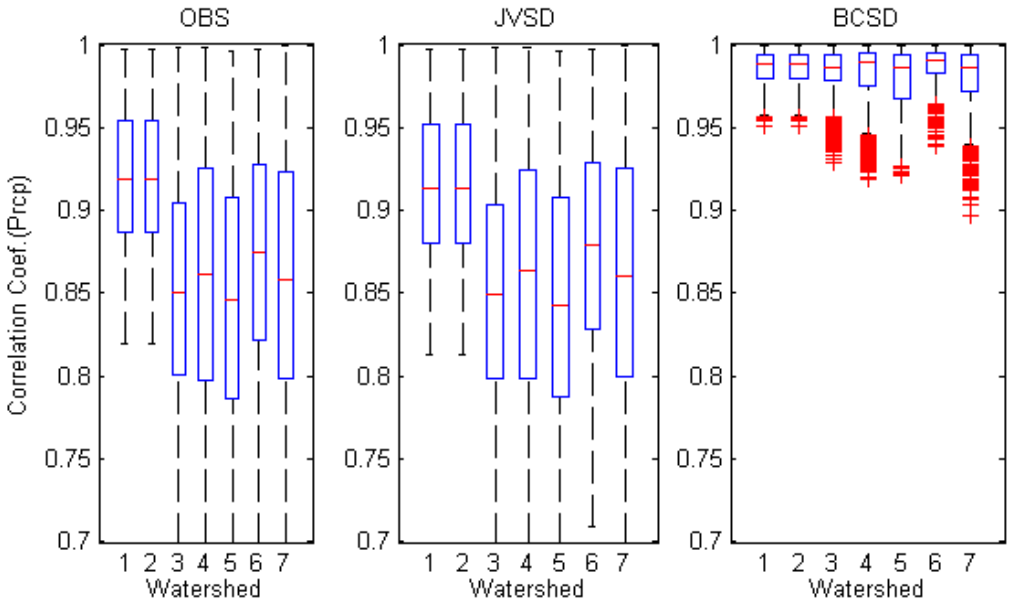

Figure 3.14: Box-plots of the pair-wise correlation coefficients across the ACF sub-basins: (1) Buford, (2) West Point, (3) George, (4) Woodruff, (5) Montezuma, (6)Albany, and (7) Bainbridge.

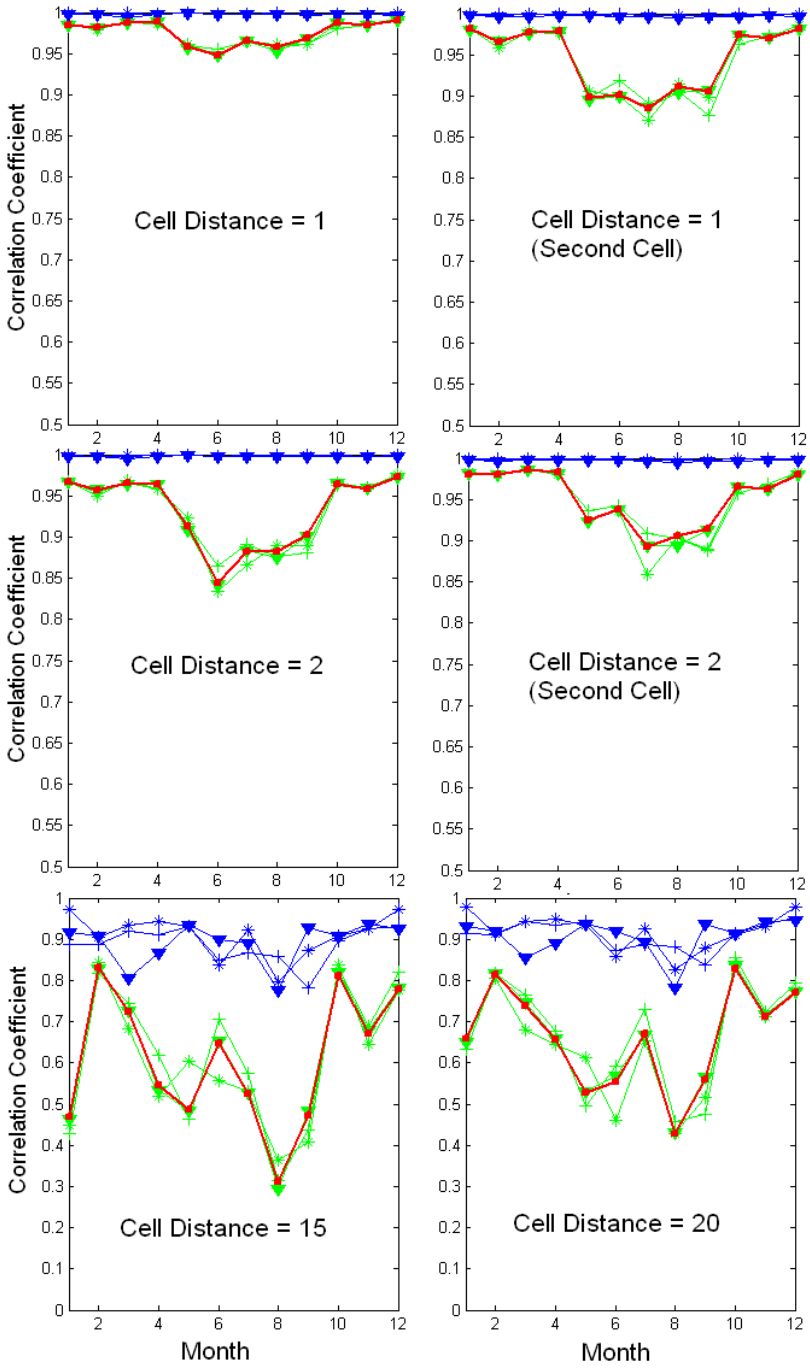

Figure 3.15: Spatial Correlation Comparison between Precipitation Observations (red), BCSD (blue), and JVSD (green) for four GCMs, Various Grid Cell Distances, and Months. The Cell Pairs for the First Four Panels Are Selected from the Buford Watershed. The Cell Pairs in the Last Two Panels Include One Cell from the Buford Watershed and a Second Cell from the West Point Watershed.

Table 3.2: Watershed Coefficient of Variability (CV) in Seasonal Precipitation and Temperature for ACF Watersheds.

Watershed	Season	Precipitation			Temperature		
		OBS	JVSD	BCSD	OBS	JVSD	BCSD
Buford	DJF	0.447	0.439	0.358	0.514	0.506	0.511
	MAM	0.510	0.502	0.379	0.191	0.202	0.188
	JJA	0.561	0.572	0.388	0.090	0.088	0.087
	SON	0.553	0.562	0.456	0.442	0.451	0.440
West Point	DJF	0.446	0.461	0.389	0.379	0.384	0.389
	MAM	0.534	0.528	0.442	0.169	0.192	0.442
	JJA	0.524	0.532	0.422	0.078	0.125	0.422
	SON	0.612	0.606	0.544	0.358	0.372	0.544
George	DJF	0.455	0.450	0.411	0.298	0.312	0.411
	MAM	0.552	0.562	0.464	0.153	0.167	0.464
	JJA	0.556	0.567	0.438	0.064	0.119	0.438
	SON	0.689	0.691	0.592	0.301	0.345	0.592
Woodruff	DJF	0.474	0.469	0.432	0.260	0.248	0.423
	MAM	0.577	0.572	0.493	0.138	0.126	0.493
	JJA	0.539	0.531	0.439	0.054	0.059	0.439
	SON	0.692	0.679	0.616	0.267	0.265	0.616
Montezuma	DJF	0.461	0.452	0.396	0.329	0.327	0.329
	MAM	0.526	0.518	0.442	0.159	0.156	0.158
	JJA	0.569	0.542	0.425	0.073	0.072	0.071
	SON	0.645	0.630	0.425	0.327	0.326	0.326
Bainbridge	DJF	0.486	0.466	0.561	0.274	0.271	0.268
	MAM	0.553	0.543	0.422	0.142	0.139	0.141
	JJA	0.547	0.521	0.467	0.059	0.058	0.056
	SON	0.708	0.711	0.596	0.279	0.275	0.277

3.4.2 Comparison with Dynamic Downscaling Methods

In this section, JVSD and BCSD are compared with the dynamic downscaling methods used in the North American Regional Climate Change Assessment Program (NARCCAP).

High resolution climate scenarios have been produced by NARCCAP using regional climate models (RCMs). The RCMs are nested within coupled Atmospheric-Ocean GCMs for the historical period 1971-2000 and for the future period 2041-2070

(NARCCAP, 2010). Several RCM/GCM combinations have been run and some of the products are available through the ESG (Earth System Grid; http://www.earthsystemgrid.org/) data distribution center. In the comparison presented here, results from one typical RCM/GCM combination corresponding to the Canadian GCM3 run4 data (cccma_cgcm3_1 sresa2, Run 4) are selected.

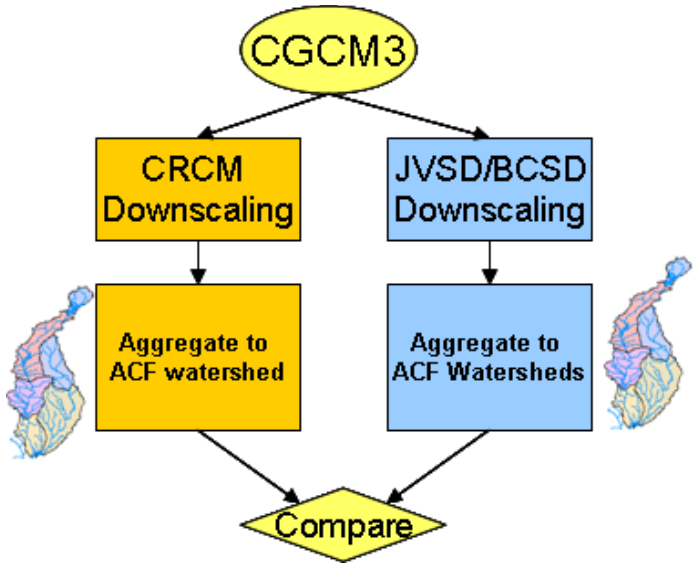

Figure 3.16: Comparison Process of JVSD with Dynamic Downscaling Methods from the NARCCAP Dataset (CRCM/CGCM3) for the Future Period 2041-2070.

As illustrated in **Figure 3.16**, the results from CGCM3/SRESA2/RUN4 were downscaled using JVSD, BCSD, and CRCM/CGCM3 dynamic methods. The resulting precipitation and temperature fields are aggregated over the ACF watersheds, and comparisons are made among the aggregated time series.

It is noted that the CGCM3 experiment provides boundary conditions for the CRCM run (Randel, 2007) without any bias correction. Therefore, the downscaled data inherit the original GCM biases. To account for this inconsistency, JVSD was implemented and compared with CGCM3 with and without bias correction.

To facilitate the comparison, the data values are expressed in frequency curve form (**Figures 3.17** and **3.18**). The graphs comprising these figures correspond to the ACF watersheds and include four curves corresponding to the dynamically downscaled data (blue line), BCSD downscaled data (pink line), JVSD downscaled data without bias correction (cyan line), and JVSD downscaled data with bias correction (green line). (BCSD data without bias correction is not available.) The pair-wise statistical differences between these curves were assessed using the Kolmogorov-Smirnov test as reported in **Table 3.3**.

First, the results show that there is no significant statistical difference between dynamic downscaling (DDS) and JVSD without bias correction. This conclusion applies for both temperature and precipitation at the 0.05 and the 0.01 significance level. (The only exception is DDS and JVSD precipitation for the George watershed which is marginally different at the 0.05 significance level, but not at 0.01.) A plausible explanation for this interesting finding is that JVSD generates spatially coherent temperature and precipitation fields for the entire ACF, much like a dynamic downscaling scheme also does. Furthermore, temperature and precipitation over the ACF geographic region are fairly uniform.

Second, comparing JVSD with bias correction and DDS indicates that the former is significantly different from the latter for both temperature and precipitation at 0.05 and 0.01 significance levels. (Buford temperature is the only exception where the two frequency distributions cannot be assessed as different at the 0.01 significance level, but the test statistic is marginal.) This finding combined with the favorable JVSD (BC) comparison with observed data (in previous sections) leads to the conclusion that

dynamic downscaling without some form of bias correction may not be adequate for climate change assessments. This conclusion is corroborated by Wood et al., 2004, who assess the seasonal hydrologic response in the Columbia River Basin using dynamically downscaled climate scenarios with and without bias correction.

Third, comparing BCSD and JVSD with bias correction indicates that significant precipitation differences exist for all watersheds at the 0.05 significance level, while only Buford, West Point, and Woodruff remain clearly significant at the 0.01 level. Temperature distributions, on the other hand, are not found to be statistically different at 0.05 or 0.01, with the exception of Buford. The statistical differences between JVSD (BC) and BCSD result from the several differences between these two methods: joint variable downscaling versus marginal distribution downscaling, coherent basin-wide versus individual grid downscaling, and different handling of extreme distribution values.

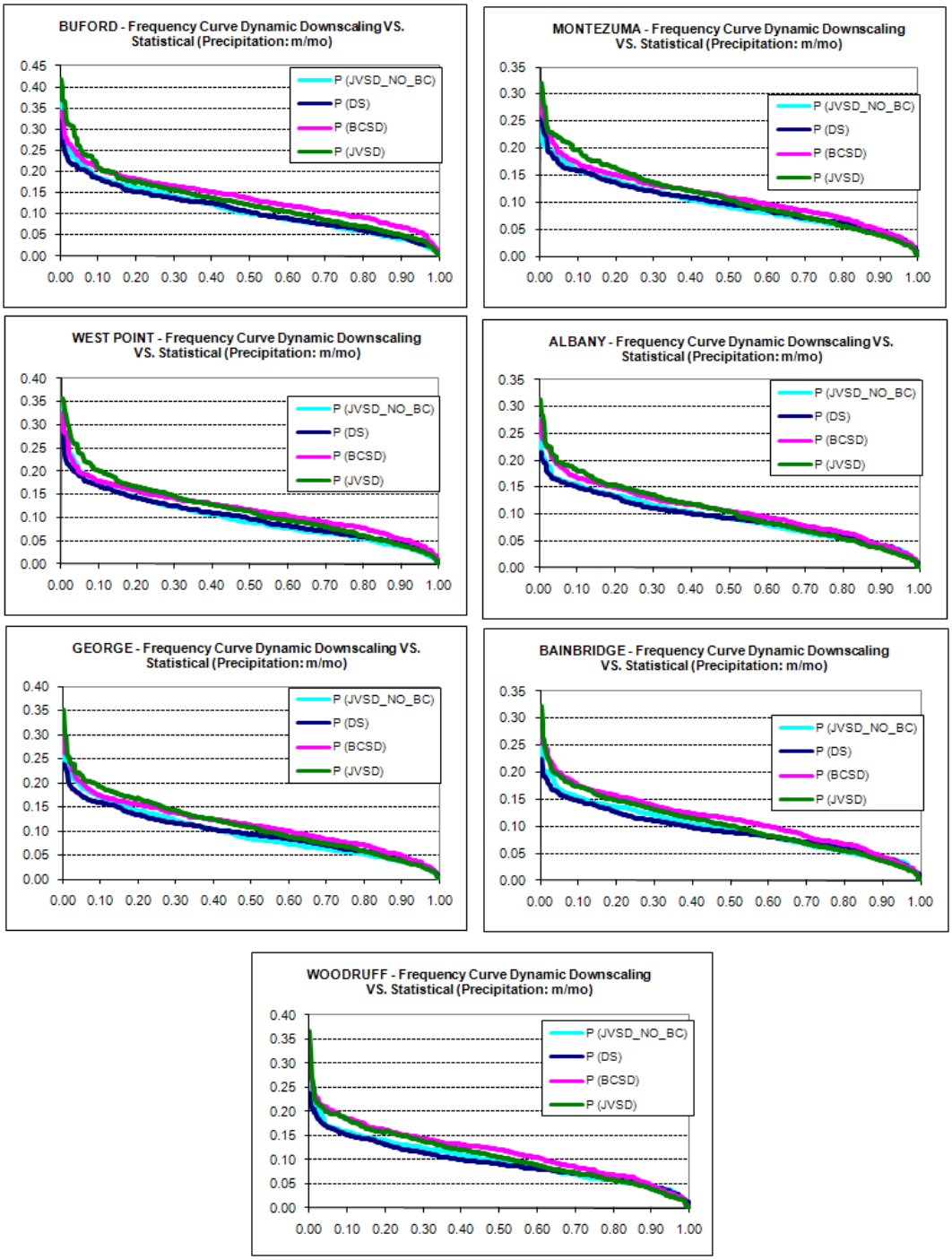

Figure 3.17: Comparisons of Downscaled Precipitation Frequencies for ACF Watersheds based on NARCCAP Methods, BCSD, JVSD with no bias correction, and JVSD with bias correction.

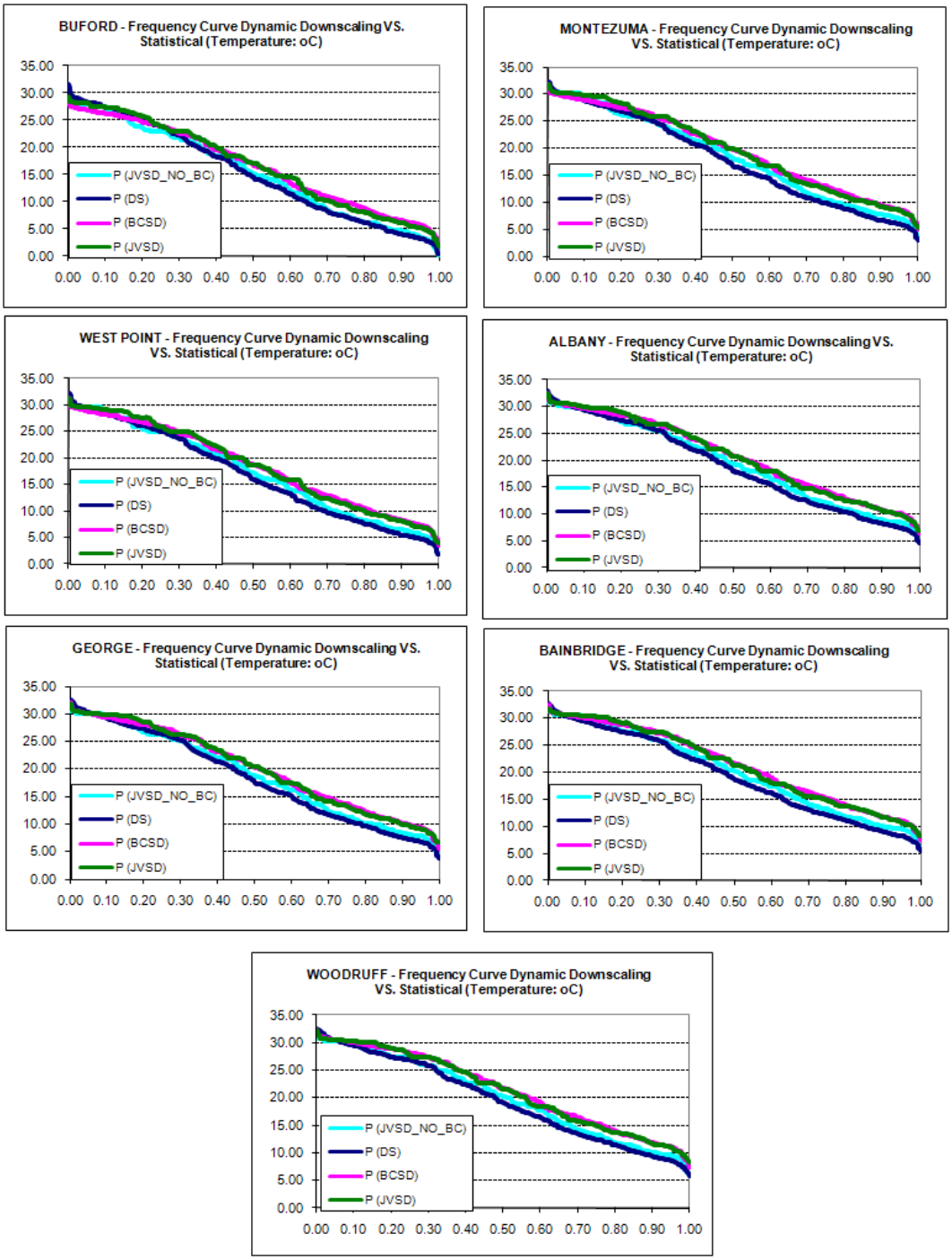

Figure 3.18: Comparisons of Downscaled Temperature Frequencies for ACF Watersheds based on NARCCAP Methods, BCSD, and JVSD without bias correction, and JVSD with bias correction.

Table 3.3: Evaluation of Statistical Differences Among BCSD, JVSD (Bias Corrected), JVSD, and Dynamic Downscaling (DDS); ACF Precipitation and Temperature; "DIFF" Denotes Statistical Difference and "-" Denotes No Statistical Difference. Number of Data Values N=384.

K-S Test Statistic = $\max_x \lvert F_1(x) - F_2(x) \rvert$							
Precipitation							
	Buford	West Point	George	Montezuma	Albany	Bainbridge	Woodruff
JVSD-DDS	0.0599	0.0599	0.1094	0.0625	0.0547	0.0859	0.0859
JVSD(BC)-DDS	0.1302	0.1328	0.1589	0.1406	0.1615	0.1458	0.1536
BCSD-JVSD(BC)	0.1380	0.1211	0.1211	0.1064	0.1085	0.1094	0.1242
Temperature							
	Buford	West Point	George	Montezuma	Albany	Bainbridge	Woodruff
JVSD-DDS	0.0703	0.0651	0.0729	0.0781	0.0703	0.0755	0.0651
JVSD(BC)-DDS	0.1120	0.1328	0.1328	0.1406	0.1406	0.1510	0.1380
BCSD-JVSD(BC)	0.1320	0.1042	0.0870	0.1016	0.0651	0.0729	0.0547
Significant level 0.05 ($K_{0.05}$ = $[-\frac{1}{2}(\frac{1}{N}+\frac{1}{N})\ln(\frac{\alpha}{2})]^{\frac{1}{2}} =$ **0.098)**							
Precipitation							
	Buford	West Point	George	Montezuma	Albany	Bainbridge	Woodruff
JVSD-DDS	-	-	DIFF	-	-	-	-
JVSD(BC)-DDS	DIFF	DIFF	DIFF	DIFF	DIFF	DIFF	DIFF
BCSD-JVSD(BC)	DIFF	DIFF	DIFF	DIFF	DIFF	DIFF	DIFF
Temperature							
	Buford	West Point	George	Montezuma	Albany	Bainbridge	Woodruff
JVSD-DDS	-	-	-	-	-	-	-
JVSD(BC)-DDS	DIFF	DIFF	DIFF	DIFF	DIFF	DIFF	DIFF
BCSD-JVSD(BC)	DIFF	DIFF	-	DIFF	-	-	-
Significant level 0.01 ($K_{0.01}$ = $[-\frac{1}{2}(\frac{1}{N}+\frac{1}{N})\ln(\frac{\alpha}{2})]^{\frac{1}{2}} =$ **0.117)**							
Precipitation							
	Buford	West Point	George	Montezuma	Albany	Bainbridge	Woodruff
JVSD-DDS	-	-	-	-	-	-	-
JVSD(BC)-DDS	DIFF	DIFF	DIFF	DIFF	DIFF	DIFF	DIFF
BCSD-JVSD(BC)	DIFF	DIFF	DIFF	-	-	-	DIFF
Temperature							
	Buford	West Point	George	Montezuma	Albany	Bainbridge	Woodruff
JVSD-DDS	-	-	-	-	-	-	-
JVSD(BC)-DDS	-	DIFF	DIFF	DIFF	DIFF	DIFF	DIFF
BCSD-JVSD(BC)	DIFF	-	-	-	-	-	-

3.5 Assessing Climate Changes of the ACF Basin

This section assesses the ACF precipitation and temperature change implied by the GCM scenario runs. In this regard, monthly temperature and precipitation climatologies of all 13 GCM A1B scenarios for the seven ACF sub-basins are first shown in **Figure 3.19**. All sub-basins show increasing temperature trends, with higher increases during spring and fall. Precipitation is projected to increase during late fall and winter and decrease during spring for upstream watersheds (Buford, West Point, and Montezuma). The change direction over the first and second halves of the century is generally similar, with the second half experiencing somewhat larger changes. These observations apply also to the A2 scenarios (not shown).

The previous results provide information on mean monthly trends. Critical climate change impacts, however, are also associated with changes of other distributional statistics (e.g., extreme precipitation and temperature values). To assess such changes, **Figures 3.20** and **3.21** present monthly box plots of the historical and future precipitation and temperature scenarios (A1B and A2) for two ACF watersheds, Buford (at the ACF headwaters) and Woodruff-Bainbridge (before the river enters into Florida). In each figure, the historical box-plots are denoted "H1 through H12" while the two future scenarios are denoted "FF1 through FF12" (for the first 50 years of the 21st century) and "FS1 through FS12" (for the second 50 years). The future box-plots include data from all 13 future scenarios, while the historical box-plots include only historical data. These figures indeed show that climate change impacts are not uniform across the months of the year. More specifically, these figures support the following observations:

(1) Buford Precipitation: **Figure 3.20** shows that mean precipitation increases during December through March, decreases during May through August, and remains stable in late spring (April and May) and early fall (September and October). The largest increase occurs in March, while the largest decrease occurs in July and August.

The upper quartile (UQ) of the monthly precipitation distribution increases during December through June, with the largest increase occurring in March and April (exacerbating potential flooding impacts). UQ decreases in October and November.

The lower quartile (LQ) of the monthly precipitation distribution increases in January, February, and October, and decreases in March through August. July and August register the largest such decrease, raising concerns for summer water availability.

(2) Buford Temperature: Mean monthly temperature increases in all months of the year with the most pronounced increases taking place from January through May and October through December. The largest increases, in the range 2 to 2.5 ^{o}C, are associated with the A2 climate scenarios in the second half of this century.

Likewise, the monthly upper temperature quartile increases for all months, with March and September registering the largest change (of approximately 3 ^{o}C) for the A2 scenarios and the second half of the century.

The monthly lower temperature quartile also increases for all months, with the largest increases noted in February and March (of approximately 2 ^{o}C).

Other temperature statistics of interest have also been computed (e.g., consecutive summer days with temperature higher than a certain threshold) and show similar intensifying trends. These are expected to have direct impacts on human communities,

agriculture, and ecosystems, and comprise the scope of continuing assessments (Georgakakos et al., 2010).

(3) Woodruff-Bainbridge Precipitation: Unlike Buford, the Woodruff-Bainbridge watershed does not show any mean precipitation increase in spring, but it does register increases in November and December (**Figure 3.21**). Notable decreases occur in February, March, and July.

The monthly upper mean precipitation quartile increases for all months with the largest increase occurring in February through May. The monthly lower mean precipitation quartile shows a decreasing trend from January through August, with the most marked decline noted in June, July, and August. On the other hand, LQ is increasing in September, October, and December.

The A1B and A2 scenarios exhibit similar trends, with the latter somewhat exacerbated for the second 50-year period.

(4) Woodruff-Bainbridge Temperature: All three temperature statistics increase for all months of the year, all scenarios, and both 50-year future periods. The largest mean temperature increases occur from January through May and from October through December and are in the order of 2.5 – 3 ^{o}C. The largest UQ increases are in the order of 3 to 3.5 ^{o}C and occur from January through May and in September. Lastly, the largest LQ increase (2.5 – 3 ^{o}C) occurs in February.

Thus, the precipitation and temperature changes predicted for Woodruff-Bainbridge are similar to those of Buford, raising alarming concerns with respect to summer water availability and the impacts of a hotter climate on people, crops, and ecosystems.

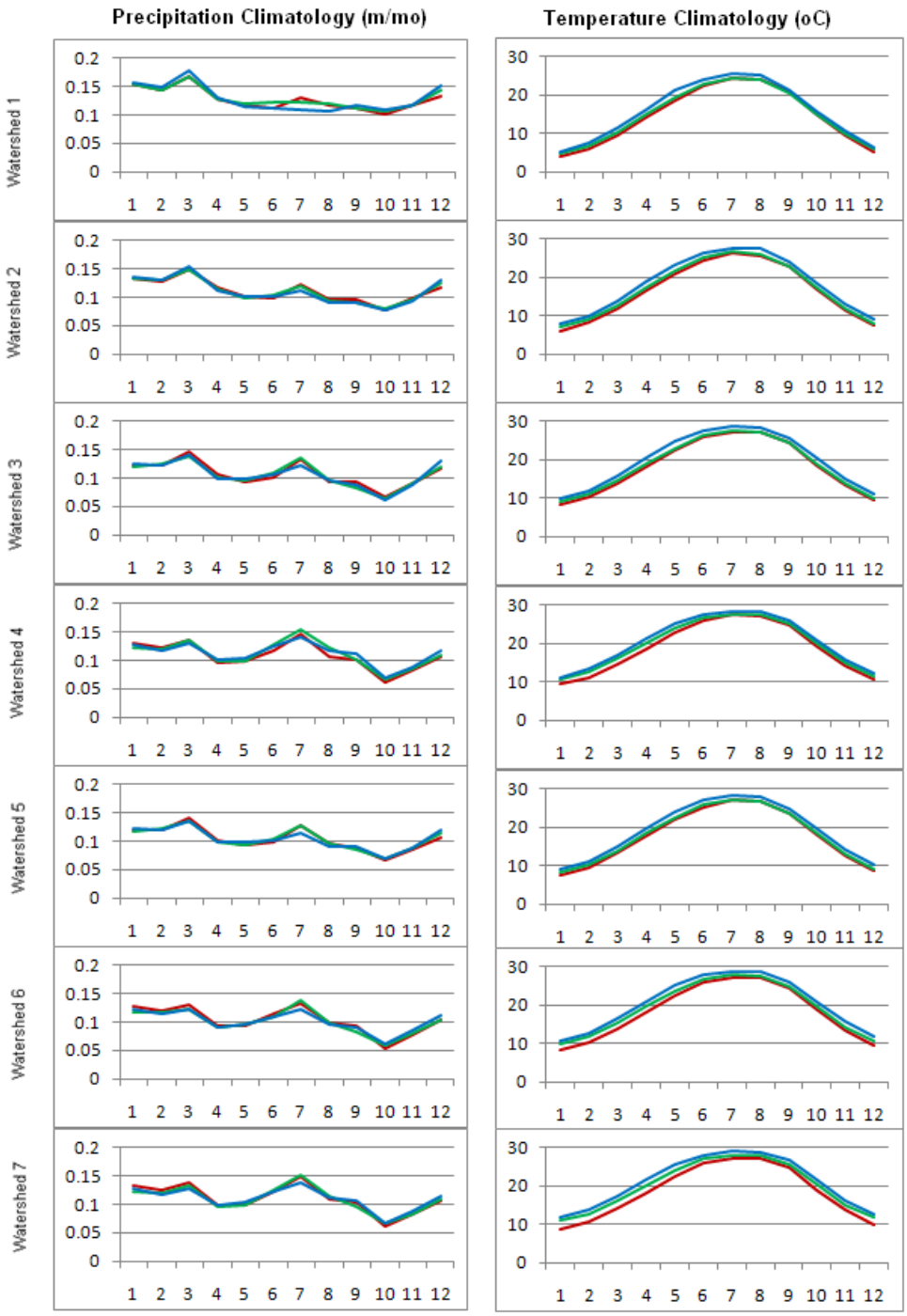

Figure 3.19: Climatologies of spatially aggregated precipitation and temperature for seven ACF watersheds: (1) Buford, (2) West Point, (3) George, (4) Woodruff, (5) Montezuma, (6) Albany, and (7) Bainbridge; Lines in Red–Observations (1950-1999); Green–JVSD downscaled (2000- 2049); Blue–JVSD downscaled (2050-2099) under A1B Scenarios.

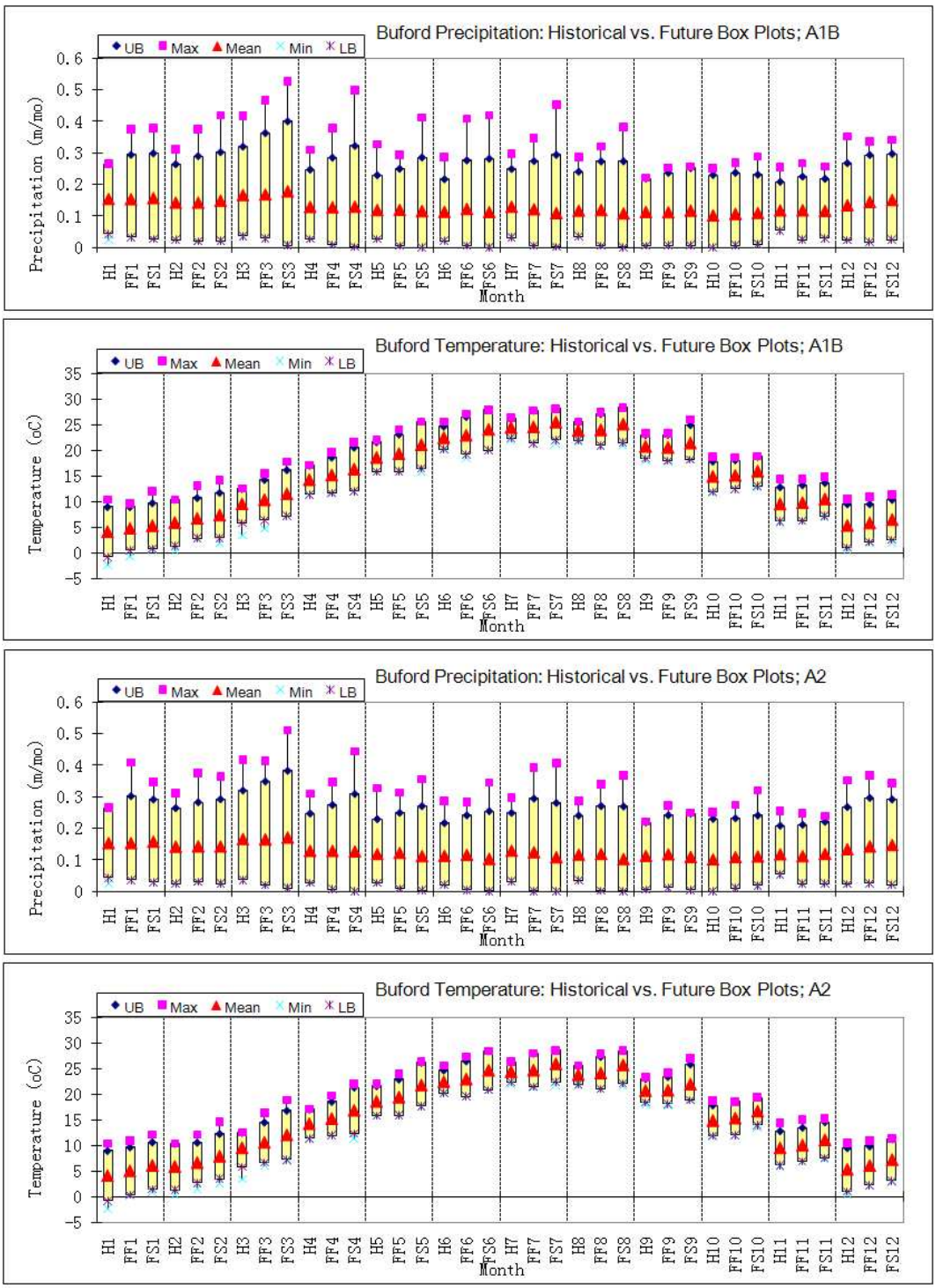

Figure 3.20: Box Plots of Monthly Historical vs. Future (A1B and A2) Watershed Precipitation and Temperature, Buford: H denotes the historical period (1950-1999); FF the first future period (2000-2049); and FS the second future period (2050-2099).

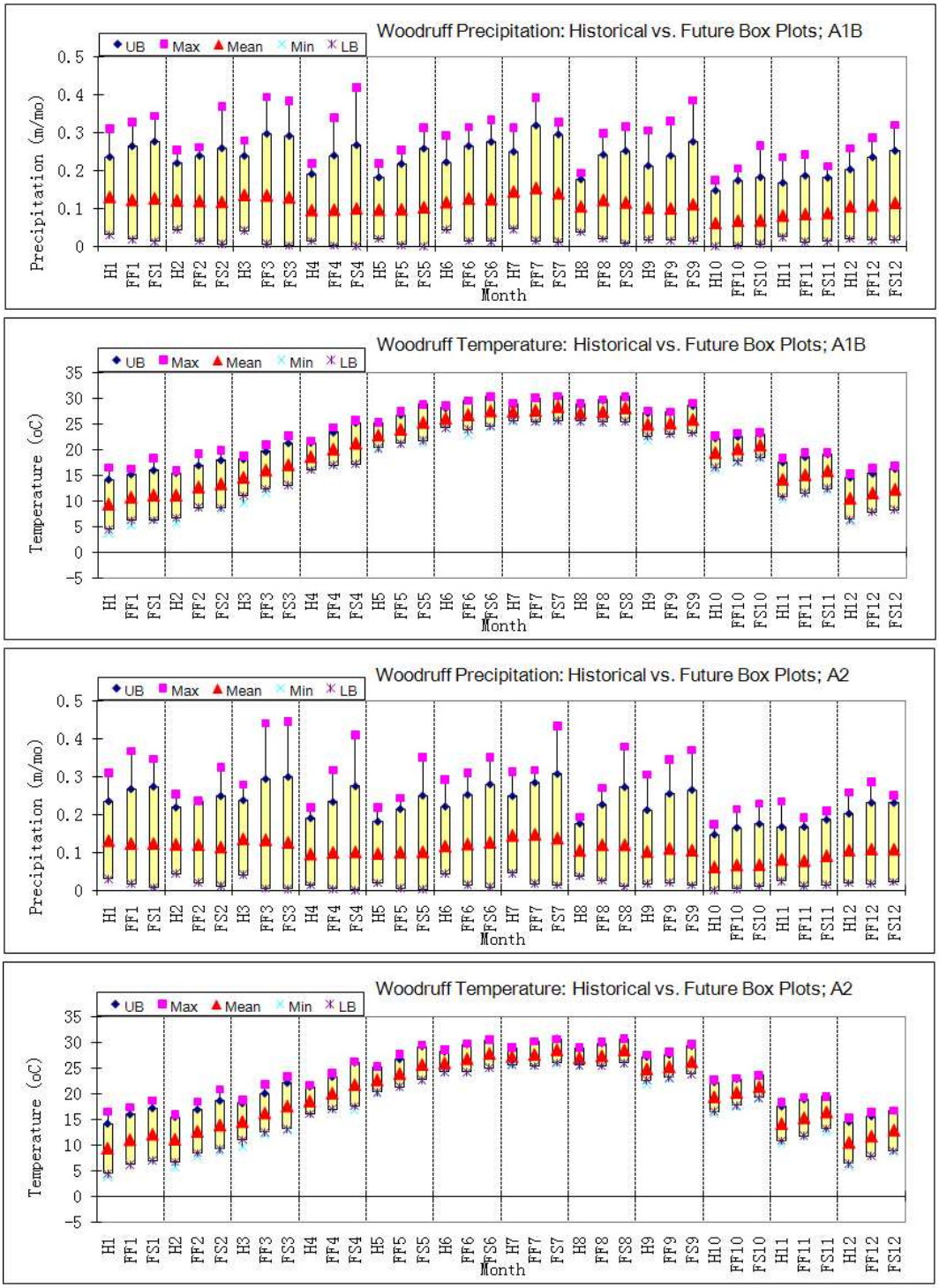

Figure 3.21: Box Plots of Monthly Historical vs. Future (A1B and A2) Watershed Precipitation and Temperature, Woodruff: H denotes the historical period (1950-1999); FF the first future period (2000-2049); and FS the second future period (2050-2099).

3.6 Conclusions

This chapter introduces a new statistical downscaling technique, named Joint Variable Spatial Downscaling—JVSD, for the generation of high resolution gridded datasets suitable for regional watershed modeling and assessments. JVSD follows the general two-step approach introduced by Wood et al., 2004, as part of the BCSD downscaling method, but it includes several distinguishing features including *(1)* joint downscaling of atmospheric fields; *(2)* identification of a constant pivotal quantity reducing the biases introduced by percentile-to-percentile mapping; *(3)* preservation of sub-grid correlations and variability; and *(4)* physical plausibility of the downscaled sequences over the entire region of interest.

Comparisons with observed historical data, BCSD, and dynamic downscaling methods are favorable and demonstrate that JVSD has distinct advantages over existing methods. JVSD can also be used to post-process dynamic downscaling results to correct for remaining biases.

Application of the method to the Apalachicola-Chattahoochee-Flint (ACF) river basin (for all IPCC GCM scenarios) leads to the following conclusions:

Mean monthly temperature exhibits increasing trends over the ACF basin for all seasons and all A1B and A2 scenarios. Most significant are the A2 temperature increases in the 2050 – 2099 time periods. The most pronounced temperature increase is projected to occur in winter, spring, and fall. Temperature highs and lows also increase. In the southern ACF watersheds, mean precipitation generally exhibits a mild decline, except in late winter when it shows an increase. For the northern ACF watersheds, mean precipitation increases are noted in winter (as in the south) but also early spring. In

addition to mean trends, the precipitation distribution “stretches” with higher highs and lower lows. It is notable, however, that southeast US and ACF precipitation in summer and early fall is impacted by hurricane-induced tropical storms which are not well represented in the current GCMs.

We have applied the JVSD method to generate downscaling dataset for the whole study basins in Georgia. We present the complete results of the climate assessments (with the corresponding hydrological assessments) for all six study river basins in **Chapter 6**.

CHAPTER 4

HYDROLOGIC MODELING

Hydrologic models have been broadly used in climate change assessments (Lettenmaier and Rind, 1992; Stamm et al., 1994; Conway, 1998; Wood et al., 2004; Maurer, 2007). This chapter presents a novel lumped conceptual watershed model (Georgakakos et al., 2010) and discusses a new model calibration method based on control and optimization theory.

The proposed watershed model includes multiple storages with non-linear storage-release functions, percolation functions, and deep infiltration functions, characterized by a few model parameters estimated by applying inductive modeling approaches. Model parameters are estimated using a recursive identification methodology suitable for multiple, inter-linked modeling components. The new model has been applied to large and intermediate scale watersheds (10^2 to 10^4 square miles) in Georgia at monthly, weekly, and daily time resolutions. The calibrated Georgia watershed models are employed to characterize the hydrologic responses under the historical climate and the future climate scenarios.

4.1 Model Formulation

4.1.1 Model System Diagram

The model formulation is similar to that of a lumped parameter Sacramento model type, and is intended to simulate the hydrologic processes of infiltration/percolation, evapotranspiration, and surface and subsurface runoff (**Figure 4.1**) in monthly, weekly, or daily basis.

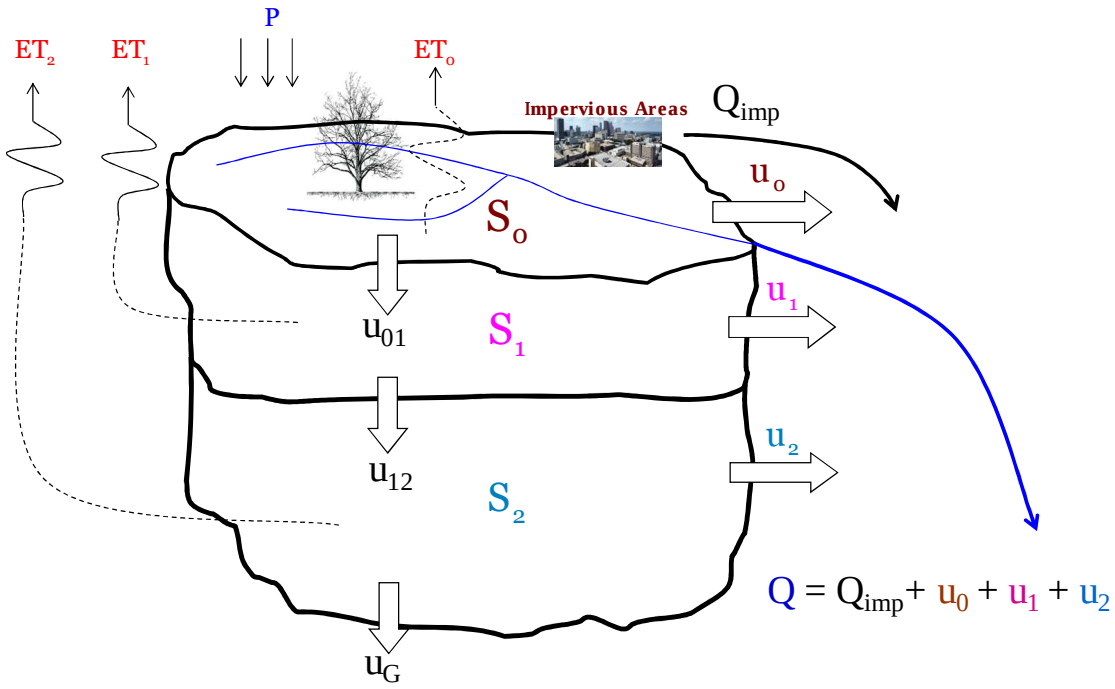

Figure 4.1: Hydrologic Modeling System Schematic (Source: Georgakakos et al., 2010).

Model inputs include precipitation and potential evapotranspiration demand (PET) averaged over the watershed area. The model includes one surface and two subsurface moisture storage layers, with water contents S_0, S_1, and S_2. Water enters the top model layer as precipitation, P, and, after some losses to surface retention, it infiltrates/percolates to the lower storage layers. Precipitation falling on impervious areas contributes immediately to runoff (Q_{Imp}). Storage layers may be depleted by evapotranspiration ET_0, ET_1, and ET_2, or runoff to the stream u_0, u_1, and u_2. Evapotranspiration depends on PET as well as storage. Runoff depends on storage through the storage-runoff functions $u_0(S_0)$, $u_1(S_1)$, and $u_2(S_2)$. Total runoff, Q, to the stream is the sum of all runoff contributions, $Q = Q_{Imp} + u_0(S_0) + u_1(S_1) + u_2(S_2)$. The

infiltration/percolation functions u_{01} and u_{12} are key model elements and depend on various model variables. In addition to the evapotranspiration, storage-runoff, and infiltration/percolation functions, model parameters include storage capacities. These functions and parameters are calibrated from contemporaneous observations of precipitation, PET, and total watershed runoff.

A notable difference between this and the Sacramento model formulation is the distinction of soil moisture as tension and free water. The assumption underlying the model implementation is that the apportionment, storage, and release of soil moisture to and from tension and free water storage occur at time scales much faster than a month or a week. Thus, at coarse time resolutions, tension and free water can be combined into an aggregate soil moisture storage which can adequately represent the observed storage-runoff process. Distinguishing soil moisture storage in tension and free water components at finer time scales (e.g., daily or hourly) will be assessed based on the concomitant improvements in model performance.

Furthermore on an hourly time scale, the infiltration process is controlled by the soil infiltration capacity and the availability of surface water supply. However, at larger time scales (e.g., monthly and weekly), the detailed infiltration dynamics is not observable. Thus, over monthly and weekly intervals, it can be assumed that surface water (that is not retained in surface storage or does not become runoff from impervious surfaces) enters the upper sub-surface storage, provided that it is not filled to capacity.

4.1.2 Soil Moisture Storages

Three soil moisture storages represent three layers of the hydrologic model as shown in **Figure 4.1**: the surface layer, the upper soil moisture layer, and the lower soil moisture

layer. For each layer, the water balance dynamics controls the water flux getting through them.

Surface Storage: S_0

The dynamics of the surface water storage is represented by the storage-runoff function $u_0(S_0)$. This storage begins to fill during significant precipitation events when subsurface storage is filled to capacity. While water released from this storage may develop over a period of few days, it is assumed that the storage depletion process (to become runoff) will be fully completed over a period of a month without carryover effects. Thus, a simple water balance representation equating surface water storage (less evaporation) to surface runoff would be adequate. This particular assumption was tested with Georgia watersheds by using both a fully dynamic surface water element as well as the simpler water balance representation. The calibration process showed that for monthly and weekly models the optimal storage-release functions $u_0(S_0)$ are nearly vertical, validating the assumption that, over a monthly time step, release from surface storage is practically instantaneous. However, for daily models explicit surface storage-runoff storage is necessary.

Upper Soil Storage: S_1

The dynamics of the upper soil storage is represented by the storage-runoff function $u_1(S_1)$. The upper storage is filled by water infiltrated from the surface when precipitation starts. When the accumulated soil moisture exceed certain threshold values, it begins to release significant amount of water by following the storage-runoff function $u_1(S_1)$. We will assume that the storage-release rule is a monotonic function (i.e., no hysteresis) defined only on the storage S_1. The soil moisture of the upper layer can also

infiltrate into the lower soil layer as water flux u_{02}. The assumption implies that in catchment or watershed systems, the small-scale (e.g., hill-slope system) hydrological processes are averaged so that it can be implicitly treated as a homogenous storage, whose release only depends on the average soil moisture.

The water flux between the upper and lower soil layers may depend on several variables (such as actual storages, precipitation, and evapotranspiration). The form of this relationship will be identified as part of the parameter estimation process.

Lower Soil Storage: S_2

The dynamics of the surface water storage is represented by the storage-runoff function $u_2(S_2)$. The lower storage is primarily in charge of the base flow of the river runoff. The release function is also assumed to be a monotonic function defined only on the storage S_2.

4.1.3 Water Fluxes and Dynamics

In keeping with the previous comments and assumptions, the mathematical model formulation is as follows:

Impervious Storage Runoff: Q_{imp}

$$Q_{imp}(k) = a_{imp}\, P(k),$$

Retention Storage: S_{ret}

$$S_{ret}(k) = \max\left\{ a_{ret}\, \frac{PET(k)}{\max\{PET\}}\, P(k),\ b_{ret}\, P(k) \right\},$$

Effective Precipitation: P_{eff}

$$P_{eff}(k) = P(k) - S_{ret}(k) - Q_{imp}(k),$$

In the above equation, k is the monthly interval index, P(k) is the precipitation depth (averaged over the watershed area), a_{imp} is a constant coefficient, PET(k) is the potential evapotranspiration demand during month k (averaged over the watershed area), max{PET} is the maximum monthly PET over the simulation horizon, and a_{ret} and b_{ret} are constant coefficients.

Evapotranspiration: ET_i, (i = 0, 1, 2)

$$ET_i(k) = PET(k)\left[\frac{S_i(k) + S_i(k+1)}{2\sum_{i=0,1,2} S_i^c}\right], \quad i = 0, 1, 2,$$

In the above equation, S_i^c is the capacity of storage i, i=0, 1, 2 for each layer. Other various forms including proportionality and exponent coefficients were also tested for the above relationships between ET, PET, and the monthly-average storage i as a fraction of the total storage capacity. However, in all Georgia watersheds, the above relationship performs best.

Groundwater Flux: u_G

The groundwater flux u_G may represent surface water loss to or gain from the deeper groundwater system. This interaction can take place through the lower soil moisture storage or directly through the stream channel. These two possibilities can be modeled as follows:

(i) Interaction through the lower soil moisture storage:

$$S_2(k+1) = S_2(k) - ET_2(k) - u_2(k) + u_{12}(k) - u_G(k).$$

(ii) Interaction through the stream channel:

$$Q(k) = Q_{imp}(k) + u_0(k) + u_1(k) + u_2(k) - u_G(k).$$

The u_G flux can then be identified and by an iterative process described in the parameter estimation section.

4.1.3 Storage Dynamics

(i) Storage $S_1(k+1)$ *not* constrained by capacity limit:

$$S_1(k+1) = S_1(k) + P_{eff}(k) - ET_1(k) - u_1(k) - u_{12}(k),$$

$$S_2(k+1) = S_2(k) - ET_2(k) - u_2(k) + u_{12}(k) - u_G(k),$$

$$S_0(k+1) = 0,$$

$$u_0(k) = 0.$$

(ii) Storage $S_1(k+1)$ constrained by capacity limit:

$$S_1(k+1) = S_1^c,$$

$$Q_{sat}(k) = [S_1(k) + P_{eff}(k) - ET_1(k) - u_1(k) - u_{12}(k)] - S_1^c,$$

$$S_2(k+1) = S_2(k) - ET_2(k) - u_2(k) + u_{12}(k) - u_G(k),$$

$$S_0(k+1) = 0,$$

$$u_0(k) = Q_{sat}(k) - ET_0(k).$$

Although the above dynamical relationships are expressed in monthly time steps, the actual simulation is performed at a finer resolution (e.g., daily intervals) to identify whether and when storage capacity limits are reached. This is necessary, because when

subsurface storages become saturated, the form of their dynamical relationships and fluxes change.

Storage-Runoff Functions (u_i, i=1,2):

$$u_i(k) = u_i[(S_i(k)+S_i(k+1))/2], i = 1, 2.$$

The functional forms of these relationships are identified as part of the model calibration process.

Percolation Functions (u_{12} and u_G):

$$u_{12}(k) = u_{12}\left[S_1(k), S_2(k), P_{eff}(k), ET_1(k), ET_2(k)\right].$$

The functional form of this relationship is also identified as part of the model calibration process.

Total Watershed Runoff (Q):

$$Q(k) = Q_{imp}(k) + u_0(k) + u_1(k) + u_2(k).$$

4.2 Parameter Estimation

The parameter estimation (or model identification) process aims to identify a set of model parameters and functions such that model output matches with actual observations (total runoff Q) as best as possible. The model parameters and functions can be distinguished in two categories.

The first category includes parameters and functions of structural importance that govern the dynamical model response and the interaction/linkage among its structural components and processes (i.e., soil storages and runoff). This *primary parameter set* includes:

- Total storage capacity, S^c;
- Lower soil moisture storage runoff function, $u_2(S_2)$;
- Upper soil moisture storage runoff function, $u_1(S_1)$;
- Upper and lower soil storage capacities, S_1^c and S_2^c; and
- Percolation function, $u_{12}(S_1, S_2, \ldots)$.

The second parameter category includes parameters that fine-tune model response, within the structural framework established by the primary parameters, to capture other hydrologic response aspects. This *secondary parameter set* includes:

- Impervious area runoff parameter, a_{imp};
- Retention Storage parameters, a_{ret} and b_{ret}; and
- Deep groundwater flux, $u_G(S_2)$ or $u_G(Q)$.

This distinction is made here, because simultaneous estimation of all parameters, all too often, leads to parameter estimates assuming modeling roles for which they are not designed. The second reason for the estimation approach introduced in this work is to systematically and incrementally add processes and parameters that are necessary to explain system behavior, not based on a preconceived model design.

The estimation process is iterative and consists of *(1)* generating initial estimates of the parameters and functions, *(2)* iteratively refining the primary parameters and functions until no further improvements can be achieved, and *(3)* repeating the process for other secondary parameter values to fine-tune model performance.

4.2.1 Initial Parameter and Function Estimates

The estimation process begins by assuming initial parameter values for the retention storage, impervious runoff, and deep percolation terms. In this first step, deep percolation (i.e., percolation to or from groundwater aquifers) is assumed negligible. The other terms can also be initially assumed negligible. For the initial parameter values a_{imp}, a_{ret}, and b_{ret} can be used to generate initial estimates of the impervious area runoff, Q_{imp}, retention storage S_{ret}, and effective rainfall P_{eff}:

$$Q_{imp}(k) = a_{imp}\, P(k),\ k=1,\ldots,\ N;$$

$$S_{ret}(k) = \max\left\{ a_{ret}\, \frac{PET(k)}{\max\{PET\}}\, P(k),\ b_{ret}\, P(k) \right\},\ k=1,\ldots,N;\ \text{and}$$

$$P_{eff}(k) = P(k) - S_{ret}(k) - Q_{imp}(k),\ k=1,\ldots,N,$$

where N is the total number of months in the historical horizon used for calibration.

Then, the storage equations become:

$$S_1(k+1) = S_1(k) + P_{eff}(k) - PET(k)\left[\frac{S_1(k) + S_1(k+1)}{2\,S^c}\right] - u_1(k) - u_{12}(k),$$

$$S_2(k+1) = S_2(k) - PET(k)\left[\frac{S_2(k) + S_2(k+1)}{2\,S^c}\right] - u_2(k) + u_{12}(k).$$

Adding the above dynamical equations results in the following aggregate soil storage equation:

$$S(k+1) = S(k) + P_{eff}(k) - PET(k)\left[\frac{S(k) + S(k+1)}{2\,S^c}\right] - u_1(k) - u_2(k),$$

where $S(k) = S_1(k) + S_2(k)$, and $u_1(k) + u_2(k) = Q - Q_{imp}$ (total runoff from soil storage). Substituting the runoff terms by the observed total runoff ($Q - Q_{imp}$), yields an aggregate storage relationship with only one unknown: the total aggregate soil storage capacity S^c (**Figure 4.2**). However, determining the correct S^c value is not obvious, as different S^c values (and the observed forcing of P, PET and Q) simply give rise to different storage sequences. The key to selecting the most suitable S^c value is to examine the global behavior of the storage sequence it generates and determine the one most consistent with the expected physical system response.

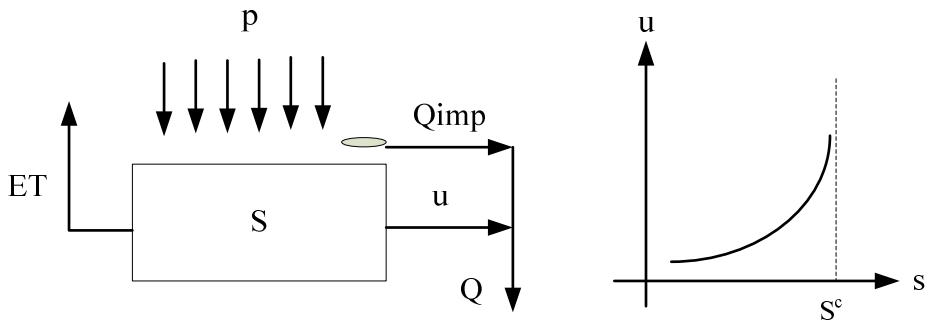

Figure 4.2: Hydrologic Model with One Storage Element.

More specifically, the expected behavior of the hydrologic system is to have a smooth and monotonic response of runoff relative to storage. This is expected to hold particularly during periods of storage depletion when the dominant runoff contribution comes from the lower soil storage. Thus, if the observed data does not contain errors, the correct S^c value should generate a storage sequence such that when

$S(k+1) < S(k)$, $S(n+1) < S(n)$, and $[S(k+1)+S(k)]/2 < [S(n+1)+S(n)]/2$,

it should also hold that $Q(k) < Q(n)$ for all such values of k and n.

Namely, during storage depleting periods, the runoff corresponding to ranked storage values (in, say, descending order) should also adhere to the same ranking. To be

sure, because of the existing data errors in the observed values of P, PET, and Q, this relationship is not expected to be perfect. But, the value of S^c that generates storages that adhere to this criterion as best as possible would represent the best S^c estimate. While this is the main idea for identifying the initial S^c estimate, several quantitative criteria (that have been tested in this work) can be used to guide this process.

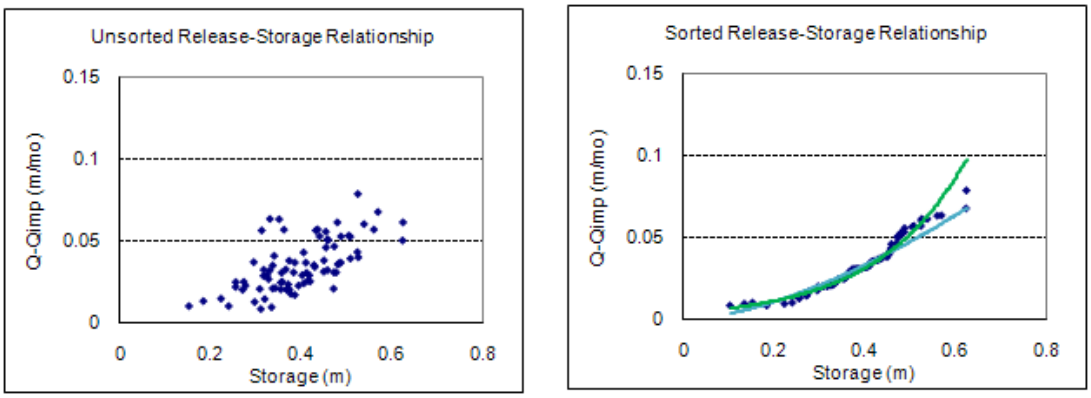

Figure 4.3: Unsorted and Sorted Release-Storage Relationships Identified from the One Aggregated Soil Storage Model. (Example from Buford Monthly Watershed Model)

Figure 4.3 illustrates the release-storage relationships identified from the Buford monthly model with one aggregated soil storage. The point scatter plot on the left shows the simulated storage during the depleting periods and the corresponding releases from the soil. The storage capacity was estimated to be about 0.63 meter for this watershed. The plot on the right shows the sorted release-storage relationships (both storage and release sequences are sorted individually) and two nonlinear approximations: the green line – exponential function and blue line – the power function.

An important side benefit of the above procedure is the identification of the lower storage runoff function $u_2(S_2)$. This function can be estimated by the ranked $(Q\text{-}Q_{imp})$ versus ranked S relationship corresponding to the best S^c estimate. As indicated earlier,

these rankings do not include all runoff-storage paired values generated by the dynamical equation, but only those that comply with depleting storage conditions. Because the lower storage is depleted last, the basis of this relationship should be the lower part of the aggregate storage range, for example, the lower one third. This relationship can then be approximated through a suitable analytical function such as a power function:

$$u_2 = \beta_{2,1} S_2^{\beta_{2,2}}$$

where $\beta_{2,1}$ and $\beta_{2,2}$ are constant coefficients.

In the next step, we will identify the storage capacity and storage-release function for the upper soil layer. **Figure 4.4** shows the two-storage model compared to the previous aggregate storage model. The previous procedure can be repeated to provide initial estimates of S_1^c and of $u_1(S_1)$. This involves substituting the newly obtained estimates of S^c and $u_2(S)$ into the aggregate storage equation and repeating the ranking process for S and $[Q-Q_{imp}-u_2(S)]$. The best value of S_1^c is that for which the ranked data exhibit an almost one to one change of Q versus S. This is because when the system is saturated, $Q-Q_{imp}$ is dominated by u_0 which equals the storage in excess of S_1^c. The ranked $[Q-Q_{imp}-u_2(S)]$ versus S relationship can then be analytically approximated to provide an initial estimate of the $u_1(S_1)$ function. As emphasized, these are only *initial* estimates to be revisited in the following stages of the estimation process.

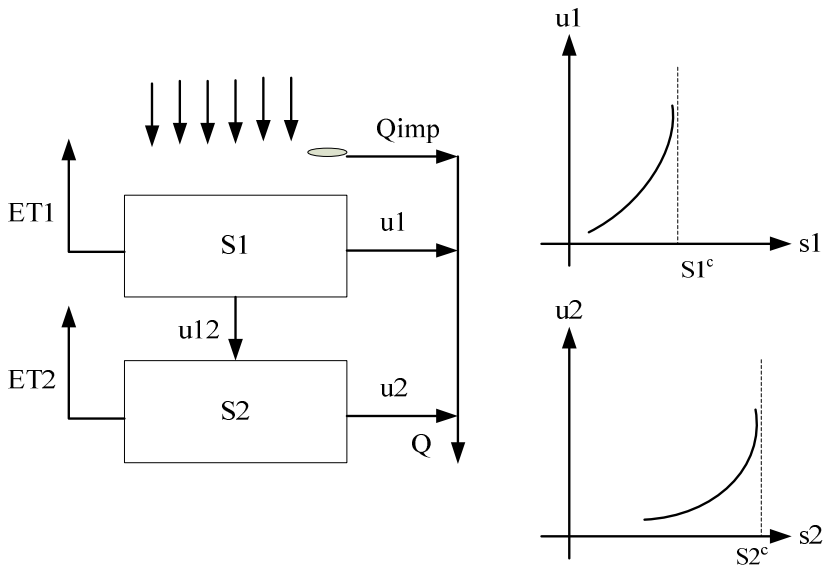

Figure 4.4: Hydrologic Model with Two Storage Elements.

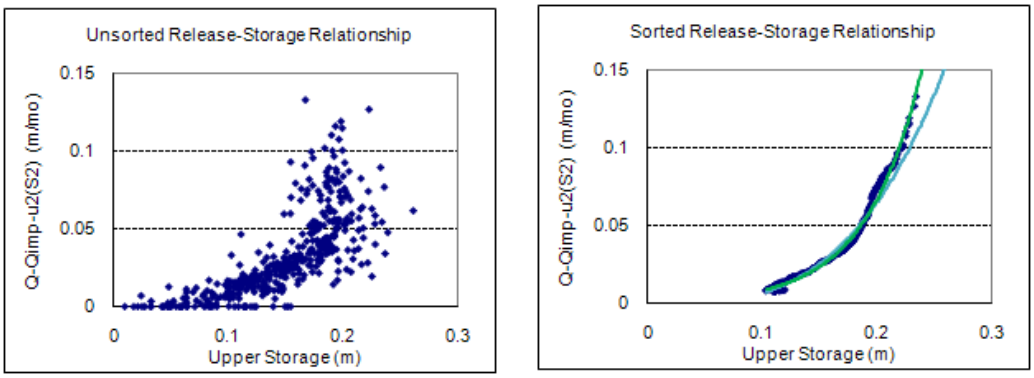

Figure 4.5: Unsorted and Sorted Release-Storage Relationships for the Upper Storage Identified from the Two-Soil-Storage Model. (Example from Buford Monthly Watershed Model)

At this stage, initial estimates of S^c, S_1^c, S_2^c (= S^c - S_1^c), $u_1[S_1(k/k+1)]$, and $u_2[S_2(k/k+1)]$ have been obtained, where the notation $S_i(k/k+1)$ is used to denote the average S_i storage value over the interval k. The last, and most crucial task in the initial estimation cycle, is to identify the percolation function u_{12}. To this end, the individual storage equations are re-instated as follows:

$$S_1(k+1) = S_1(k) + P_{eff}(k) - PET(k)\left[\frac{S_1(k/k+1)}{S^c}\right] - u_1[S_1(k/k+1)] - u_{12}(k),$$

$$S_2(k+1) = S_2(k) - PET(k)\left[\frac{S_2(k/k+1)}{S^c}\right] - u_2[S_2(k/k+1)] + u_{12}(k).$$

Consider a time step k with known initial storages $S_1(k)$ and $S_2(k)$. Assuming at first that $u_{12}=0$, the dynamical equations can be propagated to yield the end of the period storages $S_1(k+1)$ and $S_2(k+2)$. This step requires a few iterations due to the dependence of $\{ET_i, u_i, i=1,2\}$ on the end storage $S_i(k+1)$, but convergence is fast, requiring only two to three iterations. This one-step computation also provides runoff estimates $u_i[S_i(k/k+1)]$, i=1,2, which are used next to determine an optimal value for u_{12}. More specifically, this is accomplished by comparing the value of the model generated runoff, $(u_1 + u_2)$, to the observed $(Q-Q_{imp})$. If these two quantities are equal, then u_{12} is indeed zero. Otherwise, the estimation process proceeds to determine the best u_{12} such that the values of $(u_1 + u_2)$ and $(Q-Q_{imp})$ are as close as possible. This is a one-step, constrained optimization problem, where u_{12} is constrained to be within

$0 \le u_{12} \le \min\{S_1(k), S_2^c - S_2(k)\}$,

and the storage variables are constrained to be within their applicable ranges. However, for each time step k, the solution can easily be obtained via an exhaustive, one dimensional search.

This process generates a series of u_{12} values $\{u_{12}(k), k=0, 1, 2, \ldots, N-1\}$ that are most consistent with the observed data and the other initial parameters and functions. These values are used as the basis for relating u_{12} to other system variables that would be

available when the model runs in predictive mode (i.e., when Q is not known). Various functional forms were tested in this work for all Georgia watersheds. The best and most robust performance is obtained by the following relationship:

$$u_{12} = \alpha_0 + \alpha_1 ET_2(k) + \alpha_2 \frac{ET_1(k)}{ET_2(k)} + \alpha_3 S_2(k) + \alpha_4 \frac{S_1(k)}{S_2(k)} + \alpha_5 P_{eff}(k),$$

where α_0, α_1, α_2, α_3, α_4, and α_5 are constant regression coefficients. Furthermore, the continuing application of the model for several other Georgia basins supports the general validity of this functional form. However, all models tested use a monthly time step, and the best u_{12} form may be different for daily or sub-daily time resolutions. **Figure 4.6** shows the optimized u_{12} versus the estimated u_{12} by the above equation.

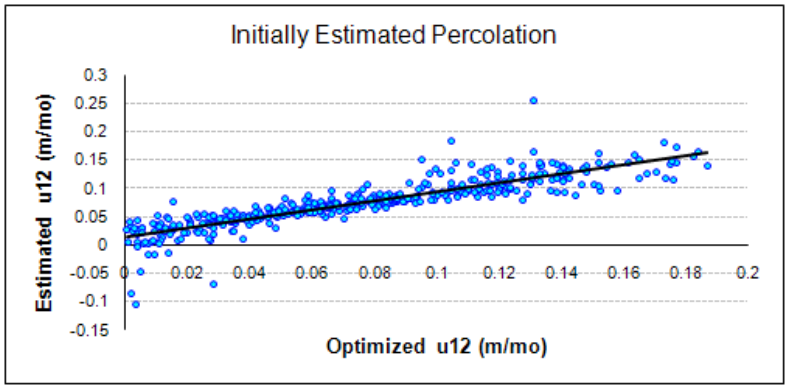

Figure 4.6: Initially Estimated Percolation by Using the Linear Regression Equations. (Example from Buford Monthly Watershed Model)

After the initial estimation of the parameters and functions, the model can be run in a predictive mode, and its performance can be assessed relative to observed runoff. Various criteria can be adopted to assess the model performance including the minimization of the sum of the square error or the absolute difference between model

predictions and observations, and the maximization of the Pearson and Spearman correlation (average and monthly), among others. For a more unbiased assessment, a split sample approach can be adopted where a portion of the historical record is retained for model verification purposes.

4.2.2 Parameter and Function Refinement

In keeping with the above, parameter and function refinement proceeds iteratively as follows:

(1) Select a_{imp}, a_{ret}, and b_{ret};

(2) Select S_0^c, S_1^c, and S_2^c, and estimate $u_2(S_2)$ from the aggregate storage model;

(3) Estimate $u_1(S_1)$ and $u_{12}(P_{eff}, ET_2, ET_1/ET_2, S_2, S_1/S_2)$ from the full model form and iterate until the model performance criterion is optimized;

(4) Repeat Steps (2) to (4) until the best performing parameter and function set $\{S_0^c, S_1^c, S_2^c, u_2(S_2), u_1(S_1)$, and $u_{12}(P_{eff}, ET_2, ET_1/ET_2, S_2, S_1/S_2)\}$ is obtained;

(5) Repeat Steps (1) to (5) until all model parameters are refined and model performance is optimized;

(6) Identify data outliers by comparing each data point (predicted minus observed value) against the error distribution of the corresponding month;

(7) Repeat Steps (1) through (7) until no model performance improvement is noted.

Step (6) was found to be useful in generating more unbiased model parameters but also in pointing out data inconsistencies needing correction. In some of the ACF watersheds, outliers occurred at a rate substantially higher than the statistically acceptable level. The parameter estimation process is computationally efficient, requiring only a few minutes on a high end personal computer.

4.3 Estimation of Potential Evapotranspiration

A significant water loss from a drainage basin is evapotranspiration (ET). ET is the sum of evaporation and plant transpiration from the Earth's surface to the atmosphere. The actual ET is a function of the ground air temperature, wind speed, humidity, and other ambient environmental variables. The actual ET is hard to measure directly. Instead, evaporation pans are used to provide measurements of the combined effect of temperature, wind, humidity, and radiation on actual ET.

4.3.1 Pan Evaporation

A typical class-A evaporation pan (**Figure 4.7**) is circular, 10 inches deep, and 47 1/2 inches in diameter and is constructed of monel metal. The evaporation pan is installed on wooden support. The support is set on the ground in a grassy site, away from bushes, trees, and other obstacles. The amount of evaporation to the nearest hundredth inch from the pan is measured every day. The measurement day begins with the pan filled to exactly two inches (5 cm) from the pan top. At the end of 24 hours, the amount of water to refill the pan to exactly two inches from its top is measured. If precipitation occurs in the 24-hour period, it is taken into account in calculating the evaporation. Sometimes precipitation is greater than evaporation, and measured increments of water must be dipped from the pan.

Other elements recorded include wind movement, water and air temperatures, and precipitation. The Class-A pan is usually installed with an anemometer and a floating minimal-maximal thermometer to measure the wind speed and average water-surface temperature. This is because that the amount of evaporation is a function of temperature,

humidy, wind, and other ambient conditions. Evaporation from a natural body of water is usually at a lower rate because the body of water does not have metal sides that get hot with the sun.

Figure 4.7: U.S. National Weather Service Class-A Evaporation Pan. (Acquired from NWS website: http://www.crh.noaa.gov/lbf/?n=evap_pan on March 21, 2011)

4.3.2 Free-Water Evaporation

The pan evaporation can be used to estimate the free-water evaporation. Free-water evaporation can also be defined as lake evaporation. An evaporation pan is different from a lake in that it has less heat-storage capacity, and thus it lacks surface- or ground-water inputs and outputs.

Kohler et al. (1955) developed an empirical equation to estimate free-water evaporation:

$$\mathrm{ET_{fw}} = 0.7\left[ET_{pan} \pm 0.00064 \cdot P \cdot \alpha_{pan}\left(0.37 + 0.00255 \cdot v_{pan}\right)\left|T_{span} - T_a\right|^{0.88}\right].$$

where ET_{pan} and $\mathrm{ET_{fw}}$ are daily pan evaporation and free-water evaporation, respectively, in cm/day; P is the atmospheric pressure in mb v_{pan} is the average wind

speed at a height of 15 cm above the pan in km/day; T_{span} and T_a are the daily average water-surface temperature and the air temperature in ^{o}C; and the sign ($\pm$) is "+" when $T_{span} > T_a$ and "–" when $T_{span} < T_a$. The pan coefficient α_{pan} is estimated form the following empirical equation (Linsley, et al., 1982):

$$\alpha_{pan} = 0.34 + 0.0117 \cdot T_{span} - \left(3.5 \times 10^{-7}\right)\left(T_{span} + 17.8\right)^3 + 0.0135 \cdot v_{pan}^{0.36}.$$

The pan coefficient varies between 0.15 and 0.9 for a typical class-A evaporation pan. The free-water evaporation can also be used to estimate the Potential evapotranspiration demand (PET), which is the amount of water that *could* be evaporated from open water surfaces and transpired by vegetation assuming unlimited water supply. The PET measures the ability of the lower atmosphere to transport moisture away from the land surface. At stations where the pan evaporation measurements are available, the PET (or reference crop evapotranspiration) can be estimated by the above free-water evaporation equation.

4.3.3 Daily PET Estimation

In places where pan evaporation recorders are not available, hydrologists have developed various methods to estimate PET, based on different assumptions, requirements, and regional climate specifications (Grismer, 2002). PET estimation techniques include temperature based methods (e.g., Thornthwaite, 1948, Hamon, 1963, and Hargreaves-Samani, 1985), radiation-based methods (e.g., Turc 1961, Makkink, 1957, and Priestley-Taylor, 1972), and combination methods (e.g., Penman, 1948). In a comparative investigation of several monthly PET methods, Lu (2005) concluded that Priestley-Taylor, Turc, and Hamon's equation are suitable for watershed-scale

applications in the southeastern United States. The Hamon's equation discussed by Lu (2005) has the following form:

$$PET = 0.1651 \times Ld \times RHOSAT \times KPEC$$

PET: daily PET (mm/day);

Ld: daytime length (i.e., time from sunrise to sunset in multiples of 12 hours);

RHOSAT: saturated vapor density (g/m^3) at the daily mean air temperature (T_{mean});

$$RHOSAT = 216.7 \times ESAT / \left(T_{mean} + 273.3\right)$$

$$ESAT = 6.108 \times \exp\left(17.26939 \times T_{mean} / \left(T_{mean} + 237.3\right)\right)$$

T_{mean}*:* daily mean air temperature (^oC);

ESAT: saturated vapor pressure (*mb*) at the given T_{mean};

KPEC: calibration coefficient set to 1.2 for the southeast US;

Thus, the only input data needed for the Hamon's method is "*Air Temperature at 2 meters*".

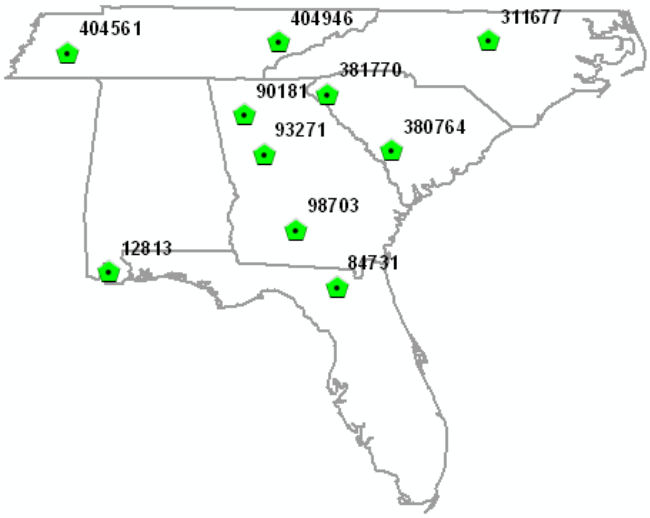

Figure 4.8: Southeast US Meteorological Stations with over 75% Percent Complete Temperature and Pan Evaporation Data from 1909 to Present.

Before using the Hamon's PET estimation approach, it is desirable to quantify and, if possible, improve its accuracy. Toward this end, data from all meteorological stations in the Southeast US with daily records at least 75% complete (number of recorders are larger than 27,000 for both temperature and pan evaporation) from 1909 up to present are identified (**Figure 4.8**) and their data retrieved from the National Climatic Data Center(NCDC) . The daily PET is then estimated using the Hamon's PET equation and the free-water evaporation (Linsley, 1982).

PET is estimated from Lu's (2005) version of the Hamon's equation based on the ***daily mean temperature*** (T_{mean}), and also based on the ***daily maximum temperature*** (T_{max}). The coefficient *KPEC* is also calibrated for each month of the year such that the means of the calculated PET values match the means of the free-water evaporation.

Figure 4.9 shows the daily PET versus the free-water evaporation for June, July, and August for two typical stations located in north and South Georgia. The top panel of graphs depicts the estimated PET values based on the mean daily temperature. PET estimates based on the maximum daily temperature are depicted in the graphs of the bottom panel. The PET means in the lower panels are adjusted through calibration of the *KPEC* coefficient to match the means of free-water evaporation (for each month). In the top panel, the calibration coefficient is set to value used by Lu (2005). In each plot, the linear regression line that passes through the origin is also shown together with the associated R-square value. The results show that for all months, the PET estimates based on the daily maximum temperature provide a distinctly better approximation of the free

water evaporation values than those obtained by the original Hamon's equation. This is evident by comparing the slope of the regression line and the R-square values. This conclusion holds true for all months of the year (in addition to those shown) and all stations tested.

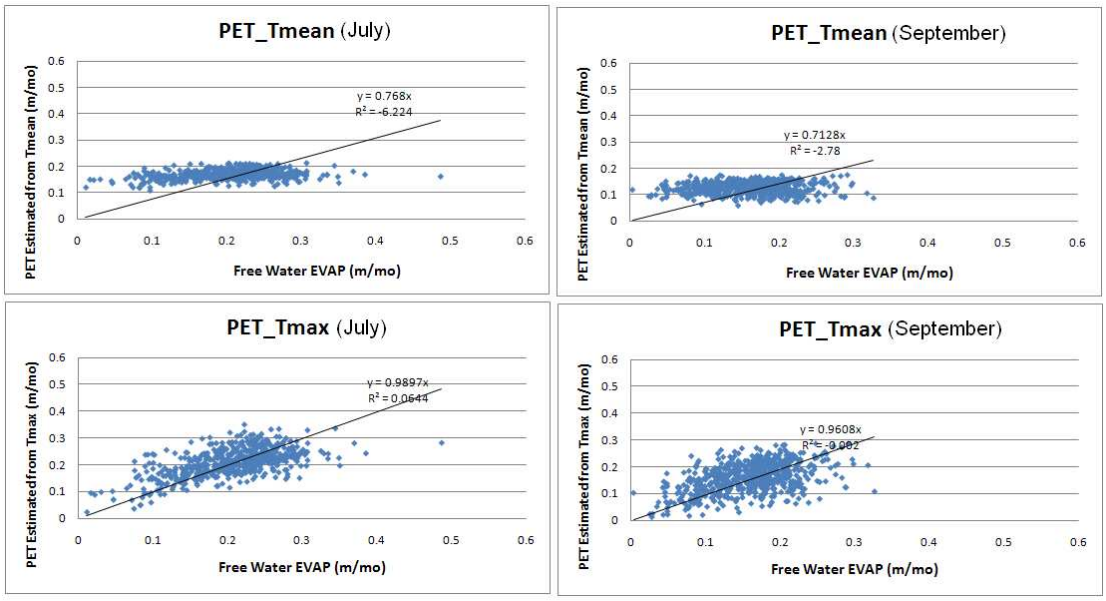

Figure 4.9: Daily PET Estimation based on the Daily Mean Temperature (Top Panel) and Daily Maximum Temperature (Bottom Panel) for Station 93271: July and September. The PET Estimated from the Daily Maximum Temperature Provide a Distinctly Better Approximation of the Free Water Evaporation Values than Those Obtained by the PET Estimated from the Daily Mean Temperature.

4.3.4 Monthly PET Estimation

In this section, we will investigate the performance of estimating monthly PETs by using Hamon's method. Traditional Hamon's approach for monthly PET estimation uses monthly averaged daily mean temperature and Hamon's equations as discussed in the previous section. We have shown in **Section 4.3.3** that the daily maximal temperature is a better predictor for daily PET estimation. In monthly resolution, the following

discussions show that the monthly-averaged daily maximal temperature is also a better predictor than the -averaged daily mean temperature in estimating monthly PET. In addition, it will be shown that the nonlinear form of the Hamon's equation introduces additional errors, but it will also be shown that these biases can be rectified by a fairly straightforward modification of the Hamon's implementation approach.

Traditional Hamon's Approach for monthly PET Estimation:

In the following discussions, we compared two different PET calculation approaches: first, we applied the traditional Hamon's equation and the monthly PET is calculated by using the monthly averaged daily mean temperature T_{mean}; second, we calculated the daily PET by using the daily maximal temperature T_{max} and then the monthly PET is calculated by averaging the calculated daily PET.

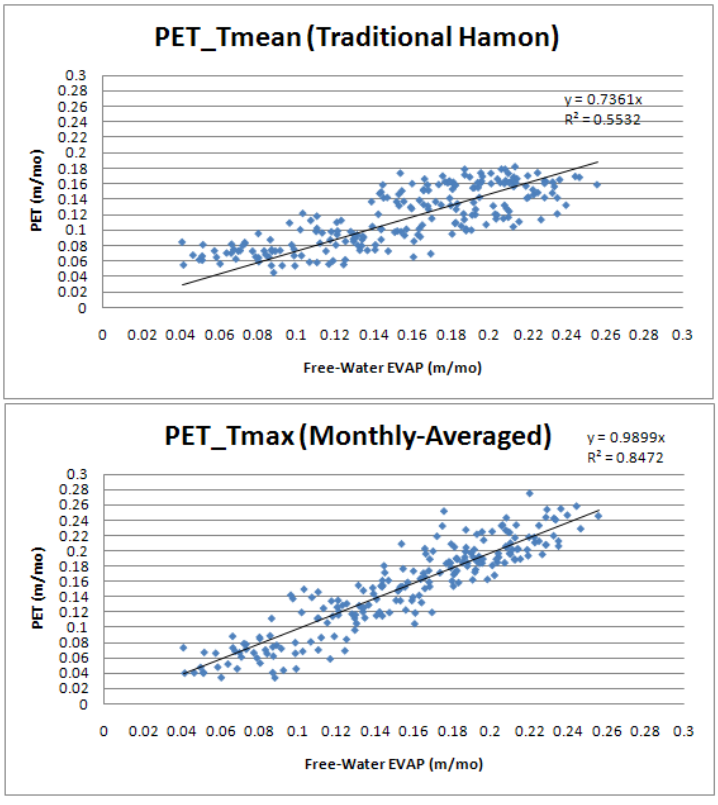

Figure 4.10: Comparison of Two PET Calculation Approaches for Station 93271: (1) Using the Traditional Hamon's Equation and the Monthly PET is Calculated by Using the Monthly-Averaged Daily Mean Temperature (top), and (2) Using the Daily Maximal Temperature to Calculate Daily PET and the Monthly PET Is Calculated by Averaging the Calculated Daily PET (bottom).

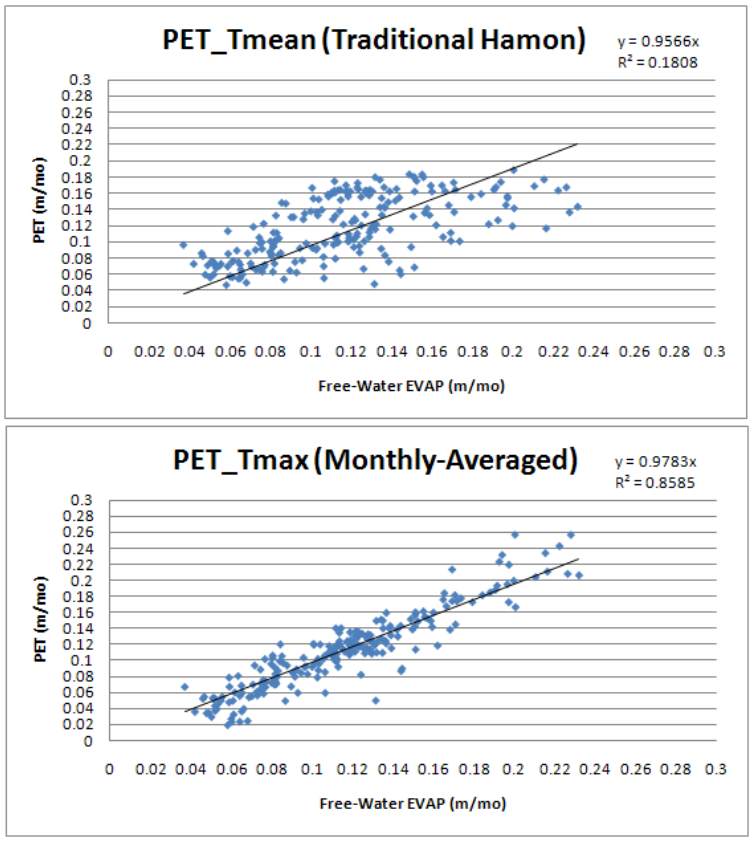

Figure 4.11: Comparison of Two PET Calculation Approaches for Station 381770: (1) Using the Traditional Hamon's Equation and the Monthly PET is Calculated by Using the Monthly-Averaged Daily Mean Temperature (top), and (2) Using the Daily Maximal Temperature to Calculate Daily PET and the Monthly PET is Calculated by Averaging the Calculated Daily PET (bottom).

As shown in **Figure 4.10** and **11**, the traditional Hamon's method tends to underestimate the PET for high temperature and overestimate the PET for low temperature. **Figure 4.10** and **4.11** shows that using the daily maximal temperature to

calculate the monthly-averaged PET is apparently better than using the traditional Hamon's method. This is evident by comparing the slope of the regression line (ideally close to 1) and the R-square values. This conclusion holds true for all stations tested. However, in applying the monthly-averaged method the daily maximal temperature is required. When only the monthly-averaged maximal temperature is available, we develop a modified Hamon's approach to calculate the PET as described in the following section.

Modified Hamon's Approach for Monthly PET Estimation:

In the following discussions, we developed a quadratic form of the Hamon's equation to taking into account the nonlinear feature of the exponential function used in the traditional Hamon's method. We than compared the PET calculated from the modified Hamon's method with the monthly-averaged daily PET discussed in the previous section.

Because of the nonlinear feature of the Hamon's equation, in monthly resolution, the parameters of PET equations need to be recalibrated. In daily resolution, the PET can be estimated from the daily maximal temperature.

$$PET = KPET \cdot \exp\left(\frac{17.26939 \cdot T_{\max}}{T_{\max} + 237.3}\right) / \left(T_{\max} + 273.3\right)$$

This equation can be approximated by the following Taylor Series at T_0.

$$PET = \left(f(T_0) + f'(T_0) \cdot (T_{\max,i} - T_0) + f''(T_0) \cdot \frac{(T_{\max,i} - T_0)^2}{2!} + \cdots \right)$$

where, $f'(T)$ and $f''(T)$ are the first and second derivatives of the original PET function:

$$f'(T) = -\frac{1}{(T+273.3)^2}\cdot\exp\left(\frac{17.3\cdot T}{T+237.3}\right) + \frac{1}{T+273.3}\cdot\left(\frac{17.3}{T+237.3}-\frac{17.3\cdot T}{(T+237.3)^2}\right)\cdot\exp\left(\frac{17.3\cdot T}{T+237.3}\right)$$ and

$$f''(T) = \frac{2}{(T+273.3)^3}\cdot\exp\left(\frac{17.3\cdot T}{T+237.3}\right) - \frac{2}{(T+273.3)^2}\cdot\left(\frac{17.3}{T+237.3}-\frac{17.3\cdot T}{(T+237.3)^2}\right)\cdot\exp\left(\frac{17.3\cdot T}{T+237.3}\right) + \frac{1}{T+273.3}\cdot\left(\frac{-34.6}{(T+237.3)^2}+\frac{34.6\cdot T}{(T+237.3)^3}\right)\cdot\exp\left(\frac{17.3\cdot T}{T+237.3}\right)\cdot + \frac{1}{T+273.3}\cdot\left(\frac{17.3}{T+237.3}+\frac{34.6\cdot T}{(T+237.3)^2}\right)^2\cdot\exp\left(\frac{17.3\cdot T}{T+237.3}\right)$$

Then, the PET equation can be expressed as the following.

$$PET = KPET\cdot\left(C_2 T_{\max}^2 + C_1 T_{\max} + \cdot C_0\right)$$

In the month PET equation, for each calendar month, the three coefficients C_2, C_1 and C_0 can be calculated from the following equations:

$$C_2 = \frac{1}{2} f''(T_0),$$

$$C_1 = f'(T_0) - f''(T_0)\cdot T_0,$$

$$C_0 = f(T_0) - f'(T_0)\cdot T_0 + \frac{1}{2} f''(T_0)\cdot(T_0)^2, \text{ and}$$

$$T_0 = T_{\max}.$$

The monthly PET then can be calculated by summing the daily PETs.

$$PET_{monthly} = KPET\cdot C_2\sum_{i=1}^{Nd} T_{\max,i}^2 + KPET\cdot C_1\sum_{i=1}^{Nd} T_{\max,i} + KPET\cdot C_0\cdot Nd$$

Notice that $\sum_{i=1}^{Nd} T_{\max,i}^2 = Nd \cdot VAR(T_{\max}) + Nd \cdot [E(T_{\max})]^2$ and $\sum_{i=1}^{Nd} T_{\max,i} = Nd \cdot E(T_{\max})$,

then the above equation can be expressed as:

$$PET_{monthly} = KPET \cdot Nd \cdot \{C_2 \cdot [VAR[T_{\max}] + (E[T_{\max}])^2] + C_1 \cdot E[T_{\max}] + C_0\}.$$

$$C_2 = \frac{1}{2} f''(T_0),$$

$$C_1 = f'(T_0) - f''(T_0) \cdot T_0,$$

$$C_0 = f(T_0) - f'(T_0) \cdot T_0 + \frac{1}{2} f''(T_0) \cdot (T_0)^2, \text{ and}$$

$$T_0 = E[T_{\max}].$$

The three coefficients C_2, C_1 and C_0 can be calculated by using the monthly average maximal temperature E[*Tmax*]. Therefore, the above quadratic form of PET equation is expressed in the function both the average and the variance of the daily maximal temperature for a certain month. Another method to calculate PET is to use directly the Hamon's equation and the average daily maximal temperature to calculate the monthly PET.

$$PET_{monthly} = KPET \cdot \exp\left(\frac{17.26939 \cdot E(T_{\max})}{E(T_{\max}) + 237.3}\right) / (E(T_{\max}) + 273.3)$$

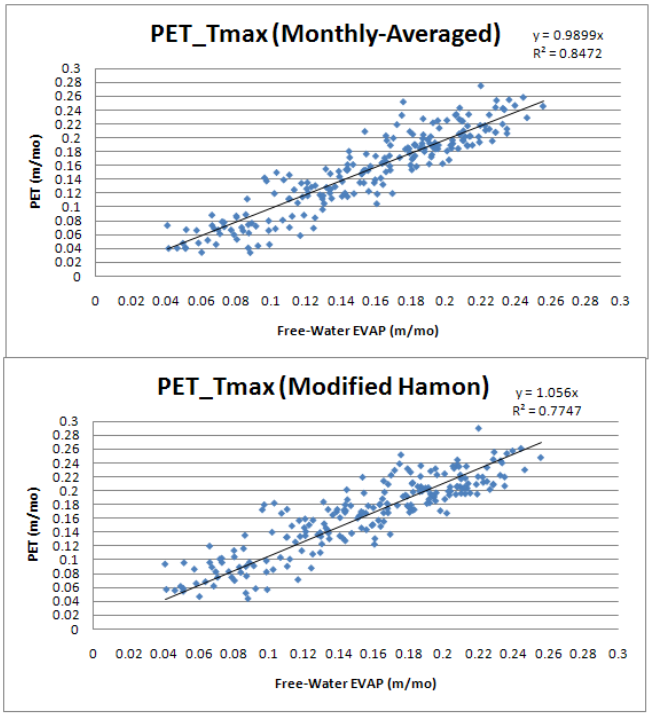

Figure 4.12: Comparison of Two PET Calculation Approaches for Station 93271: (1) Using the Daily Maximal Temperature to Calculate Daily PET and the Monthly PET is Calculated by Averaging the Calculated Daily PET (bottom), and (2) Using the Monthly-Averaged Daily Maximal Temperature and the Modified Hamon Method (bottom).

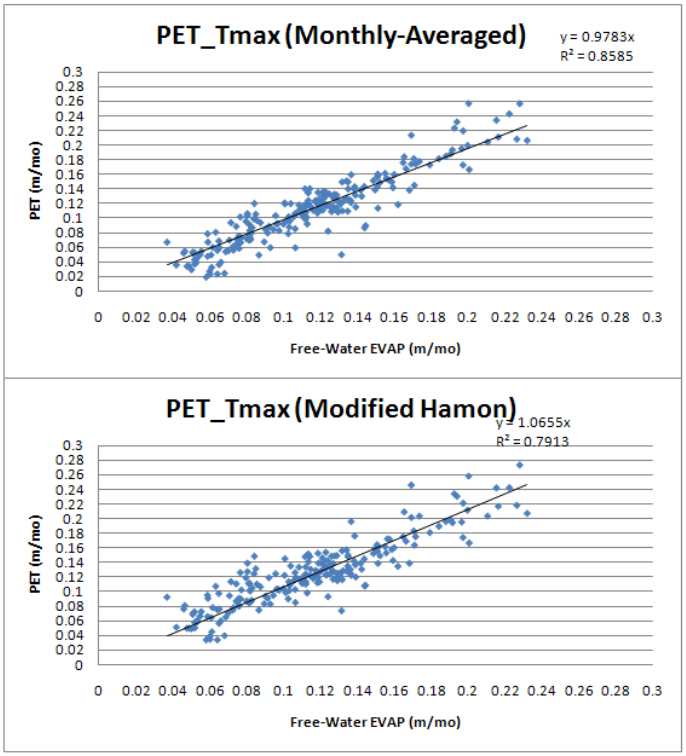

Figure 4.13: Comparison of Two PET Calculation Approaches for Station 381770: (1) Using the Daily Maximal Temperature to Calculate Daily PET and the Monthly PET is Calculated by Averaging the Calculated Daily PET (bottom), and (2) Using the Monthly-Averaged Daily Maximal Temperature and the Modified Hamon's Method (bottom).

Figures 4.12 and 4.13 plot the monthly PET versus the monthly free-water evaporation for selected stations located in north Georgia and south Georgia. The PETs are calculated from both the monthly-averaged daily PET (upper panel) and the modified Hamon's method by using monthly-averaged daily mean temperature (bottom panel). In the upper panel, the means of PETs are adjusted by calibrating the calibration coefficient to match the means of free-water evaporation for each month. In each plot, two fitted lines are plotted: one is forced to pass the origin point and the other is set free to have offset from the origin point. Regression equations and values of R-square (the square of the correlation coefficient) are also plotted in each figure. **Figures 4.12 and 4.13 also**

show that the modified Hamon's method is a good approximation of the monthly-averaged daily PET approach. This is evident by comparing the slope of the regression line and the R-square values. The equations proposed in this section will be used to calculate the PETs as inputs into the hydrological models.

4.4 Hydrologic Model Calibration for ACF Watersheds

The watershed model is developed for six ACF sub-watersheds: Buford, West Point, George, Montezuma, Albany, and Woodruff-Bainbridge. Monthly hydro-climatic data (precipitation, temperature, potential evapotranspiration, and watershed runoff) for these watersheds are collected or calculated for the period from 1939 to 2007. The ACF watershed models were then calibrated over this period using the procedure outlined earlier.

4.4.1 Monthly Models

Precipitation

Monthly precipitation sequences for each ACF watershed are generated by aggregating existing gridded data over each watershed. The gridded dataset used in this study were obtained from the PRISM (Parameter-elevation Regressions on Independent Slopes Model) climate mapping system (Daly et al., 1997).

The precipitation climatology in **Figure 4.14** shows that all ACF basins exhibit a similar monthly precipitation pattern with highs in March and July and lows in October. The July high and October low become more pronounced for watersheds in lower latitudes. The Buford watershed, extending in the Blue Ridge Mountains, receives the

highest precipitation amounts in all months. It is also observed that annual precipitation may vary by as much as 40 percent of its long term mean.

In the following calibration study, we will use the maximum temperature to calculate PET values as inputs to the hydrologic models. The monthly maximal, minimal, and average temperature sequences are obtained from the PRISM dataset.

Unimpaired Flow

Unimpaired flows are the river flows that would have been observed in the absence of human water use and regulation. The unimpaired flow sequences used in this study were initially developed by the U.S. Army Corps of Engineers (USACE) as part of the ACF Comprehensive Study for the period from 1939 to 1993. This dataset was extended to 2001 by USACE Mobile District in September 2003. A further extension to 2007 was carried out recently by the Georgia EPD as part of the Georgia Water Plan.

Models without Groundwater Fluxes

Watershed runoff is influenced by several factors (including catchment size, location, slope, soil type, vegetation, land use, and time scale). Runoff coefficient is defined as the percentage of precipitation that appears as runoff over a certain time period. The long term runoff coefficient for each sub-basin is computed by dividing the average incremental unimpaired flow values by the corresponding average precipitation.

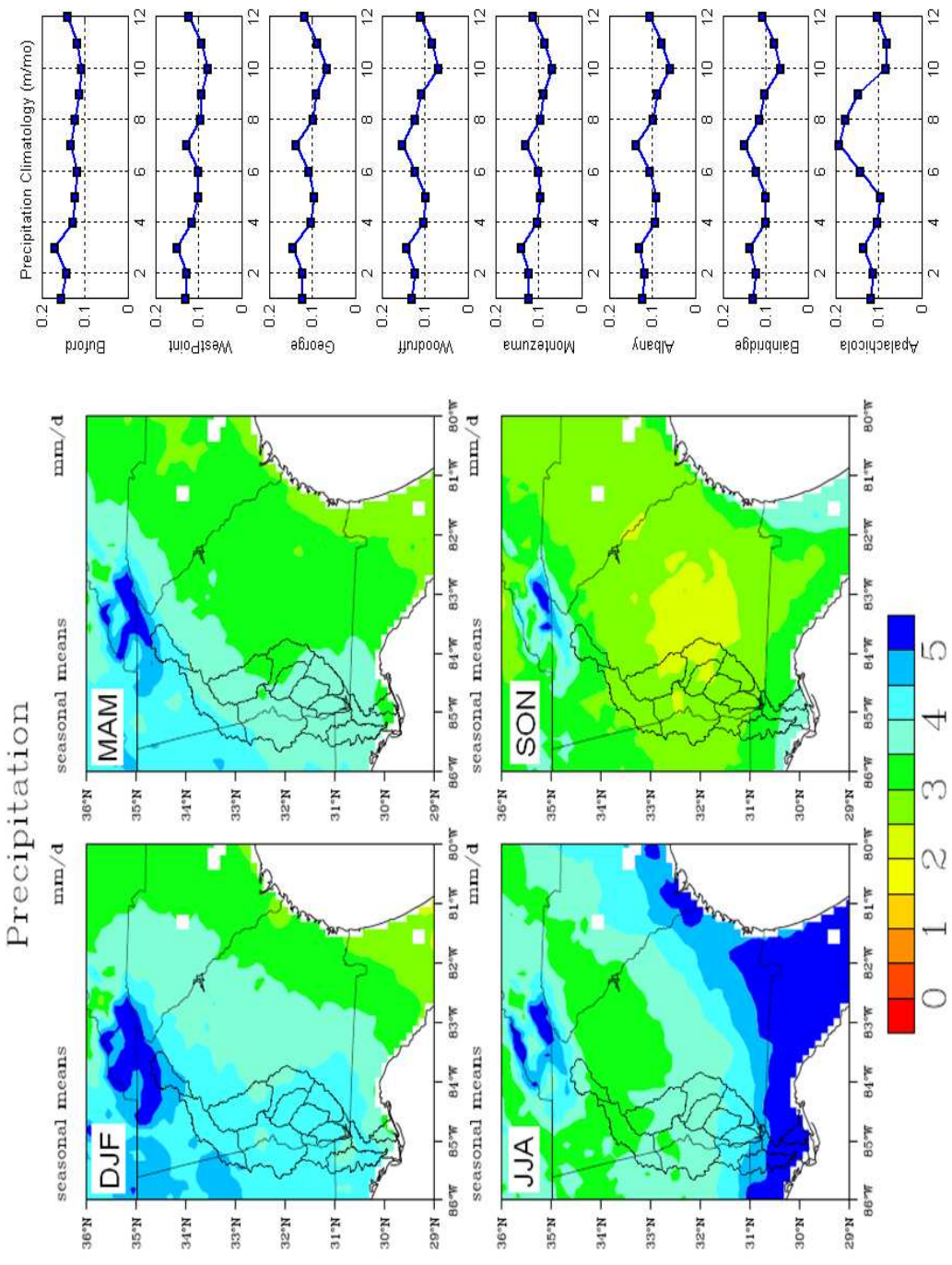

Figure 4.14: Precipitation Climatology for ACF Sub-basins.

Potential Evapotranspiration (PET)

All hydrologic models are first calibrated in monthly time steps by following the iterative parameter estimation process described in **Section 4.2**. Parameters are estimated

for the two-storage hydrologic models with power release functions, linear approximations of percolation functions, and other secondary components (e.g., u_0, Q_{imp}, and S_{ret}). No groundwater fluxes are assumed in the first calibration round.

Figures 4.15 provide a graphical comparison of Buford observed and simulated runoff and plots of the upper and lower soil moisture storage. Specifically, **Figure 4.15 (a)** shows the mean and standard derivation of monthly observed runoff and monthly simulated runoff. **Figure 4.15 (b)** shows the mean and standard derivation of monthly observed runoff ranks and monthly simulated runoff ranks. **Figures 4.15 (c)** and **(d)** plot the release curves of the lower and upper storage layers. The red lines are polynomial approximations and the blue lines are power function approximations. **Figure 4.15 (e)** shows the optimized u_{12} versus the estimated u_{12} (percolation functions). **Figure 4.16** shows the time series of the (a) simulated versus the observed runoff, (b) simulated soil moisture for upper and lower storages, (c) precipitation and PET, and (d) normalized errors of the simulated runoff. Similar results and comparisons for West Point, George, and Montezuma watersheds (**Figure 4.17-4.22**) are also plotted in the figures.

Table 4.1 shows the results of the model calibration exercise in a monthly and daily resolution for the ACF basin. **Table 4.2** reports average global statistics for model-generated and observed runoff. As shown in the tables, the overall model performance is good. Most model predictions are within ±10% of the observed values. The global Pearson and Spearman correlation coefficients are all higher than 0.9. The number of data outliers (number of points out of $\mu \pm 2.5\sigma$ bands) is between 3% - 5% of the historical records.

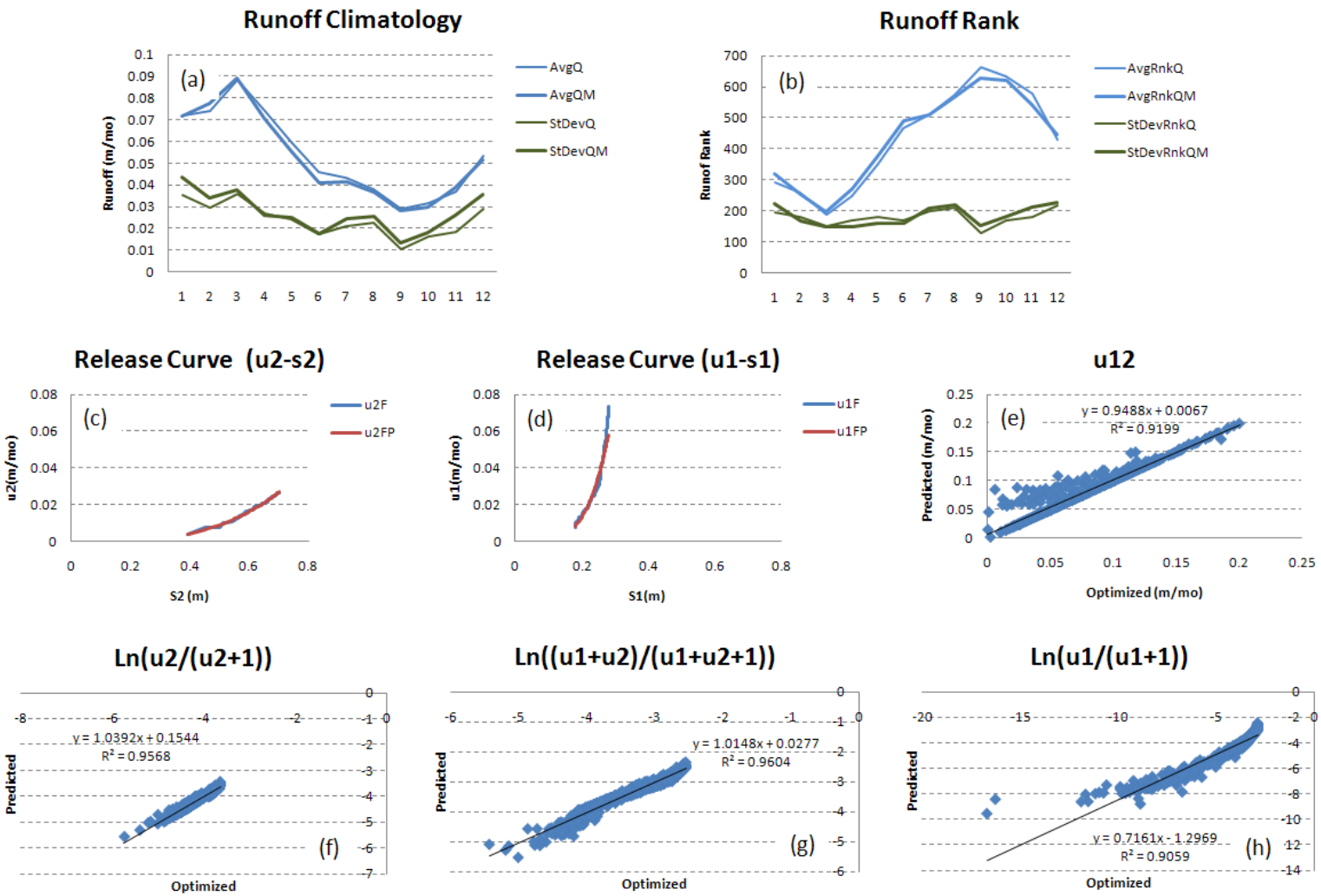

Figure 4.15: Model Calibration for Buford Watershed: Estimated Storage-Release Curves for Both Upper and Lower Soil Storages: (a) Runoff Climatology Comparison, (b) Runoff Rank Climatology Comparison, (c) Release Curve for the Lower storage, (d) Release Curve for the Upper Storage, (e) Optimized u12 Versus the Estimated u12, (f) Optimized u2 Versus the Estimated u2 in Log Space, (g) Optimized u1+u2 Versus the Estimated u1+u2 in Log Space, and (h) Optimized u1 Versus the Estimated u1 in Log Space.

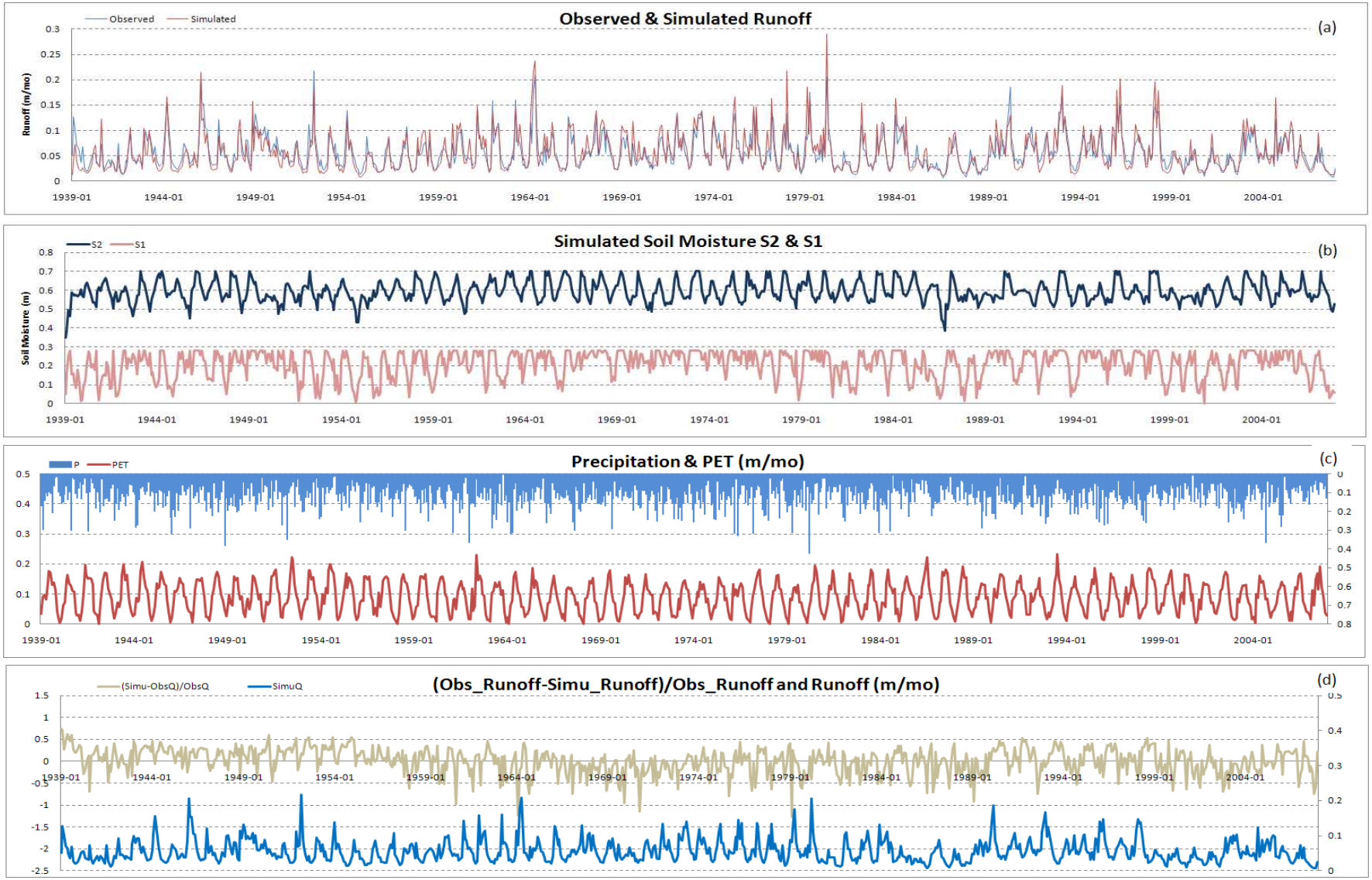

Figure 4.16: Hydrological Simulation for Buford Watershed: (a) Observed Versus Simulated Runoff, (b) Simulated Soil Moisture for the Lower and Upper Storages, (c) Precipitation and PET as Inputs, and (d) Normalized Runoff Simulation Errors.

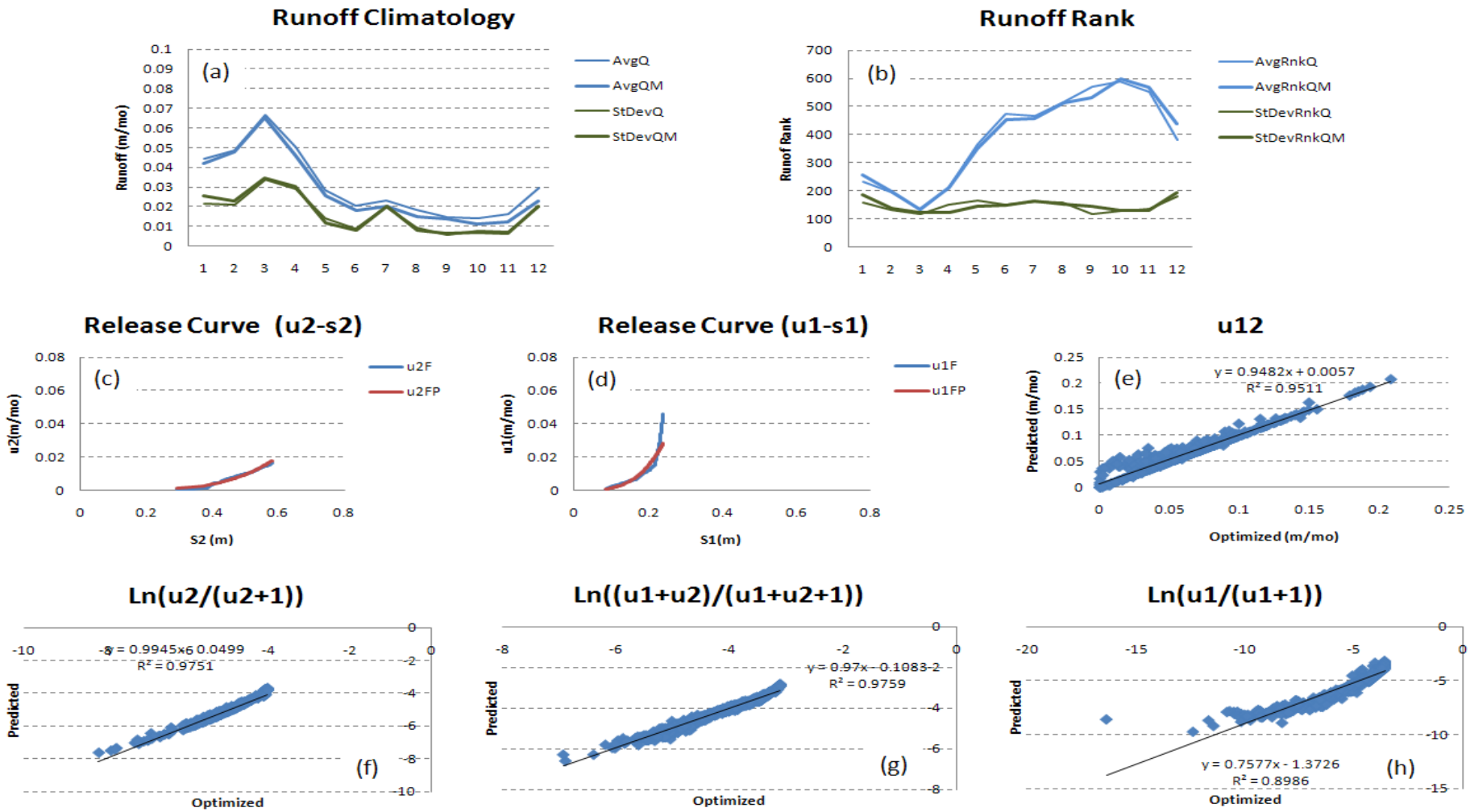

Figure 4.17: Model Calibration for West Point Watershed: Estimated Storage-Release Curves for Both Upper and Lower Soil Storages: (a) Runoff Climatology Comparison, (b) Runoff Rank Climatology Comparison, (c) Release Curve for the Lower storage, (d) Release Curve for the Upper Storage, (e) Optimized u12 Versus the Estimated u12, (f) Optimized u2 Versus the Estimated u2 in Log Space, (g) Optimized u1+u2 Versus the Estimated u1+u2 in Log Space, and (h) Optimized u1 Versus the Estimated u1 in Log Space.

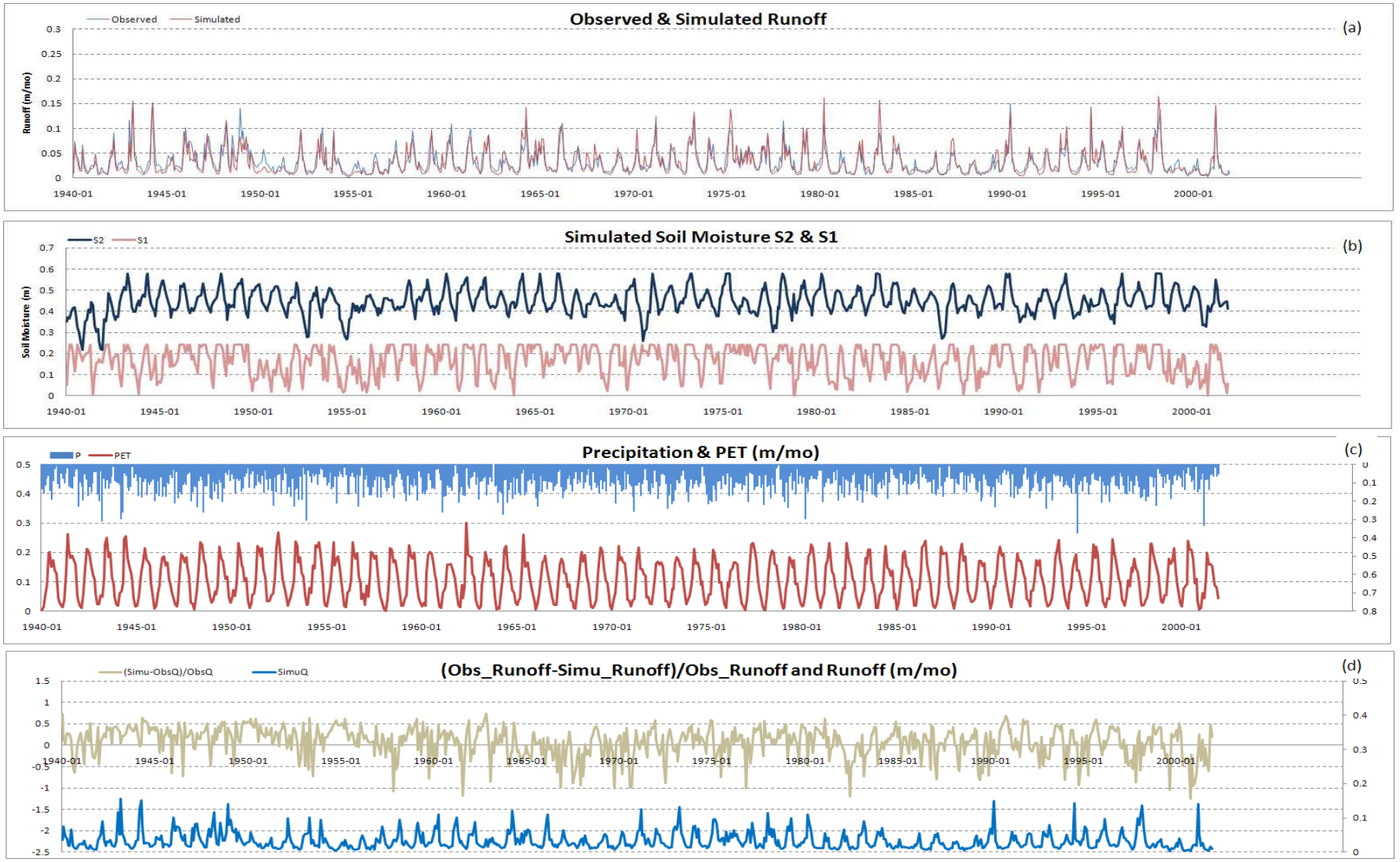

Figure 4.18: Hydrological Simulation for West Point Watershed: (a) Observed Versus Simulated Runoff, (b) Simulated Soil Moisture for the Lower and Upper Storages, (c) Precipitation and PET as Inputs, and (d) Normalized Runoff Simulation Errors.

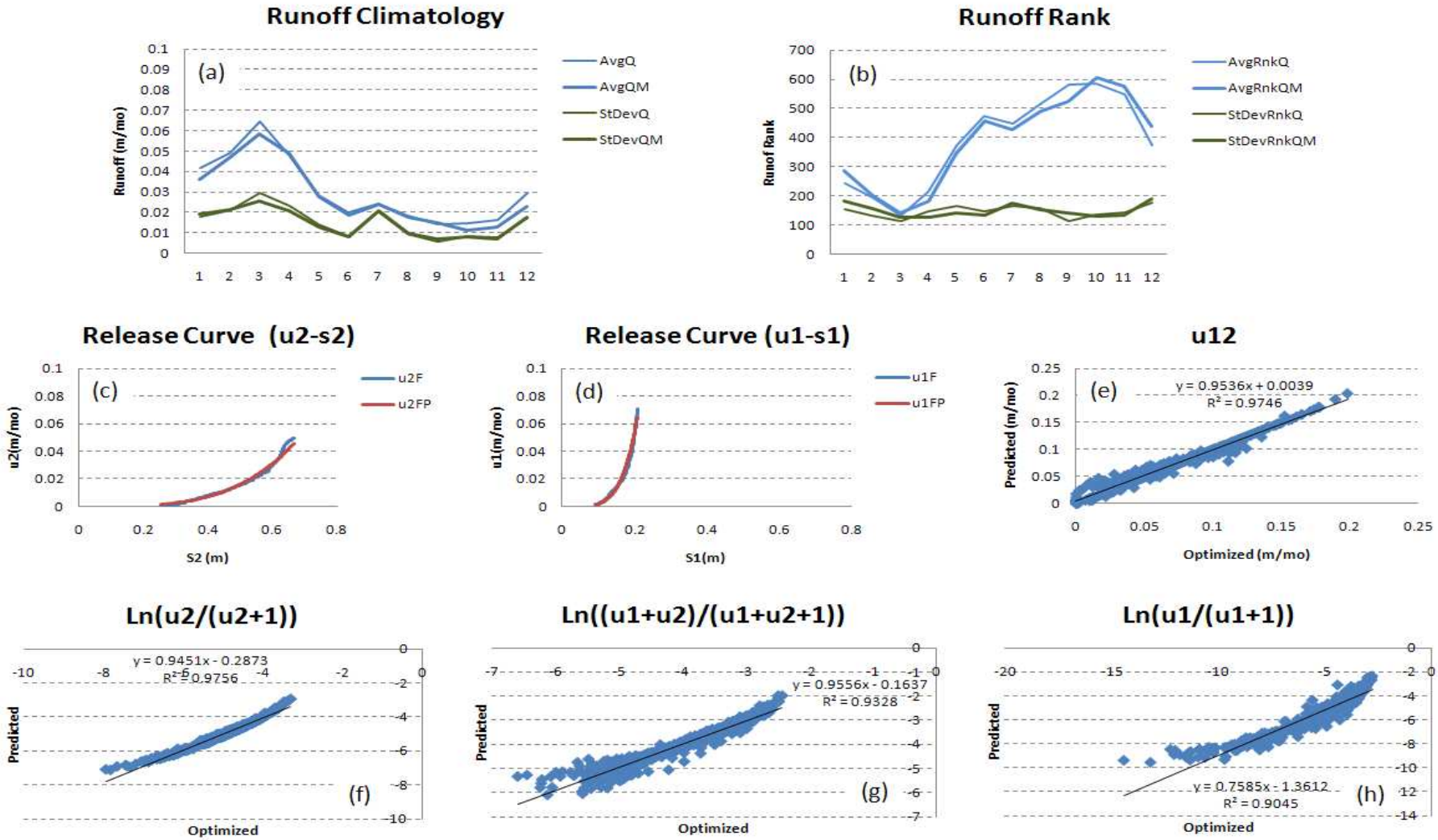

Figure 4.19: Model Calibration for W.F. George Watershed: Estimated Storage-Release Curves for Both Upper and Lower Soil Storages: (a) Runoff Climatology Comparison, (b) Runoff Rank Climatology Comparison, (c) Release Curve for the Lower storage, (d) Release Curve for the Upper Storage, (e) Optimized u12 Versus the Estimated u12, (f) Optimized u2 Versus the Estimated u2 in Log Space, (g) Optimized u1+u2 Versus the Estimated u1+u2 in Log Space, and (h) Optimized u1 Versus the Estimated u1 in Log Space.

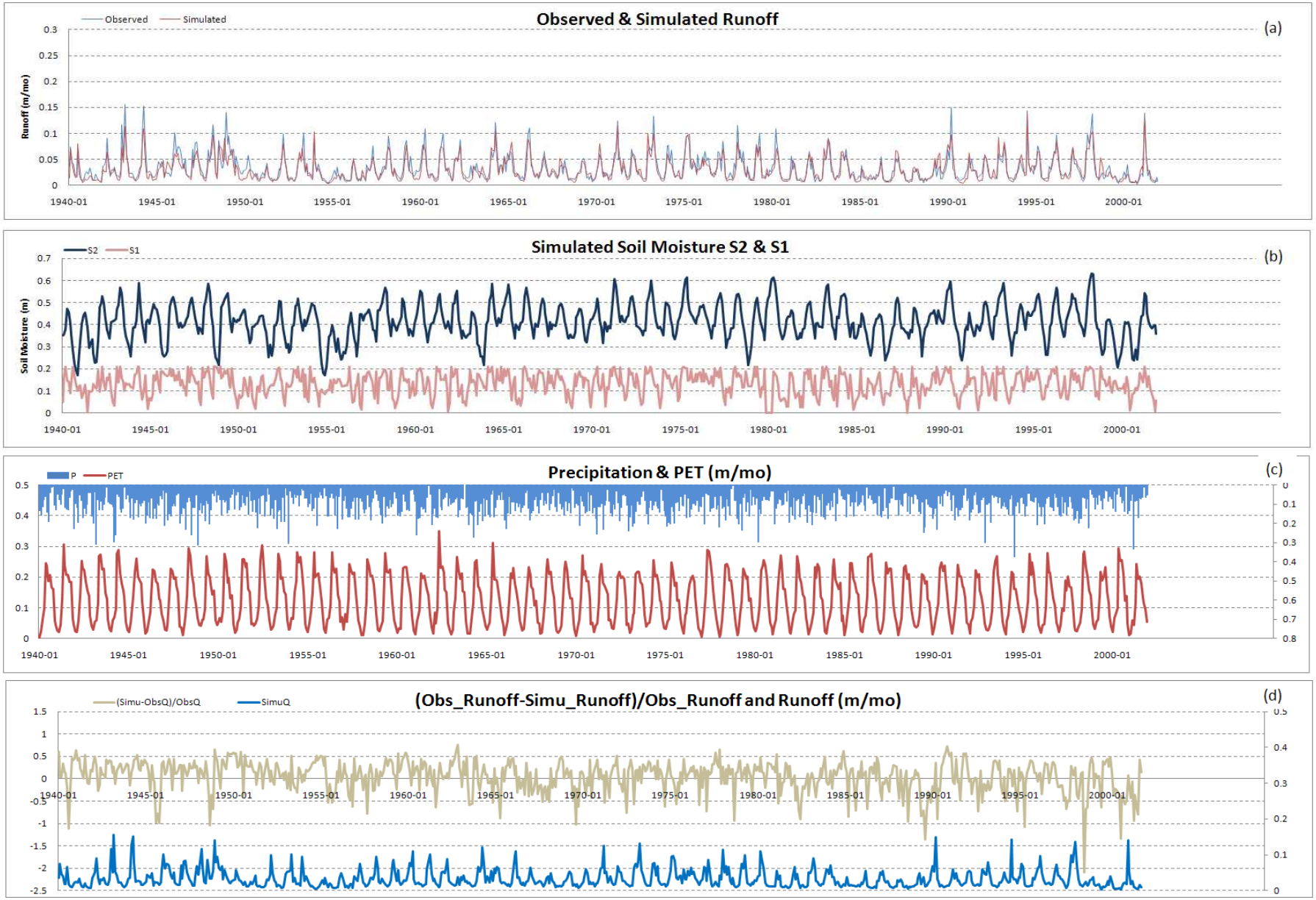

Figure 4.20: Hydrological Simulation for W.F. George Watershed: (a) Observed Versus Simulated Runoff, (b) Simulated Soil Moisture for the Lower and Upper Storages, (c) Precipitation and PET as Inputs, and (d) Normalized Runoff Simulation Errors.

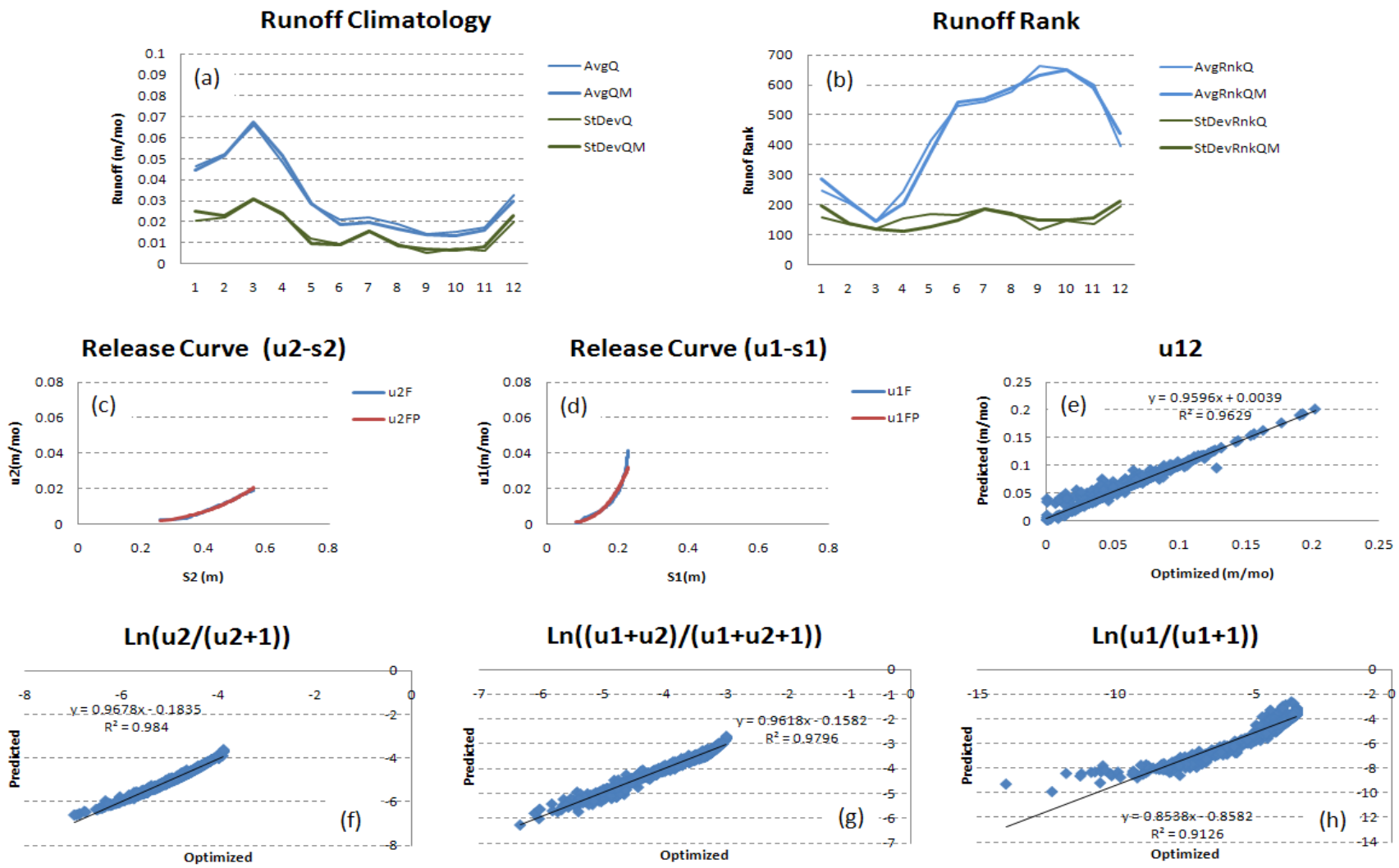

Figure 4.21: Model Calibration for Montezuma Watershed: Estimated Storage-Release Curves for Both Upper and Lower Soil Storages: (a) Runoff Climatology Comparison, (b) Runoff Rank Climatology Comparison, (c) Release Curve for the Lower storage, (d) Release Curve for the Upper Storage, (e) Optimized u12 Versus the Estimated u12, (f) Optimized u2 Versus the Estimated u2 in Log Space, (g) Optimized u1+u2 Versus the Estimated u1+u2 in Log Space, and (h) Optimized u1 Versus the Estimated u1 in Log Space.

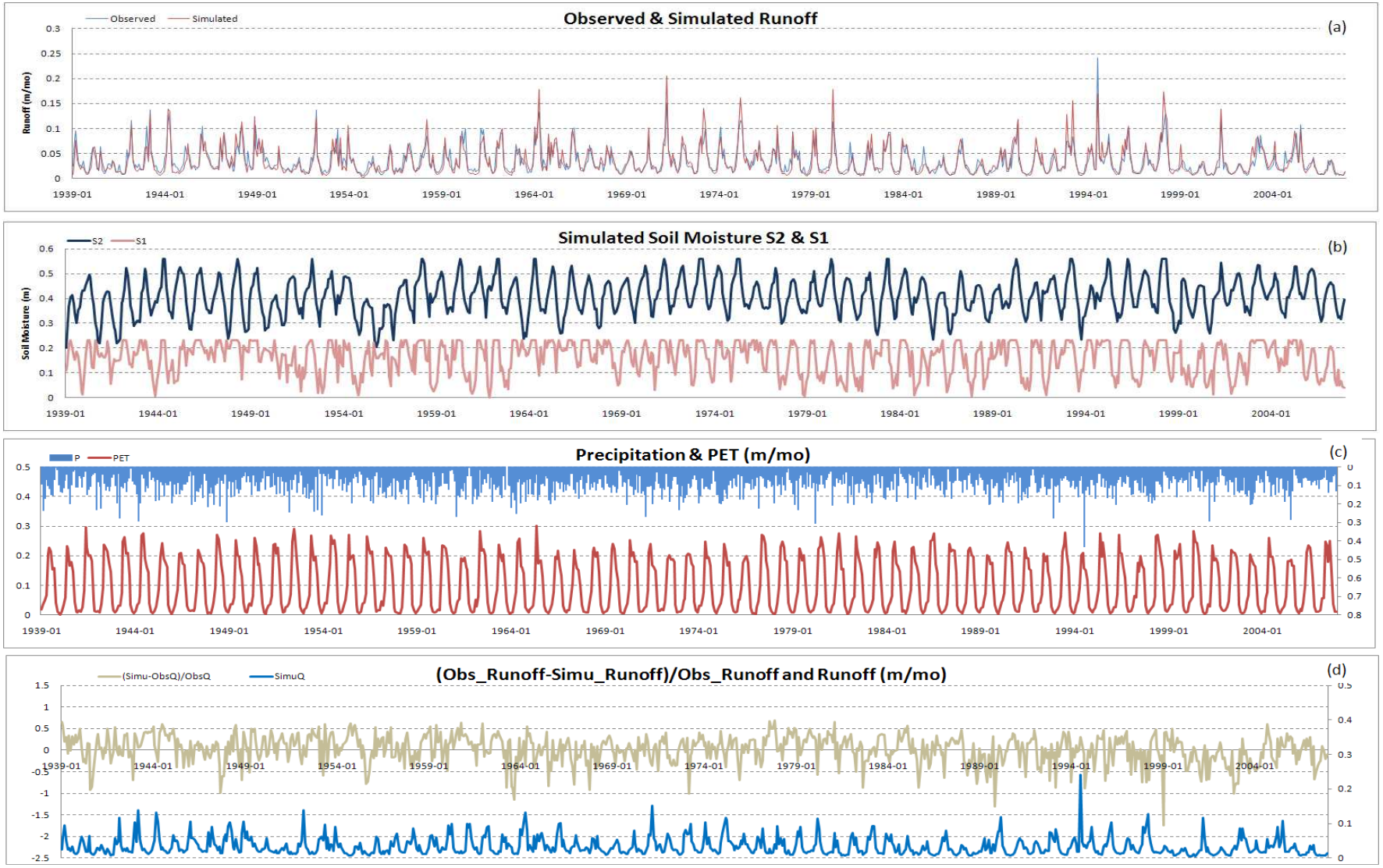

Figure 4.22: Hydrological Simulation for Montezuma Watershed: (a) Observed Versus Simulated Runoff, (b) Simulated Soil Moisture for the Lower and Upper Storages, (c) Precipitation and PET as Inputs, and (d) Normalized Runoff Simulation Errors.

Table 4.1: Watershed Model Parameters for ACF Sub-basins.

	Buford	W. Point	George	Montezuma	Albany	Wdrff-Bnbrdge
Storage Capacity and Impervious Area Coefficient0.71						
S^c	0.98	0.85	0.88	0.79	0.68	0.89
S_1^c	0.70	0.58	0.67	0.56	0.46	0.45
S_2^c	0.28	0.24	0.21	0.23	0.24	0.28
a_{imp}	0.0446	0.0480	0.0430	0.0510	0.0280	0.0220
Storage-Release Functions						
BetaPwr(2,1)	0.0367	0.1812	0.2023	0.1342	0.3284	20.3589
BetaPwr(2,2)	2.8748	4.2638	3.6610	3.2431	3.1107	4.3863
BetaPwr(1,1)	6.2349	4.3579	12.8766	4.9963	8.9089	3.9369
BetaPwr(1,2)	4.1261	3.5349	4.2279	3.4424	3.8090	3.5688
Percolation Function						
Constant	0.2414	0.0804	0.0499	0.0621	0.0409	0.0704
ET_2	0.2792	0.1712	0.1041	0.1459	0.3244	0.3663
ET_1/ET_2	-0.7579	-0.5478	-0.5683	-0.4876	-0.2754	-0.3427
S_2	-0.2647	-0.0980	-0.0370	-0.0602	-0.0500	-0.1112
S_1/S_2	0.5692	0.4571	0.4782	0.4117	0.2306	0.2859
P_{eff}	0.3540	0.4668	0.5542	0.4611	0.4119	0.4009
ErrSTDu12	0.0170	0.0155	0.0162	0.0175	0.0257	
Groundwater Function						
Constant	-	-	-	-	-0.011	-0.018
a1	-	-	-	-	0.4233	0.4670
a2	-	-	-	-	-3.487	-5.8519
a3	-	-	-	-	21.441	34.806

Table 4.2: Model Performance Measures of ACF Sub-basins.

	Buford	W. Point	George	Montezuma	Albany	Wdrff-Bnbrdge
Global Average Statistics						
AvgQ	0.0536	0.0314	0.0310	0.0322	0.0270	0.0355
AvgQM	0.0518	0.0287	0.0288	0.0313	0.0244	0.0332
StDevQ	0.0306	0.0295	0.0231	0.0237	0.0228	0.0221
StDevQM	0.0317	0.0257	0.0222	0.0251	0.0217	0.0229
AvgRnkQ	432.7	388.7	386.2	432.2	392.4	389.2
AvgRnkQM	434.4	389.7	386.4	431.7	386.9	384.5
StDevRnkQ	235.2	214.0	212.4	236.6	209.5	212.6
StDevRnkQM	233.9	212.1	212.2	236.7	213.9	213.4
Global Correlation Coefficients and Error Statistics						
Pcorr	0.9170	0.9373	0.9283	0.9343	0.9237	0.9022
SpCorr	0.9112	0.9080	0.9032	0.9162	0.9116	0.9018
QRMSE/Q	0.2392	0.3144	0.3175	0.2813	0.3284	0.2488
RnkQRMSE/Rnk	0.4376	0.5078	0.5058	0.4777	0.5087	0.4484
QAbsQError/Q	0.1917	0.2181	0.2160	0.2283	0.2193	0.2012
Outliers %	3.8%	3.9%	4.2%	4.8%	4.6%	4.3%

Models with Groundwater Fluxes

As shown in **Figure 4.23**, the groundwater flux u_G can represent a loss from the surface water system to deep aquifer percolation, or a gain in the opposite direction. This interaction can take place through the lower soil moisture storage layer or through the stream channel (**Figure 4.23**). For interaction through the lower storage layer, the u_G can be added to the dynamics as shown below:

$$S_2(k+1) = S_2(k) - ET_2(k) - u_2(k) + u_{12}(k) - u_G(k).$$

For interaction through the stream channel, u_G can be represented as follows:

$$Q(k) = Q_{imp}(k) + u_0(k) + u_1(k) + u_2(k) - u_G(k).$$

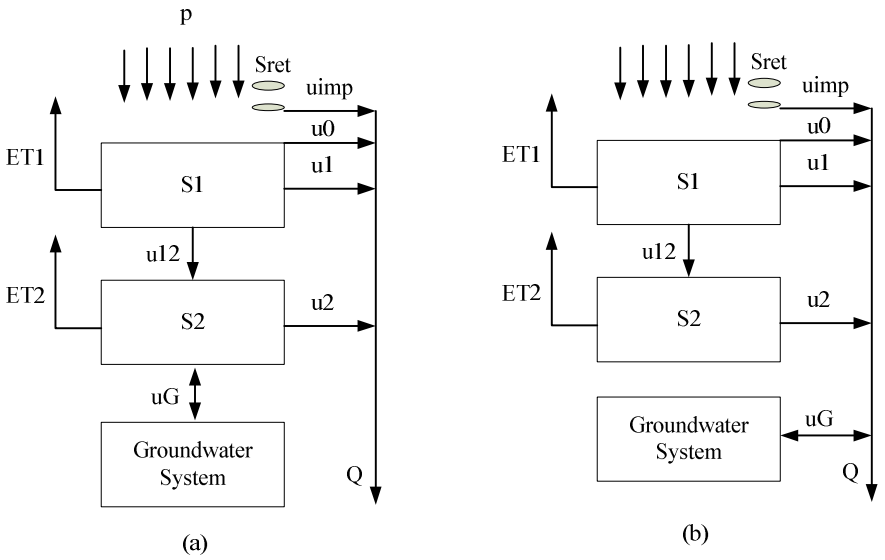

Figure 4.23: Alternative Forms of Groundwater Interaction with the Surface Water System: (a) Interaction through the Lower Soil Storage; and (b) Interaction through the Stream Channel.

Either of the above forms of groundwater-surface water interaction can be handled by the watershed model. However, in calibrating the model for the Georgia

watersheds, u_G was best included through the stream channel. Therefore, in what follows, the applicable model structure is the one shown on the right of **Figure 4.23**.

Flux u_G is estimated by an iterative process similar to that for the percolation flux u_{12}. At every step k, u_G is optimized by minimizing the errors between the observed and simulated flows. This process generates a series of u_G values $\{u_G(k), k=0, 1, 2, \ldots, N-1\}$ that are most consistent with the observed data and the other model functions and parameters. These values are used as the basis for relating u_G to other system variables that would be available when the model runs in predictive mode. After testing several variables, the total model runoff is identified as the best predictor variable. Namely, u_G is best related to Q' where

$$Q'(k) = Q_{imp}(k) + u_0(k) + u_1(k) + u_2(k) \ ,$$

and the u_G-Q' relationship is expressed in a polynomial form:

$$u_G(k) = \alpha_0 + \alpha_1 Q'(k) + \alpha_2 [Q'_s(k)]^2 + \alpha_3 [Q'_s(k)]^3$$

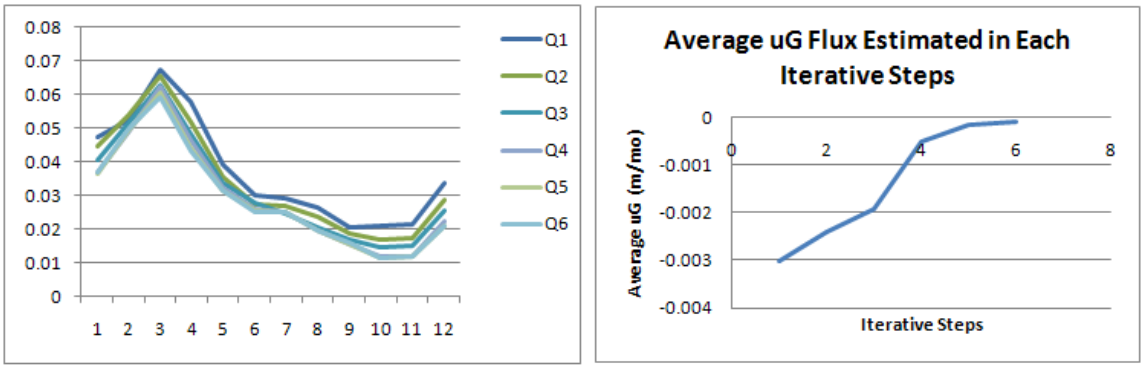

Figure 4.24: Iterative Estimates of the Groundwater Flux u_G for the Woodruff-Bainbridge Watershed: Simulated Runoff Climatology Calculated after Each Iterative Step (Left), and Identified uG Flux Changes Estimated in Each Iterative Step (Right).

After initializing the u_G sequences and after estimating the related groundwater function, the parameters and functions estimated previously without considering u_G needs to be adjusted by an iterative calibration of the storage capacities and other parameters. The iterative process ends when the change (annual average) of u_G between two adjacent iterations is less than 0.1% of the annual precipitation and when the updated storage capacities remain invariant (**Figure 4.24**).

The simulated u_G sequence and its climatology are plotted in **Figure 4.25**. It is estimated that the annual averaged upward groundwater flux rate is about 0.008 m/month for Woodruff-Bainbridge watershed. **Figure 4.26** depicts the average ET/P, (Total Runoff)/P, (Qimp+u0)/P, and Ug/P for each watershed after including the groundwater recharge/discharge flux. As demonstrated in the above tables and graphs, the ratio of ET to P is generally higher in lower latitude watersheds. Take ACF basin as an example, the watersheds are located in four distinct latitude regions: *(1)* Buford; *(2)* West Point and Montezuma; *(3)* George and Albany; and *(4)* Woodruff-Bainbridge.

For watersheds in lower latitudes, ET/P increases and (Total Runoff)/P decreases. Ostensibly, Woodruff-Bainbridge (W-B) is an exception to these trends if no groundwater components are included. For Woodruff-Bainbridge and Albany watersheds, there are strong surface water - groundwater interactions which generally results in net water gain for the surface system. The groundwater component is used to simulate this interaction, and compensates for the increased watershed outflow by decreasing the evapotranspiration to precipitation ratio and increasing the runoff coefficient beyond their hydro-climatically consistent values.

Figure 4.27 through **Figure 4.30** shows the final results and comparison of Woodruff-Bainbridge and Albany watershed between observed and simulated runoff. It also provides a graphical comparison between observed and simulated runoff, plots of the upper and lower soil moisture storage.

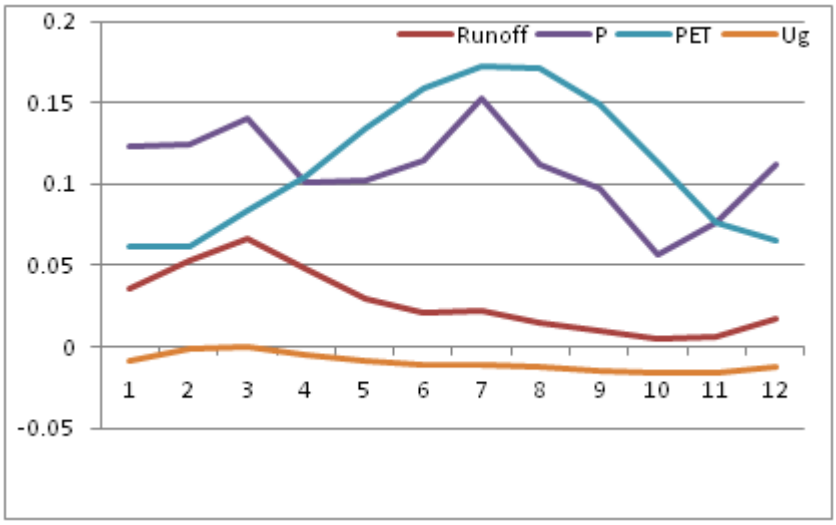

Figure 4.25: Climatology of Modeled Runoff and Groundwater Recharge for Woodruff-Bainbridge.

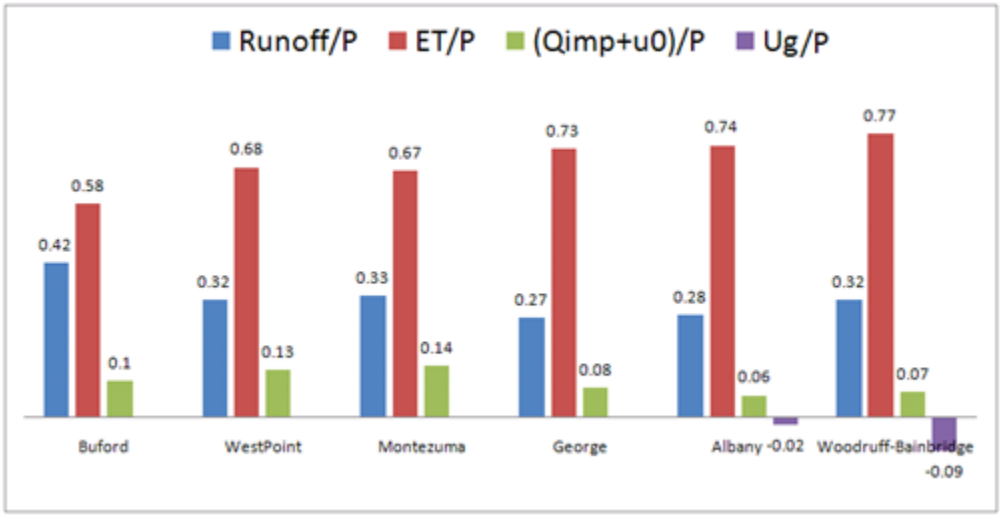

Figure 4.26: Average Hydrologic Response by Watershed (1901 - 2009) with including Groundwater Recharge flux Ug.

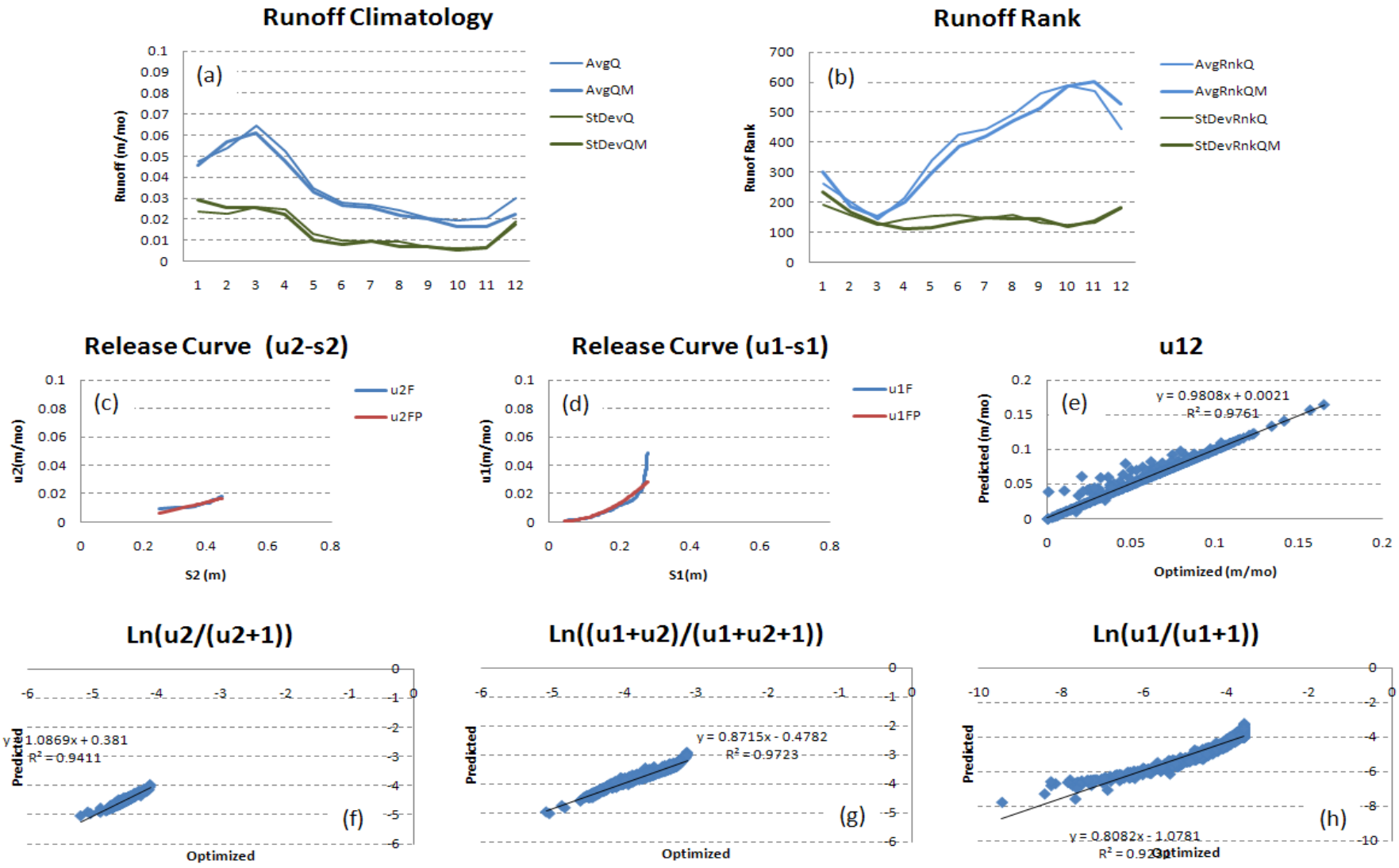

Figure 4.27: Model Calibration for Woodruff-Bainbridge Watershed: Estimated Storage-Release Curves for Both Upper and Lower Soil Storages: (a) Runoff Climatology Comparison, (b) Runoff Rank Climatology Comparison, (c) Release Curve for the Lower storage, (d) Release Curve for the Upper Storage, (e) Optimized u12 Versus the Estimated u12, (f) Optimized u2 Versus the Estimated u2 in Log Space, (g) Optimized u1+u2 Versus the Estimated u1+u2 in Log Space, and (h) Optimized u1 Versus the Estimated u1 in Log Space.

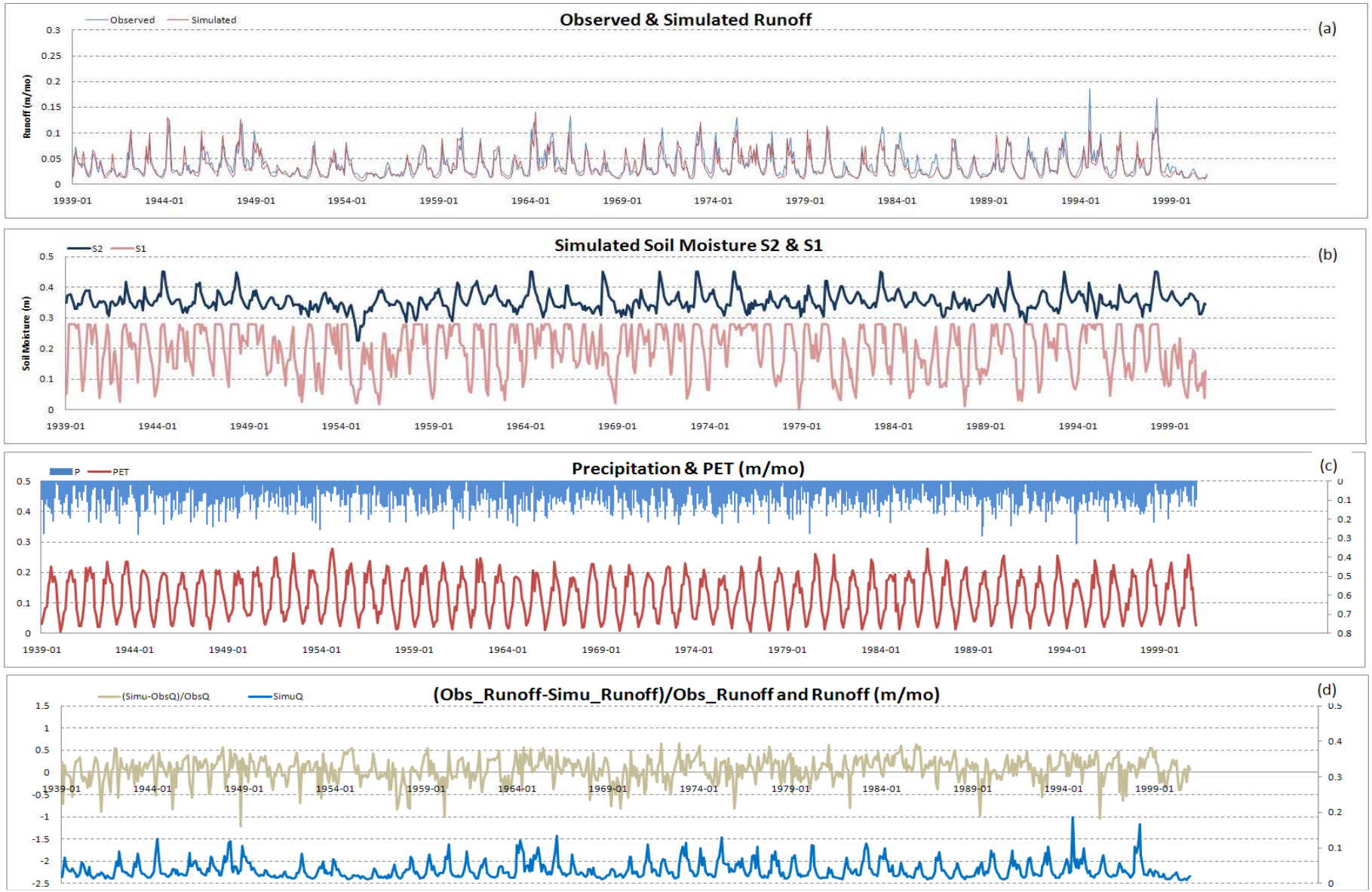

Figure 4.28: Hydrological Simulation for Woodruff-Bainbridge Watershed: (a) Observed Versus Simulated Runoff, (b) Simulated Soil Moisture for the Lower and Upper Storages, (c) Precipitation and PET as Inputs, and (d) Normalized Runoff Simulation Errors.

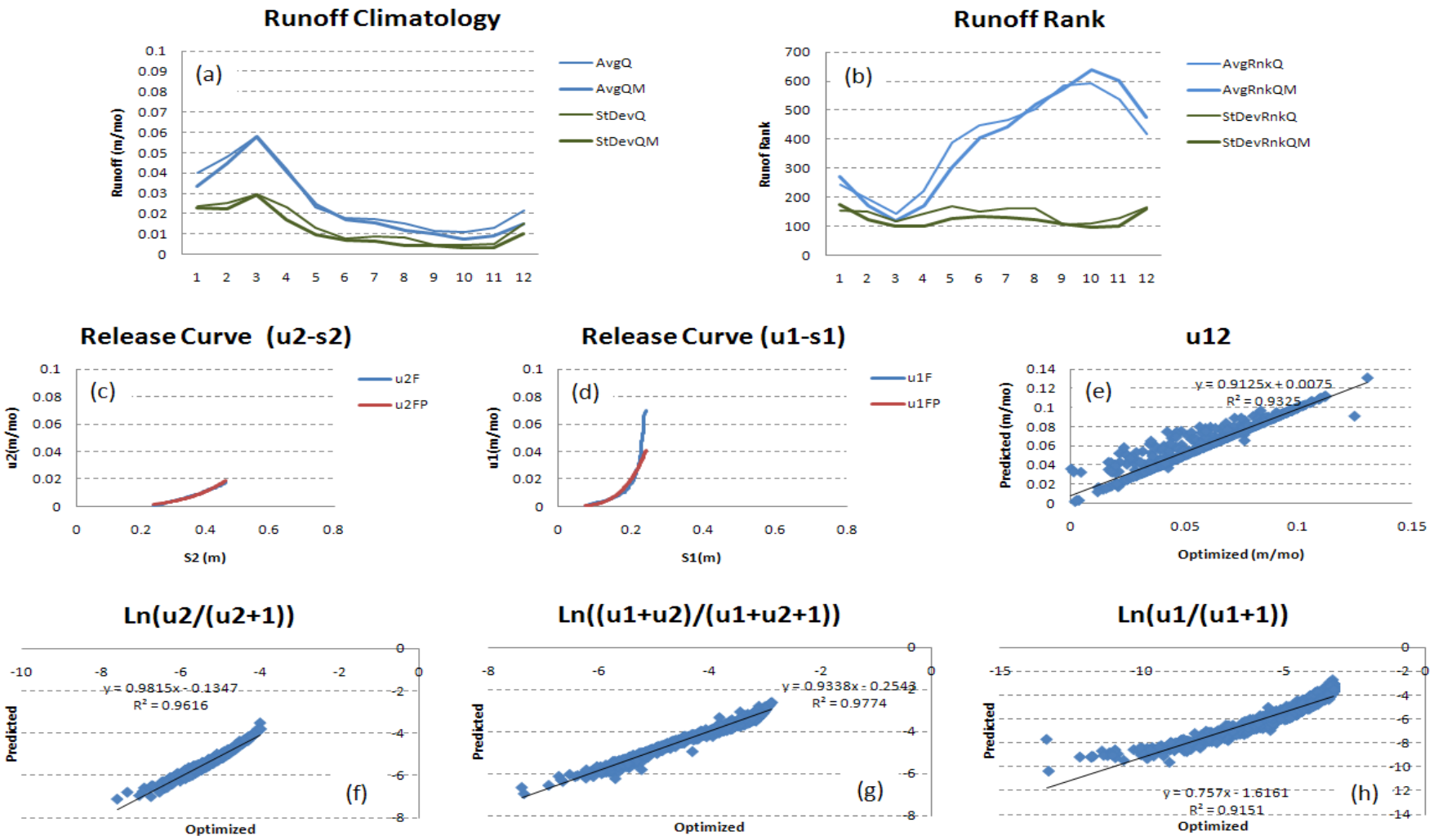

Figure 4.29: Model Calibration for Albany Watershed: Estimated Storage-Release Curves for Both Upper and Lower Soil Storages: (a) Runoff Climatology Comparison, (b) Runoff Rank Climatology Comparison, (c) Release Curve for the Lower storage, (d) Release Curve for the Upper Storage, (e) Optimized u12 Versus the Estimated u12, (f) Optimized u2 Versus the Estimated u2 in Log Space, (g) Optimized u1+u2 Versus the Estimated u1+u2 in Log Space, and (h) Optimized u1 Versus the Estimated u1 in Log Space.

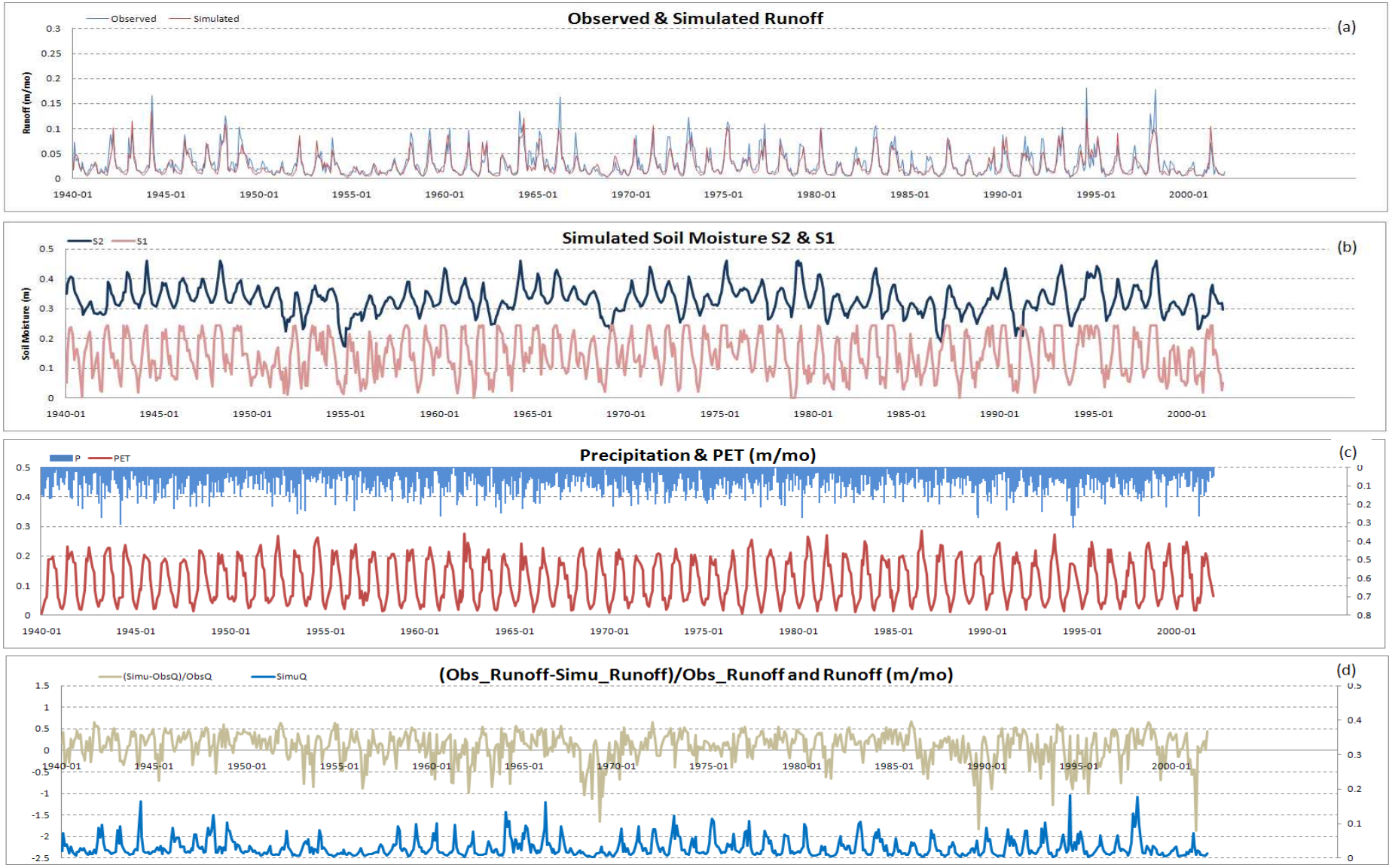

Figure 4.30: Hydrological Simulation for Albany Watershed: (a) Observed Versus Simulated Runoff, (b) Simulated Soil Moisture for the Lower and Upper Storages, (c) Precipitation and PET as Inputs, and (d) Normalized Runoff Simulation Errors.

4.4.2 Weekly Models

In this section, the downward modeling philosophy is employed to build the weekly and daily hydrologic models for all sub-basins in Georgia. These models work on finer temporal resolutions than the models developed in the previous section. In the monthly time scale, the two-storage model structure was found to be adequate in simulating the dynamics of the watershed processes. In developing the weekly and daily models, this premise is again investigated.

The following results are obtained by calibrating a two-storage model in both weekly time steps for the upper Oconee River sub-basin (Athens watershed). In addition to the Athens watershed, we also checked other three upstream watersheds: Buford watershed (upper Chattahoochee River), Montezuma watershed (upper Flint River), and Jackson watershed (upper Ocmulgee River).

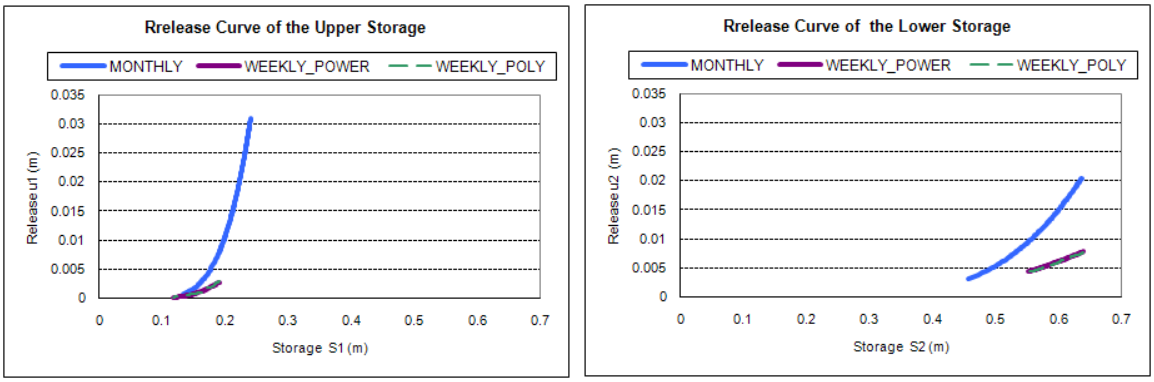

Figure 4.31: Release Curves for the Upper and Lower Storage in Weekly Hydrologic Model for the Athens Watershed.

Figure 4.31 compares the monthly release curves to the weekly release curves of both the upper and lower storages. It shows that the lower storage capacity S_2^c does not change from the monthly model to the weekly model; but the upper storage capacity S_1^c decreases from 0.24 to 0.19. For the weekly model, the piece-wise linear approximations

of the release relationships match the power function approximations for the Athens watershed. Similar results are observed for other three watersheds.

The Pearson correlation between observed and simulated flow is about 0.93. **Table 4.3** shows the performances (correlation coefficients and normalized errors) of the runoff simulations for these four watersheds. It shows that for all four watersheds, the Pearson correlations are high (0.91-0.93) and the normalized errors of simulated runoffs are comparable to the monthly models (0.24-0.25), implying that the two-storage model structure is sufficient for the weekly model. **Figure 4.32** shows the observed and simulated flows in weekly steps for the above four watersheds.

Table 4.3: Performance Measures of Four Georgia Watersheds Weekly Model with Two Storages.

Two-Storage(Weekly)	OOA_Athens	OOA_Jackson	ACF_Buford	ACF_Montezuma
Pcorr	0.9279	0.9205	0.9080	0.9150
SPCorr	0.9102	0.9009	0.8868	0.8936
QRMSE/Q	0.3161	0.3215	0.3691	0.3255
RnkQRMSE/RnkQ	0.3958	0.3963	0.4092	0.4016
QAbsQError/Q	0.2459	0.2465	0.2595	0.2516

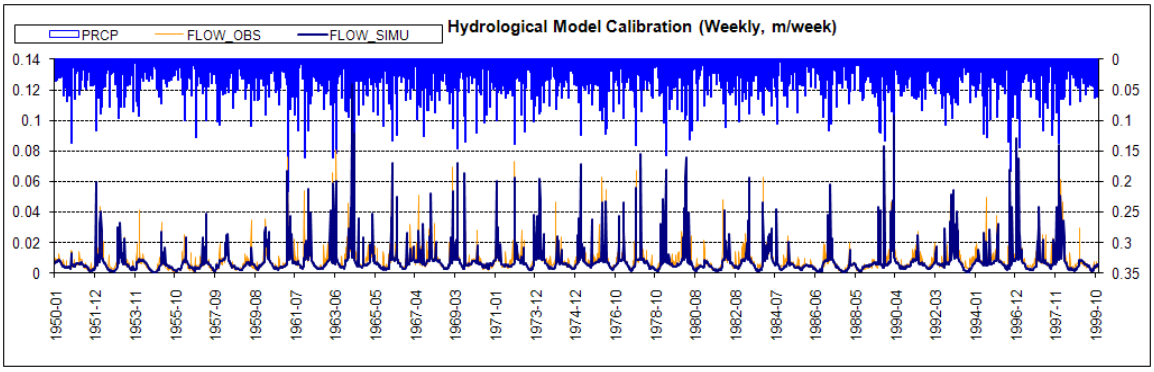

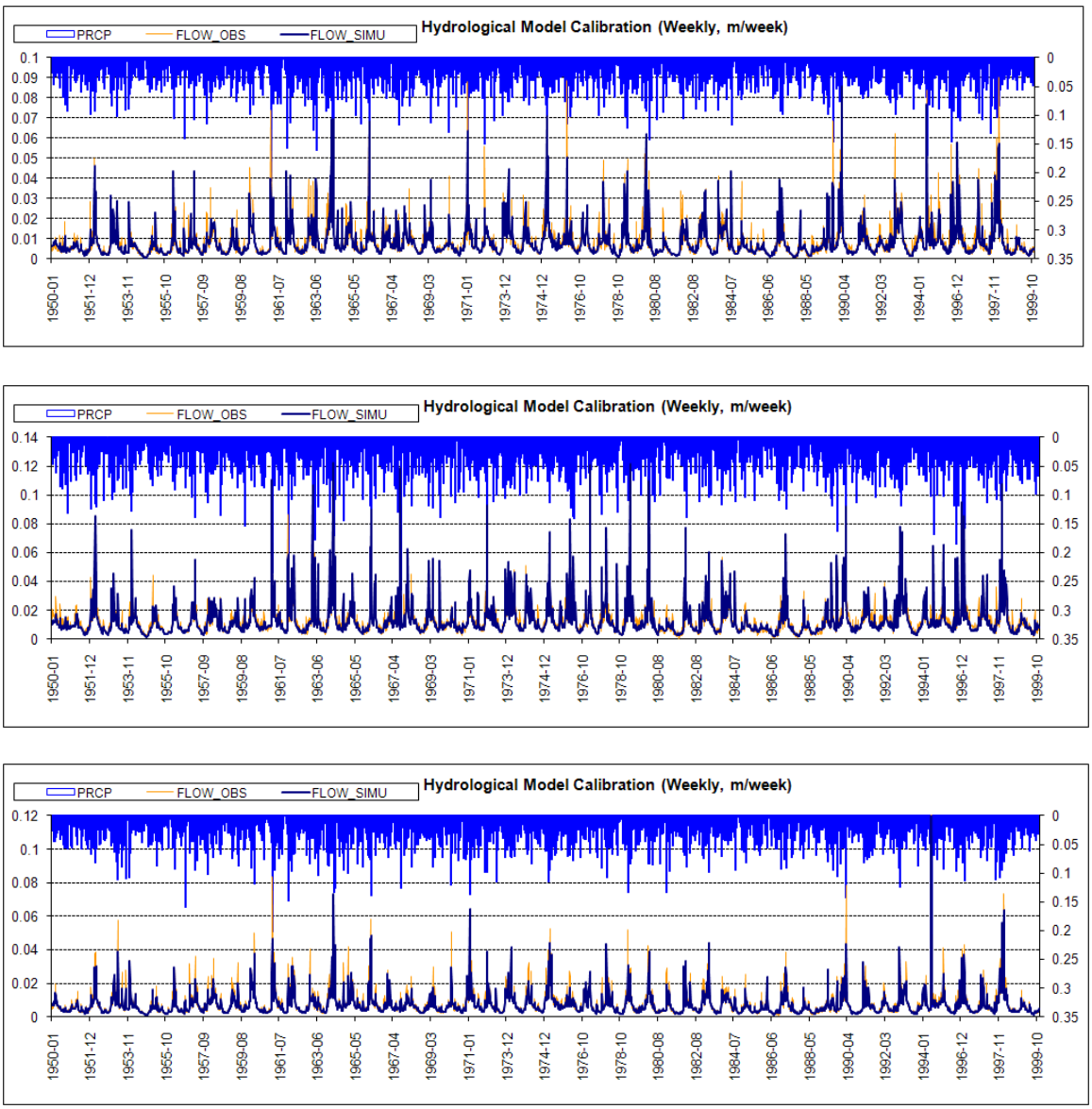

Figure 4.32: Observed and Simulated Flows of the Weekly Hydrologic Model for four Georgia Watershed: Athens, Jackson, Buford and Montezuma (Top to Bottom, 1950-1999).

4.4.3 Daily Models

In this section, the two-storage model structure is applied to the upper Oconee River Basin (Athens watershed) in daily time steps. In addition to the Athens watershed, we also checked other three upstream watersheds: Buford watershed (upper

Chattahoochee River), Montezuma watershed (upper Flint River), and Jackson watershed (upper Ocmulgee River).

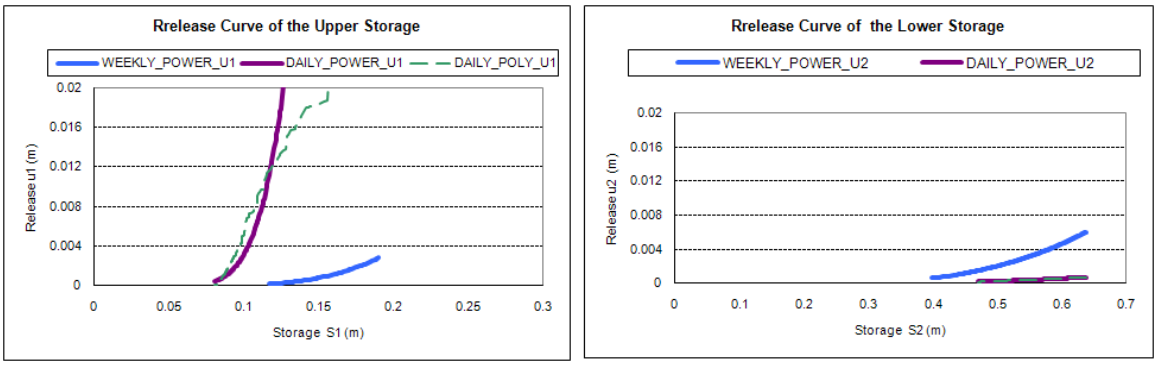

Figure 4.33: Release Curves for the Upper and Lower Storage in Daily Hydrologic Model for the upper Oconee River Basin (near Athens).

Figure 4.33 compares the weekly release curves to the daily release curves of both the upper and lower storages. It shows that the lower storage capacity S_2^c does not change from the weekly model (thus monthly model) to the daily model; but the upper storage capacity S_1^c decreases from 0.19 to 0.14.

Figure 4.33 also shows that the two storages show different changes in approximating the storage-release relationships. For the lower storage, the piece-wise linear approximation matches with the power function approximation very well, implying the dynamics of the lower storage can still be well represented by the power function form for the Athens watershed. However, for the upper storage, significant discrepancies can be observed between the piece-wise linear approximation and the power function approximation (green vs. purple). Such discrepancies suggest that the dynamics of the upper layer soil cannot be well represented by a single storage or a single release function.

Table 4.4: Performance Measures of Four Georgia Watersheds Daily Model with Two Storages.

Two-Storage(Daily)	OOA_Athens	OOA_Jackson	ACF_Buford	ACF_Montezuma
Pcorr	0.8964	0.8734	0.8823	0.8621
SPCorr	0.8623	0.8549	0.8210	0.8581
QRMSE/Q	0.3592	0.4145	0.4432	0.3672
RnkQRMSE/RnkQ	0.5569	0.5873	0.5120	0.5020
QAbsQError/Q	0.3123	0.3348	0.3291	0.3368

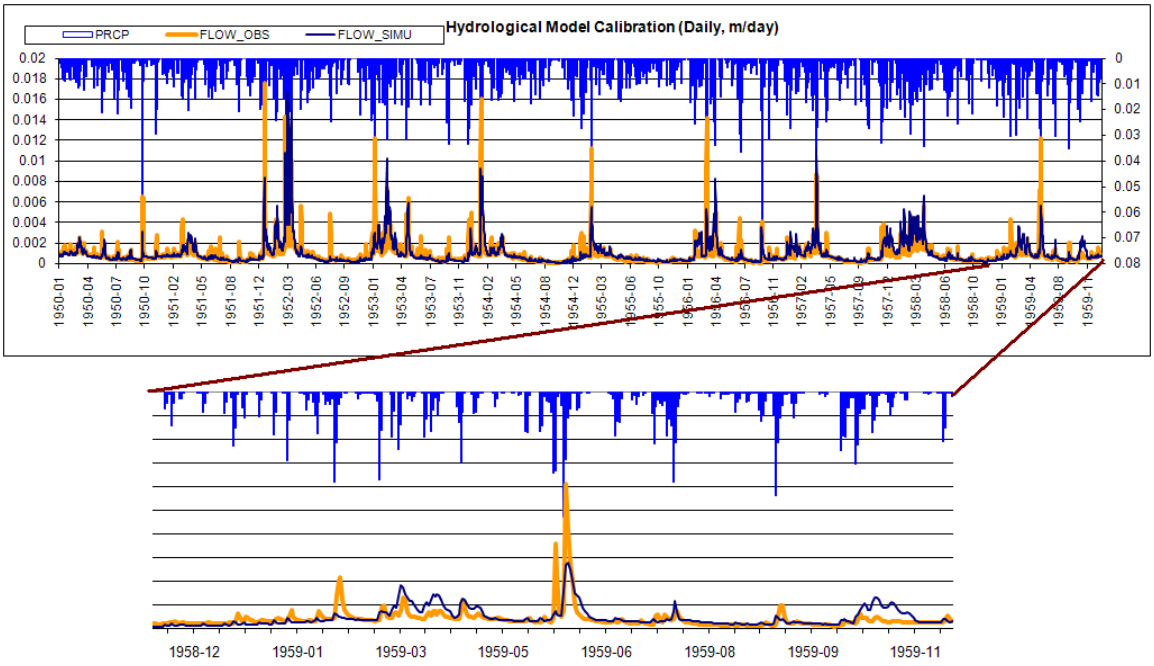

Figure 4.34: Observed and Simulated Flows of the Daily Hydrologic Model (with Two-Storage) for four Georgia Watershed: Athens, Jackson, Buford and Montezuma (Top to Bottom, 1950-1999).

The Pearson correlation between observed and simulated flow is about 0.89.

Table 4.4 shows the performances (correlation coefficients and normalized errors) of the runoff simulations for these four watersheds. It shows that for all four watersheds, the Pearson correlations are lower than the monthly and weekly models (0.86-0.89) and the normalized errors of simulated runoffs are higher than monthly and weekly models (0.31-0.34), implying that the two-storage model structure is not sufficient for the daily model.

Figure 4.34 shows the simulated and observed daily runoff by using a two-storage model. The simulated runoff generally underestimates peak flows and overestimates low flows. Such errors suggest that a more sophisticated model structure may be necessary for the daily hydrological model. A new surface storage needs to be added into the model structure to represent the surface dynamics of the hydrological system in the daily time resolution. As already discussed earlier, this is the role of the surface water storage S_0. This storage begins to fill during significant precipitation events when subsurface storage (S_1) is filled to capacity. Water release from storage S_0 may develop over a period of one to a few days. The inclusion of this storage element converts the model to the structure shown in **Figure 4.24**.

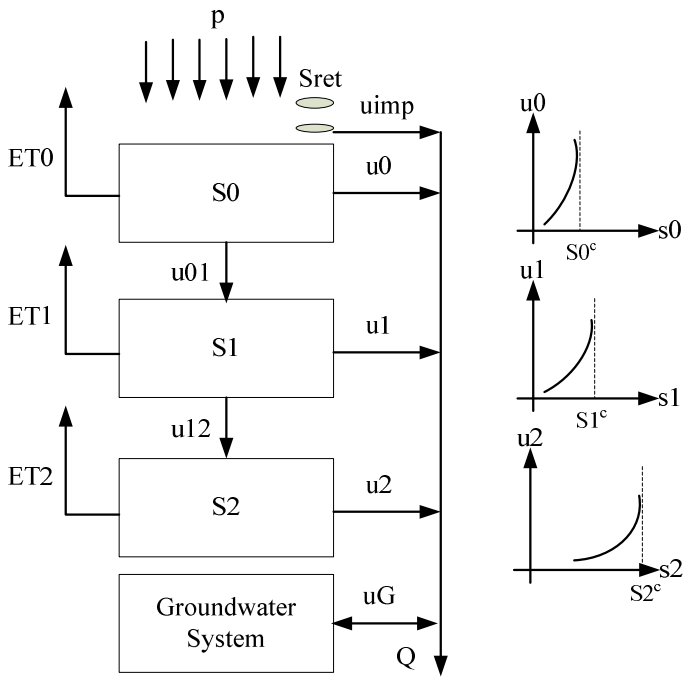

Figure 4.35: Hydrologic Model Structure for Daily Time Resolution

For the daily model structure shown in **Figure 4.35**, the system dynamics are rewritten as the following equations.

(i) Storage $S_1(k+1)$ and $S_0(k+1)$ *not* constrained by capacity limit:

$$S_1(k+1) = S_1(k) + u_{01}(k) - ET_1(k) - u_1(k) - u_{12}(k),$$

$$S_2(k+1) = S_2(k) - ET_2(k) - u_2(k) + u_{12}(k) - u_G(k),$$

$$S_0(k+1) = S_0(k) + P_{eff}(k) - ET_0(k) - u_0(k) - u_{01}(k),$$

(ii) Storage $S_0(k+1)$ but not $S_1(k+1)$ constrained by capacity limit:

$$S_0(k+1) = S_0^c,$$

$$Q_{sat}(k) = [S_0(k) + P_{eff}(k) - ET_0(k) - u_0(k) - u_{01}(k)] - S_0^c,$$

$$S_1(k+1) = S_1(k) + u_{01}(k) - ET_1(k) - u_1(k) - u_{12}(k),$$

$$S_2(k+1) = S_2(k) - ET_2(k) - u_2(k) + u_{12}(k) - u_G(k),$$

(iii) Storage $S_0(k+1)$ and $S_1(k+1)$ constrained by capacity limit:

$$S_0(k+1) = S_0^c,$$

$$S_1(k+1) = S_1^c,$$

$$Q_{sat}(k) = [S_0(k) + P_{eff}(k) - ET_0(k) - u_0(k)] - S_0^c,$$

$$S_2(k+1) = S_2(k) - ET_2(k) - u_2(k) + u_{12}(k) - u_G(k),$$

$$u_{01}(k) = 0$$

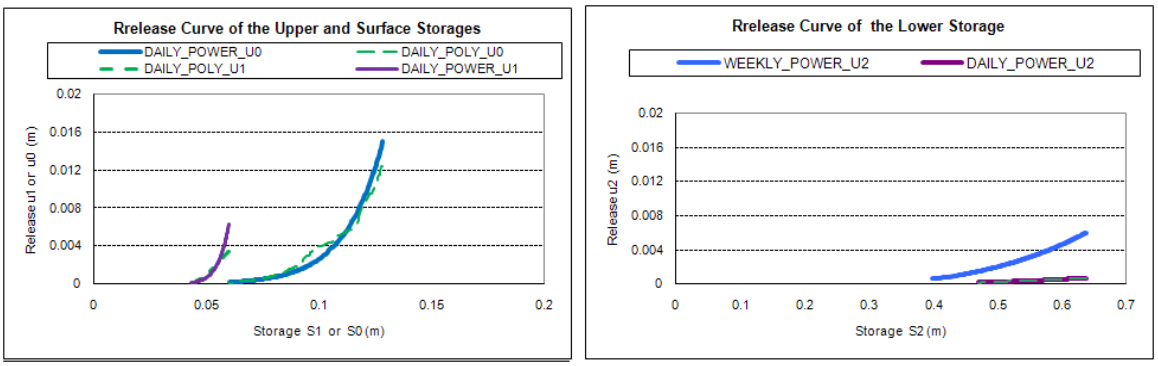

Figure 4.36: Release Curves for the Surface, Upper and Lower Storage in Daily Hydrologic Model for the upper Oconee River Basin (near Athens).

The three-storage model is next applied to the upper Oconee River Basin. **Figure 4.36** shows the calibrated weekly and daily release curves of all model storages. This figure shows that by adding the surface storage, the upper storage capacity does not change very much (around 0.14) from the two-storage model to the three storage model, and the surface storage capacity is identified to be about 0.07 with an offset of about 0.04. Both curves fit the piece-wise linear approximations fairly well.

Table 4.5: Performance Measures of Four Georgia Watersheds Daily Model with Three Storages.

Three-Storage(Daily)	OOA_Athens	OOA_Jackson	ACF_Buford	ACF_Montezuma
Pcorr	0.9301	0.9162	0.9141	0.9026
SPCorr	0.9195	0.9046	0.9038	0.8923
QRMSE/Q	0.2735	0.3124	0.3806	0.3840
RnkQRMSE/RnkQ	0.4086	0.3388	0.3937	0.4264
QAbsQError/Q	0.2587	0.2903	0.2926	0.2771

The Pearson correlation between observed and simulated flow is 0.93. **Table 4.5** shows the performances (correlation coefficients and normalized errors) of the runoff simulations for these four watersheds by using the three-storage models. It shows that for all four watersheds, the Pearson correlations are high (0.90-0.93) and the normalized errors of simulated runoffs are comparable to the monthly models (0.26-.29), implying

that the two-storage model structure is sufficient for the weekly model. **Figure 4.37** shows the observed and simulated flows in weekly steps for the above four watersheds.

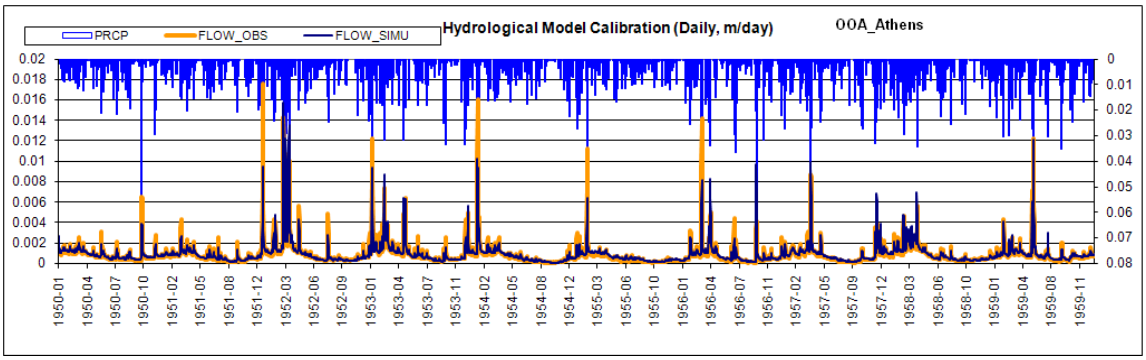

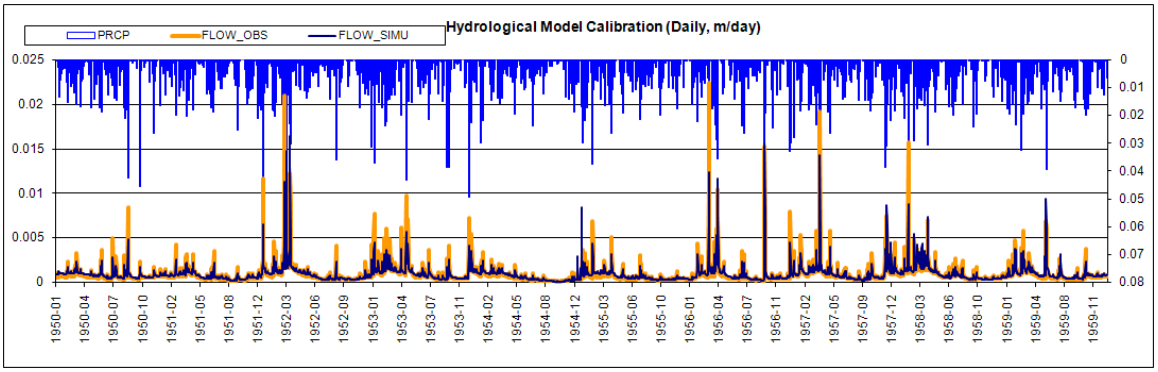

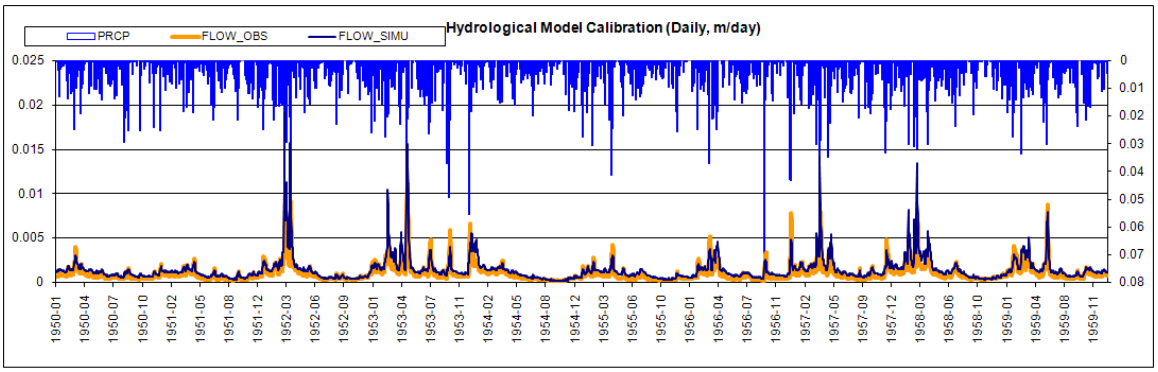

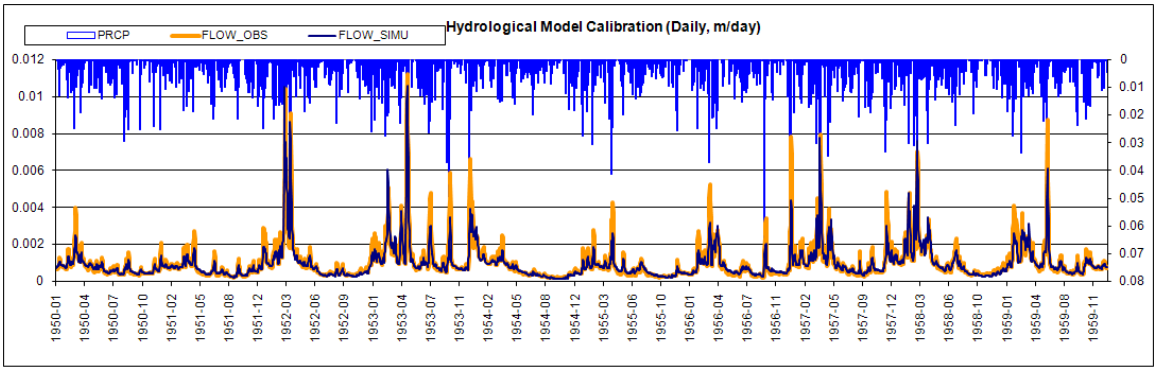

Figure 4.37: Observed and Simulated Flows of the Daily Hydrologic Model (with Three-Storage) for four Georgia Watershed: Athens, Jackson, Buford and Montezuma (Top to Bottom, 1950-1999).

4.5 Conclusions

Hydrologic models are important components of assessing regional climate change impacts on hydrological systems. This chapter introduces and describes a newly developed lumped conceptual watershed model that can serve this purpose.

- The daily PET Hamon's method can be improved by using the daily maximum temperature than by using the daily mean temperature.
- The monthly PET Hamon's method can be improved by using the modified approach presented in Section 4.3.4.
- The proposed lumped hydrological model has several water balance elements the parameters of which can be estimated through a data-driven estimation process.
- The performances of monthly simulated watershed models demonstrate the validity and good simulation skill for all ACF watershed models as well as other watershed modes in Georgia. Most model predictions are within $\pm$10% of the observed values. The global Pearson and Spearman correlation coefficients are all higher than 0.9. The number of data outliers is between 30 and 50, or 3% - 5% of the historical records.
- The proposed hydrological model can also be applied to finer temporal resolutions, such as weekly and daily time steps. The two-storage model is sufficient for the weekly model with the model parameters and release functions changed accordingly. The storage capacity and release curves of the lower layer remain unchanged from monthly models to weekly models.

- The two-storage model is generally insufficient for the daily time scale, and an additional surface storage element needs to be added. With this addition, the model exhibits good performance in simulating daily runoff.

The monthly hydrological models calibrated in this chapter for all Georgia watersheds will be employed to develop regionalization relationships between model parameters and watershed descriptors in the next chapter. They will also be employed to simulate the hydrological responses under historical and future climate change scenarios in **Chapter 6**.

CHAPTER 5

HYDROLOGIC MODEL REGIONALIZATION

Hydrological measurements (e.g., catchment runoff) are often limited both temporally and spatially. Data deficiencies in ungauged and poorly-gauged watersheds pose challenges in the calibration and the verification of hydrologic models. Hydrologic regionalization is the process of extrapolating hydrological behavior from well-calibrated watershed models to ungauged or poorly-gauged watersheds within a certain region.

This chapter investigates the regionalization of the hydrologic model for the southeastern United States by building relationships between calibrated hydrologic parameters (e.g., storage capacity) and catchment characteristics (e.g., land cover, area, altitude, slope, and soil type). To build the regionalization relationships, this study employs the monthly models developed and calibrated in **Chapter 4**for 45 watersheds. The main model parameters that will be regionalized include *(1)* storage capacities S_1^c, and S_2^c; *(2)* storage-release functions $u_1(S_1)$ and $u_2(S_2)$ with four model parameters ($\beta_{1,1}$, $\beta_{1,2}$, $\beta_{2,1}$, and $\beta_{2,2}$); *(3)* impervious area coefficient (a_{imp}) and *(4)* percolation function u_{12} with six parameters (α_0, α_1, α_2, α_3, α_4, and α_5).

5.1 Explanatory Variables

Model regionalization involves the development of statistically significant relationships between model parameters and explanatory variables. After a list of potentially useful explanatory variables has been compiled, a preliminary investigation is carried out in which variables are screened for inclusion. This preliminary investigation aims at

screening out variables that *(1)* do not significantly explain the values of the model parameters; *(2)* may be subject to large measurement errors; or *(3)* may duplicate other explanatory variables. The following potential explanatory variables, collected from different sources, are compiled and aggregated for each catchment to be assessed against the calibrated hydrologic model.

5.1.1 Dimension and Topography Dataset

The topographic data are derived from the digital elevation models (DEMs) of the National Elevation Dataset (NED) developed by USGS (Gesch, 2007; Gesch et al., 2002). NED data are distributed in geographic coordinates in units of decimal degrees and in conformance with the North American Datum of 1983 (NAD 83) spatial coordinate. These data are available nationally at resolutions of one arc-second (about 30 meters) and one-third of an arc-second (about 10 meters), and in limited areas at one-ninth of an arc-second (about three meters).

The DEM dataset of NED are geo-referenced and processed by the ArcGIS Geospatial Analysis toolbox (under NAD_1983_Lambert_Conformal_Conic). **Figure 5.1** shows the topographic map of Georgia from the NED dataset. For each catchment, the following ten quantities are aggregated and computed:

- topo_area: area of the catchment;
- topo_perimeter: perimeter of the catchment area;
- topo_avg_att: average altitude of the catchment area;
- topo_min_att: minimal altitude of the catchment area;
- topo_max_att: maximal altitude of the catchment area;
- topo_var_att: variance of the altitude within the catchment area;

- topo_avg_slope: average slope gradient (calculated for each DEM cell with respective to neighborint cells) of the catchment area;
- topo_min_slope: minimal slope gradient of the catchment area;
- topo_max_slope: maximal slope gradient of the catchment area; and
- topo_var_slope: variance of the slope gradient within the catchment area.

5.1.2 Climate Dataset

The watershed climate data are derived from PRISM (Parameter-elevation Regressions on Independent Slopes Model) climate mapping system (Daly et al., 1997) discussed in **Chapter 4**. The following four variables are used in the regionalization study:

- clm_avg_prcp: average precipitation within the catchment area;
- clm_avg_pet: average PET within the catchment area;
- clm_var_prcp: variance of precipitation within the catchment area; and
- clm_var_pet: variance of PET within the catchment area.

5.1.3 Soil Dataset

The soil data are derived from the Soil Survey Geographic (SSURGO) database developed by the Natural Resources Conservation Service (NRCS) the U.S. Department of Agriculture. The SSURGO database, which provides the most detailed level of soil information, was designed primarily for the planning and management of natural resources as they relate to farms and ranches, landowner/users, townships, counties, or parishes. The following 13 soil measurements are used:

- soil_avg_ slopegradd: the difference in elevation between two points, expressed as a percentage of the distance between those points;

- soil_avg_slopegradw: the difference in elevation between two points, expressed as a percentage of the distance between those points;
- soil_avg_blockdepmin: the distance from the soil surface to the top of a bedrock layer, expressed as a shallowest depth of components whose composition in the map unit is equal to or exceeds 15%;
- soil_avg_wtdepannumi: the shallowest depth to a wet soil layer (water table) at any time during the year, expressed as centimeters from the soil surface, for components whose composition in the map unit is equal to or exceeds 15%;
- soil_avg_wtdepaprju: the shallowest depth to a wet soil layer (water table) during the months of April through June, expressed in centimeters from the soil surface for components whose composition in the map unit is equal to or exceeds 15%;
- soil_avg_asw025wta: the volume of water that the soil can hold to a depth of 25 centimeters;
- soil_avg_asw050wta: the volume of water that the soil can hold to a depth of 50 centimeters;
- soil_avg_asw100wta: the volume of water that the soil can hold to a depth of 100 centimeters;
- soil_avg_asw150wta: the volume of water that the soil can hold to a depth of 150 centimeters;
- soil_avg_ksat: the saturated hydraulic conductivity of the soil layers;
- soil_percent_sand: percentage of sand composition of the soil column;
- soil_percent_silt: percentage of silt composition of the soil column; and
- soil_percent_clay: percentage of clay composition of the soil column.

Figures 5.2, 5.3, and **5.4** are maps of the surface soil texture, the saturated hydraulic conductivity, and the averaged soil available water capacity within Georgia, respectively.

5.1.4 Land Use and Land Cover Dataset

The Georgia Land Use Trends (GLUT) Project, completed by the natural resources spatial analysis laboratory at the University of Georgia, provides high resolution historical land cover maps for Georgia (Kramer et al., 2004). The maps were produced from Landsat TM imagery with a spatial resolution of 30m x 20m. The following 13-category land use/cover data are used in this study:

- land_avg_bdm: open sand, sandbars, sand dunes, mud (natural environmental features) as well as exposed sand from dredging and other activities;
- land_avg_qsr: exposed rock and soil from industrial uses, gravel pits, and landfills; rock outcrops, mountain tops, and barren land;
- land_avg_ow: lakes, rivers, ponds, oceans, industrial water, and aquaculture that contained water at the time of the image acquisition;
- land_avg_liu: single-family dwellings, recreation areas, cemeteries, playing fields, campus-like institutions, parks, and schools;
- land_avg_hiu: multi-family dwellings, commercial/industrial areas, prisons, speedways, junkyards, and confined animal operations; transportation, roads, railroads, airports, and runways;
- land_avg_cs: recent clearcuts, sparse vegetation, and other early successional areas;

- land_avg_df: forest composed of at least 75% deciduous trees in the canopy and deciduous woodland;
- land_avg_ef: evergreen forest composed of at least 75% evergreen trees, managed pine plantations, and evergreen woodland;
- land_avg_mf: mixed deciduous/coniferous canopies, mixed woodlands, natural vegetation within the fall line and coastal plain eco-regions, and mixed shrub/scrub vegetation;
- land_avg_rcp: row crops, orchards, vineyards, groves, and horticultural businesses; pastures and non-tilled grasslands;
- land_avg_fws: cypress gum, evergreen wetlands, deciduous wetlands, depressional wetlands, and shrub wetlands;
- land_avg_fwf: salt marshes, brackish water; and
- land_avg_nfw: freshwater marshes.

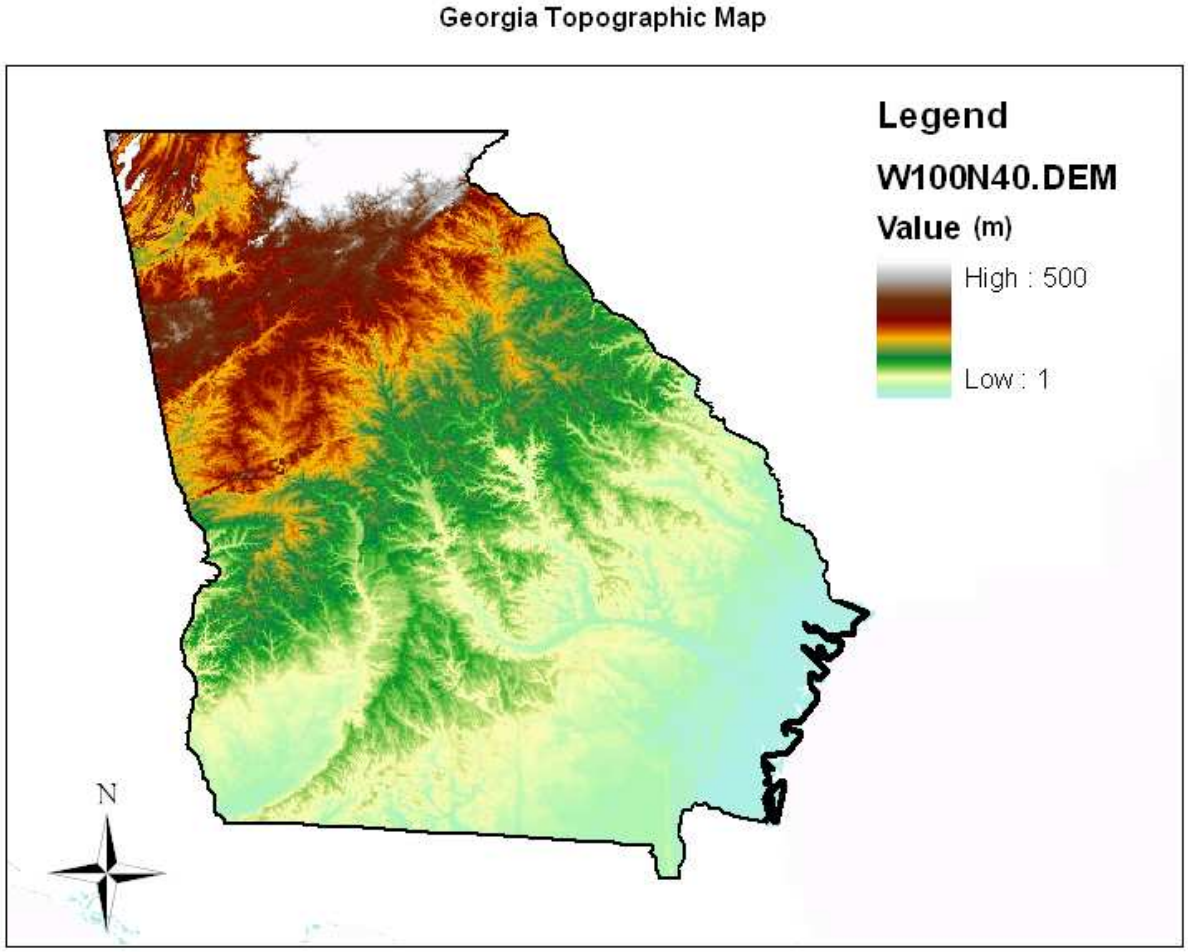

Figure 5.1 Topographic Map of Georgia.

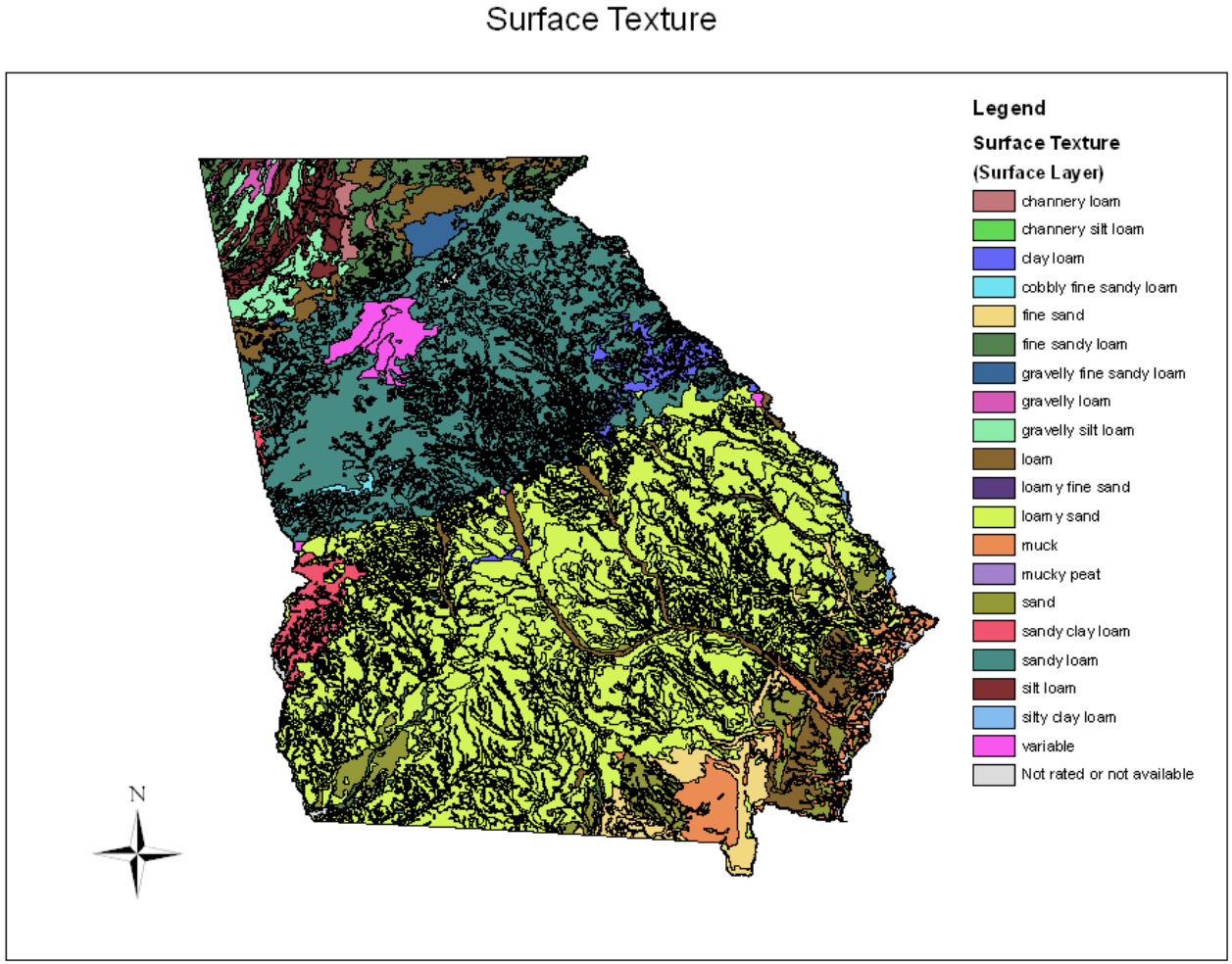

Figure 5.2 Map of the Surface Soil Texture in Georgia.

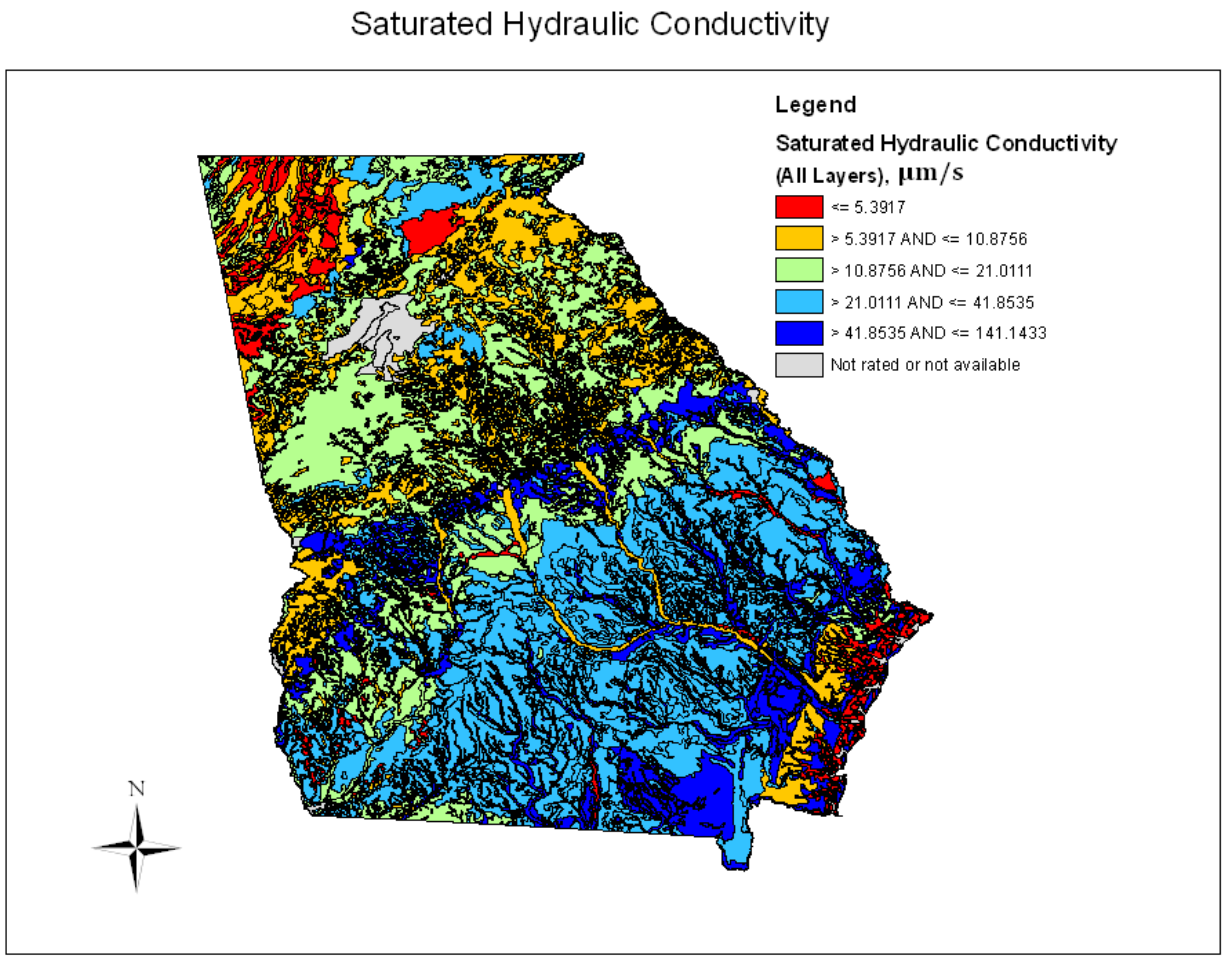

Figure 5.3 Map of Saturated Hydraulic Conductivity (µm/s) in Georgia.

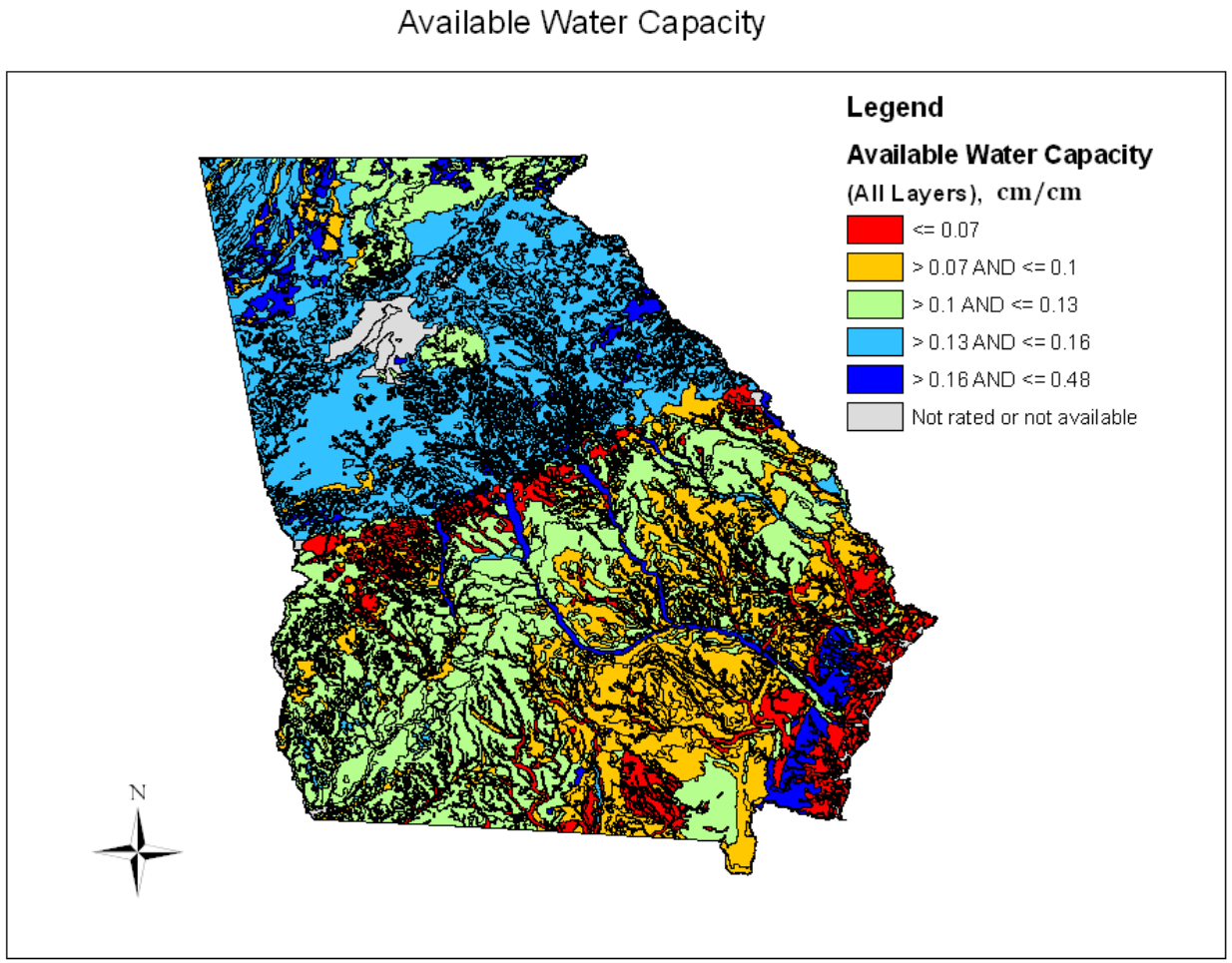

Figure 5.4 Map of Averaged Soil Available Water Capacity (cm/cm) in Georgia.

5.2 Regionalization Relationships

This section develops the regionalization relationships by screening and using the 40 predictor variables (P=40) described in the previous section. However, evaluating all of the possible alternatives is not practical, as the number of candidate variable combinations is large. To simplify the screening process and to search systematically the predictor variable set, this study employs a stepwise and automatic computer-search procedure.

5.2.1 Forward Stepwise Regression

The Forward Stepwise Regression procedure starts with an initial set of explanatory variables and iterates by adding a new variable or deleting an existing variable based on certain criteria until convergence. The forward stepwise regression search procedure is outlined below:

Step 1:

For each candidate predictor X_k (k = 1, 2, … , P-1), fit a simple linear regression model and compute the t* statistics defined by $t_k^* = \frac{b_k}{s\{b_k\}}$:

$$b_k = \frac{\sum\left(X_i - \overline{X}\right)\left(Y_i - \overline{Y}\right)}{\sum\left(X_i - \overline{X}\right)^2} \quad \text{and} \quad s\left(b_k\right) = \sqrt{\frac{MSE}{\sum\left(X_i - \overline{X}\right)^2}}.$$

In the above, X_i is the predictor variable for the ith watershed; Y_i is the observed value for the ith watershed; and MSE is the error mean square of the regression.

The predictor with the largest t* value is the first variable added to the model. However, if the t* value is less than a predefined threshold (or likewise, if the p-value is

less than a predefined level α), the program ends with no predictor variables included. In such a case, no significant predictor is identified.

Step 2:

Assume in the previous step that X_k is identified as the jth variable for entry to the relationship. The program proceeds to develop a regression model with the augmented variable dataset (X_k, …, X_{k+s}) . The new added predictor with the largest t* (corresponding to the newly added variable) is selected as a candidate for the second variable. Again, if the t* value is less than a predefined threshold (or likewise, if the p-value is less than a predefined level α), the program ends with no predictor variables included. In such a case, only one significant predictor is identified.

Step 3:

Check the t* statistics for each of the "old" variables in the previous step. The variable with the smallest t* is a candidate for deletion. If the t* value is less than a certain predefined value (or likewise, if the p-value is larger than a predefined limit α), then the variable is removed from the model.

Step 4:

Repeat Step 2 until no new variables can be added to the model and/or no old variables can be dropped from the model.

It is noted that the stepwise regression algorithm allows a predictor variable to enter the model at an early stage but possibly leave the model at subsequent steps. Before carrying out the regression, one must choose the α–to-enter and α–to-remove significance thresholds. The choice of these two values represents the balancing of opposing tendencies. By using a large α–to-enter value, more predictors enter the model,

while by using a small α–to-remove value, more predictors are dropped. In this study, the maximum acceptable α–to-enter value is set to 0.10, and the minimum α–to-remove limit is set to 0.15.

5.2.2 Regression Model for S_2^c (Lower Soil Layer Storage Capacity)

The procedure for developing the regression model for S_2^c is described in the following steps. First, begin with a null model consisting of only the intercept (and no predictors). The result shows that the intercept is significant with a probability of Pr(t) < 2e-16 of this outcome being purely random (null hypothesis). The regression model is summarized in **Table 5.1**.

Table 5.1 Regression for S_2^c with the NULL-Predictor Model.

Model Parameter: S2_Cap (m/mo)					
Predictors: NULL					
Residuals:					
	Min	1Q	Median	3Q	Max
	-0.2289	-0.0431	0.0119	0.0569	0.1419
Coefficients:					
	Estimate	Std. Err.	t value	Pr(>|t|)	
(intercept)	0.5881	0.0117	50.3300	<2e-16	

Second, identify and admit the predictor (if any) with the largest value above the predefined F limit or the smallest P-value below the α–to-enter. For this study, the α–to-enter is set to 0.1, and the obvious candidate for admission is "forest_all," with a t-value of 48.399 and Pr(t)= 1.81e-08. Then, fit a new linear model with forest_all as the explanatory variable and the intercept. The regression model is summarized in **Table 5.2**.

Table 5.2 Regression for S_2^c with the One-Predictor Model.

Model Parameter: S2_Cap (m/mo)					
Predictors: forest_all					
Residuals:					
	Min	1Q	Median	3Q	Max
	-0.1557	-0.0433	0.0199	0.0385	0.1045
Coefficients:					
	Estimate	Std. Err.	t value	Pr(>|t|)	
(intercept)	0.3032	0.0418	7.261	<2e-16	
forest_all	0.4420	0.0635	6.957	<=1.18e-8	

Third, repeat the above process for another possible predictor. This process leads to considering "canopy," with an t-value of 16.9 and p-value Pr(t) = 1.72e-4. Again, fit a new linear model with this added variable. The regression model is summarized in **Table 5.3**.

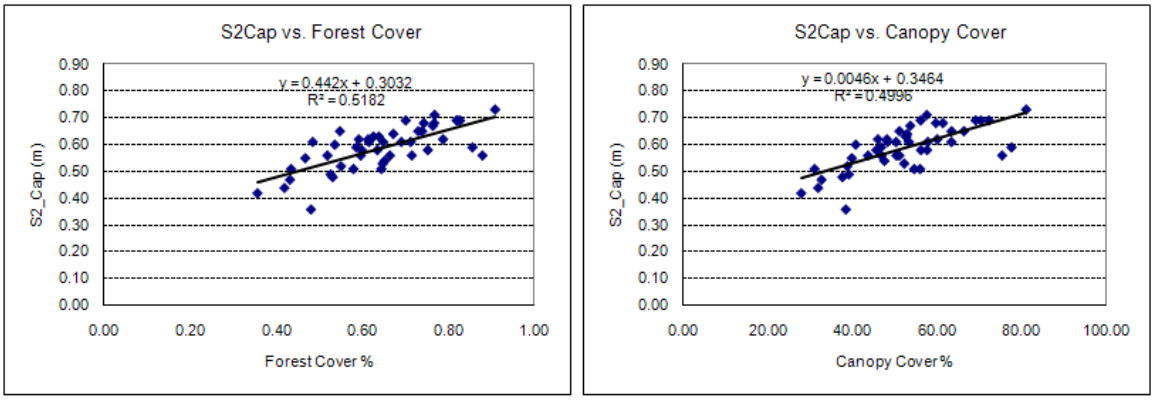

Figure 5.5 Linear Regression of the Lower Storage Capacity (S2_Cap) on the Forest and Canopy Cover Percentage.

Table 5.3 Regression for S_2^c with the Two-Predictor Model.

Model Parameter: S2_Cap (m/mo)					
Predictors: forest_all					
Residuals:					
	Min	1Q	Median	3Q	Max
	-0.1564	-0.0413	0.0156	0.0420	0.0922
Coefficients:					

	Estimate	Std. Err.	t value	Pr(>|t|)	
(intercept)	0.3851	0.0355	10.8440	<=5.18e-14	
forest_all	0.1565	0.0475	3.2970	0.0019	
avg_canopy	0.31	0.08	4.1060	0.0002	

Then, check the two-predictor model by looking into the t statistics for potential removal. This leads to p-values for both of them being smaller than the preset α–to-remove value of 0.15.

The final model is summarized above with two predictors: forest_all and avg_canopy. **Figure 5.5** shows the linear regressions for the above two predictors. The storage capacity increases as the percentage of forest cover and canopy increases.

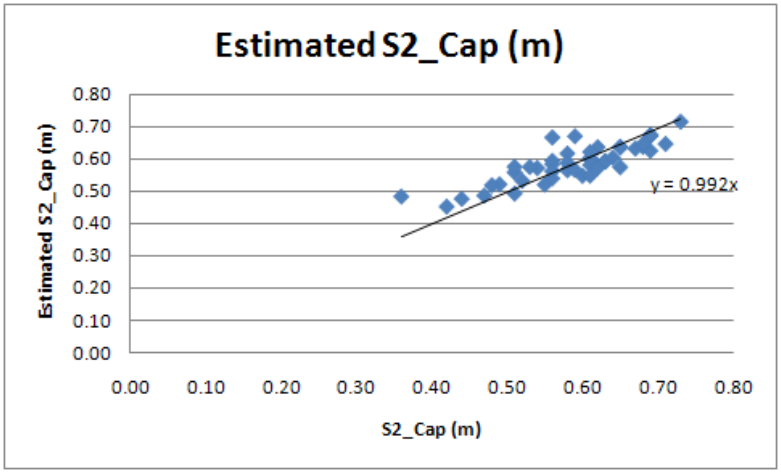

Figure 5.6 Estimated S_2^c Versus Observed S_2^c by a Two-Predictor Model (Forest and Canopy Cover).

Figure 5.6 shows the estimated S_2^c versus the observed S_2^c by the two-predictor model (**Table 5.3**). The estimated storages capacities are generally well represented (errors are within ±10% of the observed values).

5.2.3 Regression Model for S_1^c

In this section, the above stepwise regression procedure is applied to the storage capacity (S_1^c) of the upper layer. The final model contains one predictor, the volume of water that the soil can hold to a depth of 25 centimeters (aws025_awm). **Figure 5.7** shows the linear regression for the above predictor. The final regression model is summarized in **Table 5.4**. The results show that the volume of water that the soil can hold in the shallow soil column (up to 25 centimeters) is a good indicator of the storage capacity in the upper layer.

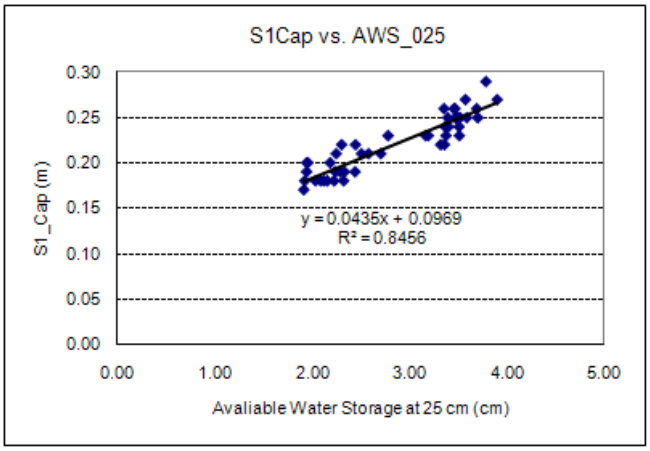

Figure 5.7 Linear Regression of the Upper Storage Capacity (S1_Cap) on Available Water Storage to a Depth of 25 Centimeters.

Table 5.4 Regression for S_1^c with the One-Predictor Model.

Model Parameter: S1_Cap (m/mo)					
Predictors: aws025_awm					
Residuals:					
	Min	1Q	Median	3Q	Max
	-0.0230	-0.0081	-0.0030	0.0084	0.0285
Coefficients:					
	Estimate	Std. Err.	t value	Pr(>|t|)	
(intercept)	0.0969	0.0082	11.8800	<=1.80e-15	
aws025_awm	0.0435	0.0028	15.7000	<2e-16	

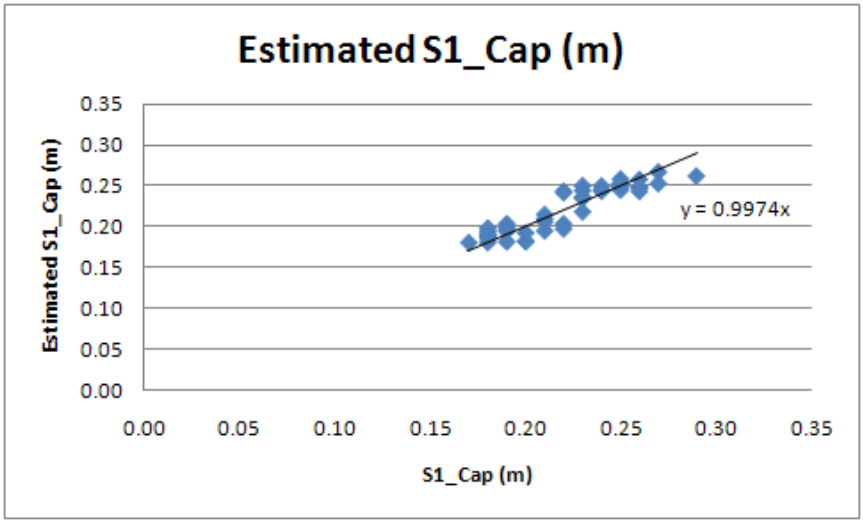

Figure 5.8 Estimated S_1^c Versus Observed S_1^c.

Figure 5.8 shows the estimated S_1^c versus the observed S_1^c by using the one-predictor model (**Table 5.4**). The estimated storage capacities represent very well the observed values (errors are within ±5% of the observed values).

5.2.4 Regression Model Lower Storage Release Function ($\beta_{2,1}$ and $\beta_{2,2}$)

In this section, the above stepwise regression procedure is applied to the parameters of the lower storage release function. The final model shows that the parameter $\beta_{2,2}$ is related to the saturated hydraulic conductivity Ksat (**Figure 5.9**). The final regression model is also summarized in **Table 5.5**.

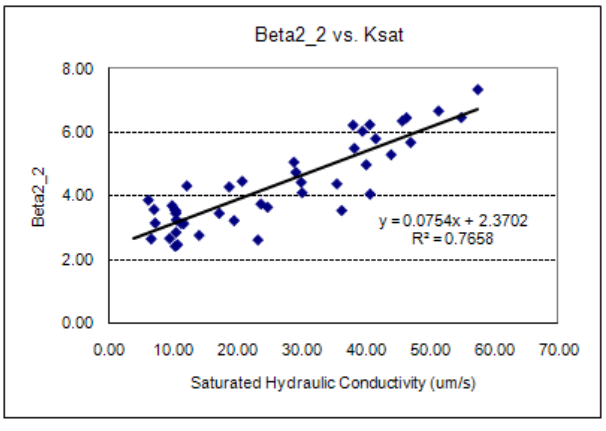

Figure 5.9 Linear Regression of the $\beta_{2,2}$ on Saturated Hydraulic Conductivity (Ksat).

Table 5.5 Regression for $\beta_{2,2}$ with the One-Predictor Model.

Model Parameter: Beta2 (m/mo)					
Predictors: Ksat					
Residuals:					
	Min	1Q	Median	3Q	Max
	-1.5626	-0.4329	0.0432	0.5150	0.9856
Coefficients:					
	Estimate	Std. Err.	t value	Pr(>|t|)	
(intercept)	2.3702	0.1796	13.6100	<2e-16	
Ksat	0.0754	0.0062	11.9500	<=1.49e-15	

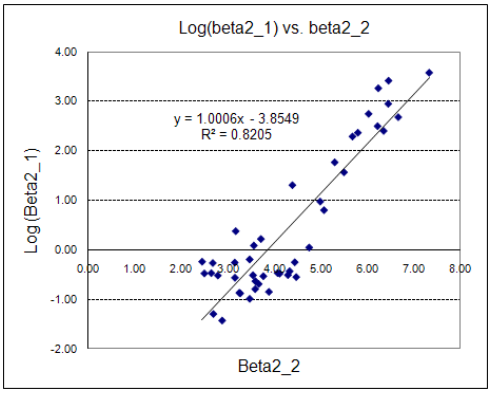

Figure 5.10 Linear Approximation of $\log(\beta_{2,1})$ by $\beta_{2,2}$.

The other parameter in the storage-release function, $\beta_{2,1,}$ is found to be strongly related to $\beta_{2,2}$. **Figure 5.10** shows that $\log(\beta_{2,1})$ can be approximated as a linear function of $\beta_{2,2}$: $\beta_{2,1} = exp(1.0006\beta_{2.2} - 3.8549)$.

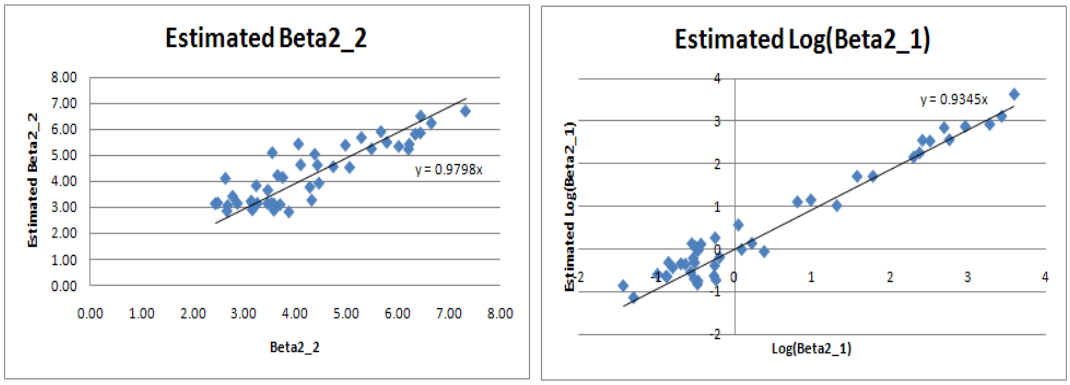

Figure 5.11 Estimated $\beta_{2,2}$ (and $\beta_{2,1}$) Versus Observed $\beta_{2,2}$ (and $\beta_{2,1}$).

Figure 5.11 shows the estimated $\beta_{2,2}$ (and $\beta_{2,1}$) versus the observed $\beta_{2,2}$ (and $\beta_{2,1}$) using the one predictor variable model (**Table 5.5**). It can be shown that the models perform well for watersheds with $\beta_{2,2} > 4.50$ and $\ln(\beta_{2,1}) > 0$. Smaller values of these coefficients are estimated with less accuracy. The smaller coefficients mostly occur for the watersheds below the fall line, where the uncertainties of flow measurements are relatively larger than the upper watersheds.

5.2.5 Regression Model for the Upper Storage Release Function ($\beta_{1,1}$ and $\beta_{1,2}$)

In this section, the stepwise regression procedure is applied to the parameters of the upper storage release function. The final model shows that parameter $\beta_{1,2}$ is related to the saturated hydraulic conductivity and the topographic slope. However, **Figure 5.12** suggests that the relationship between $\beta_{1,2}$ and the topographic slope is nonlinear. Therefore, the logarithm of the slope is used instead.

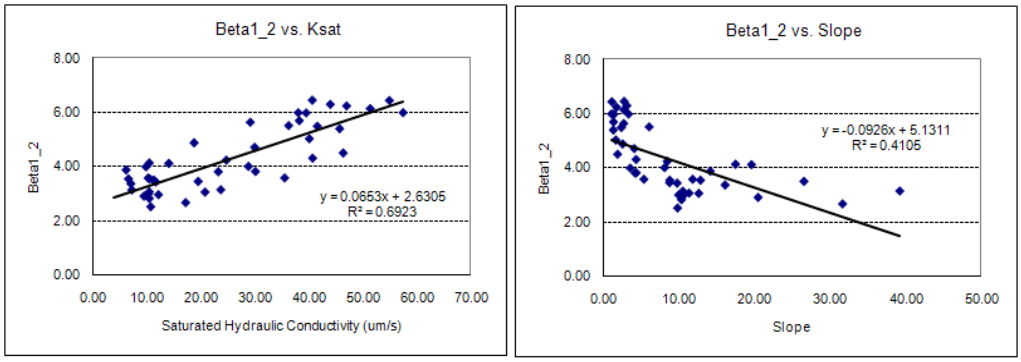

Figure 5.12 Linear Regression of $\beta_{1,2}$ on Saturated Hydraulic Conductivity and Slope.

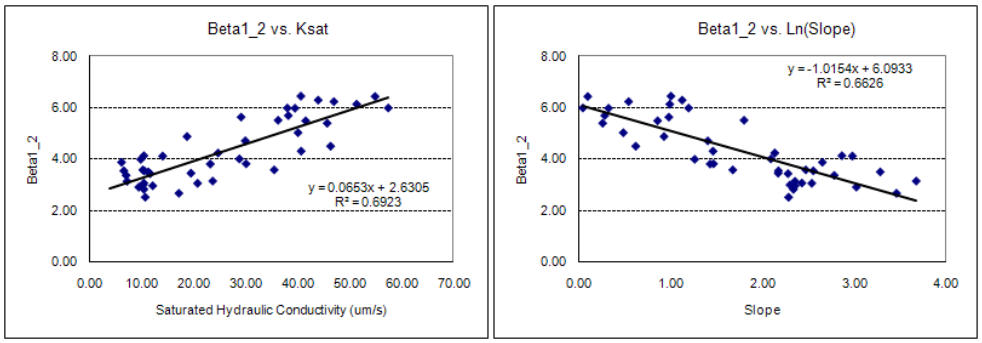

Figure 5.13 Linear Regression of $\beta_{1,2}$ on the Saturated Hydraulic Conductivity and the Logarithm of the Slope.

Figure 5.13 shows that the relationships between $\beta_{1,2}$ and the logarithm of the topographic slope. The R^2 in the $\beta_{1,2}$ – slope relationship increases from 0.4105 to 0.6626 when the ln(slope) is used instead of the slope. The final regression model is summarized in **Table 5.6**.

Table 5.6 Regression for $\beta_{1,2}$ with the One-Predictor Model.

Model Parameter: Beta1					
Predictors: Ksat, slopegradw					
Residuals:					
	Min	1Q	Median	3Q	Max
	-1. 1894	-0.4600	-0.0519	0.4504	1.1808
Coefficients:					
	Estimate	Std. Err.	t value	Pr(>|t|)	
(intercept)	4.0545	0.4923	8.236	<=1.85e-10	
Ksat	0.0411	0.0096	4.264	<=1.05e-4	
Ln(slopegradw)	-0.4512	0.1556	-2.899	<=5.81e-3	

The other parameter $\beta_{1,1}$ in the storage-release function is found to be closely related to $\beta_{1,2}$ as shown in **Figure 5.14**: $\beta_{1,1} = exp(0.9233\beta_{1.2} - 2.4073)$.

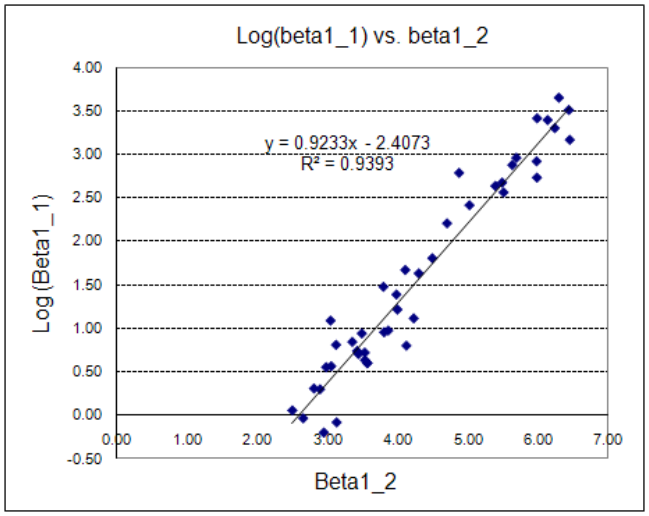

Figure 5.14 Linear Approximation of $\log(\beta_{1,1})$ as a Function of $\beta_{1,2}$.

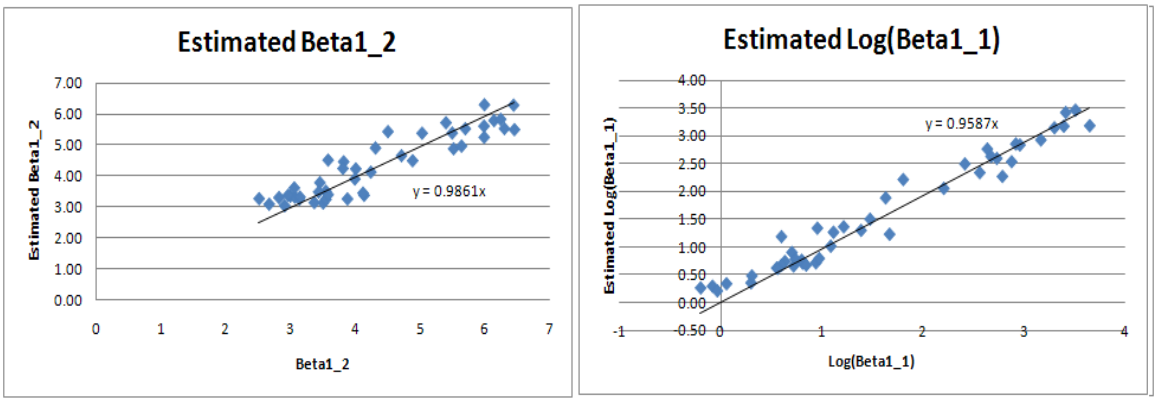

Figure 5.15 Estimated $\beta_{1,2}$ (and $\beta_{1,1}$) Versus Observed $\beta_{1,2}$ (and $\beta_{1,1}$).

Figure 5.15 shows the estimated $\beta_{1,2}$ (and $\beta_{1,1}$) versus the observed $\beta_{1,2}$ (and $\beta_{2,1}$) by using the one-predictor model (**Table 5.6**).

5.2.6 Regionalization Model for the Percolation Function (α_0, α_1, α_2, α_3, α_4, and α_5)

In Chapter 4, the percolation function is defined as follows:

$$u_{12} = \alpha_0 + \alpha_1 ET_2(k) + \alpha_2 \frac{ET_1(k)}{ET_2(k)} + \alpha_3 S_2(k) + \alpha_4 \frac{S_1(k)}{S_2(k)} + \alpha_5 P_{eff}(k),$$

where, α_0, α_1, α_2, α_3, α_4, and α_5 are constant coefficients.

Physically, the soil infiltration rate measures the rate at which soil is able to absorb rainfall or irrigation. The infiltration rate is expected to depend on soil characteristics, including ease of entry, storage capacity, and transmission rate through the soil. The texture and structure of the soil, the water content of the soil, and intensity of rainfall all play a role in controlling the infiltration rate (Horton 1933, 1940; Walker, 1987).

First, toward developing the regionalization model, possible interdependencies among the percolation function coefficients are investigated.

Figure 5.16 shows that α_3 and α_5 are highly correlated with α_1 ($R^2 = 0.89$ and $R^2 = 0.90$). Therefore, α_3 and α_5 can be obtained from:

$$\alpha_3 = -0.7637\alpha_1 - 0.0016 \text{ and}$$

$$\alpha_5 = -0.4121\alpha_1 + 0.4251.$$

Furthermore, **Figure 5.17** shows that α_4 is highly correlated with α_2 ($R^2 = 0.98$). Therefore, α_4 can be obtained from $\alpha_4 = -0.7329\alpha_2 - 0.0103$.

Thus, the regionalization process will focus on α_0, α_1, and α_2, from which the rest of the percolation function coefficient can be derived as shown above.

Second, the hypothesis that α_0, α_1, and α_2 (in monthly models) are effectively constant in watersheds with similar soil types and vegetation is investigated. As shown in **Figure 5.2**, watershed soils in Georgia are distinctly different above and below the fall line, with the former predominantly being sandy loam and the latter loamy sand. Vegetation is also likewise different above and below the fall line, as the southern watersheds are largely agricultural.

To test the previous hypothesis, an optimal set of α_0, α_1, and α_2 coefficients is determined for all watersheds above the fall line and similarly for watersheds below the fall line. The optimal coefficient sets are obtained by maximizing the correlation between the flow of the fully calibrated models (in Chapter 4) and the flow of the models using the optimal coefficient set. The optimal coefficient set is the one that maximizes the summation of these correlations across all watersheds above the fall line, and separately across the watersheds below the fall line. The models using the optimal coefficient set

also use the previously derived relationships between {α_3, α_4, and α_5} and {α_0, α_1, and α_2} to complete the model definition. In the results presented below, the optimal coefficients are denoted by α_0^*, α_1^*, and α_2^*.

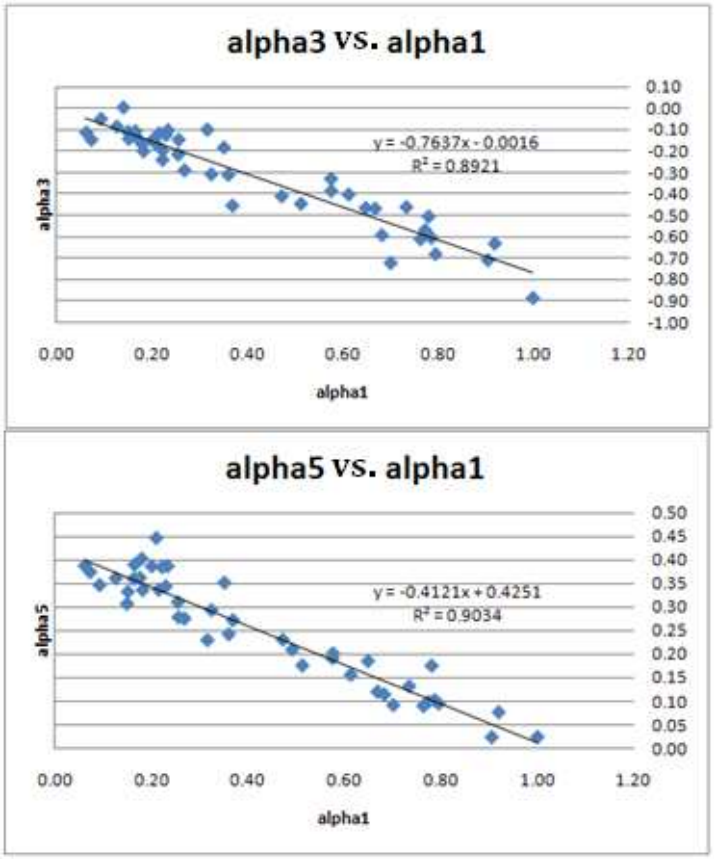

Figure 5.16 Linear Approximations of α_3 and α_5 by α_1.

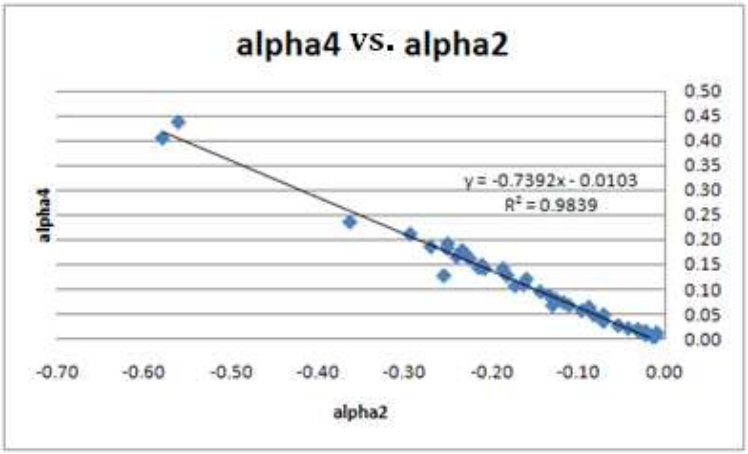

Figure 5.17 Linear Approximation of α_4 by α_2.

Table 5.7 Regionalization of α_0, α_1, α_2, α_3, α_4, and α_5 for Sandy Loam Watersheds Above the Fall Line.

	ACT_Newell	SO_Bell	OOA_Penfield	OOA_Jackson
α_0	0.07161	0.0642	0.0871	0.0626
α_1	0.1473	0.2077	0.2186	0.1595
α_2	-0.5924	-0.5321	-0.5834	-0.5394
α_3	-0.0978	-0.0861	-0.1009	-0.096
α_4	0.4789	0.4526	0.4893	0.4703
α_5	0.4695	0.4994	0.4625	0.4675
α_0*	0.079			
α_1*	0.142			
α_2*	-0.579			
α_3*	-0.110			
α_4*	0.466			
α_5*	0.467			
PCor(Qsim,Qcalib)	0.98	0.96	0.96	0.94

Table 5.8 Regionalization of α_0, α_1, α_2, α_3, α_4, and α_5 for Loamy Sand Watersheds below the Fall Line.

	ACF_Milford	OOA_Lumber	SO_Claxton	OSSS_Bemiss
α_0	0.0704	0.0927	0.1088	0.1083
α_1	0.3663	0.1404	0.2114	0.2884
α_2	-0.3427	-0.5414	-0.4961	-0.4323
α_3	-0.1112	-0.1432	-0.1991	-0.1872
α_4	0.2859	0.4146	0.3642	0.2991
α_5	0.4009	0.5747	0.5293	0.4605
α_0*	0.109			
α_1*	0.275			
α_2*	-0.453			
α_3*	-0.211			
α_4*	0.322			
α_5*	0.312			
Pcoor(Qsim,Qcalib)	0.93	0.96	0.98	0.99

Table 5.7 shows the regionalization of α_0, α_1, α_2, α_3, α_4, and α_5 for four sandy loam watersheds above the fall line: the Newell (ACT), Bell (SO), Penfield (OOA), and Jackson (OOA) watersheds. The first six rows list the calibrated α values, and the next

six rows list the regionalized α* values. The last row shows the correlation coefficients between the simulated flows (using regionalized α* values α_0*, α_1*, α_2*, α_3*, α_4*, and α_5*) and the simulated flows using the fully calibrated α values (based on observed flow data as described in Chapter 4). The table shows that the correlation coefficients between the two flow sequences are between 0.94 and 0.98. **Table 5.8** shows similar results for the four loamy sand watersheds below the fall line: Milford (ACF), Lumber (OOA), Claxton (SO), and Bemiss (OSSS) watersheds. Here too, the table shows that the correlation coefficients between the simulated flows are in the 0.93 to 0.99 range. A similar analysis can be undertaken to distinguish the influence of soil and vegetation cover.

5.2.7 Regionalization Model for Impervious Coefficient (a_{imp})

The impervious area coefficient a_{imp} determines the portion of precipitation becoming direct flow because of impervious surfaces in the watershed. **Figure 5.18** shows the calibrated a_{imp} versus the impervious area percentage obtained from the land use database. It shows that for watersheds with low impervious area percentages (< 3%; showing in red in the figure), a_{imp} values are small (0.02-0.05) and can be approximated by a linear equation. For watersheds with high impervious area percentages (>3%; showing in blue in the figure), a_{imp} values are significantly higher.

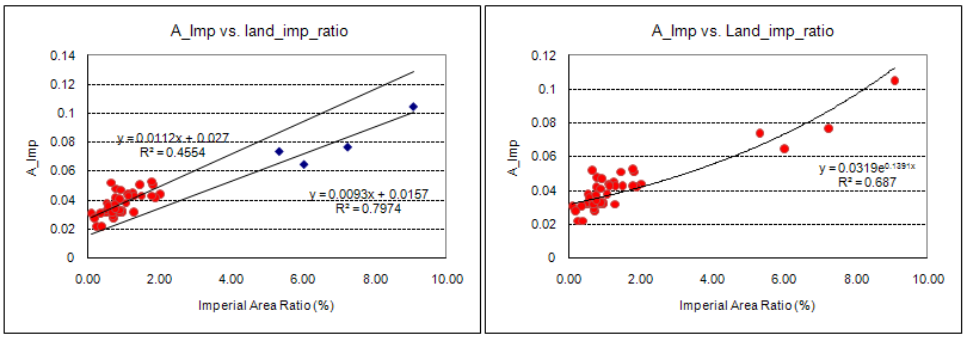

Figure 5.18 Calibrated a_{imp} Versus the Impervious Area Percentage.

The impervious area coefficient a_{imp} can be approximated by using a nonlinear form as shown in **Figure 5.18**. The nonlinear form will be used in this study:

$a_{imp} = 0.0319 \cdot \exp(0.1391 \cdot Percentage_{imp})$.

The regionalization models' performances can be assessed by several different statistics. For example, the regression residue for each parameter indicates the model assumptions and the selection of predictors. In addition, spatial correlations of the residuals can also be assessed to identify the models' performances for different locations. The spatial correlations can also indicate any spatial biases existing for different locations of the study region. However, this study focuses mainly on the applicability of the regionalization models in simulating flows in ungauged watersheds. Therefore, in the next section of the model verification, the skills of flow simulation will be verified only.

5.3 Model Regionalization Summary

- *Storage Capacity of the Lower Soil Layer:*

$S_2^c = 0.3851 + 0.1565 \cdot Percent_{forest} + 0.31 \cdot Percent_{canopy}$.

where *Percent_Forest* is the percentage of forest in the watershed, and *Percent_Canopy* is the percentage of canopy in the watershed.

- *Storage Capacity of the Upper Soil Layer:*

$S_1^c = 0.0969 + 0.0435 \cdot Aws\_025$.

where *Aws_025* is the volume of water (in cm) that the soil can hold to a depth of 25 centimeters.

- *Storage-Release Function Parameters for the Lower Layer:*

$\beta_{2,2} = 2.4450 + 0.0737 \cdot Ksat$.

$\beta_{2,1} = exp(1.0006\beta_{2.2} - 3.8549)$

where *Ksat* is the average saturated hydraulic conductivity (in µm/s) of the watershed.

- *Storage-Release Function Parameters for the Lower Layer:*

$\beta_{1,2} = 4.0545 + 0.0411 \cdot Ksat - 0.4512 \cdot \text{Ln}\ (Slope)$.

$\beta_{1,1} = exp(0.9233\beta_{1.2} - 2.4073)$

where *Ksat* is the average saturated hydraulic conductivity (in um/s) of the watershed; and *Slope* is the average slope of the watershed.

- *Percolation Function Parameters:*

Table 5.9 Summary of the Percolation Coefficients.

	Sandy Loam	Loamy Sand
α_0	0.079	0.109
α_1	0.142	0.275
α_2	-0.579	-0.453
α_3	-0.110	-0.211
α_4	0.466	0.322
α_5	0.467	0.312

Table 5.9 summarizes the percolation coefficients for the sandy loam and loamy sand watersheds in Georgia. The last three coefficients (α_3, α_4, and α_5) are calculated by the following equations:

$\alpha_3 = -0.7637\alpha_1 - 0.0016$,

$\alpha_4 = -0.7329\alpha_2 - 0.0103$, and

$\alpha_5 = -0.4121\alpha_1 + 0.4251$.

- *Impervious Area Parameter:*

$a_{imp} = 0.0319 \cdot \exp\left(0.1391 \cdot Percentage_{imp}\right)$.

where $Percentage_{imp}$ is the percentage of impervious areas in the watershed.

5.4 Assessment of Parameter Regionalization

This section employs the model regionalization procedures developed earlier to assess model performance in simulating stream flows. Four watersheds are used in the assessment. Two of these watersheds are located above the fall line and are the Newell watershed (ACT basin) and the Penfield watershed (OOA basin); the other two watersheds are located below the fall line and are the Claxton watershed (SO basin) and the Bemiss watershed (OSSS basin). The model parameters of the fully calibrated models are listed in **Table 5.10**.

Table 5.10 Fully Calibrated Parameters for the Newell watershed (ACT basin), the Penfield watershed (OOA basin), the Claxton watershed (SO basin), and the Bemiss watershed (OSSS basin).

	Above Fall Line		Below Fall Line	
	ACT_Newell	OOA_Penfield	SO_Claxton	OSSS_Bemiss
S_1^c (meter)	0.25	0.26	0.18	0.18
S_2^c (meter)	0.62	0.63	0.55	0.51
$\beta_{1,1}$	3.6299	3.9369	2455.9810	468.6540
$\beta_{1,2}$	3.1843	3.5688	6.1359	5.4890
$\beta_{2,1}$	0.1572	0.1589	487.3160	235.6790
$\beta_{2,2}$	2.4444	4.3863	6.6647	5.7955
α_0	0.0716	0.0871	0.1088	0.1083
α_1	0.1473	0.2186	0.2114	0.2884
α_2	-0.5924	-0.5834	-0.4961	-0.4323
α_3	-0.0978	-0.1009	-0.1991	-0.1872
α_4	0.4789	0.4893	0.3642	0.2991
α_5	0.4695	0.4625	0.5293	0.4605

The calibrated model parameters in **Table 5.10** are used to generate flows (calibrated flows) for the above four watersheds. The calibrated flows are then compared with the flows simulated using regionalized model parameters and with observed flows.

Table 5.11 shows the predictors of the regionalization relationships for the test watersheds. The table shows that the two watersheds above the fall line differ from the two below the fall line in that *(1)* the above-fall-line watersheds have higher percentages of forest and canopy cover than the below-fall-line watersheds; *(2)* the water capacity at a depth of 25 centimeters of the above-fall-line watersheds is higher than that of the below-fall-line watersheds; *(3)* the saturated hydraulic conductivity of the above-fall-line watersheds is much lower than that of the below-fall-line watersheds because of soil-type differences; *(4)* the above-fall-line watersheds have much higher topographic slopes than the below-fall-line watersheds; and *(5)* the soil types of the above- and below-fall-line watersheds differ as indicated earlier (i.e., sandy loams versus loamy sands respectively).

Table 5.11 Watershed Regionalization Predictors for the Newell watershed (ACT basin), Penfield watershed (OOA basin), Claxton watershed (SO basin), and Bemiss watershed (OSSS basin).

	Above Fall Line		Below Fall Line	
	ACT_Newell	OOA_Penfield	SO_Claxton	OSSS_Bemiss
Forest (ratio)	0.61	0.64	0.43	0.39
Canopy (ratio)	0.48	0.53	0.36	0.29
Aws_025 (cm)	3.47	3.47	2.12	1.92
Ksat (µm/s)	7.25	10.25	55.15	50.56
Impervious Area (percentage)	1.81	1.78	0.93	1.28
Slope (m/m)	11.78	11.78	2.69	2.36
Soil Type	Sandy Loam		Loamy Sand	

The regionalized parameters for these watershed models (derived as summarized in Section 5.3) are presented in **Table 5.12**. For the two watersheds above the fall lines, no groundwater components are involved in both the calibrated and regionalized simulations. However, for the two watersheds above the fall lines, the calibrated models

include the groundwater components. The regionalized models use the calibrated parameters for the groundwater interactions (Ug flux).

The Pearson correlations between the regionalized flows and the fully calibrated flows are between 0.93 and 0.95, implying that the regionalized models perform well.

Table 5.12 Regionalized Model Parameters for the Newell Watershed (ACT Basin), Penfield Watershed (OOA Basin), Claxton Watershed (SO Basin), and Bemiss Watershed (OSSS Basin).

	Above Fall Line		Below Fall Line	
	ACT_Newell	OOA_Penfield	SO_Claxton	OSSS_Bemiss
S_1^c (meter)	0.25	0.25	0.19	0.18
S_2^c (meter)	0.63	0.65	0.56	0.53
$\beta_{1,1}$	3.82	4.96	1037.22	787.93
$\beta_{1,2}$	3.24	3.36	5.87	5.74
$\beta_{2,1}$	0.09	0.15	458.11	210.21
$\beta_{2,2}$	2.98	3.20	6.51	6.17
a_{imp}	0.041	0.041	0.036	0.038
α_0	0.079		0.109	
α_1	0.142		0.275	
α_2	-0.579		-0.453	
α_3	-0.110		-0.211	
α_4	0.466		0.322	
α_5	0.467		0.312	
Pcorr(Qreg, Qcalib)	0.9534	0.9514	0.9407	0.9406

Figure 5.19 compares the time series of the calibrated and regionalized flows for the Newell, Penfield, Claxton, and Bemiss watersheds. The figure shows that for the two watersheds above the fall line, regionalized flows generally compare well with calibrated flows especially in low flows, while peak flows are somewhat overestimated for a few months (especially for the Athens watershed). **Figure 5.20** also shows a similar trend for the two watersheds below the fall line, with the performance during low flows being

comparable, and regionalized high flows somewhat underestimating calibrated flows (especially for the Bemiss watershed after 1974).

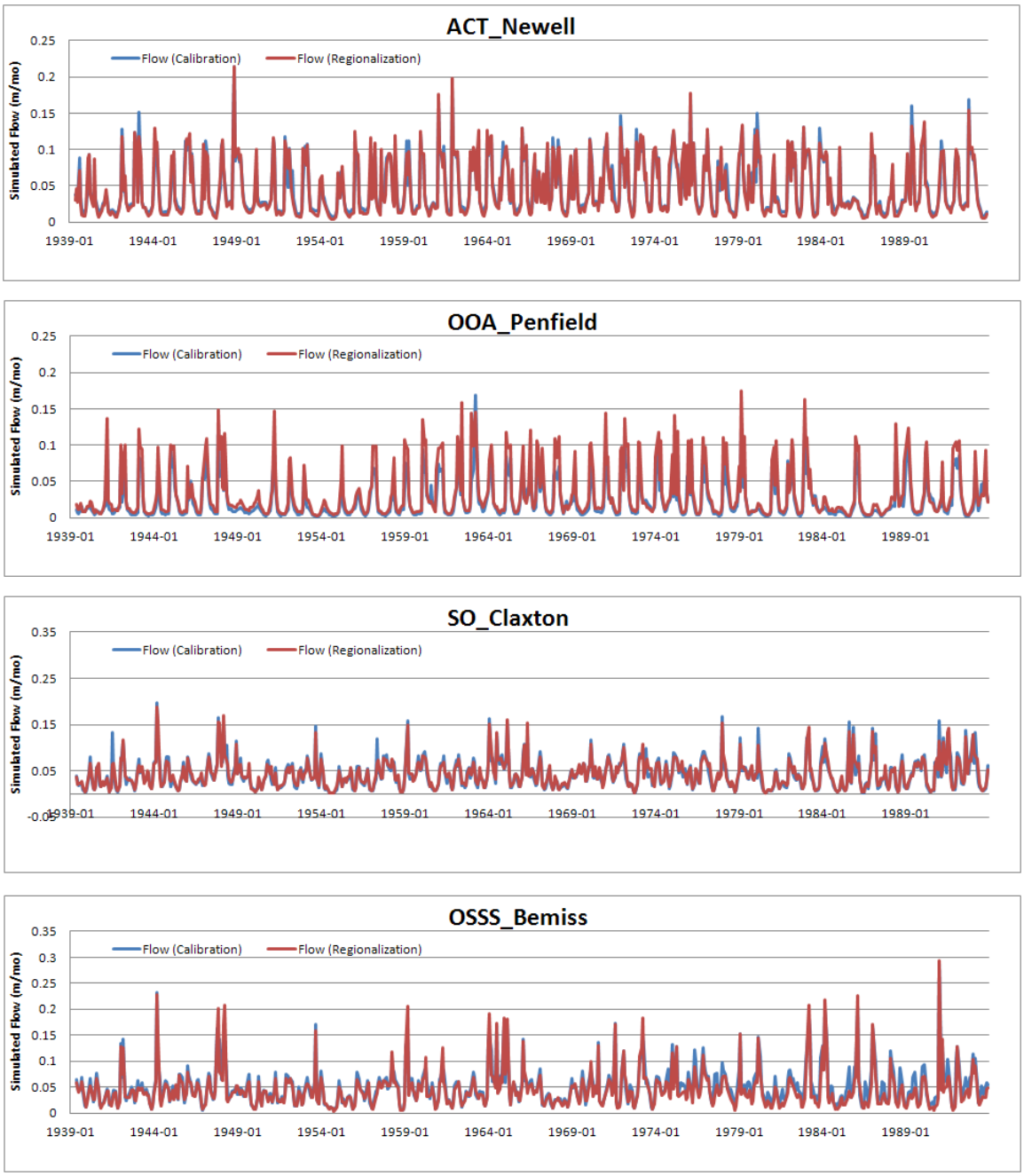

Figure 5.19: Comparison of Regionalized (Red) with Calibrated (Blue) Flows for Newell Watershed (ACT Basin), Penfield Watershed (OOA Basin), Claxton Watershed (SO Basin), and Bemiss Watershed (OSSS Basin).

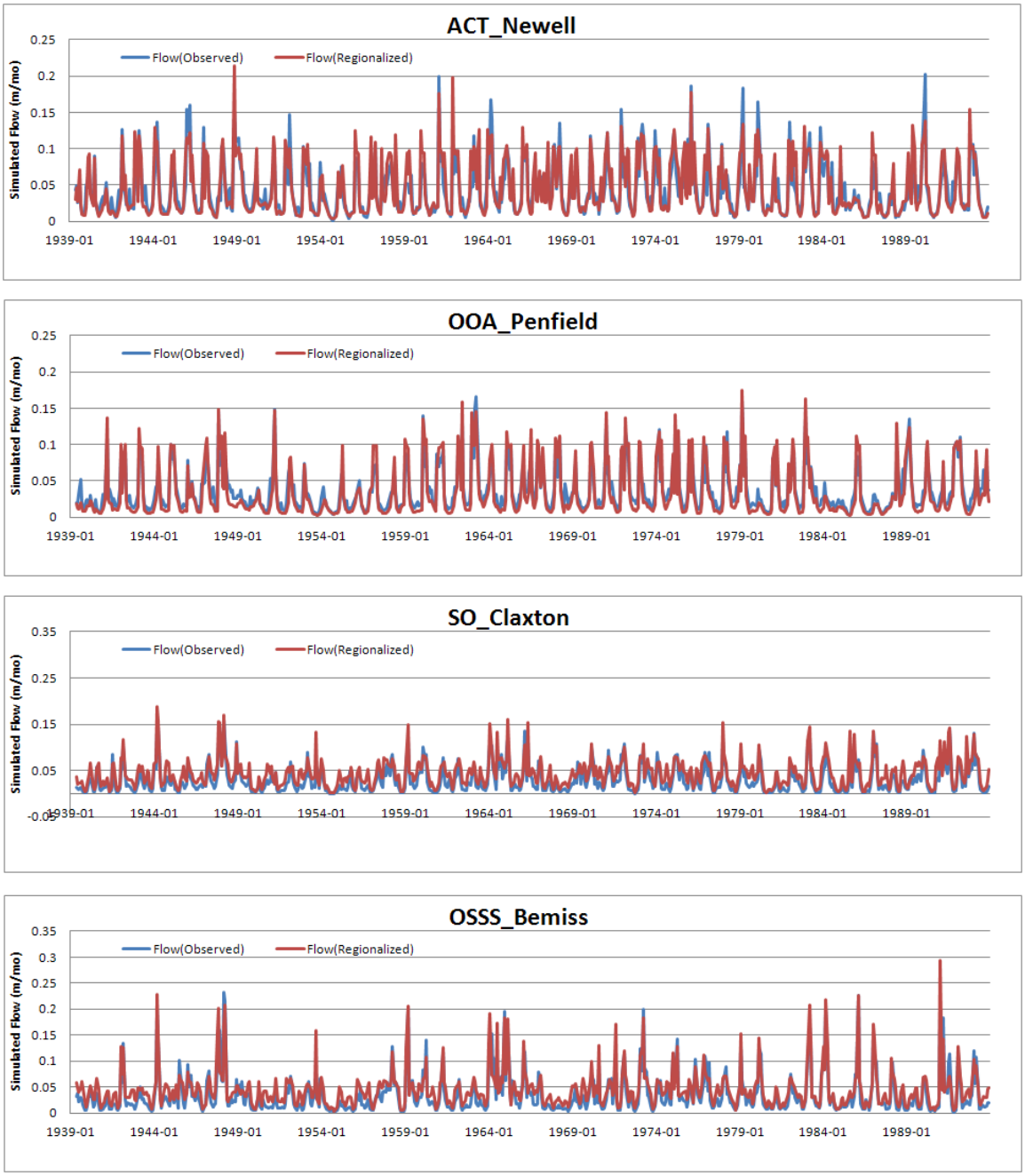

Figure 5.20: Comparison of Regionalized (Red) and Observed (Blue) flows for the Newell Watershed (ACT Basin), Penfield Watershed (OOA Basin), Claxton Watershed (SO Basin), and Bemiss Watershed (OSSS Basin).

Table 5.13 Calibrated and Regionalized Model Performance of Newell Watershed (ACT Basin), Penfield Watershed (OOA Basin), Claxton Watershed (SO Basin), and Bemiss Watershed (OSSS Basin).

Calibration Model				
	ACT_Newell	OOA_Athens	SO_Claxton	OSSS_Bemiss
Pcorr	0.9169	0.9321	0.8809	0.9020
SPCorr	0.8995	0.9115	0.8755	0.8948
QRMSE/Q	0.3507	0.3190	0.3721	0.3823
RnkQRMSE/RnkQ	0.5161	0.5091	0.5440	0.5161
QAbsQError/Q	0.2700	0.2595	0.2961	0.2830
Regionalization Model				
	ACT_Newell	OOA_Athens	SO_Claxton	OSSS_Bemiss
Pcorr	0.9013	0.8879	0.8622	0.8836
SPCorr	0.8838	0.8902	0.8433	0.8690
QRMSE/Q	0.4032	0.4029	0.4219	0.4216
RnkQRMSE/RnkQ	0.6109	0.6395	0.6701	0.5924
QAbsQError/Q	0.3166	0.3120	0.3477	0.3407
Regionalization vs. Calibration (Percentage Change)				
	ACT_Newell	OOA_Athens	SO_Claxton	OSSS_Bemiss
Pcorr	-0.0170	-0.0474	-0.0212	-0.0204
SPCorr	-0.0175	-0.0234	-0.0368	-0.0288
QRMSE/Q	0.1497	0.2630	0.1338	0.1028
RnkQRMSE/RnkQ	0.1837	0.2561	0.2318	0.1478
QAbsQError/Q	0.1726	0.2023	0.1743	0.2039

Figure 5.14 compares the time series of observed flows with regionalized flows for the Newell, Penfield, Claxton, and Bemiss watersheds. The figure shows that for the regionalized flows generally represent well the fluctuations of the monthly flows despite that there are some discrepancies in peak or low flows for all tested watersheds.

Table 5.13 illustrates the performance of the calibrated as well as the regionalized models. For the calibrated models, the above-fall-line watersheds (Newell and Penfield) exhibit higher correlation with observed flows than the below-fall-line watersheds (Claxton and Bemiss); they also have smaller normalized simulation flow errors for both

mean square errors (QRMSE and RnkQRMSE) and absolute errors (QAbsQError). However, regionalized model performance is overall satisfactory.

Table 5.13 also reports the percent change in performance between the calibrated and regionalized models. The table shows that the correlation of flows decreases approximately 2% - 4% (Pearson and Spearman correlation coefficients); the root mean square error of the flow values (QRMSE) and their ranks (RnkQRMSE) increase approximately 14%-25%; and the normalized absolute flow errors increase approximately 19% - 21%. These statistics show the additional uncertainties introduced by regionalization of the parameters and should be carefully assessed in model applications.

CHAPTER 6

CLIMATE CHANGE ASSESSMENT FOR GEORGIA

This chapter describes the potential hydrologic impacts of climate change over Georgia. The assessment utilizes the downscaled precipitation and potential evapotranspiration sequences and quantifies the corresponding watershed response in terms of watershed evapotranspiration, soil moisture, and runoff. The study utilizes the conceptual hydrologic models developed in **Chapter 4,** which simulate the important hydrologic processes operating at monthly time scales. The calibrated models are used for each watershed in both historical and future climate assessments.

6.1 Historical (Baseline) and Future Hydrologic Assessments for the ACF Basin

6.1.1 Historical Assessment

The calibrated watershed models are employed in this section to characterize the ACF hydrologic response under the historical climate from 1901 through 2009 for all ACF watersheds (**Figure 6.1**). The assessments consist of running the ACF watershed models under historical climatic forcing (of precipitation and temperature) for 109 years from 1901 to 2009 in monthly steps. The model output sequences, soil moisture, evapotranspiration, and runoff, are then used to assess the watershed response. The purpose of the assessment is to *(1)* verify whether the model hydrology is consistent with regional observations; *(2)* detect possible long term trends; and *(3)* create a baseline hydrologic response to be used as a comparison standard for the future climate assessments in the following section.

Figure 6.1: Map of ACF Watersheds: Buford, West Point, George, Montezuma, Albany and Woodruff-Bainbridge.

The results are presented in **Figure 6.2.** The five charts in this figure show the precipitation (observed), potential evapotranspiration (observed), soil moisture (simulated), actual evapotranspiration (simulated), and runoff (simulated) sequences. In each chart, the normalized two-year moving averaged sequences of the six ACF watersheds are plotted. In addition, the trend lines for Buford and Woodruff watersheds are also included.

The results support the following conclusions:

- Watershed precipitation over ACF changes mildly. (**Figure 6.2a; Table 6.1**). Over the 109 year period, the decrease (Buford, Albany, and Woodruff-Bainbridge) is approximately 1% - 4% of the early 20th century value; and the increase (West Point, George, and Montezuma) is about 1% of the early 20th century value.
- In addition, the two-year average precipitation is highly variable, reaching a maximum depth of 0.165 meters (in 1920) and a minimum depth of 0.085 meters (in 1986 and 2007-2008). In the most severe droughts (e.g., those in the early 1940's, 1950's, 1980's, 1998-2002, and 2006-2008), large precipitation deficits linger for several years. These observations are consistent with regional drought occurrences. The high inter-annual rainfall variability (up to 50% of normal) and persistence renders the watershed vulnerable to droughts and has critical implications for Lake Lanier at the watershed outlet. The lake is large relative to watershed inflow, and lake filling can take several years. On the other hand, high lake releases can deplete lake storage within a year. Thus, lake operation should adhere to and adapt based on the prevailing climate.
- Watershed potential evapotranspiration also shows a mildly decreasing long term trend (**Figure 6.2b; Table 6.1**). Over the 109 year period, this decrease is approximately

2% - 5% of the early 20th century value. The inter-annual PET variability is much less than that of the precipitation (up to 10% of normal). At the latitude of the Buford watershed, precipitation is consistently higher than PET. However, during droughts, when precipitation declines, PET increases and occasionally exceeds precipitation. The most pronounced such reversal occurred during the most recent drought (in 2006-2008). The ratio of annual average PET to annual average precipitation is approximately 0.68.

- Actual evapotranspiration generally follows the PET trend and is decreasing faster (**Figure 6.2c**) in the lower watersheds (e.g., Woodruff-Bainbridge).
- Total soil moisture storage (**Figure 6.1d; Table 6.1**) shows an increasing long term trend of about 2% in 109 years for West Point, George, and Montezuma watersheds. However, for Buford, Albany, and Woodruff-Bainbridge watersheds, total soil moisture storage shows a declining long term trend of about 1% - 2% in 109 years. This decline is solely due to the decline of the lower storage zone, while the upper storage exhibits no changing trend. The ratio of annual average S_1 to annual average P is approximately 1.5, and that of S_2 to P is approximately 4.5. Namely, the total active sub-surface storage in the rainfall-runoff process is about 6 times the amount of annual average precipitation.
- Total runoff (**Figure 6.2e; Table 6.1**) exhibits a declining trend of approximately 3% - 5% for Buford, Albany, and Woodruff-Bainbridge watersheds and an increasing trend of about 2% - 3% for West Point, George, and Montezuma watersheds in 109 years. It is notable that the most recent drought (2006 to 2008) was the *worst* two-year drought on record. More specifically, the most severe two-year droughts (in order of decreasing severity) occurred in 2006-2008, 1980's, 1940's, 1950's, 1930's, 1998-2002, 1920's, and 1900's. Furthermore, the last three major droughts (1980-1988, 1998-2002, and 2006-

2008) were most persistent. The declining trend of total runoff is due to the declining trend of the lower storage runoff. This trend implies that the watershed ability to sustain base river flows is diminishing. The runoff from the upper storage exhibits no significant trend. Across the ACF watersheds, the ratio of total annual average runoff to annual average precipitation is between 0.27 - 0.42, distinctly decreasing from north (higher latitudes) to south (lower latitudes).

- Lastly, the trend analysis is also performed for the most recent 50 years (1960-2009). It can be seen from **Figure 6.3** and **Table 6.1** that during this period *(1)* precipitation exhibits a declining trend of about 9% - 16% across all ACF watersheds; *(2)* PET exhibits an increasing trend of about 1% - 3% across all ACF watersheds (except for George where it decreases by about 0.8%); *(3)*soil moisture declines by about 3% - 6% across all watersheds; and *(4)* runoff declines by about 16% - 27% across all watersheds.

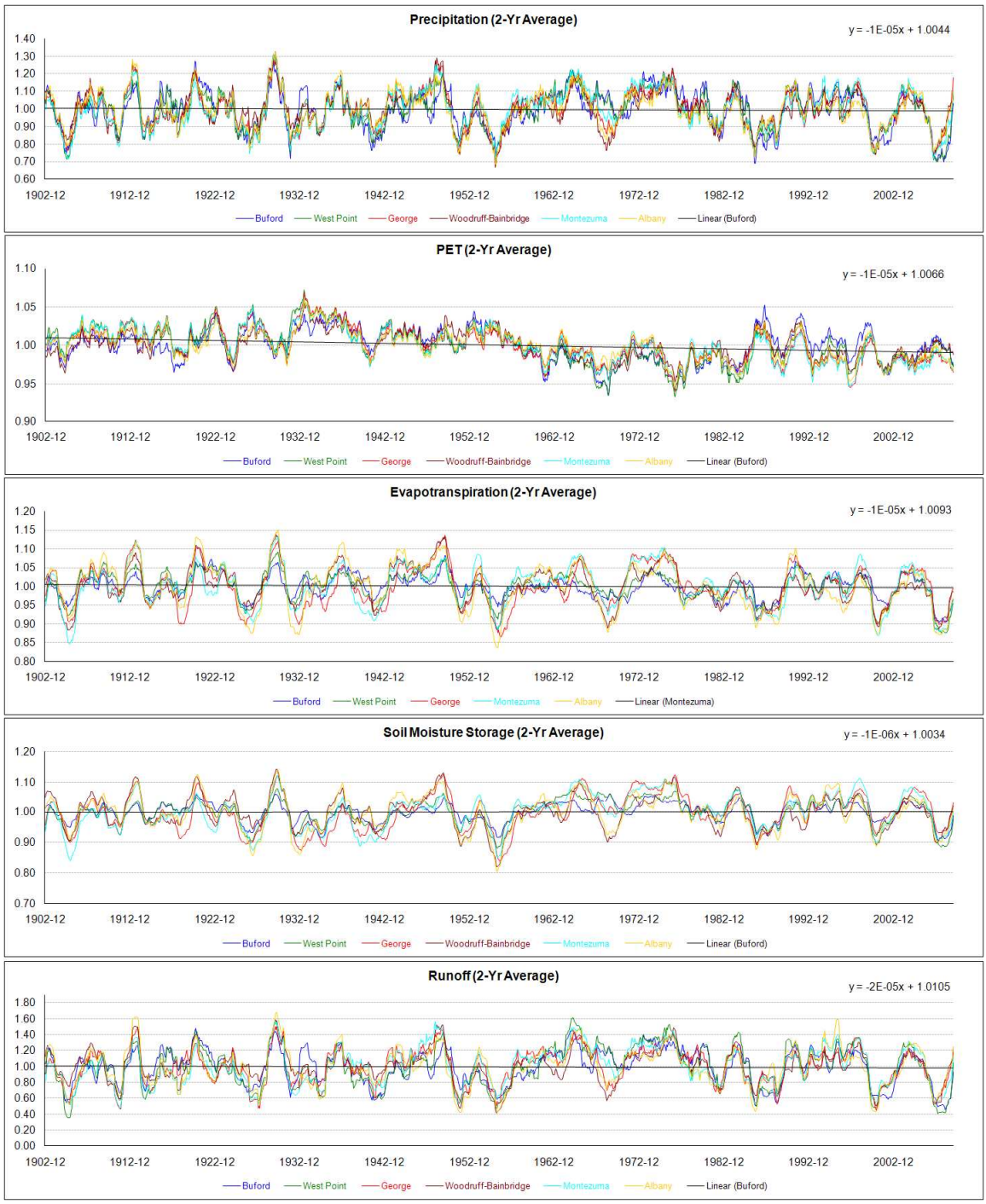

Figure 6.2: ACF Normalized, 2Yr Average Hydrologic Response (1901 - 2009).

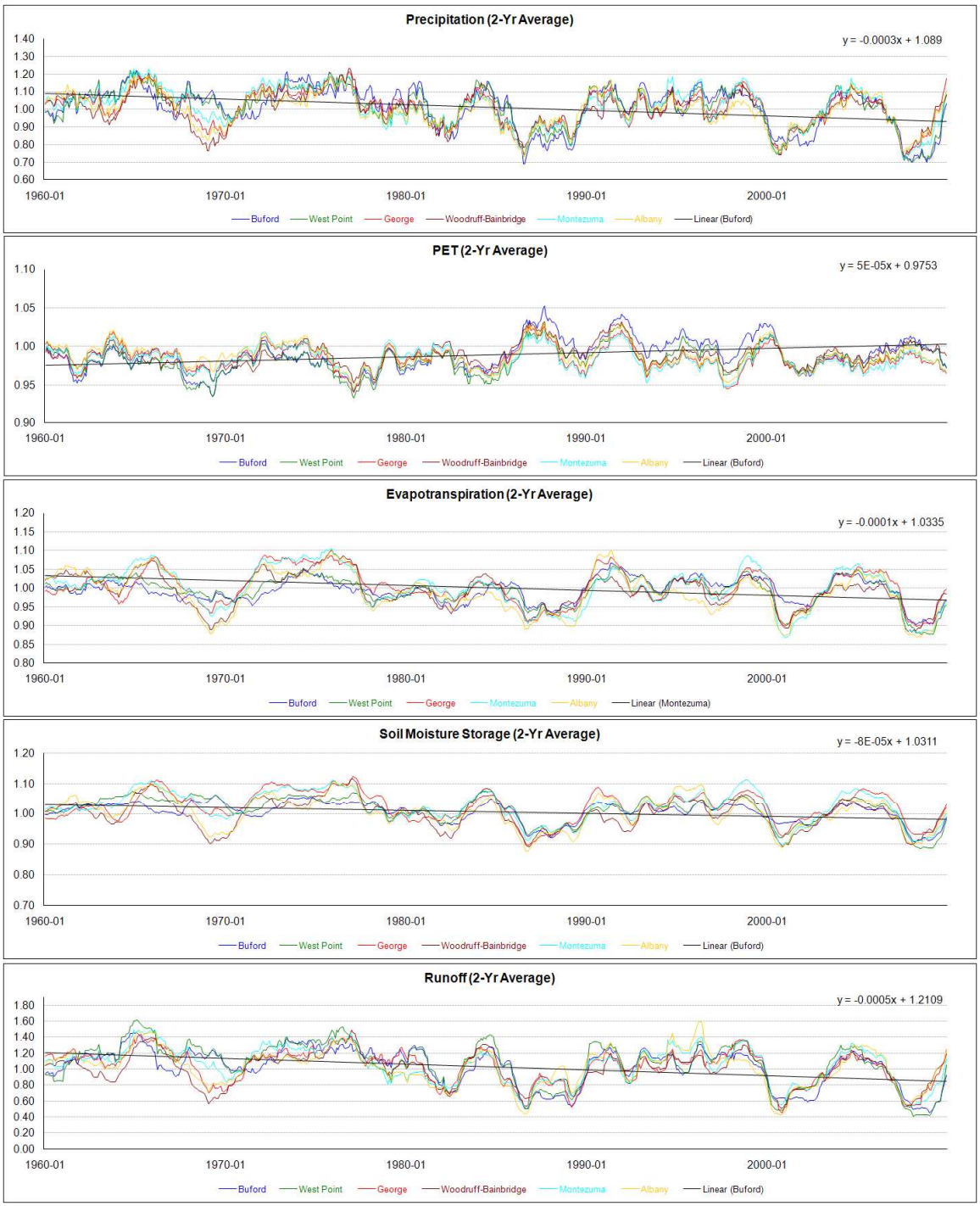

Figure 6.3: ACF Normalized, 2Yr Average Hydrologic Response (1960 - 2009).

Table 6.1 Slopes of Linear Trends for Normalized, 2Yr Average Hydrologic Variables in the ACF Basin.

	Buford	West Point	George	Montezuma	Albany	W-B
	1901-2009 (unit: 10-4 of the mean per year)					
Precipitation	-1.44	0.36	0.96	0.72	-4.32	-3.60
PET	-1.80	-4.32	-4.56	-4.68	-3.24	-2.04
Soil Moisture	-0.17	1.92	2.40	2.28	-0.36	-1.56
Runoff	-2.76	2.16	2.52	2.76	-4.08	-5.28
	1960-2009 (unit: 10-4 of the mean per year)					
Precipitation	-31.44	-32.76	-22.92	-27.60	-22.08	-18.24
PET	5.52	3.84	-1.68	3.36	1.92	2.16
Soil Moisture	-9.84	-11.40	-6.60	-11.04	-10.92	-8.88
Runoff	-54.12	-49.56	-33.60	-49.80	-41.40	-31.56
	Buford	West Point	George	Montezuma	Albany	W-B
	1901-2009 (unit: percentage increase over 109 years)					
Precipitation	-1.570	0.392	1.046	0.785	-4.709	-3.924
PET	-1.962	-4.709	-4.970	-5.101	-3.532	-2.224
Soil Moisture	-0.183	2.093	2.616	2.485	-0.392	-1.700
Runoff	-3.008	2.354	2.747	3.008	-4.447	-5.755
	1960-2009 (unit: percentage increase over 50 years)					
Precipitation	-15.720	-16.380	-11.460	-13.800	-11.040	-9.120
PET	2.760	1.920	-0.840	1.680	0.960	1.080
Soil Moisture	-4.920	-5.700	-3.300	-5.520	-5.460	-4.440
Runoff	-27.060	-24.780	-16.800	-24.900	-20.700	-15.780

6.1.2 Future Assessment

The future climate assessments are carried out by running the ACF watershed models under all A1B and A2 climate scenarios for the period from January 2000 through December 2099 (100 years) in monthly time steps. The future climate scenarios for the ACF basin are downscaled using the Joint Variable Spatial Downscaling method described in **Chapter 3**. For each of the 26 future climate scenarios (i.e., 13 A1B scenarios and 13 A2 scenarios), the assessment process is similar to the historical assessment described in the previous section. The future watershed response is characterized by two sequence ensembles, one for the A1B and a second for the A2 scenarios.

Because of the voluminous results, a more meaningful comparison would be to plot the data in the form of frequency curves. For Buford, these results are shown on **Figures 6.5** and **6.5**. The following observations can be made:

- While on average (i.e., in the vicinity of the 50% percentile), Buford precipitation is not expected to change significantly, the precipitation distribution is expected to "stretch" becoming wetter and drier than the historical climate. This assertion holds for both the A1b and A2 scenarios, with the latter stretching the distribution farther.
- Almost all future scenarios result in higher PET, evapotranspiration, and lower soil moisture storage. This effect is especially pronounced in dry years (falling below 75% of the distribution values).
- In the 15% wettest years, runoff is expected to be higher than historical. However, the rest of the future ensemble distributions portraits drier than historical runoff

conditions. Thus, the coming decades are likely to usher in more severe floods and droughts than those experienced in the past.

The previous results and conclusions are typical of all watersheds. However, they are based on frequency comparisons with all data. To examine the potential changes on a monthly basis, box plots of the historical and future scenarios were developed for each month of the year, watershed, climate scenario type (A1B or A2), and hydrologic process (precipitation, PET, soil moisture storage, and runoff). These plots are shown on **Figures 6.6** and **6.7** for the Buford watershed. In each figure, the historical box-plots are denoted "H1 through H12" while next to them are the future scenario box-plots denoted "F1 through F12." The future box-plots include data from all 13 future scenarios, while the historical box-plots include only historical data. These figures indeed show that climate change impacts are not uniform across the months of the year. More specifically, the following observations can be made:

- Mean watershed precipitation shows clear decline trends in June, July, and August, but it does not show any appreciable change for all other months of the year. However, the precipitation distributions for January through September are considerably extended (toward both ends) in comparison to the historical distributions. This relative change is observed on the A1B *and* the A2 scenarios.
- Future PET exhibits higher mean and wider range than historical PET from February to September, with the largest change observed in July and August. For these two months, the future mean PET is higher than the historical PET up to 12%, while the quartile range of the future distribution exceeds that of the historical by nearly 20%.

- Future soil moisture is clearly lower than historical in almost all months. The decline is more pronounced in late summer and the fall months and under A2 scenarios (about 6% - 10% decreasing).
- Future runoff at Buford is wetter (in the mean and the 75% percentile) than historical in February, March, and April, and drier than the historical in June, July, August, and September under A1B scenarios. In comparison, the future Buford runoff is drier in all months under the A2 scenarios.

Similar plots are also provided for the Woodruff-Bainbridge watershed in **Figures 6.26** and **6.27**. The results support the following findings:

- Mean watershed precipitation of the Woodruff-Bainbridge exhibits a decreasing trend for early spring (January, February, and March) and summer (June, July and August) of about 4% - 9% (A1B and A2). In comparison, the Buford watershed does not show such significant trends in early spring.
- Future PET of the Woodruff-Bainbridge watershed exhibits higher mean and wider range than historical PET with the largest change observed in July and August. For these two months, the future PET is higher than the historical PET up to 15% (under A2 scenarios). This increasing trend is somewhat larger than that of the Buford watershed.
- Future soil moisture of the Woodruff-Bainbridge watershed is lower than historical in most months. This change is more pronounced for summer and fall, and the decreasing percentage is larger than the Buford watershed. The average soil moisture reduction reaches up to 11% (under A2 scenarios). Even more critical is the significant decline of the future low soil moisture levels (as indicators of agricultural droughts). Summer months are particularly impacted in the southern watersheds where soil moisture

is critical for agriculture. The adverse implications of this finding cannot be over-emphasized for Georgia's economy.

- In the Woodruff-Bainbridge watersheds (and Albany watershed), noticeable mean runoff reductions begin in January and extend through July under both the A1B and A2 scenarios. Generally, under the A2 scenarios, future runoff shows more reductions than under the A1B scenarios. Under A2 scenarios and in spring and early summer months, the mean runoff reduction is 9 -16% (which is a more severe reduction than at Buford). Under the A2 scenarios and in late summer and fall months, the runoff reduction is about 6% - 16% (which is somewhat larger than at Buford).
- In summary, the Woodruff-Bainbridge watershed is expected to experience more severe precipitation, soil moisture, and runoff impacts than the Buford watershed. Similar conclusions are also observed for Albany. These findings imply that climate change impacts intensify for the southern ACF watersheds.

Similar results are shown in **Figure 6.8** through **Figure 6.27** for other ACF watersheds (West Point, George, Montezuma, Albany and Woodruff-Bainbridge).

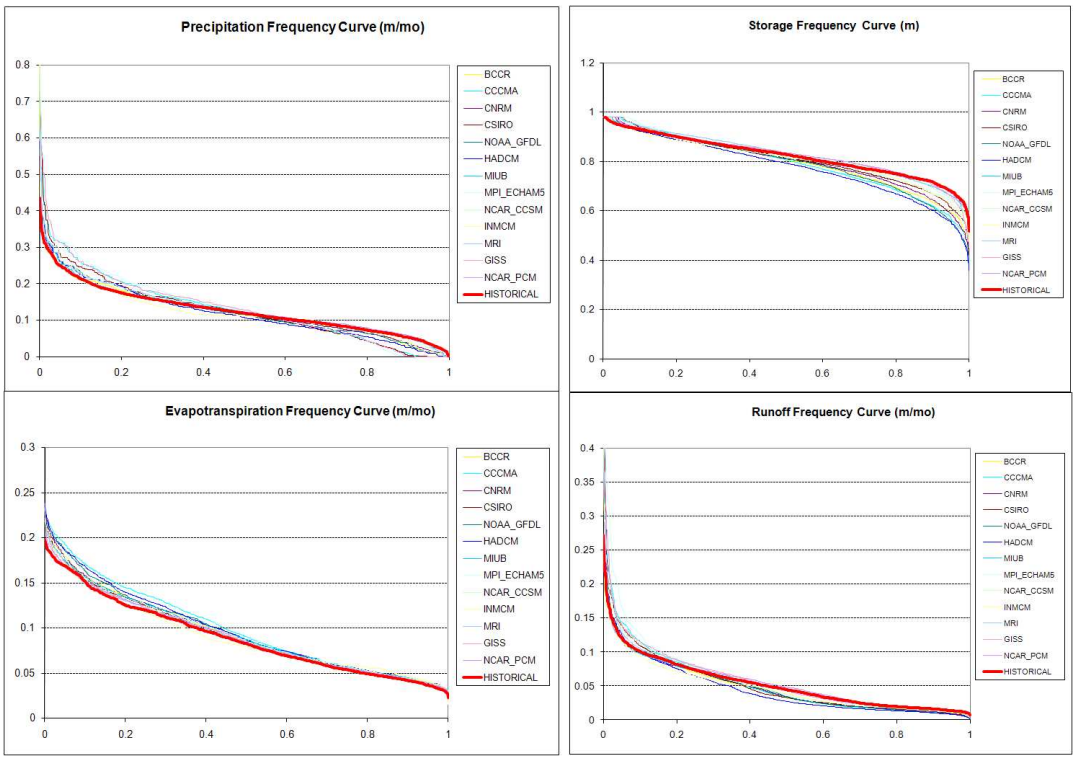

Figure 6.4: A1B Climate Scenarios (2000-2099), Buford, Frequency Curves.

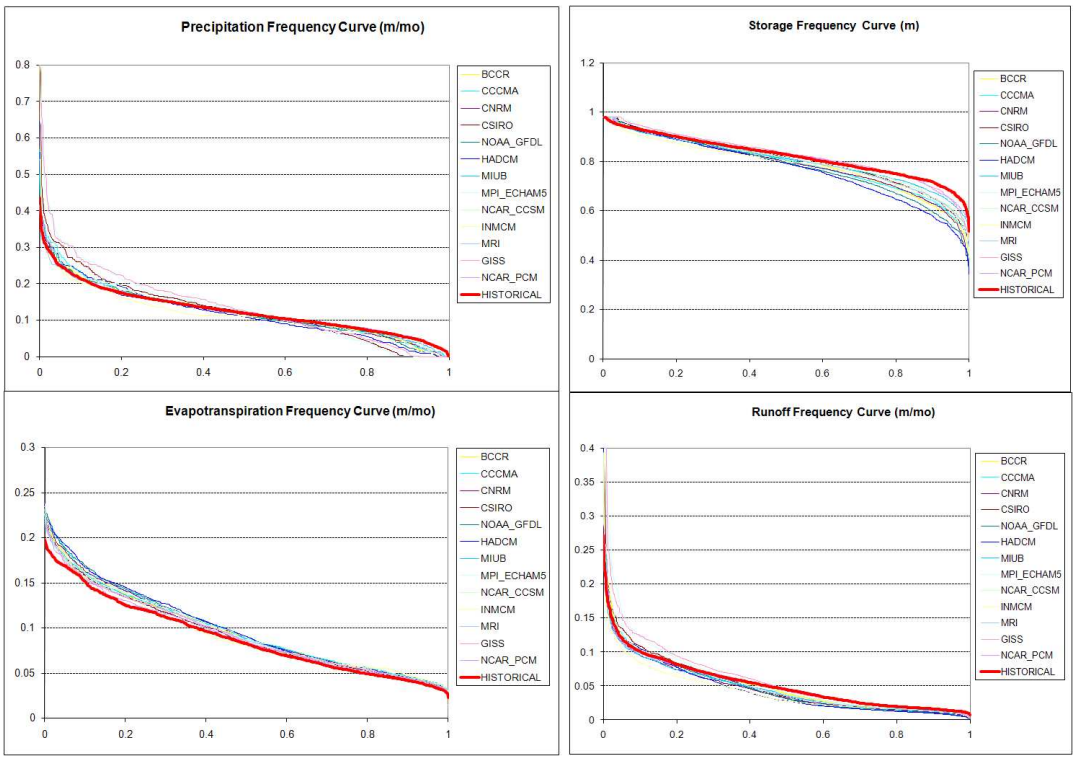

Figure 6.5: A2 Climate Scenarios (2000-2099), Buford, Frequency Curves.

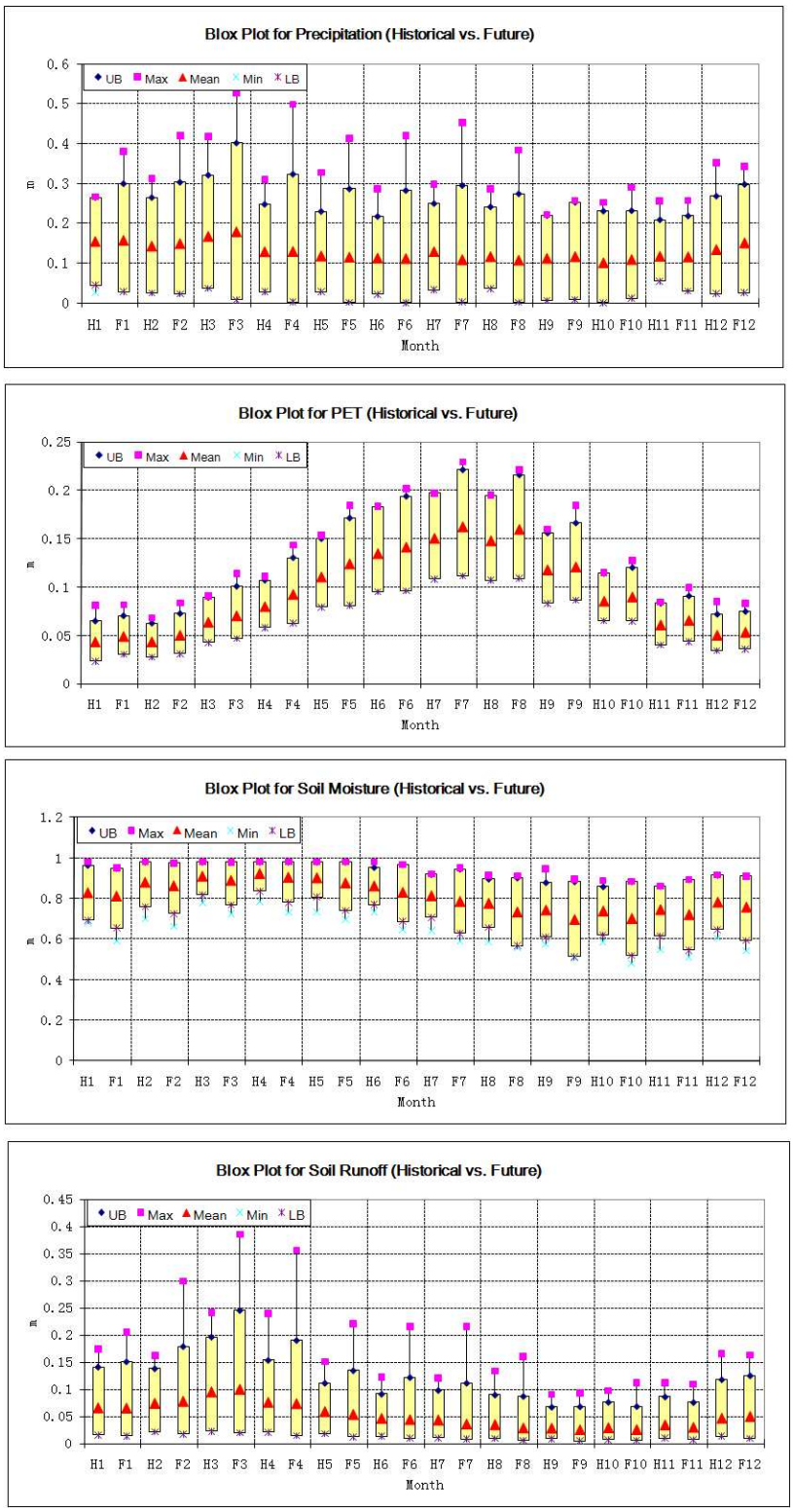

Figure 6.6: Monthly Historical vs. Future (A1B) Watershed Response, Buford. (Unit: Precipitation – m/mo; PET – m/mo; Soil Moisture – m; Runoff m/mo.)

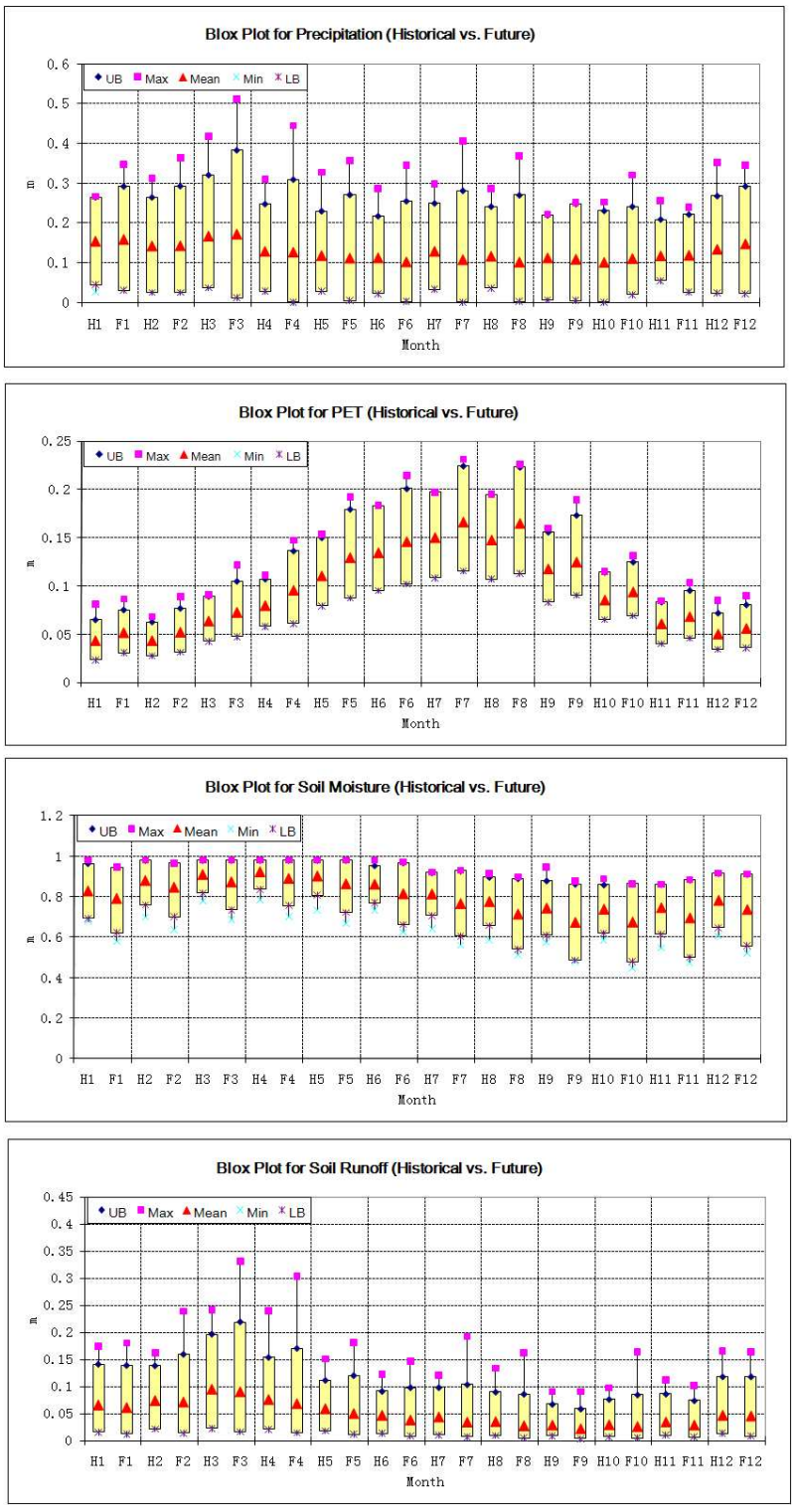

Figure 6.7: Monthly Historical vs. Future (A2) Watershed Response, Buford. (Unit: Precipitation – m/mo; PET – m/mo; Soil Moisture – m; Runoff m/mo.)

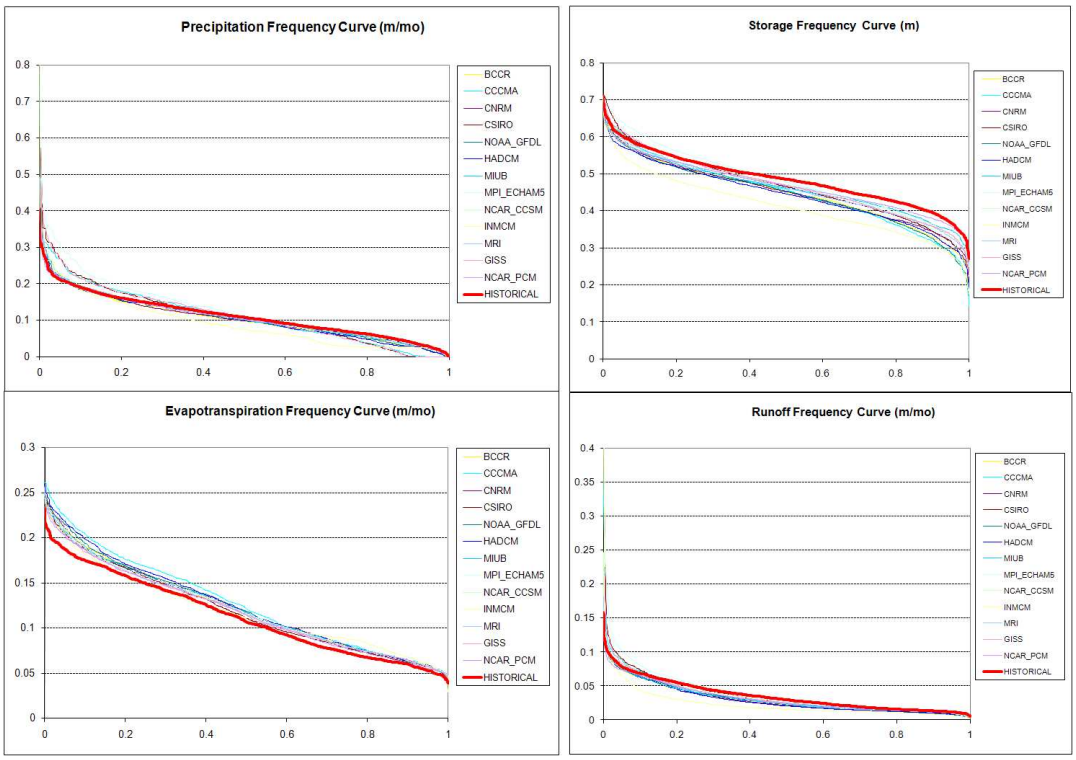

Figure 6.8: A1B Climate Scenarios (2000-2099), West Point, Frequency Curves.

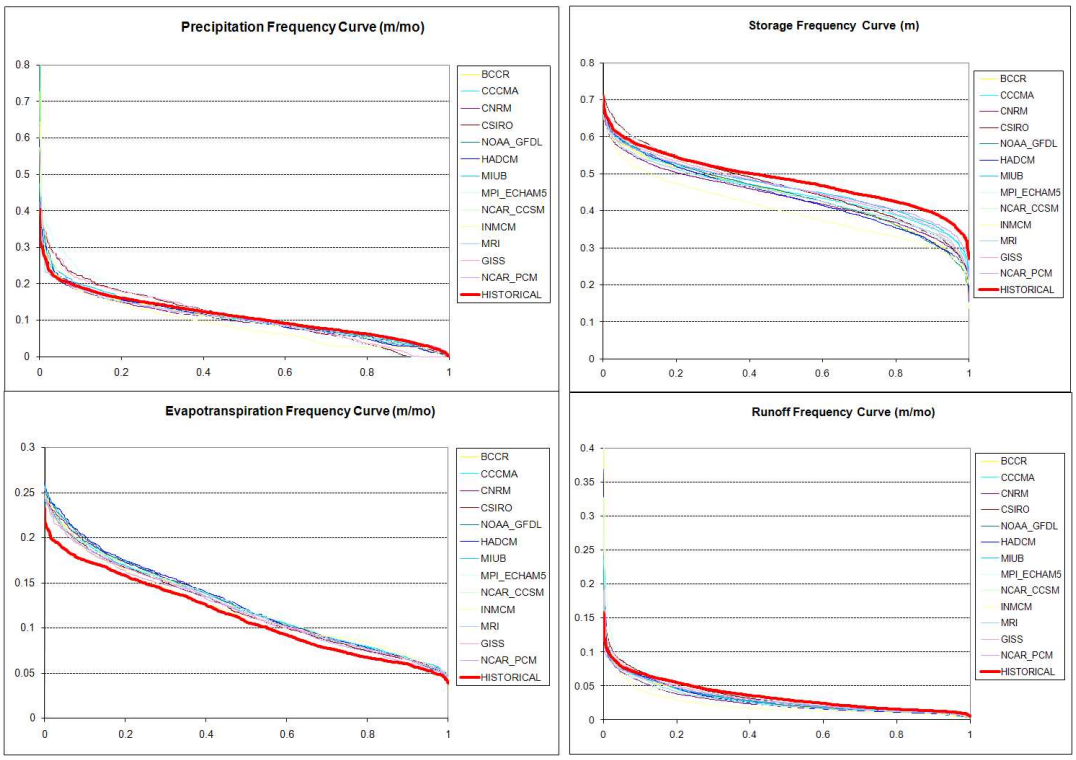

Figure 6.9: A2 Climate Scenarios (2000-2099), West Point, Frequency Curves.

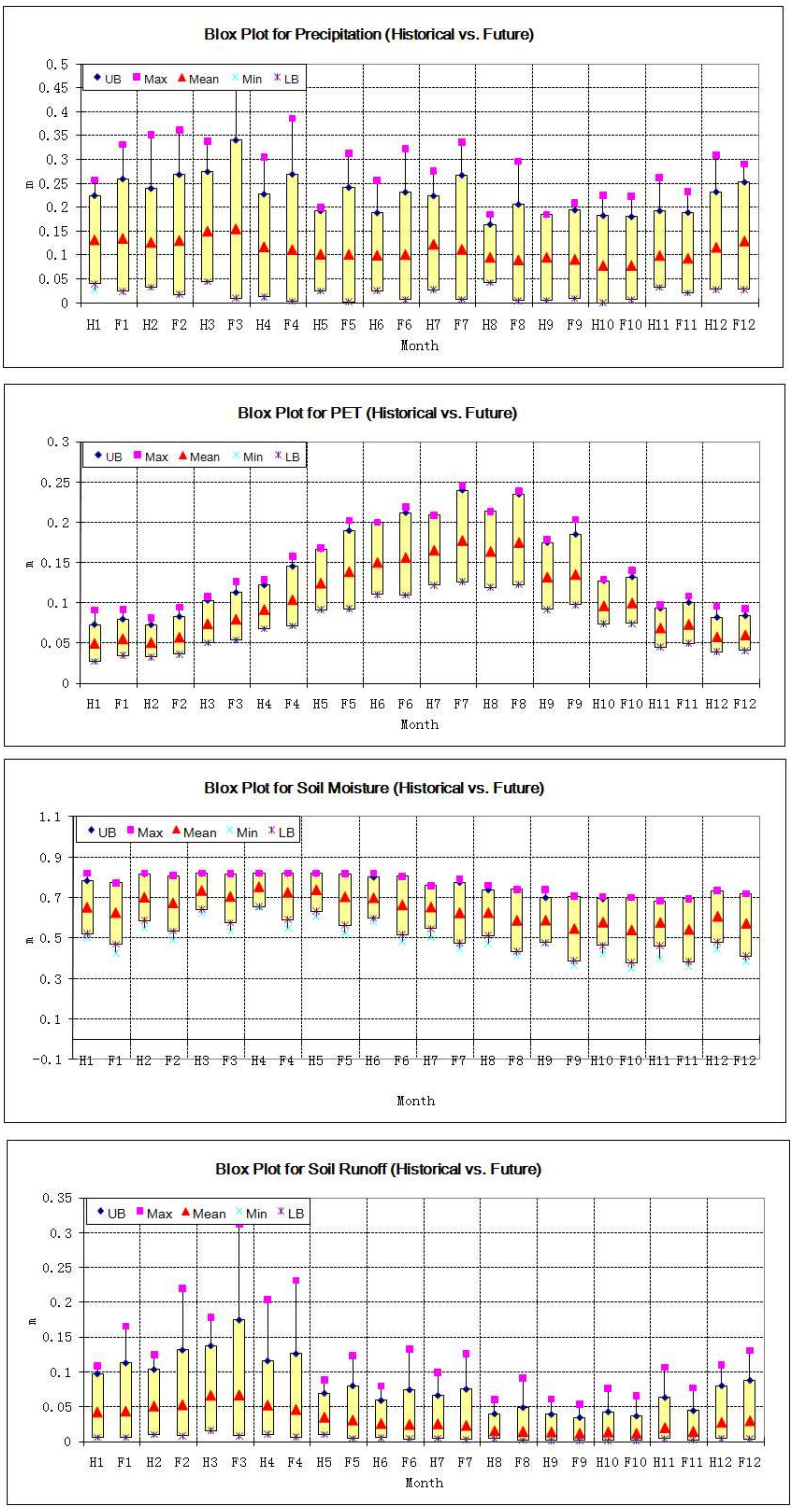

Figure 6.10: Monthly Historical vs. Future (A1B) Watershed Response, West Point.

(Unit: Precipitation – m/mo; PET – m/mo; Soil Moisture – m; Runoff m/mo.)

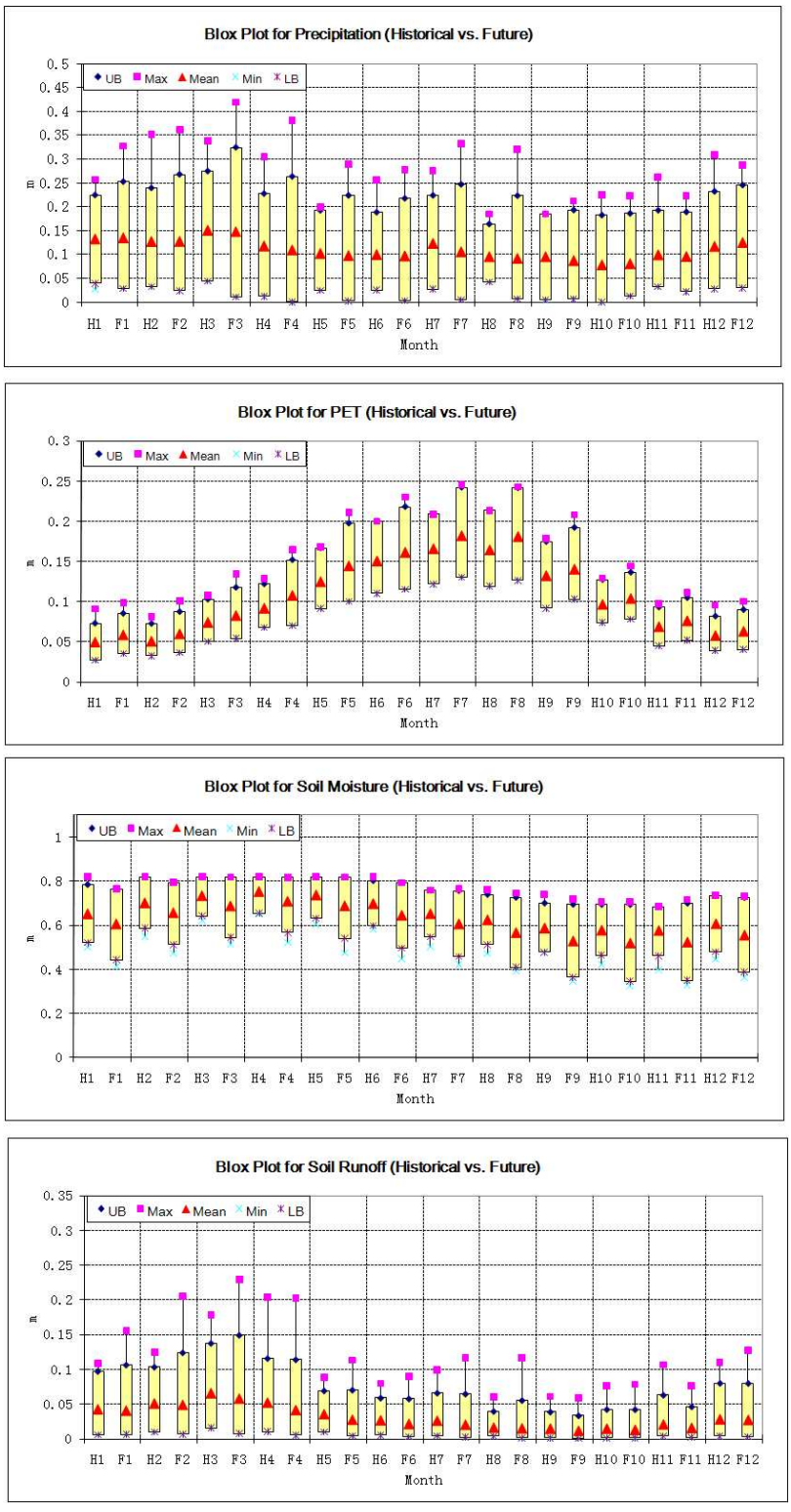

Figure 6.11: Monthly Historical vs. Future (A2) Watershed Response, West Point. (Unit: Precipitation – m/mo; PET – m/mo; Soil Moisture – m; Runoff m/mo.)

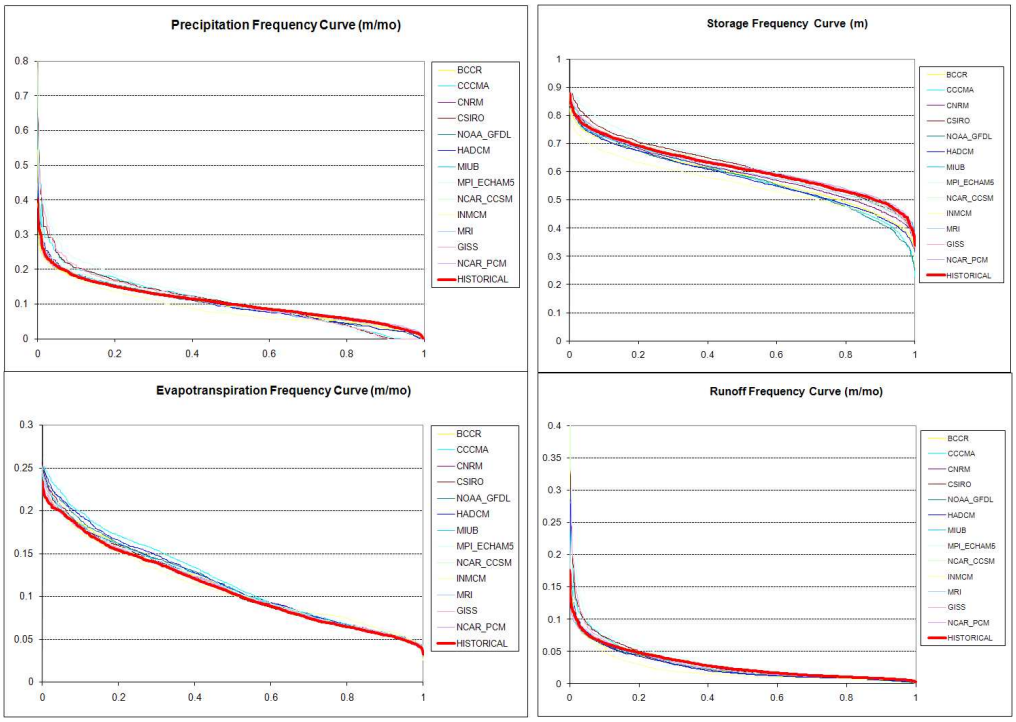

Figure 6.12: A1B Climate Scenarios (2000-2099), W.F. George, Frequency Curves.

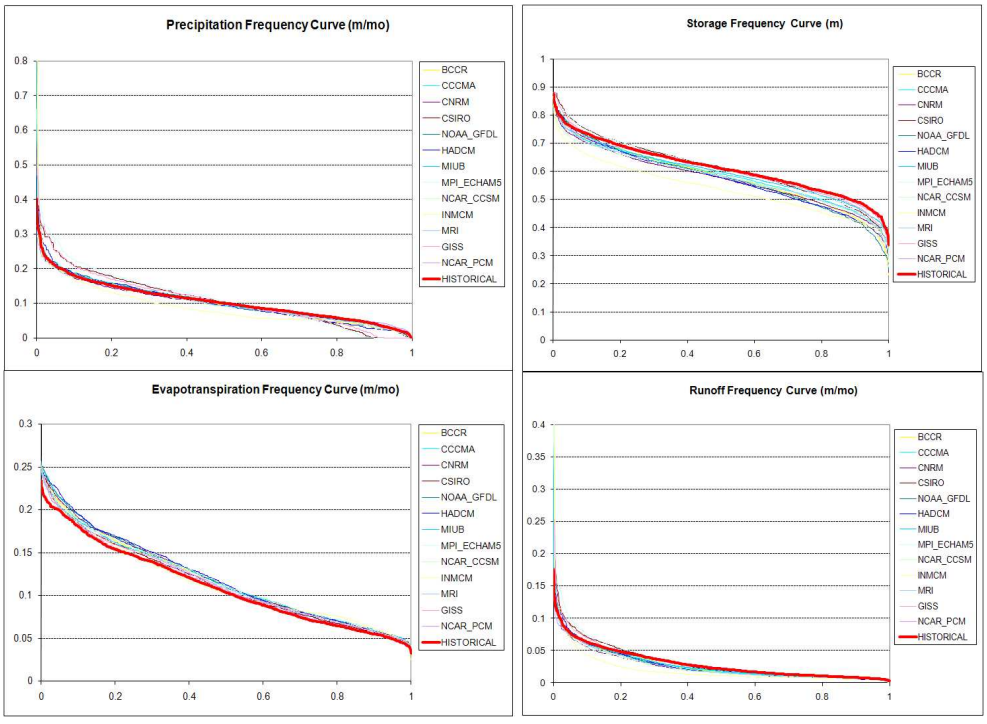

Figure 6.13: A2 Climate Scenarios (2000-2099), W.F. George, Frequency Curves.

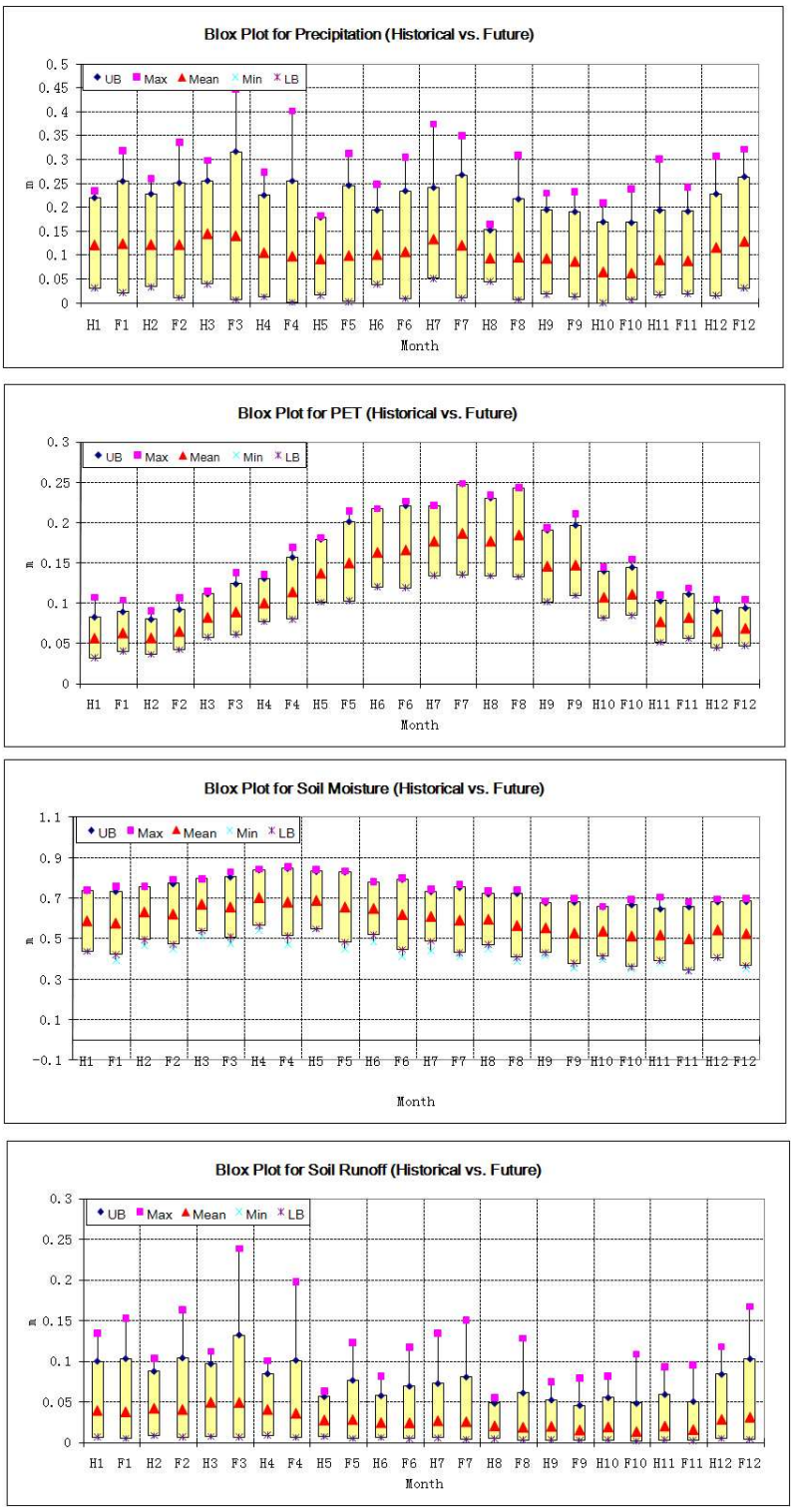

Figure 6.14: Monthly Historical vs. Future (A1B) Watershed Response, W.F. George.

(Unit: Precipitation – m/mo; PET – m/mo; Soil Moisture – m; Runoff m/mo.)

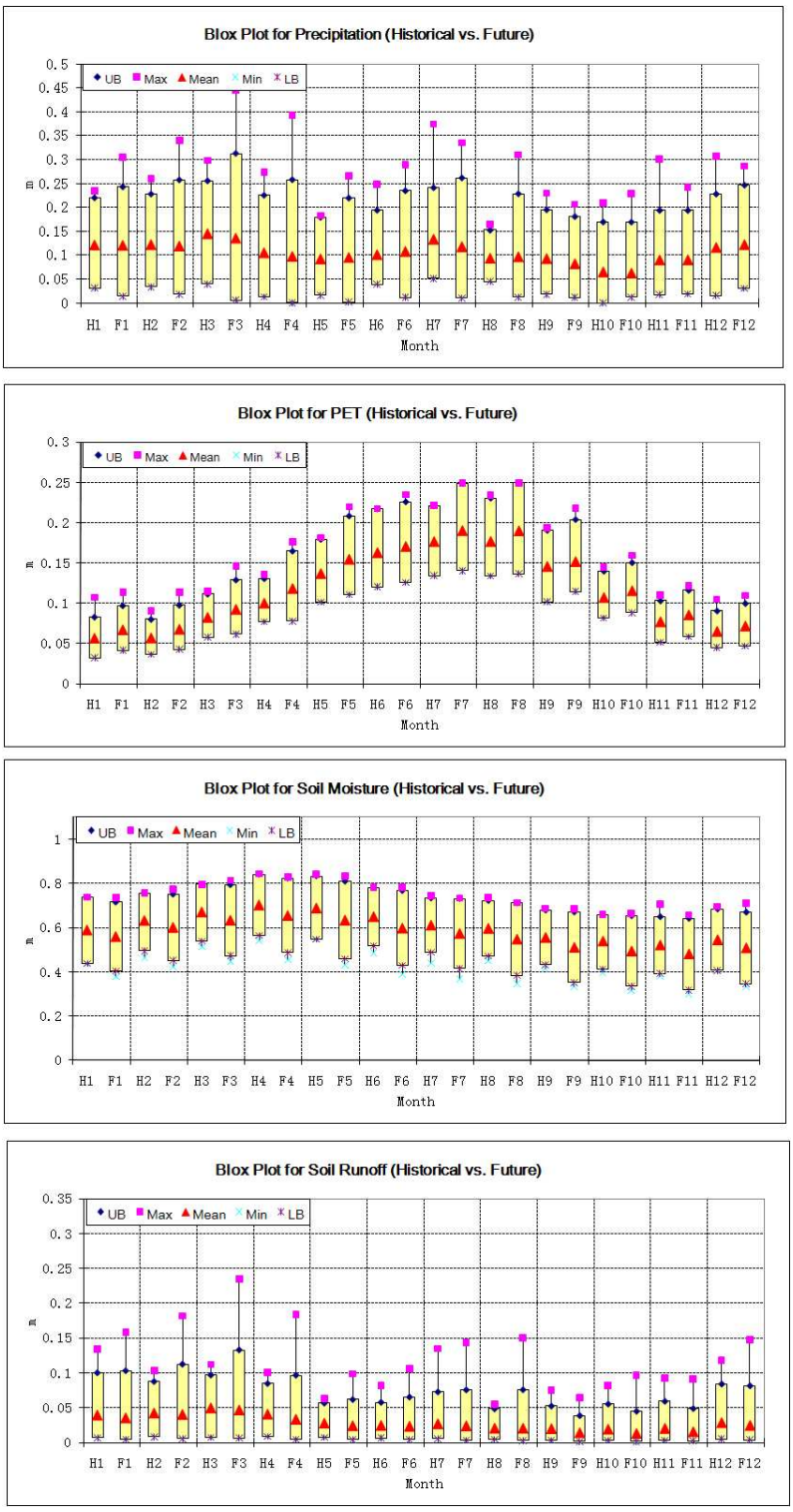

Figure 6.15: Monthly Historical vs. Future (A2) Watershed Response, W.F. George.

(Unit: Precipitation – m/mo; PET – m/mo; Soil Moisture – m; Runoff m/mo.)

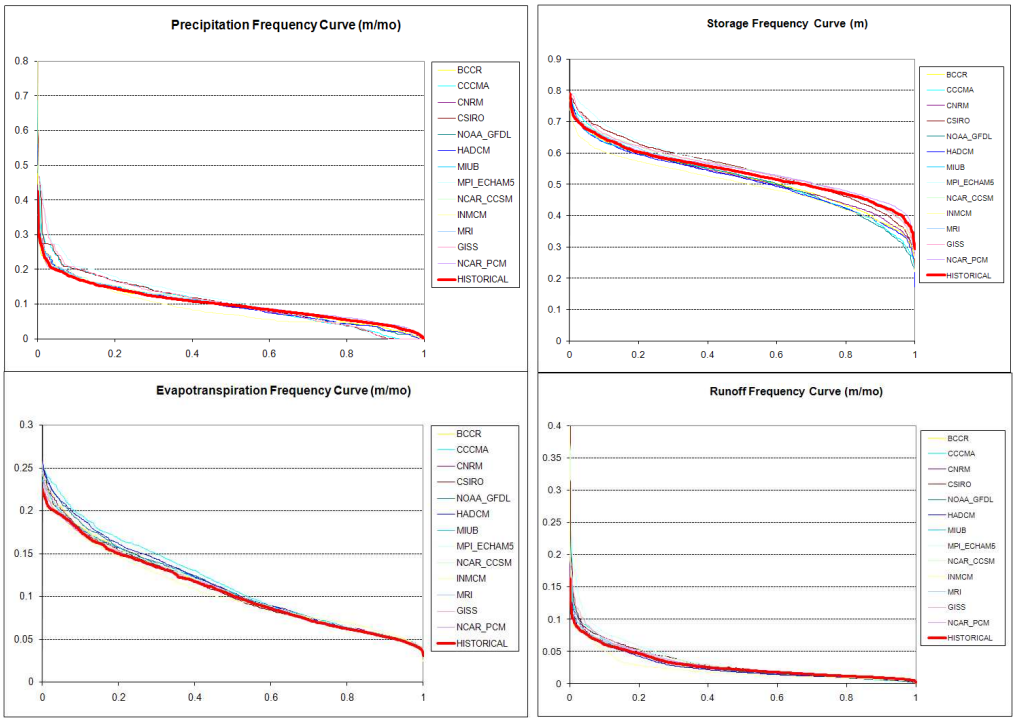

Figure 6.16: A1B Climate Scenarios (2000-2099), Montezuma, Frequency Curves

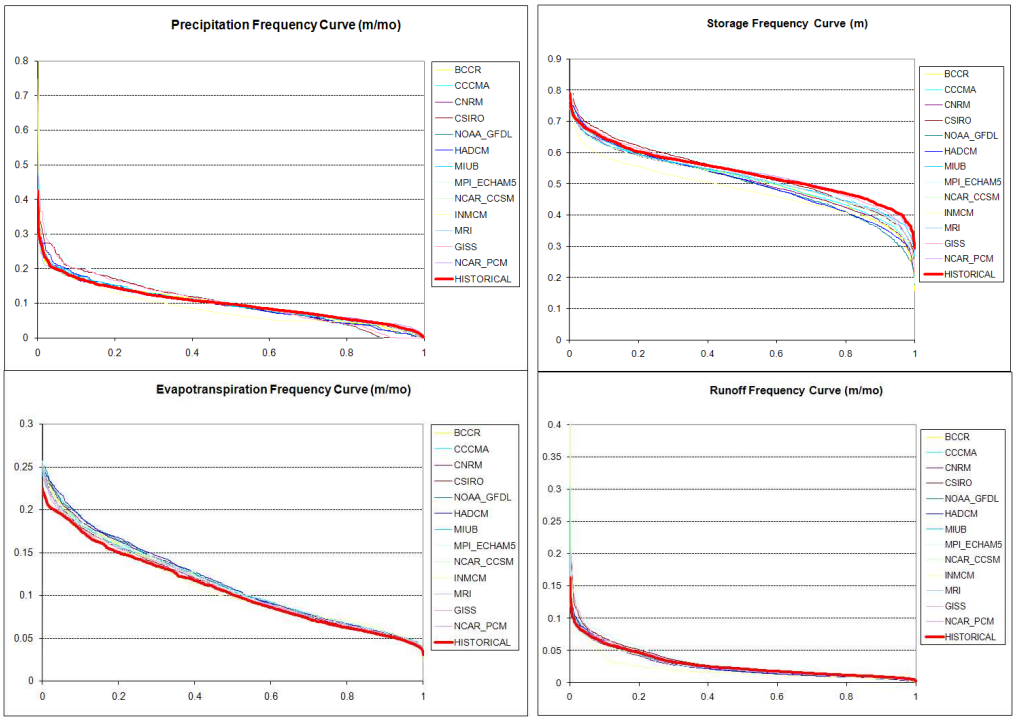

Figure 6.17: A2 Climate Scenarios (2000-2099), Montezuma, Frequency Curves.

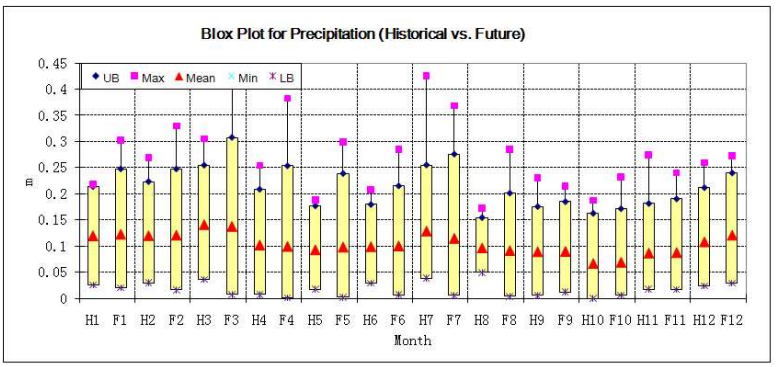

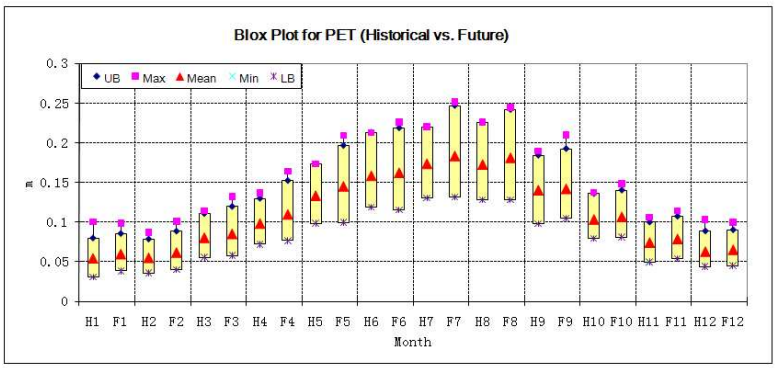

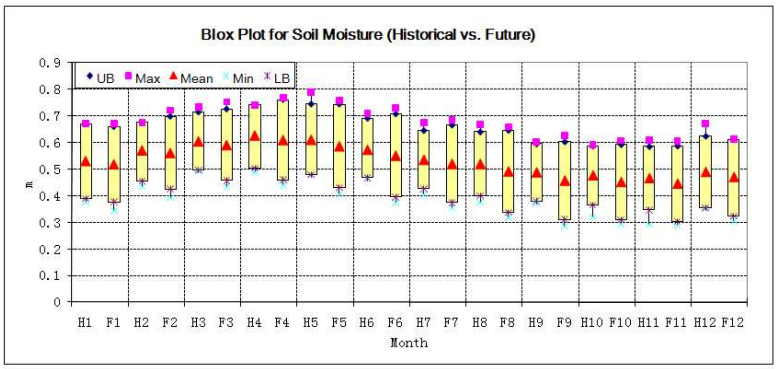

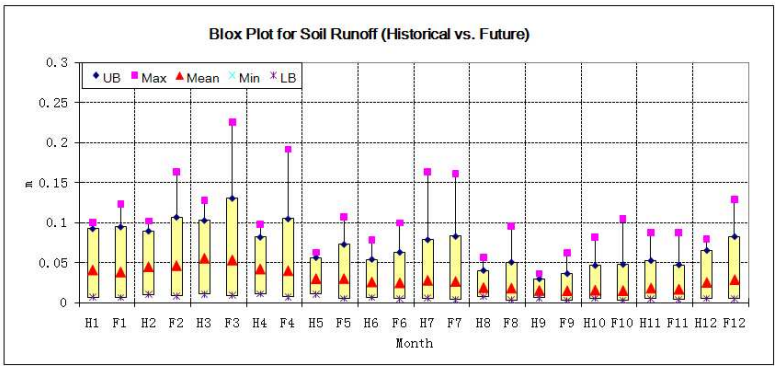

Figure 6.18: Monthly Historical vs. Future (A1B) Watershed Response, Montezuma.

(Unit: Precipitation – m/mo; PET – m/mo; Soil Moisture – m; Runoff m/mo.)

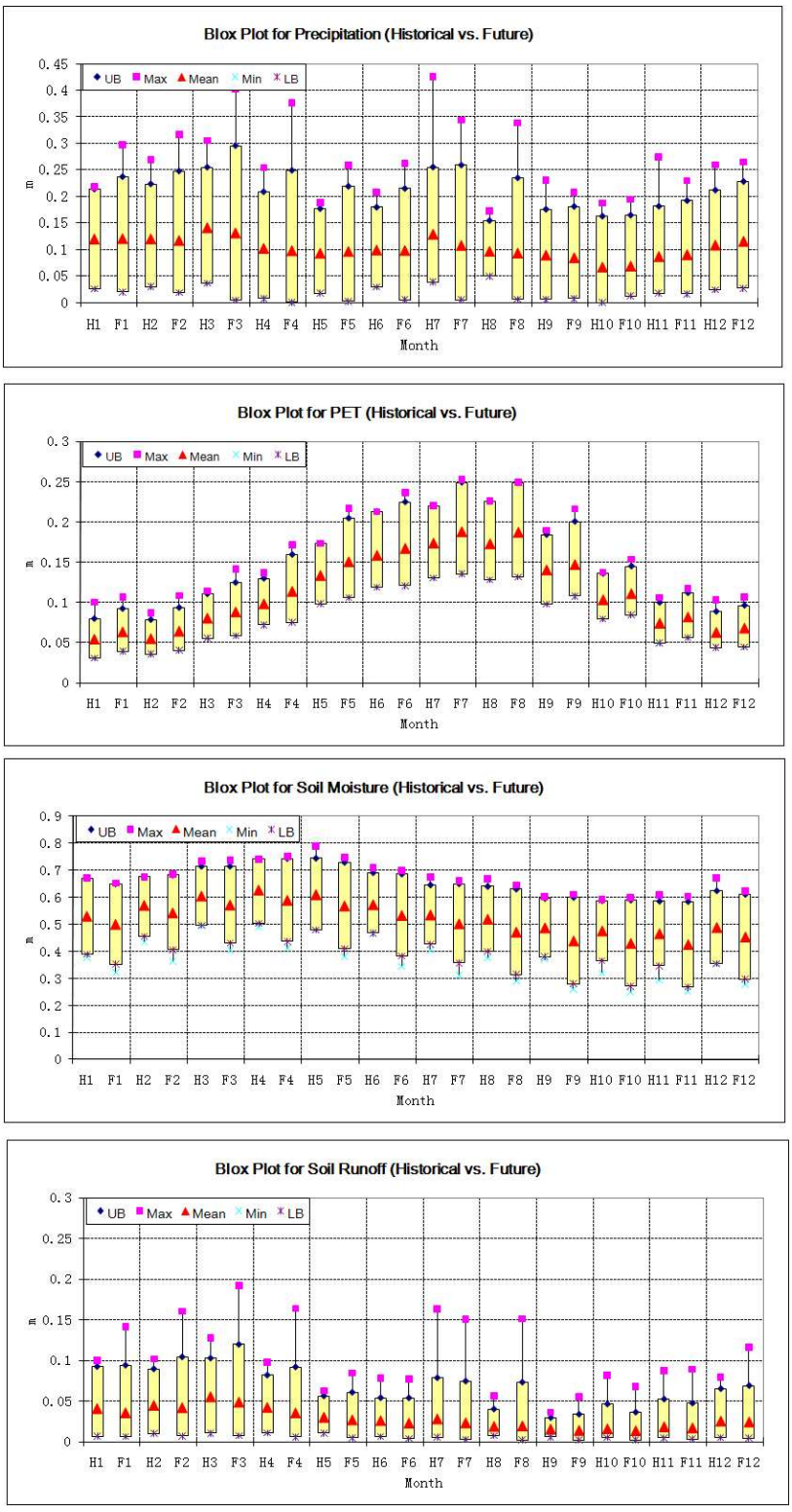

Figure 6.19: Monthly Historical vs. Future (A2) Watershed Response, Montezuma.

(Unit: Precipitation – m/mo; PET – m/mo; Soil Moisture – m; Runoff m/mo.)

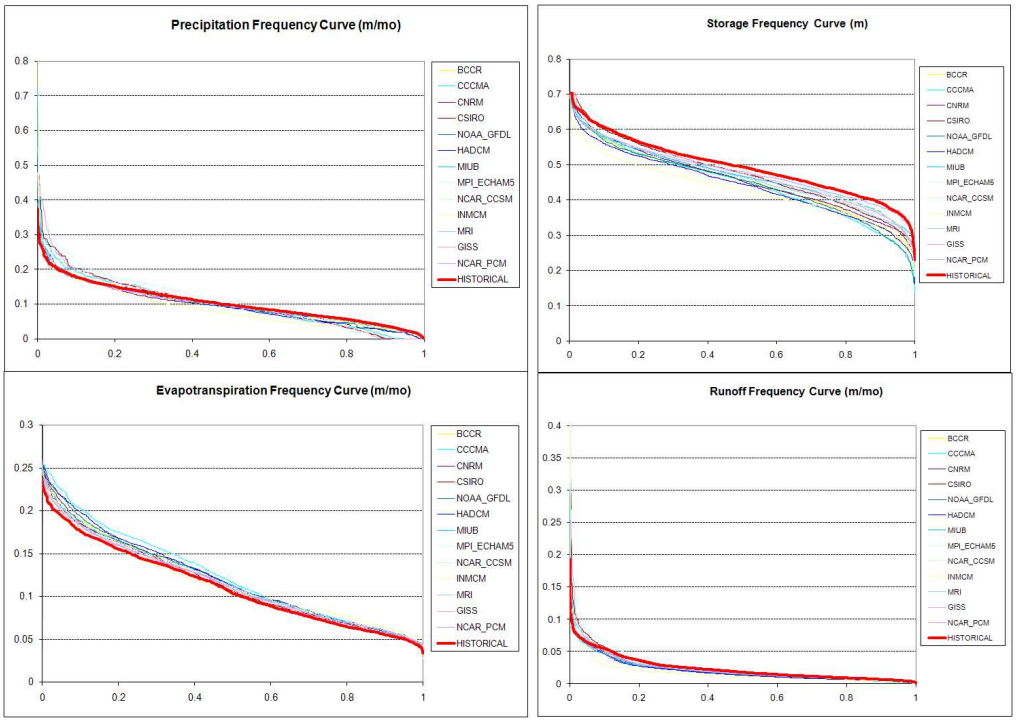

Figure 6.20: A1B Climate Scenarios (2000-2099), Albany, Frequency Curves.

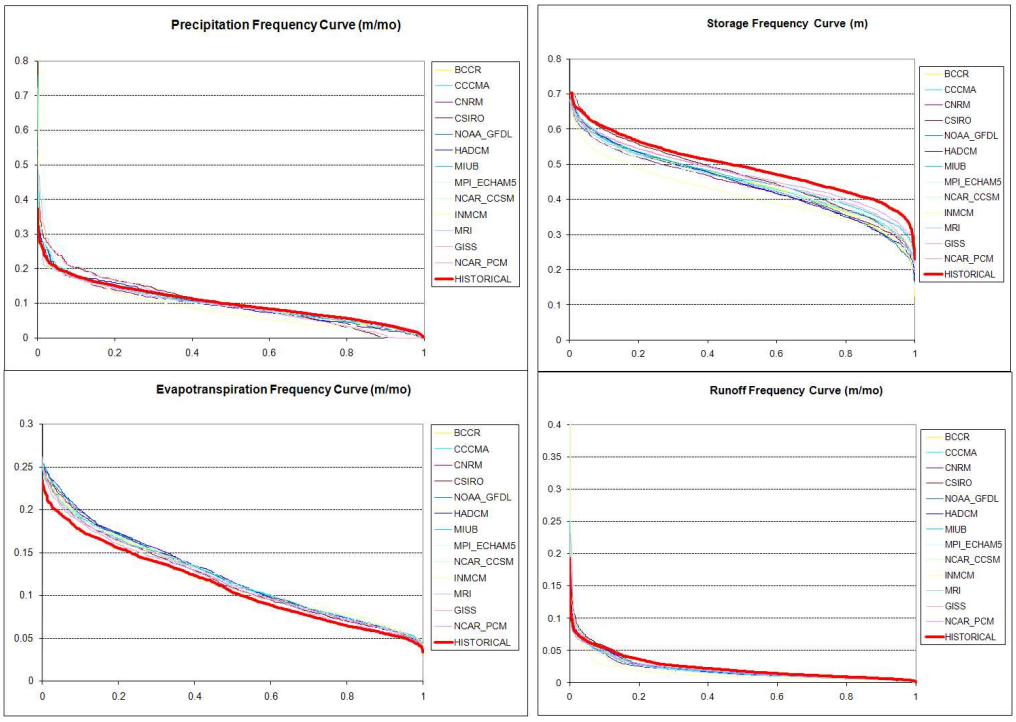

Figure 6.21: A2 Climate Scenarios (2000-2099), Albany, Frequency Curves.

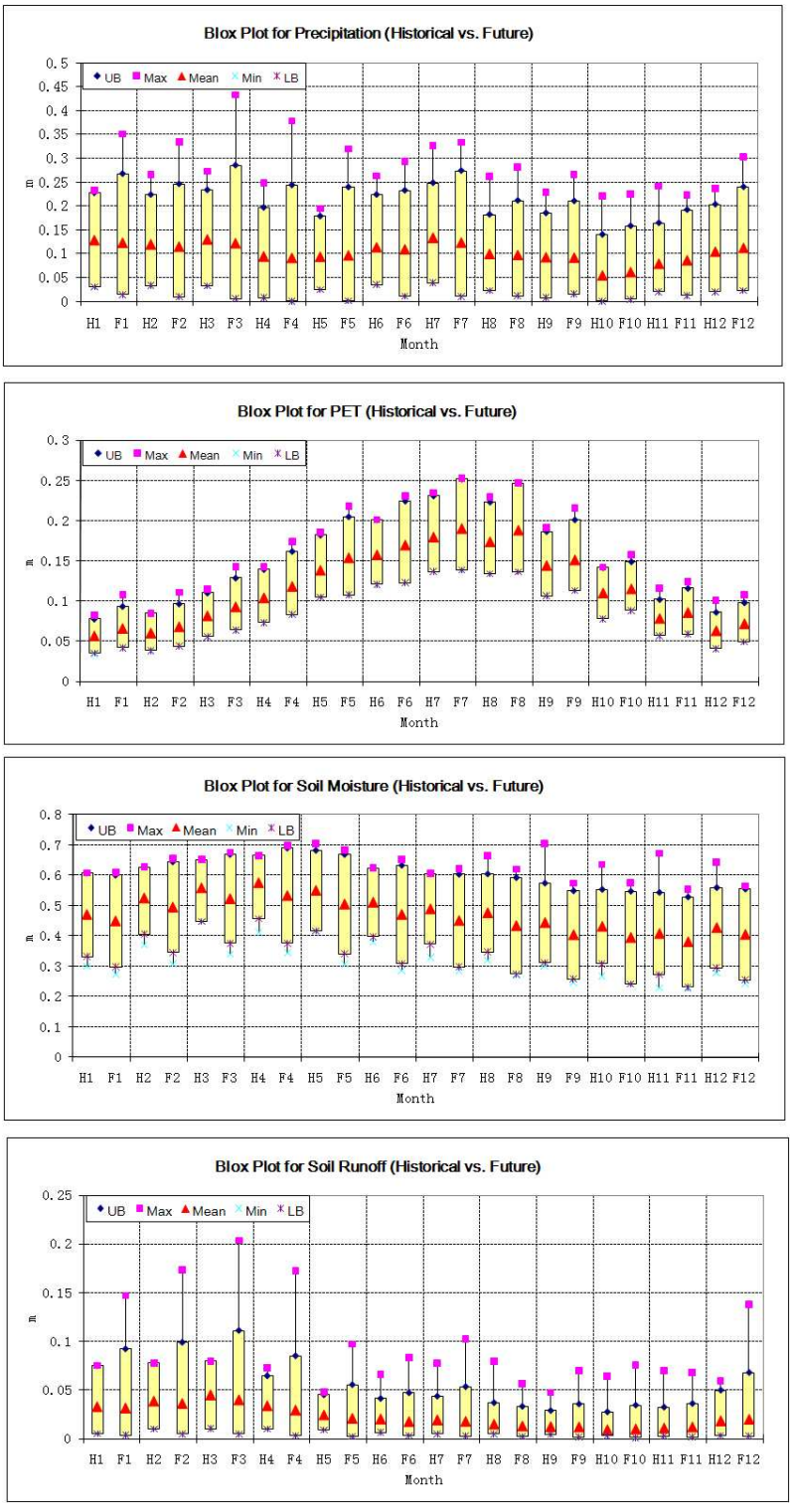

Figure 6.22: Monthly Historical vs. Future (A1B) Watershed Response, Albany. (Unit: Precipitation – m/mo; PET – m/mo; Soil Moisture – m; Runoff m/mo.)

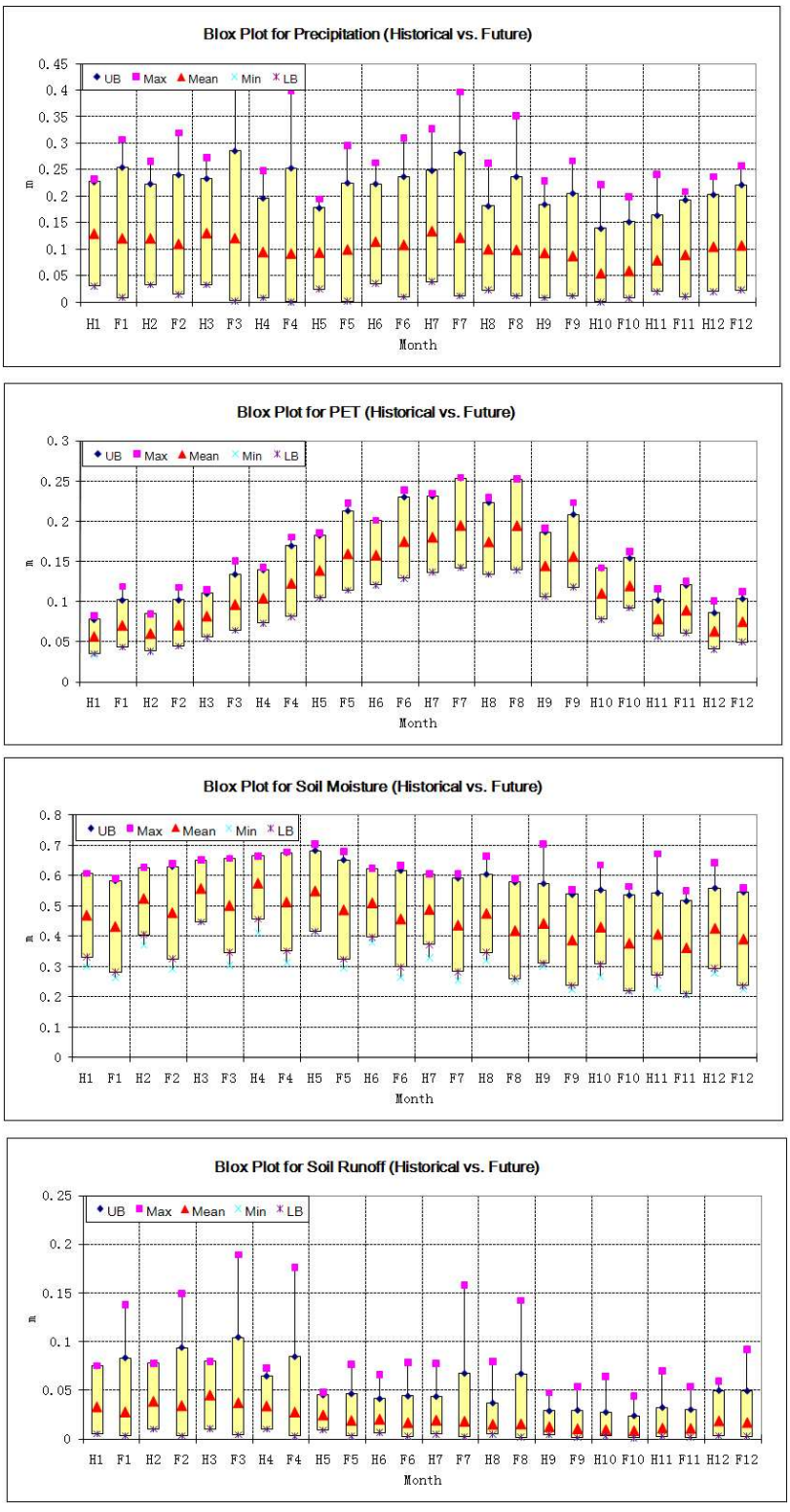

Figure 6.23: Monthly Historical vs. Future (A2) Watershed Response, Albany. (Unit: Precipitation – m/mo; PET – m/mo; Soil Moisture – m; Runoff m/mo.)

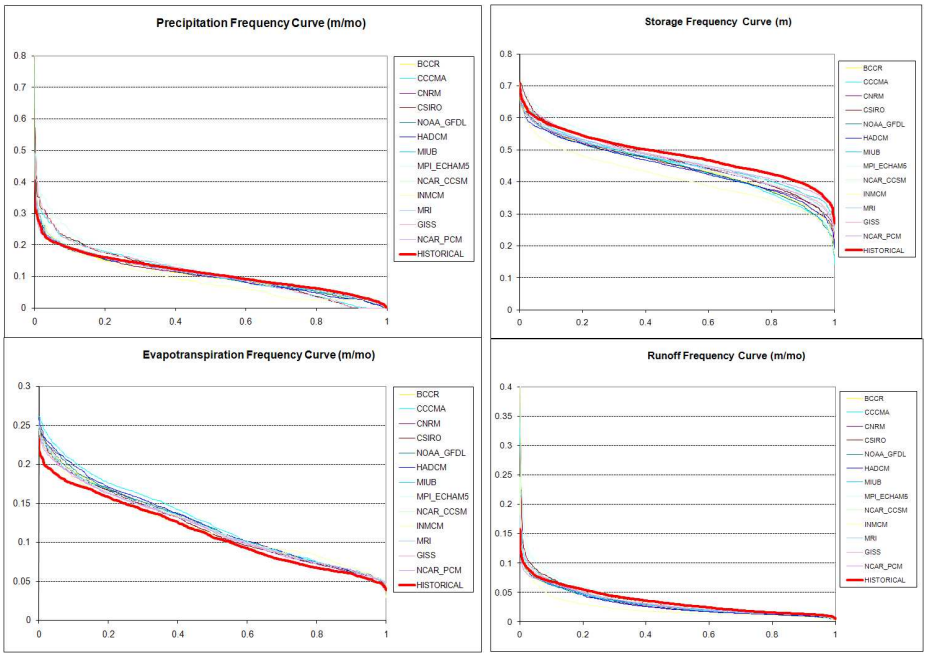

Figure 6.24: A1B Climate Scenarios (2000-2099), Woodruff-Bainbridge, Frequency.

Curves

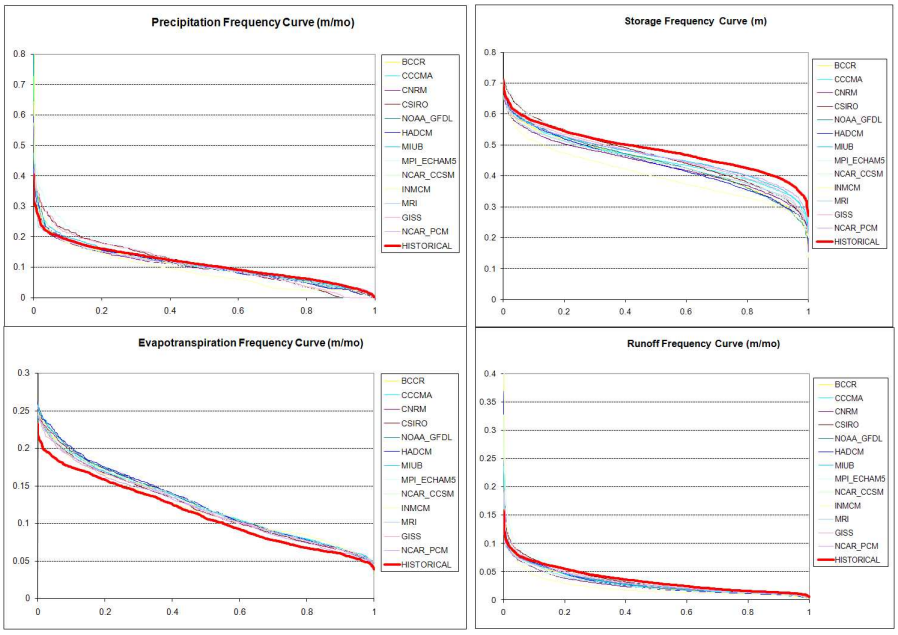

Figure 6.25: A2 Climate Scenarios (2000-2099), Woodruff-Bainbridge, Frequency.

Curves

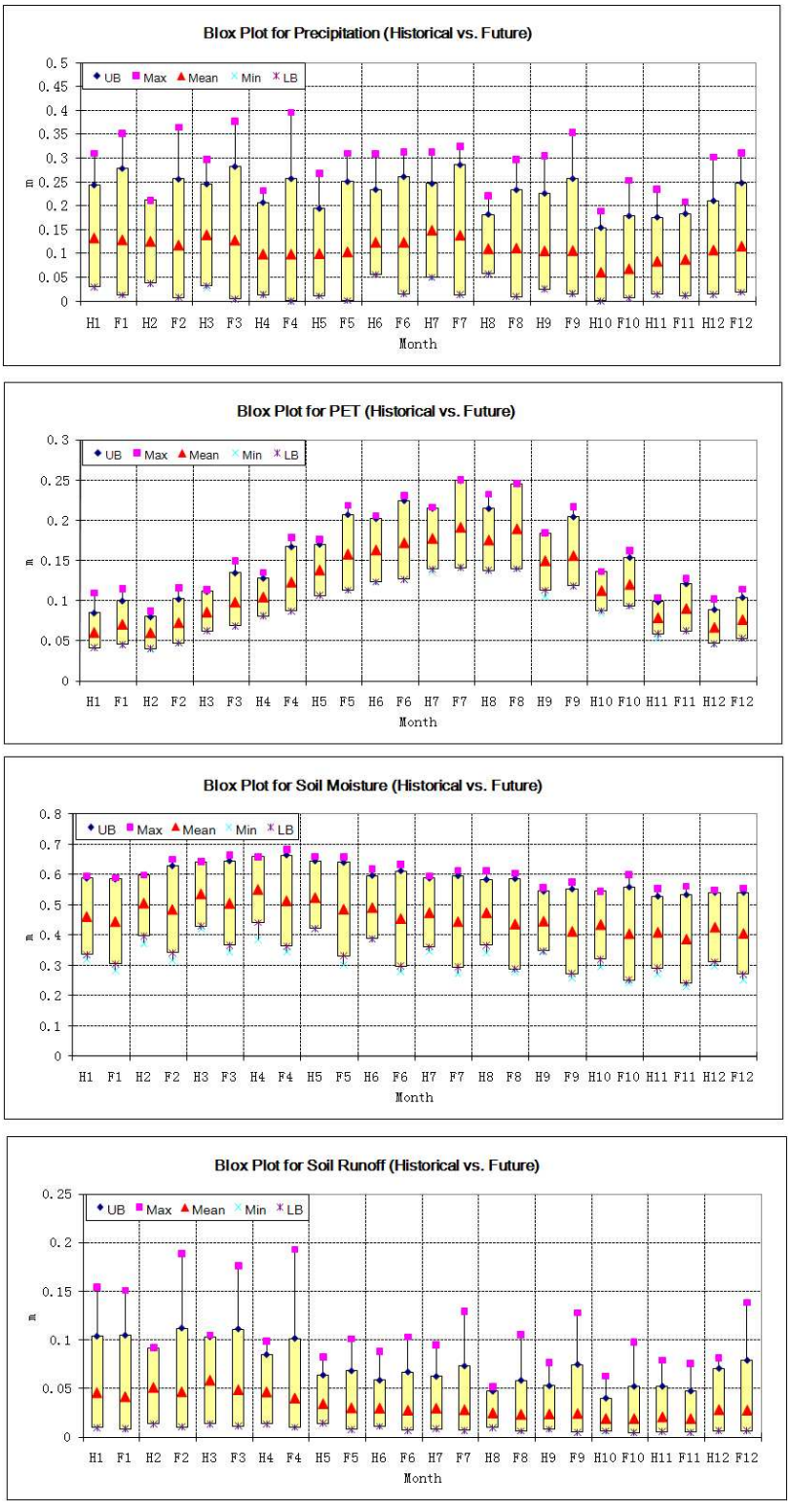

Figure 6.26: Monthly Historical vs. Future (A1B) Watershed Response, Woodruff-Bainbridge. (Unit: Precipitation – m/mo; PET – m/mo; Soil Moisture – m; Runoff m/mo.)

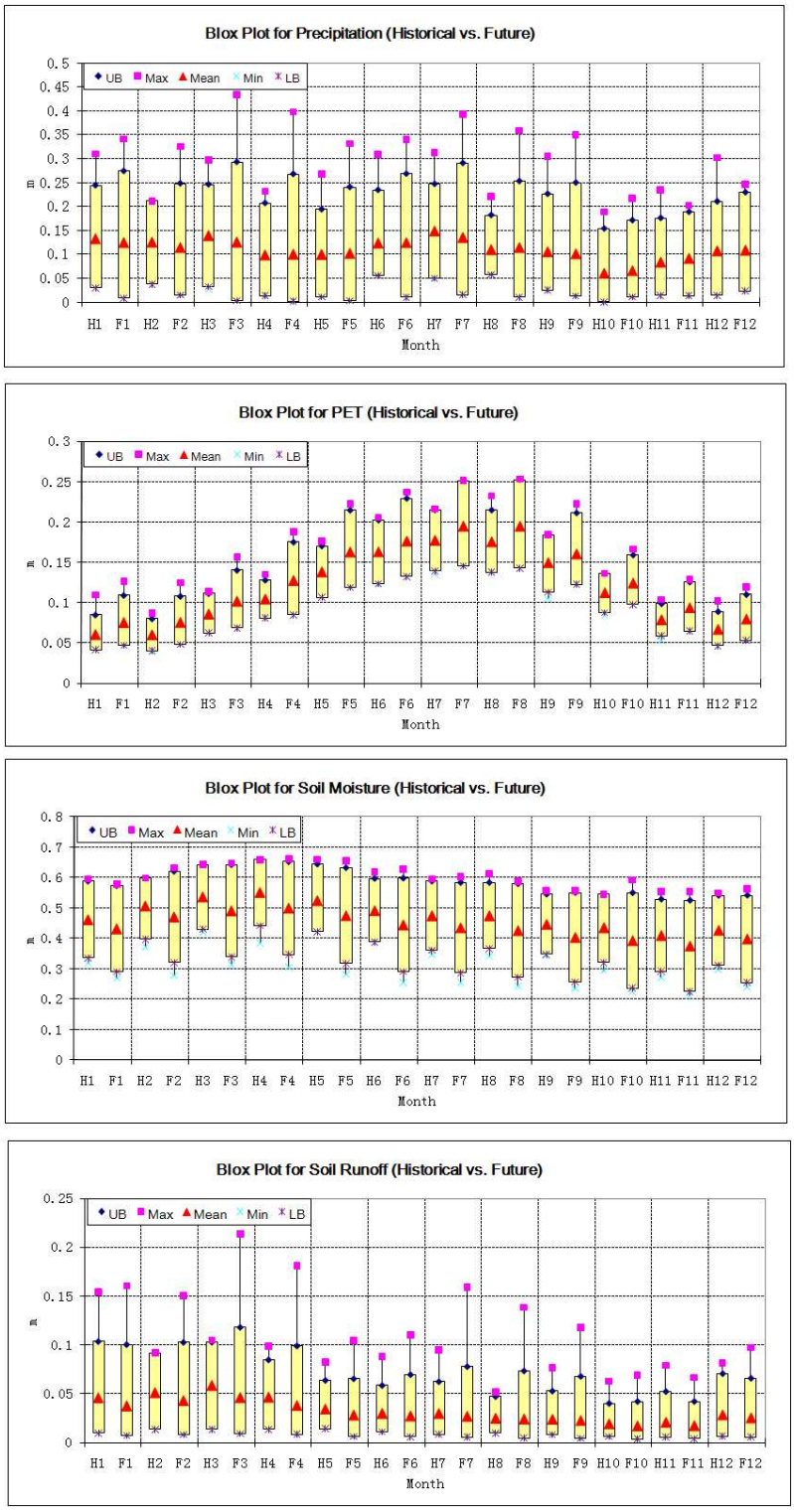

Figure 6.27: Monthly Historical vs. Future (A2) Watershed Response, Woodruff-Bainbridge. (Unit: Precipitation – m/mo; PET – m/mo; Soil Moisture – m; Runoff m/mo.)

6.2 Historical (Baseline) and Future Hydrologic Assessments for the OOA Basin

6.2.1 Historical Assessment

The historical assessment is based on observed climatic data for the period 1901 through 2009 and follows the same process described in **Section 6.1.1**. The results are also presented in a similar form.

The OOA basin watersheds are shown in **Figure 6.28**. For fiveOOA watersheds, namely, the upper Oconee watershed (Milledgeville), upper Ocmulgee watershed (Macon), lower Oconee watershed (Dublin), lower Ocmulgee watershed (Lumber, and Altamaha watershed (Doctortown), **Figure 6.29** presents the input and output sequences (normalized by their means). The results support the following observations:

- OOA basin precipitation shows a mild increasing long-term trend for all watersheds (**Figure 6.29a**; **Table 6.2**). Over the 109-year assessment period, the increase is about 1% - 3% of the early 20th century value. The drought periods coincide with those of the ACF basin (e.g., early 1940's, 1050's, 1980's 1998-2002, and 2006-2008).
- Watershed potential evapotranspiration of the entire OOA basin shows a mild decreasing long-term trend (**Figure 6.29b**; **Table 6.2**). Over the 109-year assessment period, the decrease is approximately 1% - 5% of the early 20th century value. The lower Oconee watershed experiences the largest PET decrease (~5%), and the Altamaha watershed the lowest (~1%). The inter-annual PET variability is much less than that of precipitation (up to 10% of normal).
- Total soil moisture storage shows an increasing long-term trend (**Figure 6.29d**; **Table 6.2**) of about 2% - 5% over the 109-year assessment period.

- The changes of the actual evapotranspiration are relatively small (**Figure 6.29c**) and depend on the changes of both watershed soil moisture and PET. The actual evapotranspiration increases very mildly (0.2% - 0.4%) over the 109-year assessment period.
- Total runoff exhibits an increasing trend of approximately 5% - 7% over the 109-year assessment period (**Figure 6.29e**; **Table 6.2**) for the entire OOA basin. The Altamaha river flows increase little slower than Oconee River and Ocmulgee River. Across the OOA watersheds, the ratio of total annual average runoff to annual average precipitation is between 0.26 – 0.37, distinctly decreasing from upstream (northwest) to downstream (southeast).
- Lastly, the above historical analysis is also performed for the most recent 50 years (1960-2009). It can be seen from **Figure 6.30** and **Table 6.2** that during this period *(1)* precipitation exhibits a declining trend of about 6% - 16%; *(2)* PET exhibits an increasing trend of about 1% - 3% (contrary to the corresponding 109 year trends); *(3)* precipitation decreases much faster in the upper watersheds than the lower river watersheds; *(4)* soil moisture and runoff decline in the entire OOA basin; *(5)* runoff decreases by 15% to 20% in the downstream watersheds and by 25% - 28% in the upstream watersheds.
- A comparison of the historical assessments for the OOA and ACF basins shows that their responses are fairly similar. Most notably, in the last 50 years, *(1)* precipitation in all OOA and ACF watersheds decreases significantly; *(2)* PET increases (except for George watershed); and *(3)* total runoff decreases. While the actual rates of change vary, this observation implies that this response is a regional characteristic of the southeast US

and is not particular to a specific basin. This conclusion will be revisited/verified in subsequent sections presenting assessments of other Georgia basins.

Figure 6.28: Map of OOA Watersheds: Upper Ocmulgee River (Macon), Upper Oconee River (Milledgeville), Lower Ocmulgee River (from Macon to Lumber), Lower Oconee River (from Milledgeville to Dublin), and Altamaha River (down to Doctortown).

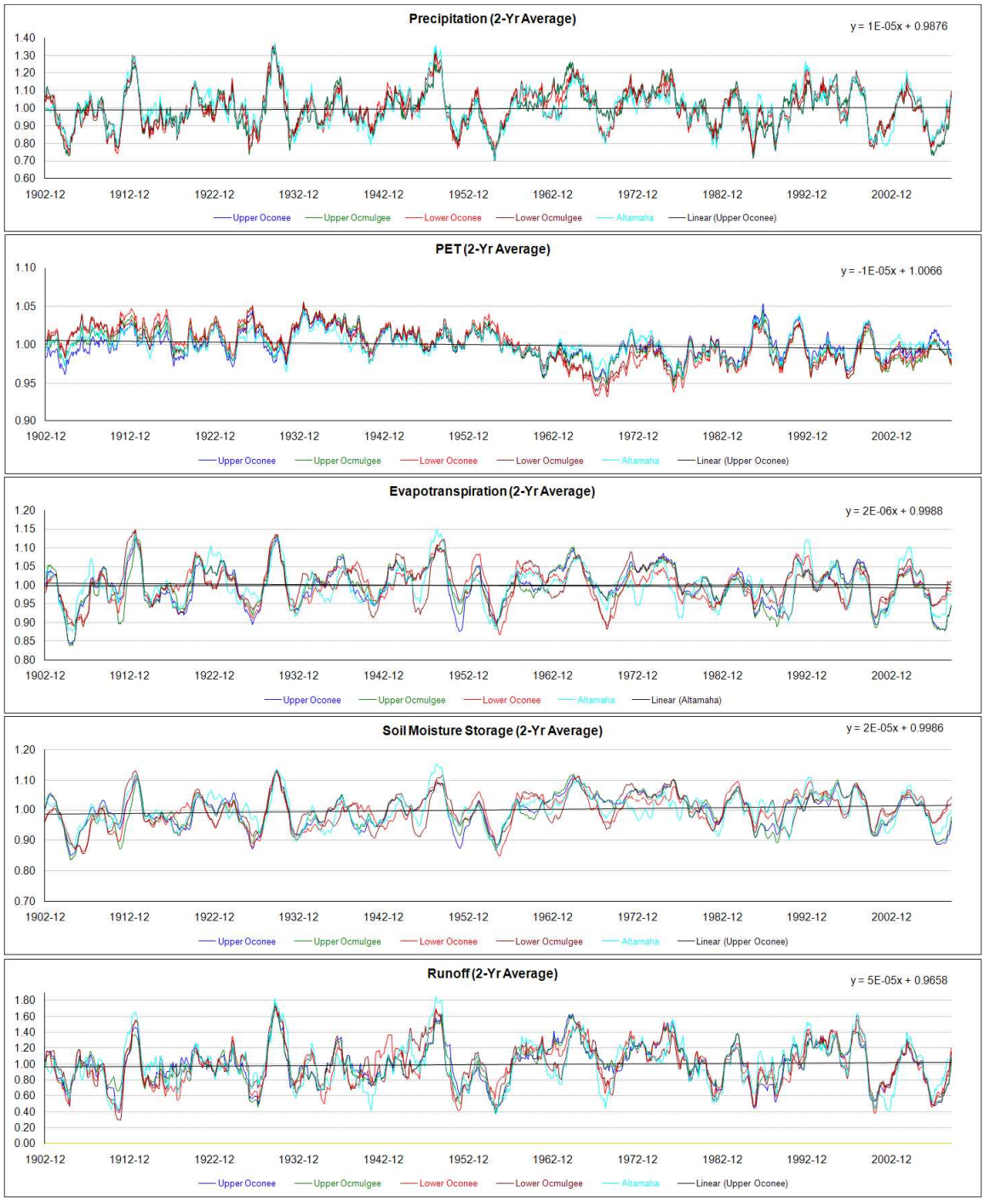

Figure 6.29: OOA Normalized, 2Yr Average Hydrologic Response (1901 - 2009).

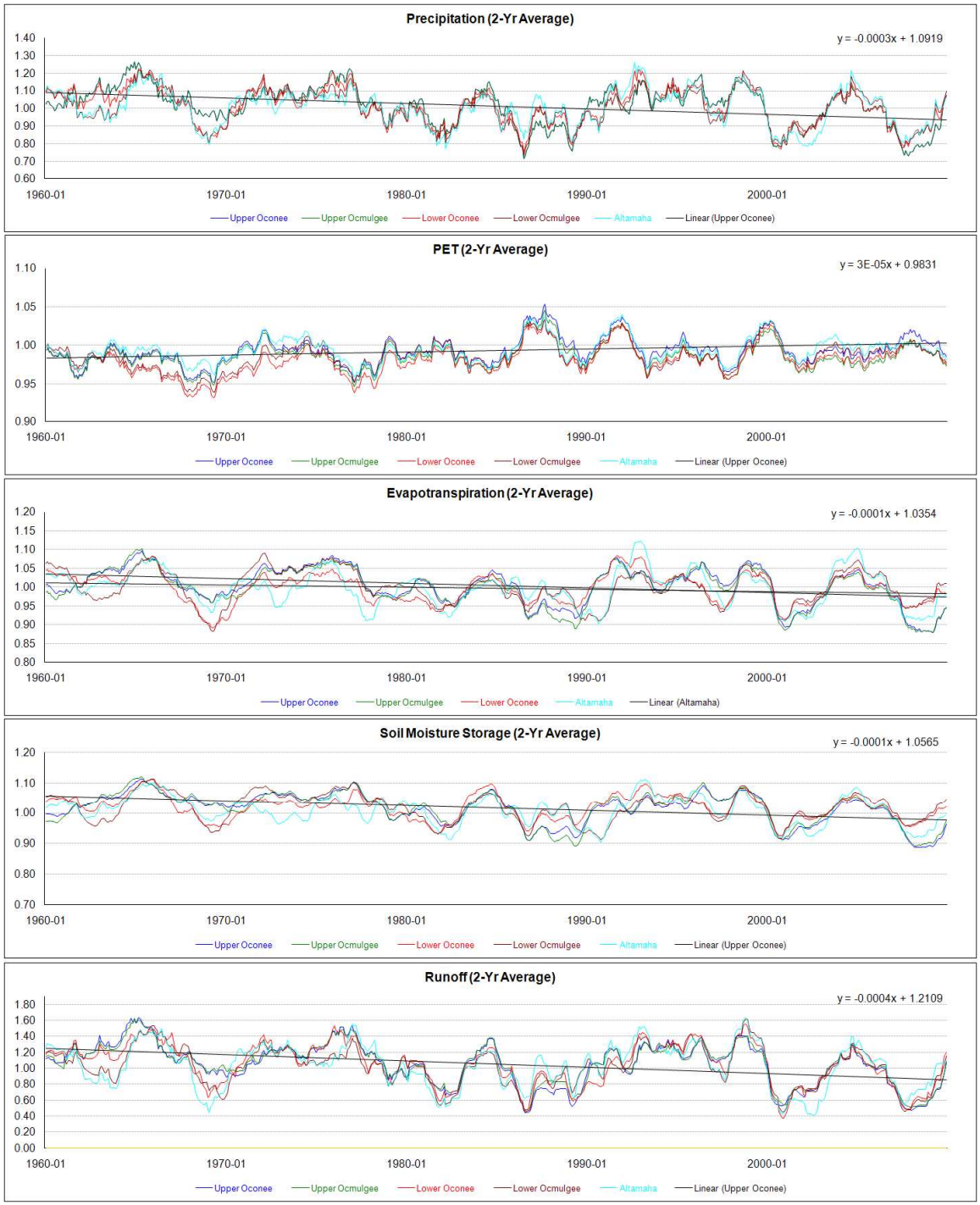

Figure 6.30: OOA Normalized, 2Yr Average Hydrologic Response (1960 - 2009).

Table 6.2 Slopes of Linear Trends for Normalized, 2Yr Average Hydrologic Variables in the OOA Basin.

	Upper Oconee	Upper Ocmulgee	Lower Oconee	Lower Ocmulgee	Altamaha
	1901-2009 (unit: 10-4 of the mean per year)				
Precipitation	1.68	1.68	2.76	1.92	0.84
PET	-1.08	-3.48	-4.80	-3.24	-1.44
Soil Moisture	2.64	3.84	5.52	4.92	2.16
Runoff	5.76	5.88	6.60	6.12	3.12
	1960-2009 (unit: 10-4 of the mean per year)				
Precipitation	-31.08	-30.96	-21.96	-15.36	-12.24
PET	3.96	1.56	4.92	4.20	2.52
Soil Moisture	-16.08	-14.04	-5.52	-7.32	-8.04
Runoff	-55.80	-49.80	-29.64	-40.44	-31.08
	Upper Oconee	Upper Ocmulgee	Lower Oconee	Lower Ocmulgee	Altamaha
	1901-2009 (unit: percentage increase over 109 years)				
Precipitation	1.831	1.831	3.008	2.093	0.916
PET	-1.177	-3.793	-5.232	-3.532	-1.570
Soil Moisture	2.878	4.186	6.017	5.363	2.354
Runoff	6.278	6.409	7.194	6.671	3.401
	1960-2009 (unit: percentage increase over 50 years)				
Precipitation	-15.540	-15.480	-10.980	-7.680	-6.120
PET	1.980	0.780	2.460	2.100	1.260
Soil Moisture	-8.040	-7.020	-2.760	-3.660	-4.020
Runoff	-27.900	-24.900	-14.820	-20.220	-15.540

6.2.2 Future Assessment

The future climate assessments utilize all A1B and A2 climate scenarios for the period from January 2000 through December 2099 (100 years) in monthly time steps. The assessment process is similar to the one presented for the ACF river basin.

Figures 6.31 through **6.38** show the assessment results in frequency curves and box plots. For the upper Oconee basin, the frequency curves are shown on **Figures 6.31** and **6.32**; for the Altamaha basin, the frequency curves are shown on **Figures 6.35** and **6.36**. These results lead to the following observations:

- While on average (i.e., in the vicinity of the 50% percentile), precipitation is not expected to change relative to the historical baseline, the precipitation distribution is expected to "stretch" becoming wetter and drier than the historical climate. This assertion holds for both the A1B and A2 scenarios, with the latter stretching the distribution farther.
- The median of the potential evapotranspiration is higher than the historical baseline under both A1B and A2 scenarios. In addition, future PET is expected to increase faster (in absolute value) for higher PET values than for lower.
- The median of the soil moisture is decreasing for most A1B scenarios and for all A2 scenarios. The future soil moisture distributions are expected to "stretch" on both ends. In addition, the depletion of soil storages are especially pronounced in dry years and for the most southern watersheds (e.g., the Altamaha watershed) and under the A2 scenarios (**Figure 6.36**).
- The median of the runoff is expected to decrease under both scenarios. The decrease of runoff in southern watersheds (e.g., Altamaha watershed) is faster than the

decrease in northern watersheds (e.g., upper Oconee watershed). In the 15% wettest years for the upper Oconee watershed and in the 8% wettest years for the Altamaha watershed, runoff is expected to be higher than historical for all scenarios (expect for the INMCM GCM scenario). Thus the coming decades are likely to bring more severe floods than those experienced in the past decades.

The box plots are shown on **Figures 6.33** and **6.34** for the Milledgeville (upper Oconee) watershed and **Figures 6.37** and **6.38** for the Altamaha watershed. The following observations can be made:

- Mean watershed precipitation exhibits clear decreasing trends in June and July for upper Oconee and Altamaha, and does not show appreciable change for all other months of the year. In the Altamaha, precipitation is decreasing from June to September and increasing from October to December. In addition, the precipitation distributions for the months from January to August are considerably extended (toward both ends) in comparison to the historical distributions for both OOA watersheds and in both A1B *and* A2 scenarios.
- Future PET exhibits a higher mean and a wider range than historical PET from February to September, with the largest change observed in July and August. For these two months, the future mean PET is higher than the historical PET up to 10% under the A1B scenarios and up to 15% under the A2 scenarios.
- Future soil moisture is lower than historical in almost all months. The change is more pronounced (10% - 15%) in the southern watersheds (e.g., Altamaha) from July to November under the A2 scenarios. For northern watersheds (e.g., upper Oconee), the largest decrease is in September and October (about 11%) under the A2 scenarios.

- Future runoff is generally drier under both A1B and A2 scenarios for all OOA watersheds. The highest decreases are in June, July, August and September by 10% - 25% under the A2 scenarios. However, for Altamaha, future runoff is expected to be wetter than historical in two winter months (November and December) by 2% - 3% under the A1B scenarios and by 2% - 5% under the A2 scenarios.
- Comparing the future changes in the OOA and ACF basins, one can note the following observations: *(1)* Most OOA and ACF watersheds clearly show precipitation reductions for the summer months (June, July, and August); *(2)* all OOA and ACF watersheds show higher PET in summer than in winter (in absolute value); *(3)* OOA and ACF runoff generally decrease in summer and fall; and *(4)* OOA and ACF southern watersheds (e.g., Woodruff-Bainbridge and Altamaha) are generally expected to experience more summer soil storage/runoff deficits than northern watersheds (e.g., Buford and Milledgeville).
- Results are presented for all OOA watersheds in **Appendix A**.

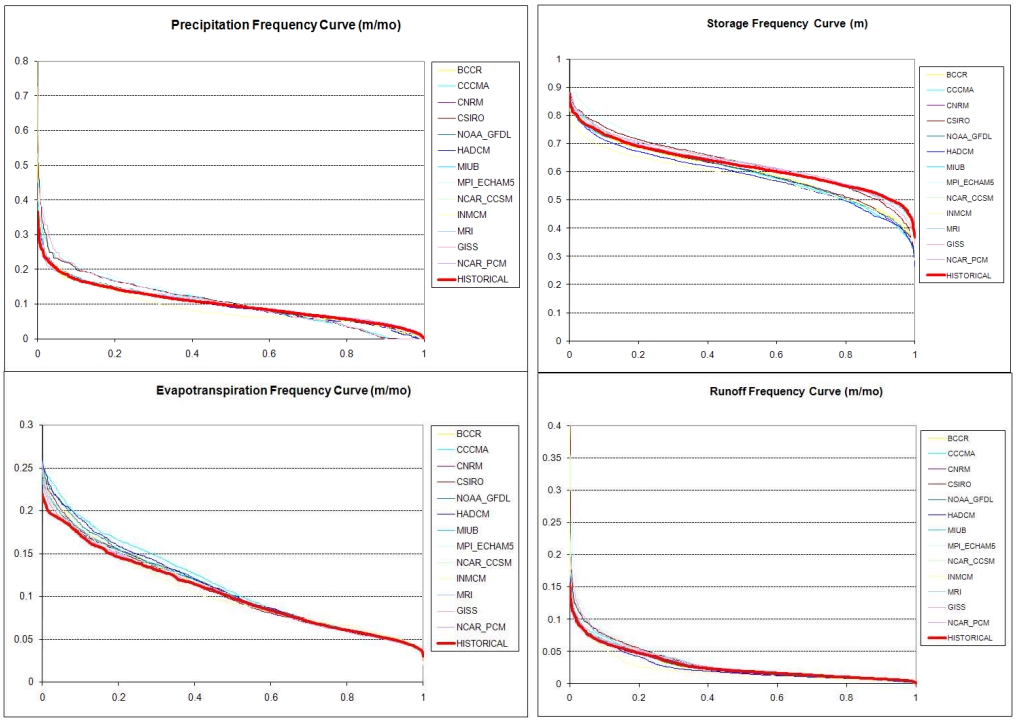

Figure 6.31: A1B Climate Scenarios (2000-2099), Upper Oconee, Frequency Curves.

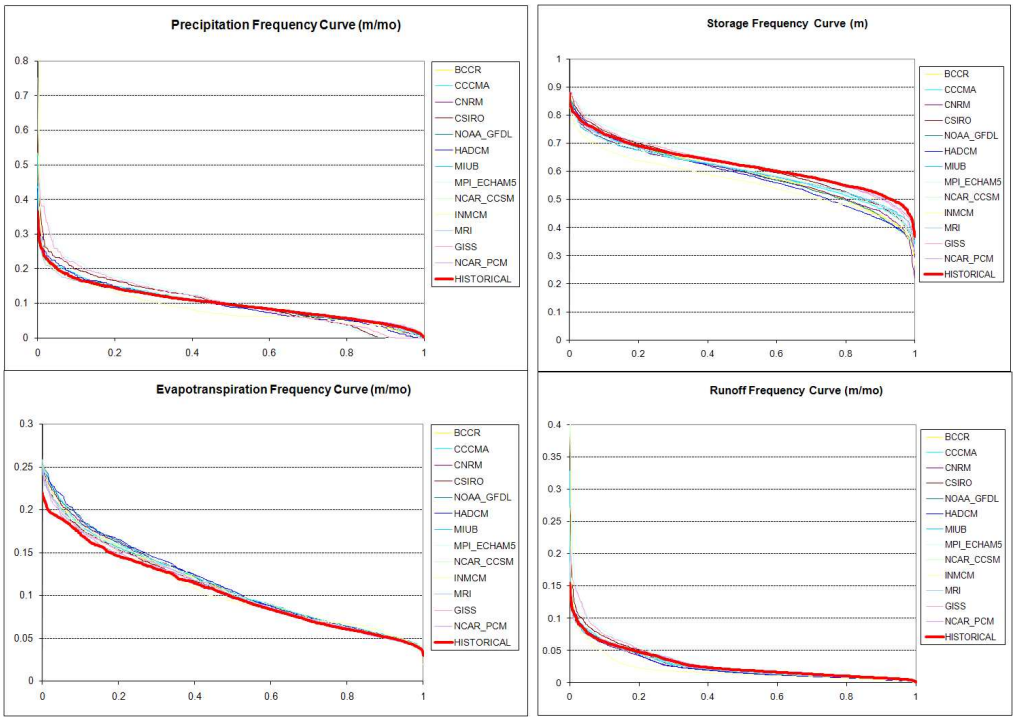

Figure 6.32: A2 Climate Scenarios (2000-2099), Upper Oconee, Frequency Curves.

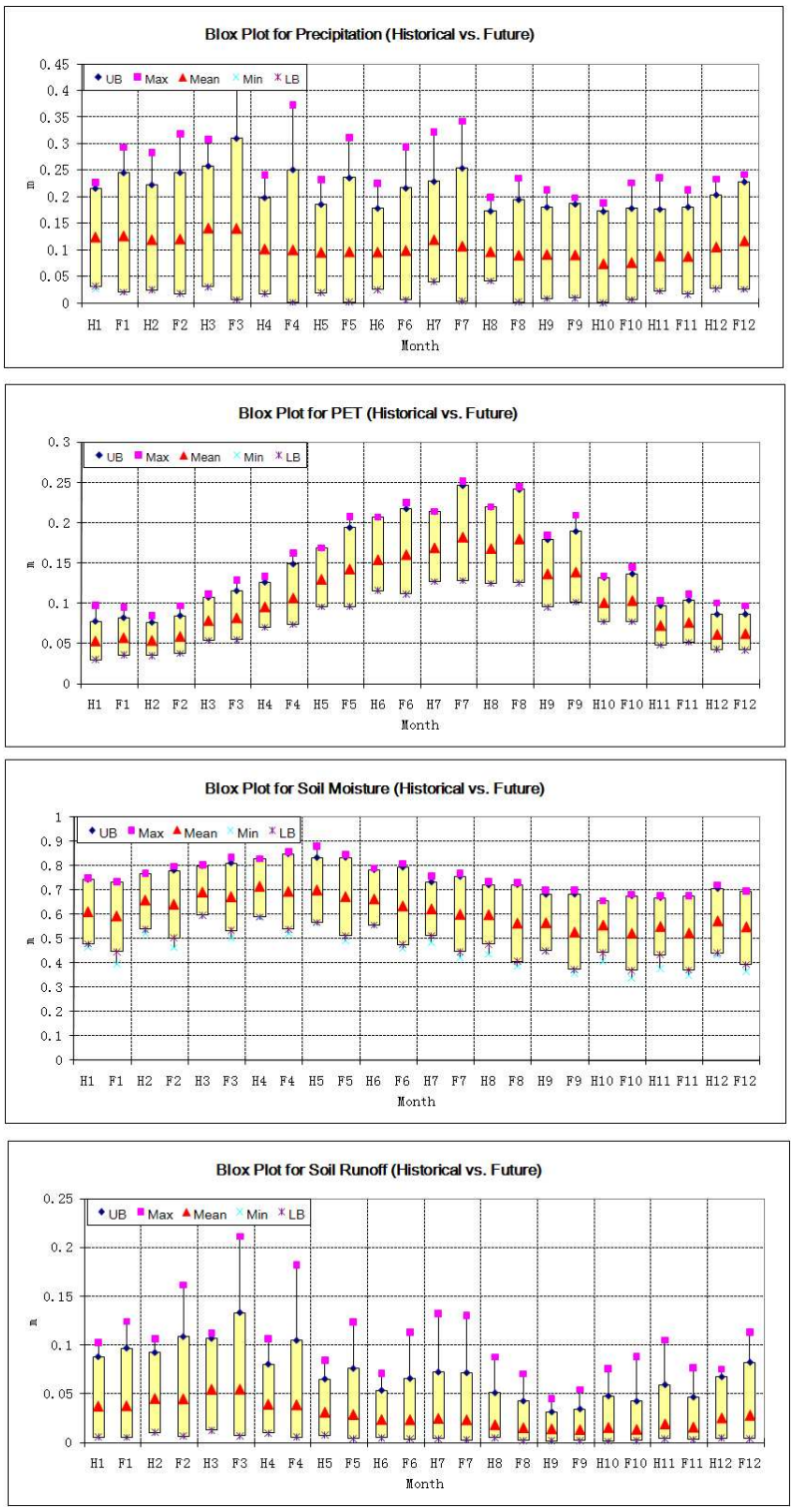

Figure 6.33: Monthly Historical vs. Future (A1B) Watershed Response, Upper Oconee.

(Unit: Precipitation – m/mo; PET – m/mo; Soil Moisture – m; Runoff m/mo.)

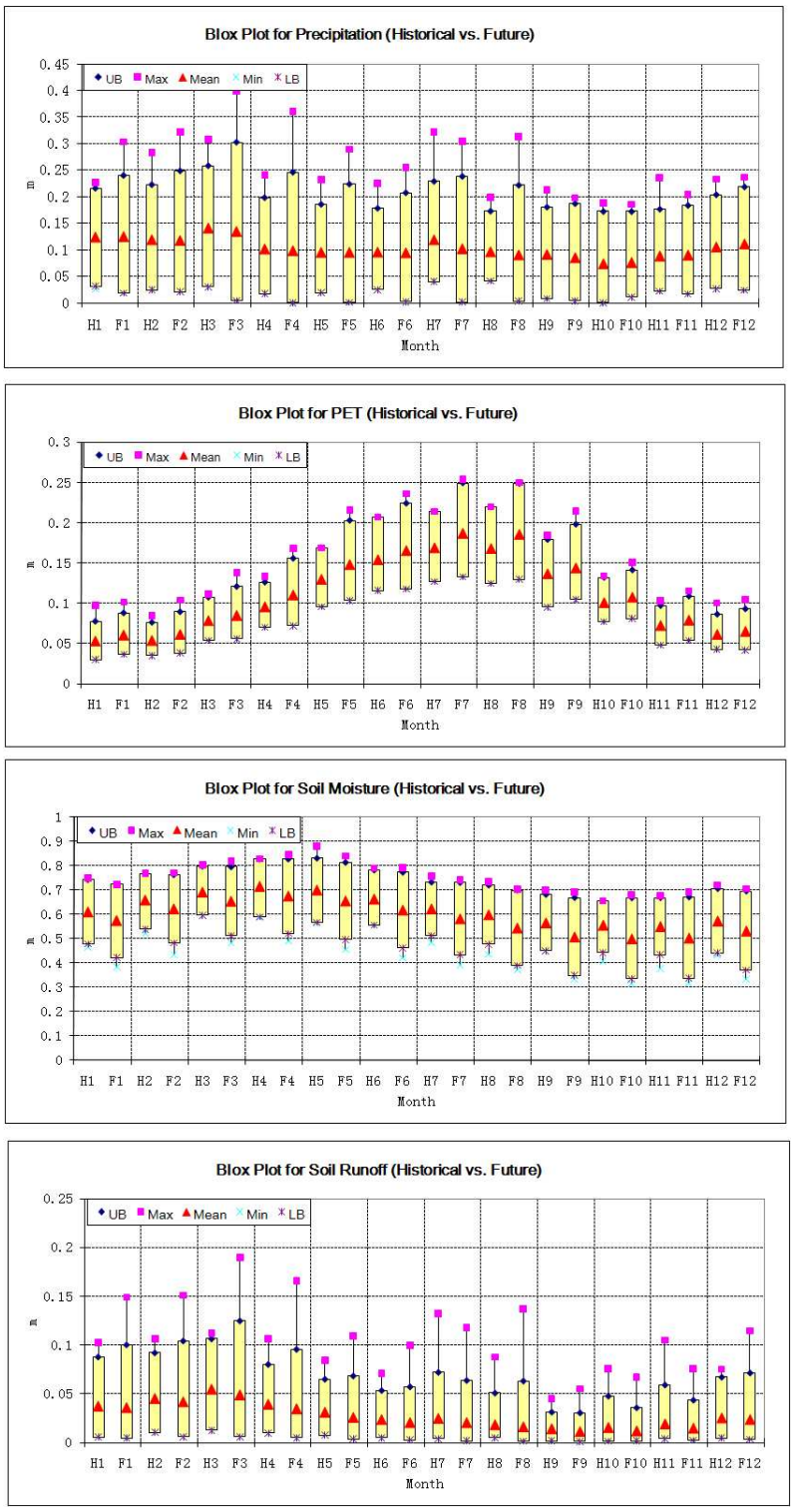

Figure 6.34: Monthly Historical vs. Future (A2) Watershed Response, Upper Oconee.

(Unit: Precipitation – m/mo; PET – m/mo; Soil Moisture – m; Runoff m/mo.)

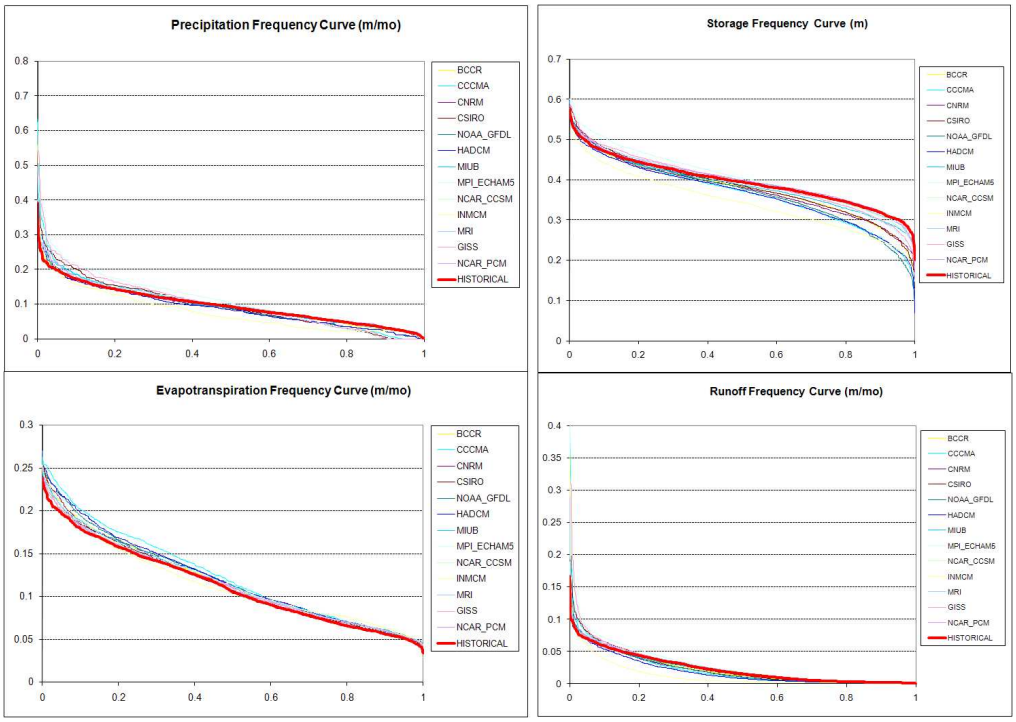

Figure 6.35: A1B Climate Scenarios (2000-2099), Altamaha, Frequency Curves.

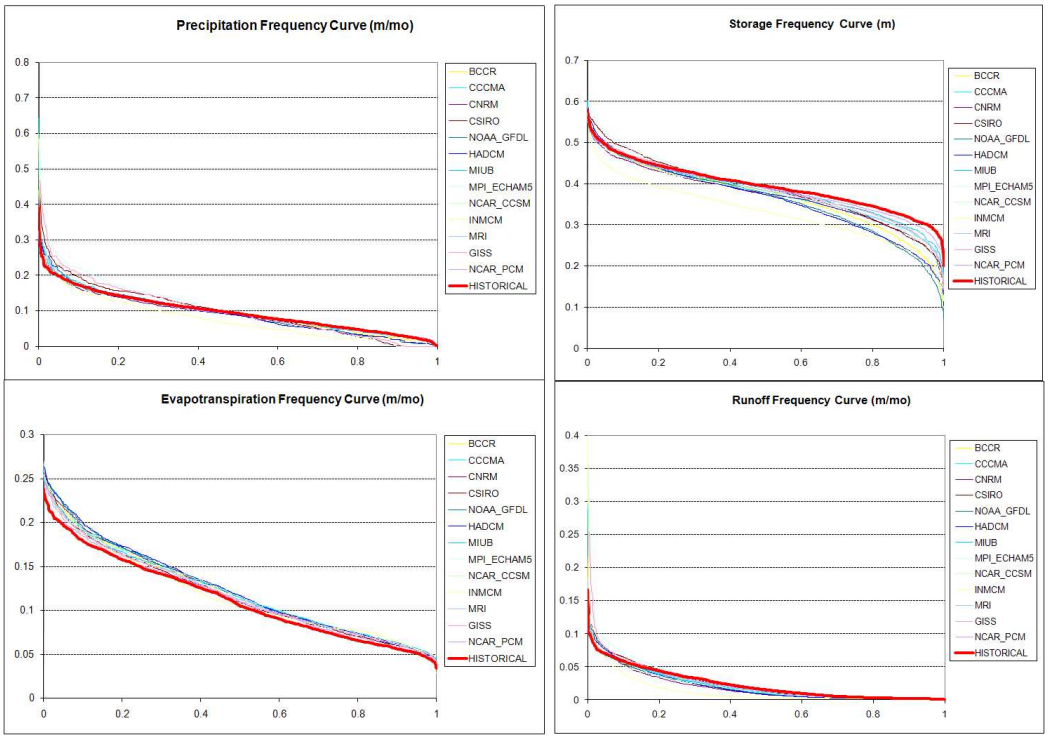

Figure 6.36: A2 Climate Scenarios (2000-2099), Altamaha, Frequency Curves.

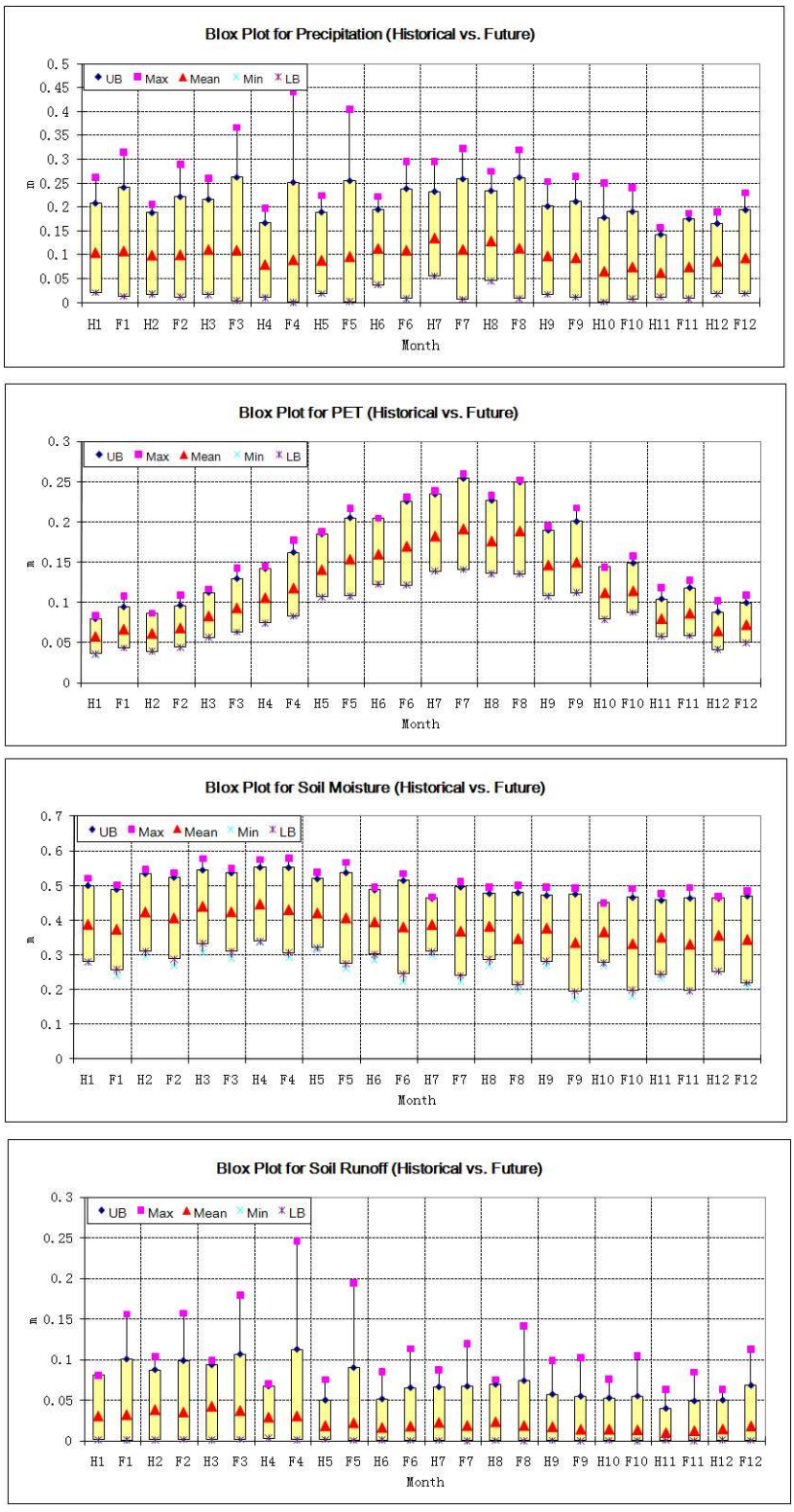

Figure 6.37: Monthly Historical vs. Future (A1B) Watershed Response, Altamaha. (Unit: Precipitation – m/mo; PET – m/mo; Soil Moisture – m; Runoff m/mo.)

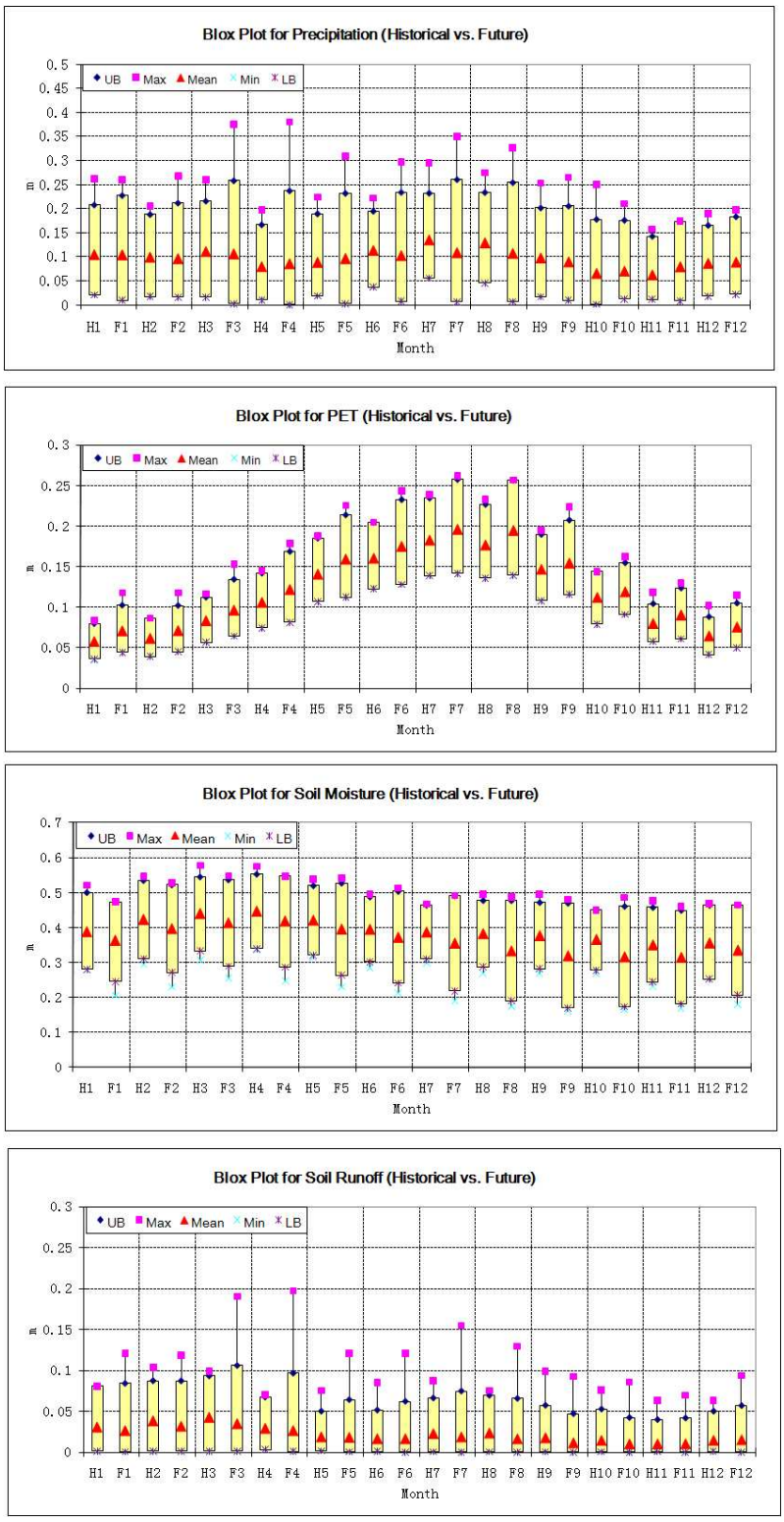

Figure 6.38: Monthly Historical vs. Future (A2) Watershed Response, Altamaha. (Unit: Precipitation – m/mo; PET – m/mo; Soil Moisture – m; Runoff m/mo.)

6.3 Historical (Baseline) and Future Hydrologic Assessments for the SO Basin

6.3.1 Historical Assessment

The calibrated SO watershed models are employed in this section to characterize the SO hydrologic response under the historical climate. This assessment is based on historical climatic data for the period 1901 through 2009, and it follows the same assessment procedures described in previous sections.

The SO study watersheds are shown in **Figure 6.39**. They include the upper Savannah watershed (Hartwell, Russell, Thurmond), the middle Savannah watershed (Augusta), the lower Savannah watershed (down to Savannah), and the Ogeechee watershed. **Figure 6.40** presents the input and output sequences (normalized by their means). The results support several comments and observations:

- Watershed precipitation in the three SO watersheds shows different long-term trends (**Figure 6.40a**; **Table 6.3**) over the 109-year assessment period. The three northern watersheds (e.g., Hartwell, Russell, and Thurmond) show a 2% - 6% precipitation decrease relative to their early 20th century value. However, the other three southern watersheds (the middle Savannah, lower Savannah, and Ogeechee) show a long-term precipitation increase by 3% - 5% relative to their early 20th century value.
- Watershed potential evapotranspiration exhibits a mild decrease by about 1% - 4% of its early 20th century value (**Figure 6.40b**; **Table 6.3**). The PET of the northern watersheds (e.g., Hartwell) decreases (~4%) faster than the southern watersheds (~2%).
- Total soil moisture storage shows different long-term trends (**Figure 6.40d**; **Table 6.3**). Total soil moisture storage shows a decreasing trend of 0.5% - 2.5% in the three

northern watersheds over the 109-year assessment period; but increases in the three southern watersheds by 2% - 6%.

- Actual evapotranspiration changes generally follow the changes of soil moisture and PET (**Figure 6.40c**). For the three northern watersheds, actual ET decreases by 1% - 3% of the early 20th century value; for the three southern watersheds, actual ET increases very mildly by 0.5% – 1% of the early 20th century value.
- Total runoff also exhibits different long-term trends (**Figure 6.40e**; **Table 6.3**). For the three northern watersheds, runoff decreases by 2% - 5% of its early 20th century value; for the three southern watersheds, runoff increases by 4% - 6% of its early 20th century value. This response is consistent with the previous finding that northern watershed precipitation decreases while southern watershed precipitation increases.
- Lastly, the above historical analysis is also performed for the most recent 50 years (1960-2009). It can be seen from **Figure 6.41** and **Table 6.3** that during this period *(1)*precipitation exhibits a declining trend of about 10% - 18% for all SO watersheds; *(2)* PET exhibits an increasing trend of about 2% - 3% for all SO watersheds; *(3)* soil moisture decreases by 5% - 8% of its early 1960s value; and *(4)* runoff decreases by 11% - 23% of its early 1960s value. Unlike the 109 historical horizon, these trends are more consistent across the OS basin watersheds, providing evidence of climatic change.
- Comparing the historical changes of the SO basin with the changes in ACF and OOA basins over the last 50 years, one concludes that *(1)* all three basins show significant precipitation reductions; *(2)* all three basins show PET increases (expect for George); and *(3)* all three basins show runoff decreases. The consistency of this response strengthens the conclusion that climatic change is regional.

Figure 6.39: Map of SO Watersheds: Upper Savannah River (Hartwell, Russell, Thurmond), Middle Savannah River (Augusta), Lower Savannah River (down to Savannah), and Ogeechee River.

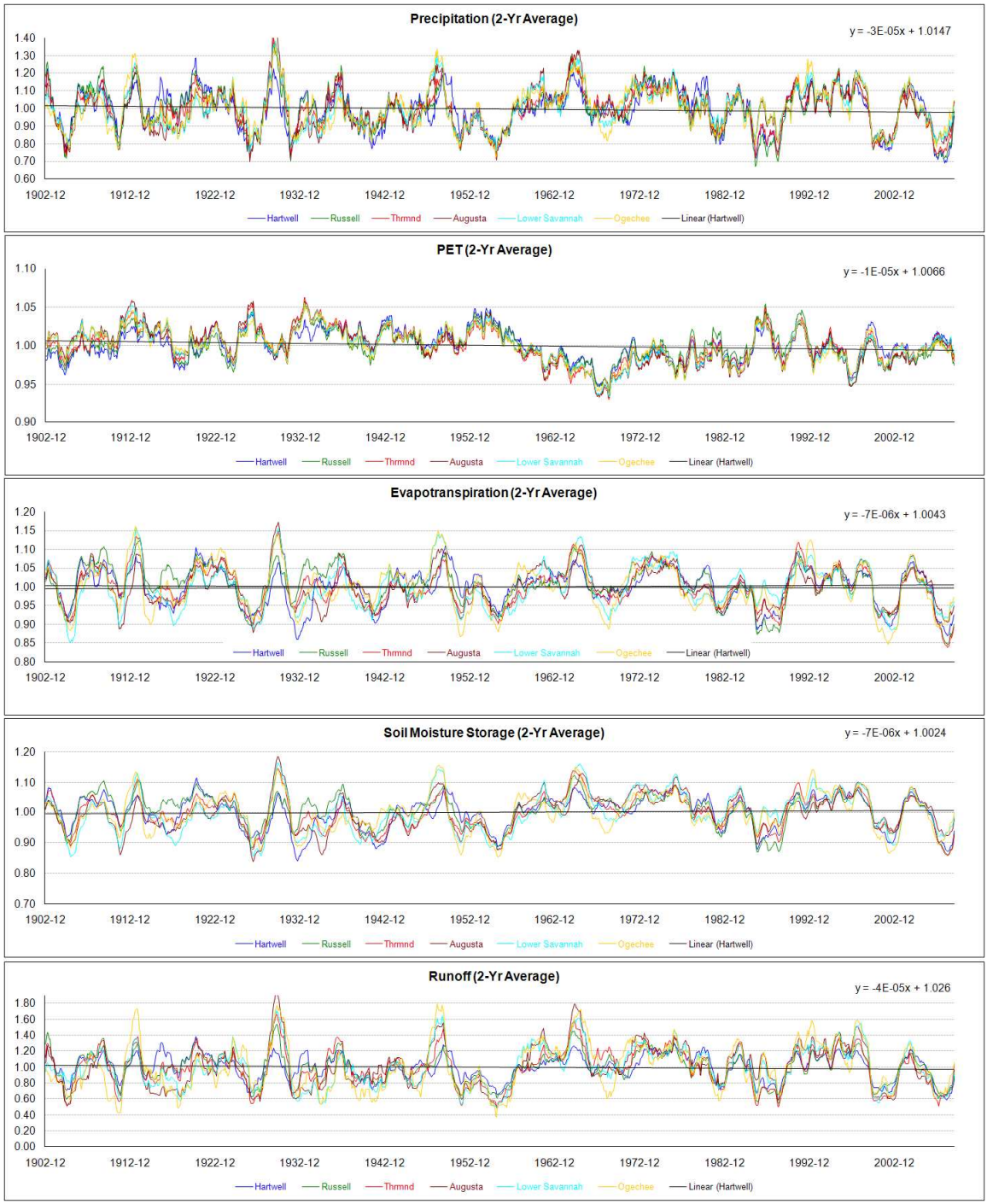

Figure 6.40: SO Normalized, 2Yr Average Hydrologic Response (1901 - 2009).

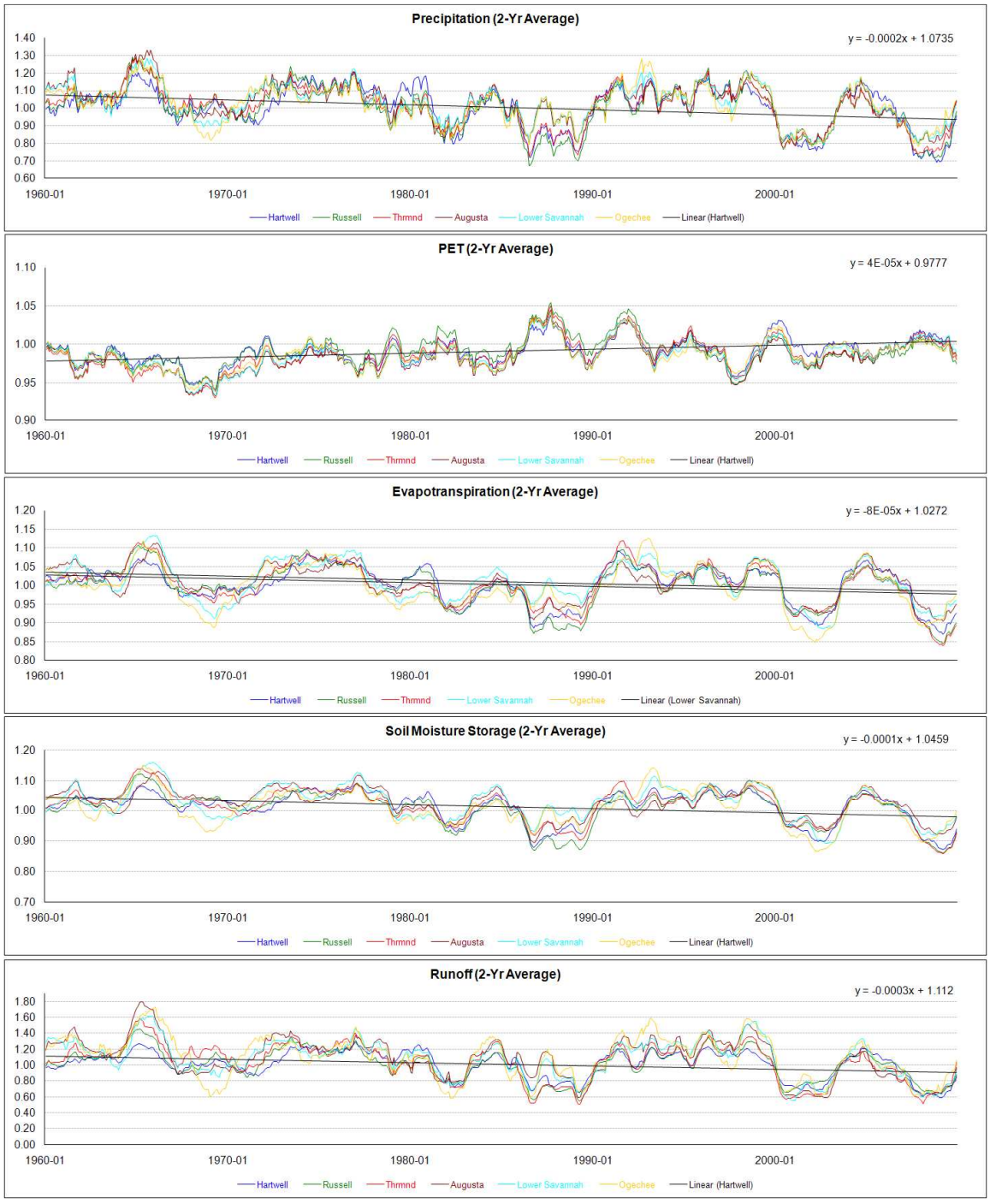

Figure 6.41: SO Normalized, 2Yr Average Hydrologic Response (1960 - 2009).

Table 6.3 Slopes of Linear Trends for Normalized, 2Yr Average Hydrologic Variables in the SO Basin.

	Hartwell	Russell	Thrmnd	Augusta	Lower Savannah	Ogechee
	1901-2009 (unit: 10-4 of the mean per year)					
Precipitation	-3.36	-6.12	-2.28	4.56	3.96	3.00
PET	-1.08	-1.56	-2.64	-3.96	-3.24	-3.00
Soil Moisture	-0.96	-2.28	-0.24	5.16	5.16	2.04
Runoff	-5.16	-4.68	-1.80	5.88	5.28	3.72
	1960-2009 (unit: 10-4 of the mean per year)					
Precipitation	-27.72	-35.52	-35.64	-30.36	-25.08	-21.48
PET	5.16	3.24	6.84	5.28	5.76	5.28
Soil Moisture	-13.08	-15.60	-16.68	-12.96	-12.48	-9.96
Runoff	-31.56	-46.08	-41.04	-29.16	-26.16	-23.28
	Hartwell	Russell	Thrmnd	Augusta	Lower Savannah	Ogechee
	1901-2009 (unit: percentage increase over 109 years)					
Precipitation	-3.662	-6.671	-2.485	4.970	4.316	3.270
PET	-1.177	-1.700	-2.878	-4.316	-3.532	-3.270
Soil Moisture	-1.046	-2.485	-0.262	5.624	5.624	2.224
Runoff	-5.624	-5.101	-1.962	6.409	5.755	4.055
	1960-2009 (unit: percentage increase over 50 years)					
Precipitation	-13.860	-17.760	-17.820	-15.180	-12.540	-10.740
PET	2.580	1.620	3.420	2.640	2.880	2.640
Soil Moisture	-6.540	-7.800	-8.340	-6.480	-6.240	-4.980
Runoff	-15.780	-23.040	-20.520	-14.580	-13.080	-11.640

6.3.2 Future Assessment

The future climate assessment consists of running the SO watershed models under all A1B and A2 climate scenarios for the period from January 2000 through December 2099 (100 years) in monthly time steps. The results and conclusions are presented in a form similar to the other Georgia Basins.

Figures 6.42 through **6.49** show the assessment results in frequency curves and box plots. The frequency curves, shown on **Figures 6.42**, **43**, **44** and **45**, lead to the following observations:

- On average (i.e., in the vicinity of the 50% percentile), precipitation is not expected to change relative to the historical baseline. However, for the Hartwell watershed, the median of the precipitation is expected to decrease by about 1% - 2%. The precipitation distribution is expected to "stretch" becoming wetter and drier than that of the historical climate. This assertion holds for both the A1B and A2 scenarios, with the latter stretching the distribution farther.
- The median of the potential evapotranspiration is higher than the historical baseline for both A1B and A2 scenarios. In addition, the future PET is expected to increase faster for higher PET values than for lower PET values.
- The median of the soil moisture decreases for most A1B scenarios and for all A2 scenarios. The future soil moisture distributions are also expected to "stretch" on both ends.
- The median of the runoff decreases under both scenarios. For the Hartwell watershed, the runoff reductions are significant for most flow scenarios. For the lower Savannah and Ogechee watersheds, runoff reductions are smaller.

The box plots are shown on **Figures 6.44** and **6.45** for Hartwell and on **Figures 6.48** and **6.49** for Ogechee. The following observations can be made:

- For Hartwell, mean watershed precipitation exhibits clear decreasing trends in June, July, and August (up to 15%), and clear increasing trends in October and December (up to 10%) under both A1B *and* A2 scenarios. For Ogeechee, (**Figures 6.45** and **6.46**) precipitation decreases in February, March, June, July and August (with the highest reduction occurring in July and August of up to 13%), and increases in April, May and from September to December (up to 15%). In addition, the precipitation distributions for almost all months are considerably extended (toward both ends) in comparison to the historical distributions for both watersheds and under both A1B *and* A2 scenarios.
- Future PET exhibits higher mean and wider range than historical PET from January to September. For these two months, the future PET is higher than the historical PET up to 20% for Hartwell watershed and up to 15% for Ogechee basin.
- Future soil moisture is clearly lower than historical in almost all months. The change is more pronounced from August to October. For Hartwell, the largest reduction is up to 11% under the A2 scenarios, and for Ogechee up to 13% under the A2 scenarios.
- Future runoff is generally drier under both A1B and A2 scenarios for all SO watersheds. For Hartwell, the largest runoff reduction is from May to November under the A2 scenarios; For Ogechee, the largest runoff reduction is from June to October also under the A2 scenarios. Runoff reductions are more pronounced in Hartwell (northern watershed) than in Ogechee(southern watershed).

- The following comments can be stated by comparing the response of the SO basin with those of the ACF and OOA basins: *(1)* most OOA, ACF, and SO watersheds show clear precipitation reductions for summer (June, July, and August); *(2)* all OOA, ACF, and SO watersheds show higher PET increases in summer than in winter (in absolute value); *(3)* ACF, OOA and SO runoff generally decreases for summer months under both A1B and A2 scenarios; and *(4)* all OOA and ACF southern watersheds are generally expected to experience higher summer soil storage runoff reduction than northern watersheds, with the exception of the SO basin where the runoff reduction in Ogechee is less than that of Hartwell.
- Results are presented for all SO watersheds in **Appendix A**.

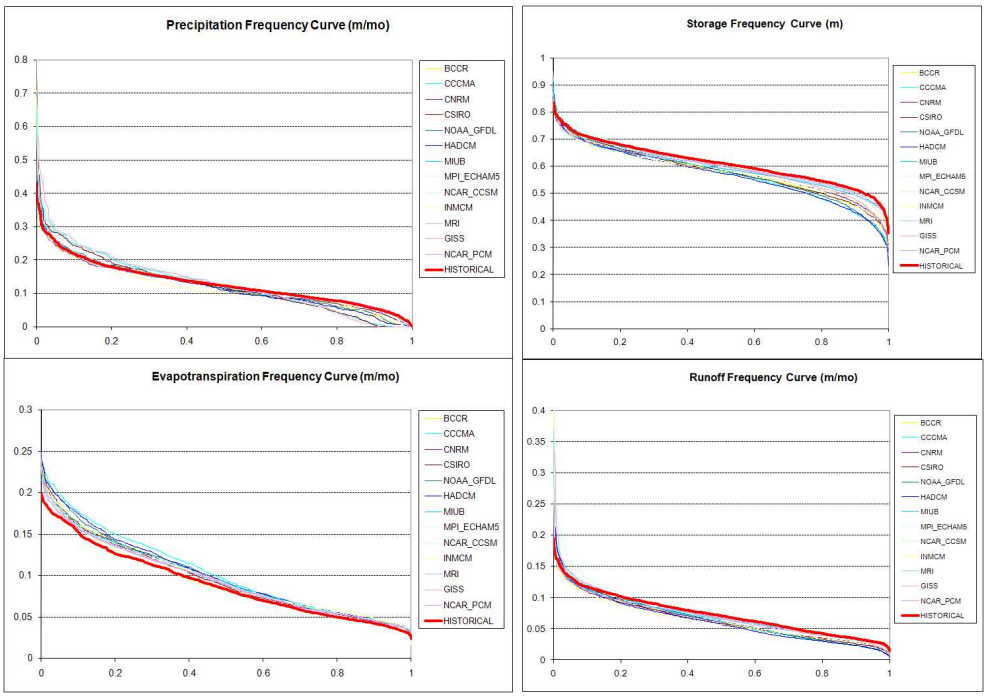

Figure 6.42: A1B Climate Scenarios (2000-2099), Hartwell, Frequency Curves.

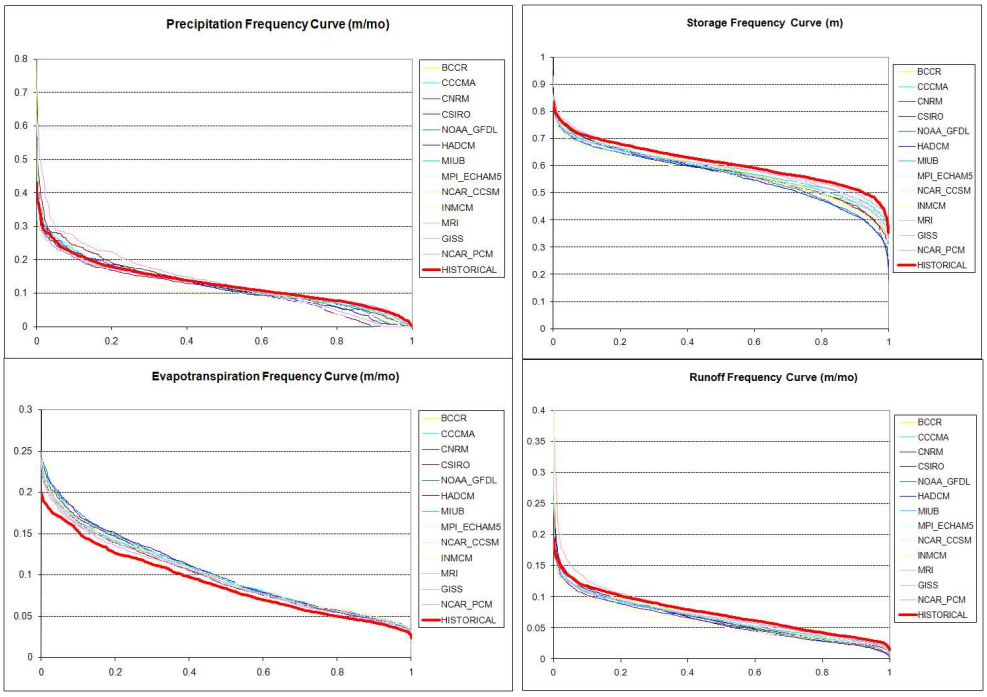

Figure 6.43: A2 Climate Scenarios (2000-2099), Hartwell, Frequency Curves.

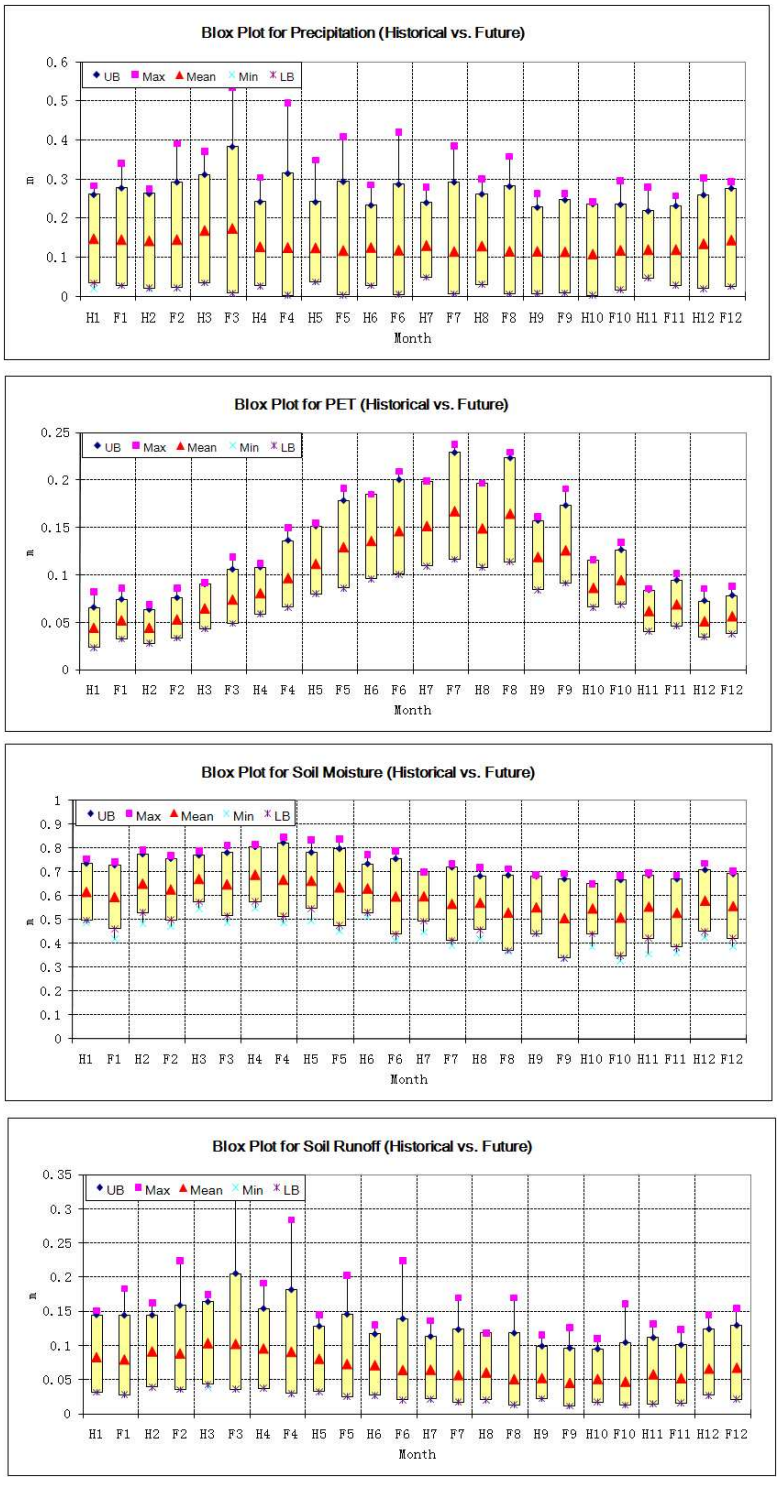

Figure 6.44: Monthly Historical vs. Future (A1B) Watershed Response, Hartwell. (Unit: Precipitation – m/mo; PET – m/mo; Soil Moisture – m; Runoff m/mo.)

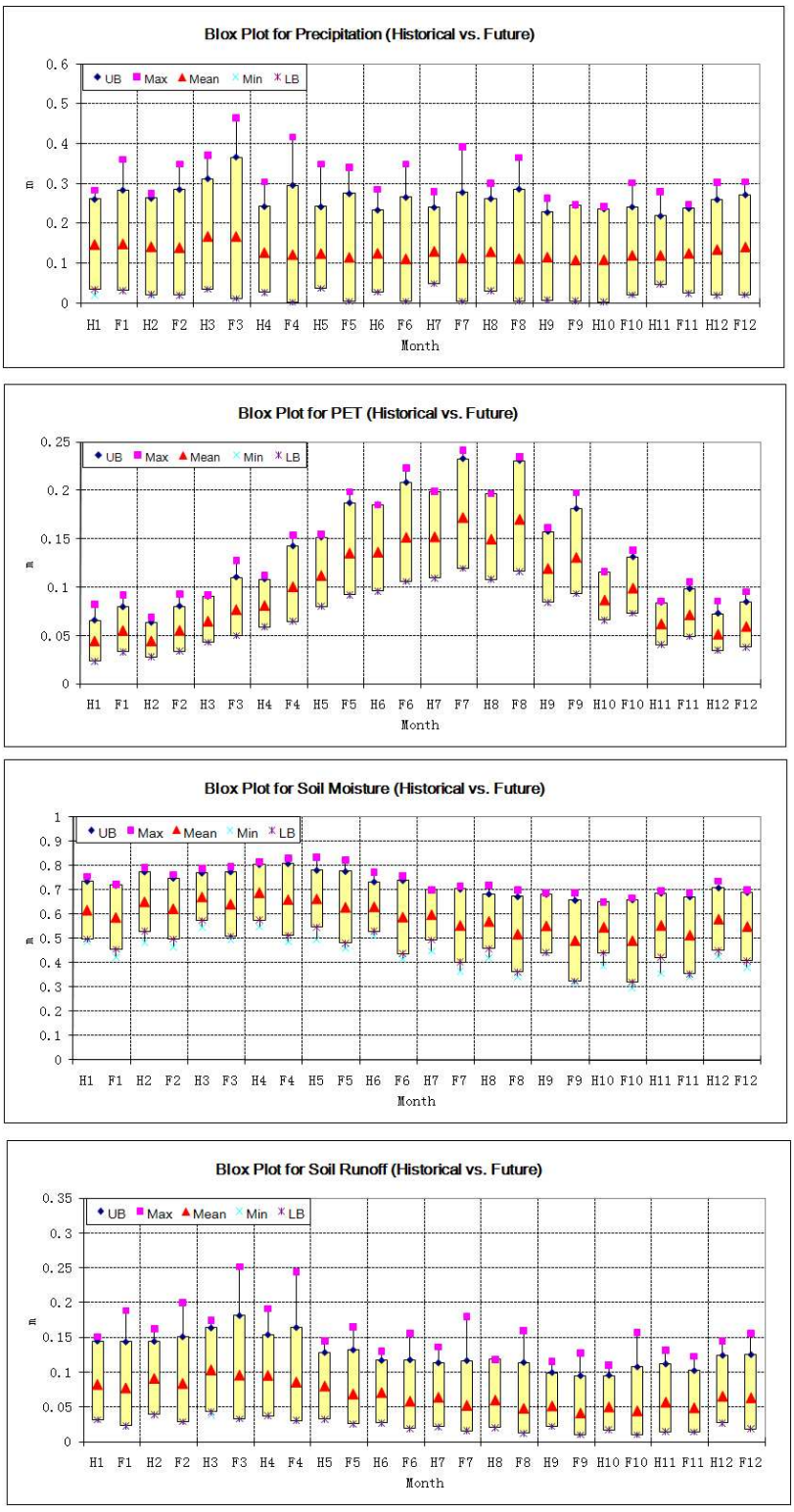

Figure 6.45: Monthly Historical vs. Future (A2) Watershed Response, Hartwell. (Unit: Precipitation – m/mo; PET – m/mo; Soil Moisture – m; Runoff m/mo.)

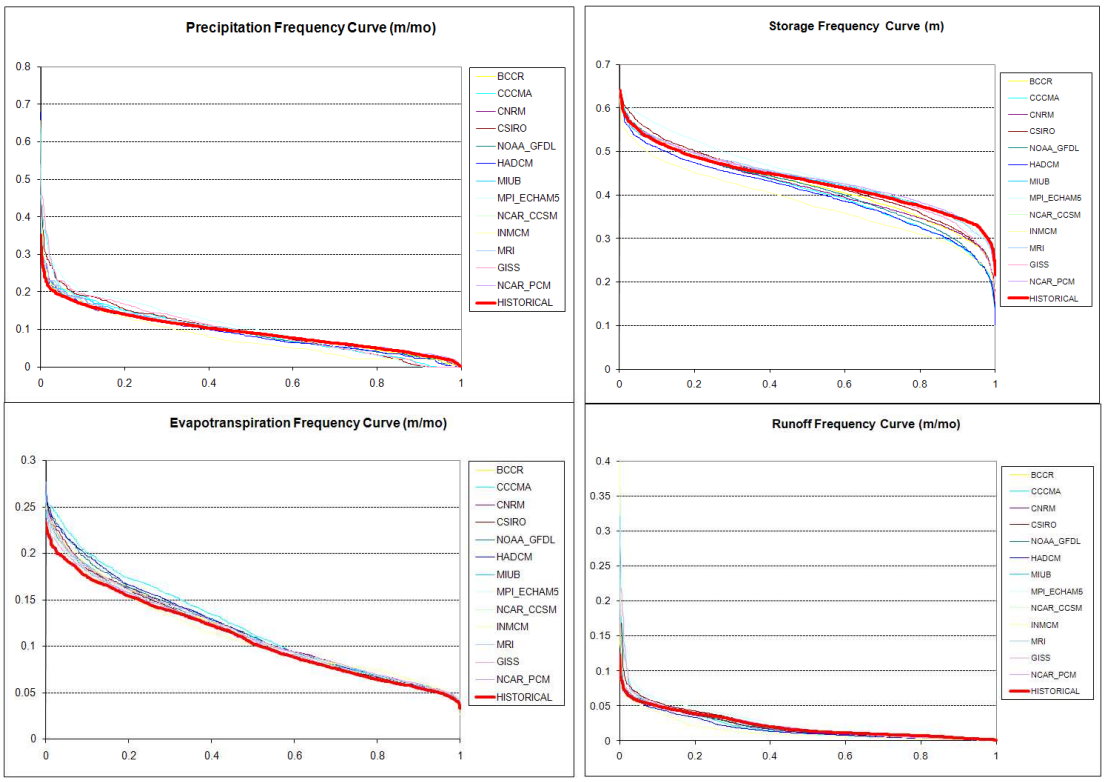

Figure 6.46: A1B Climate Scenarios (2000-2099), Ogeechee, Frequency Curves.

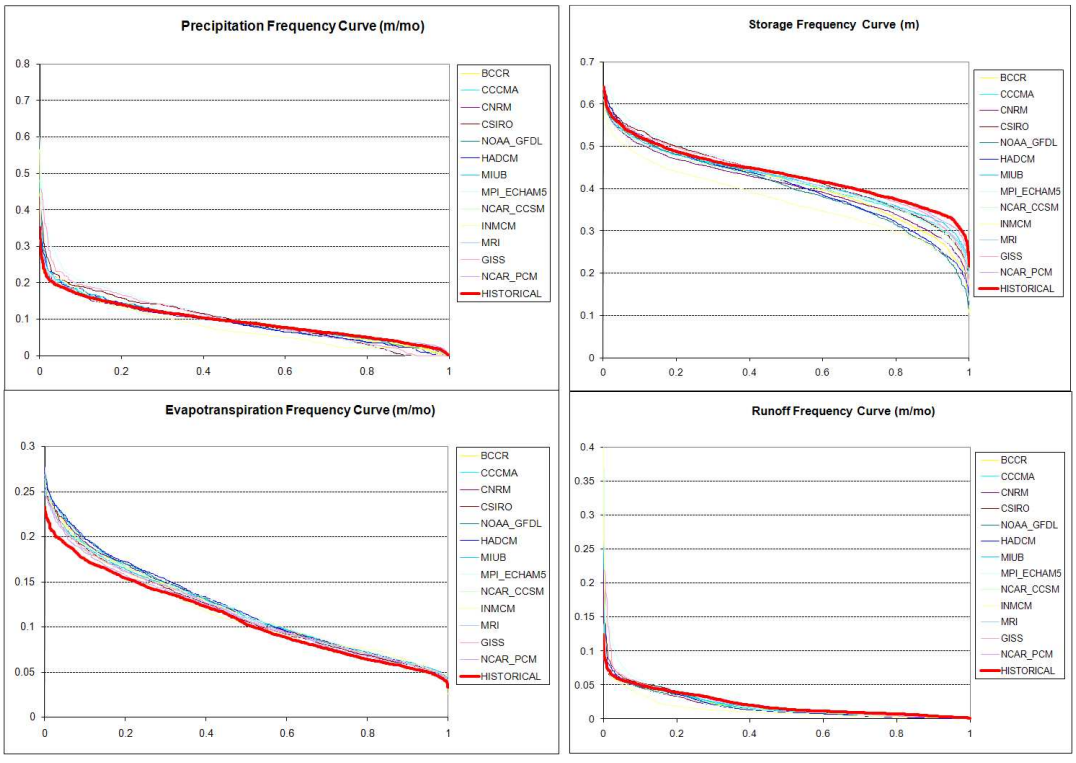

Figure 6.47: A2 Climate Scenarios (2000-2099), Ogeechee, Frequency Curves.

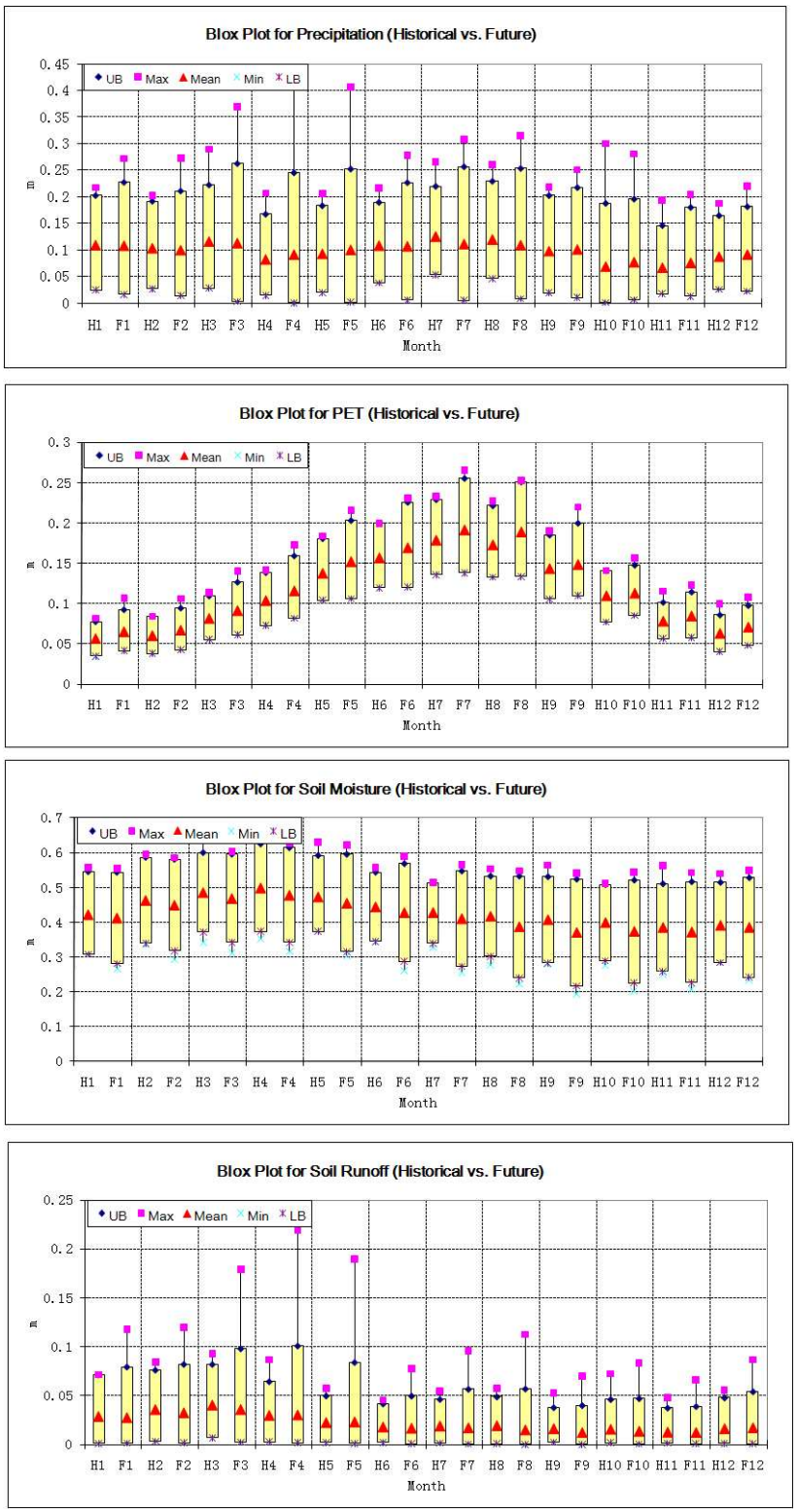

Figure 6.48: Monthly Historical vs. Future (A1B) Watershed Response, Ogeechee. (Unit: Precipitation – m/mo; PET – m/mo; Soil Moisture – m; Runoff m/mo.)

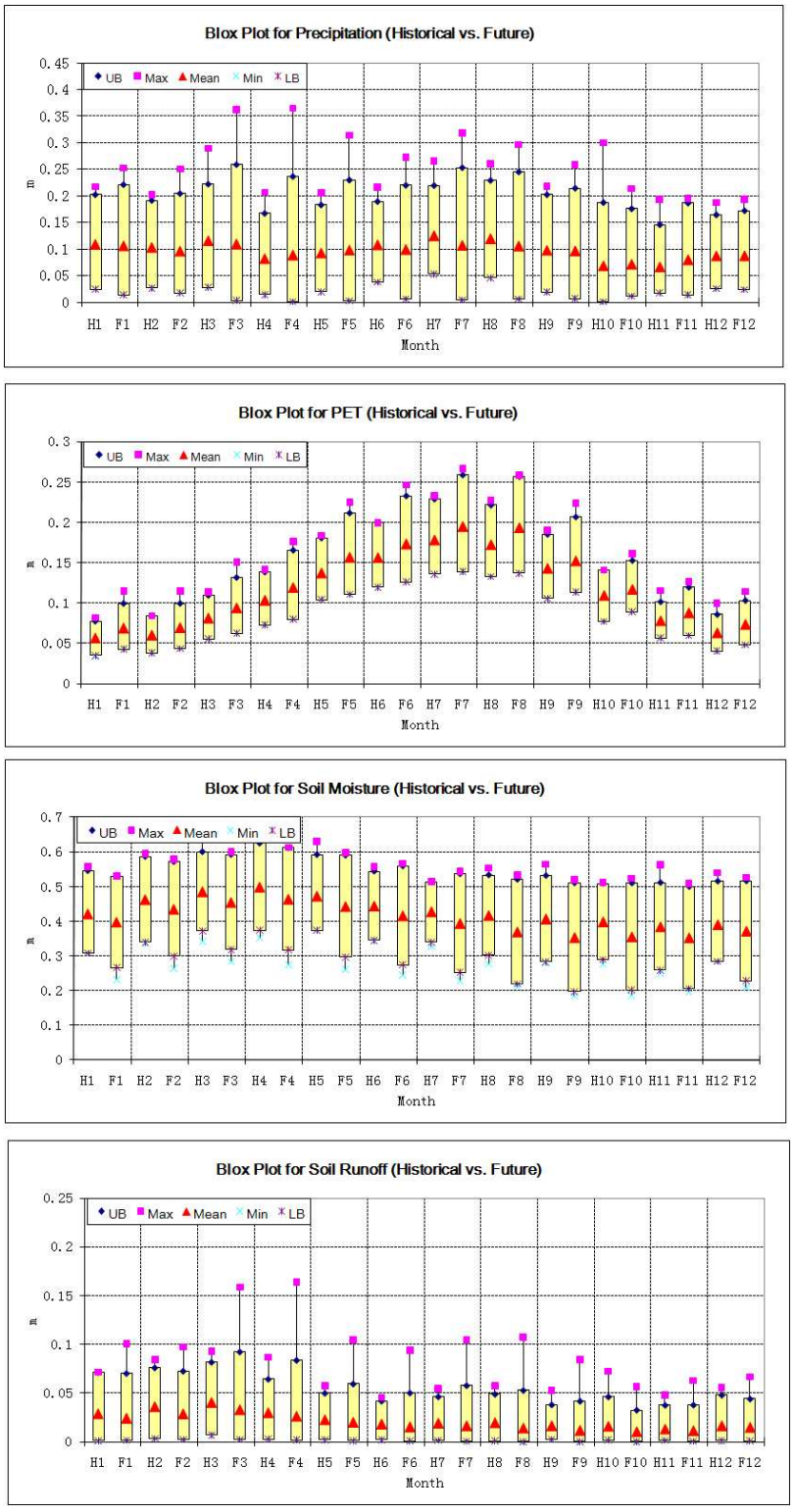

Figure 6.49: Monthly Historical vs. Future (A2) Watershed Response, Ogeechee. (Unit: Precipitation – m/mo; PET – m/mo; Soil Moisture – m; Runoff m/mo.)

6.4 Historical (Baseline) and Future Hydrologic Assessments for the Upper ACT Basin

6.4.1 Historical Assessment

The calibrated watershed models are employed in this section to characterize the upper ACT hydrologic response under the historical climate. This assessment is based on historical climatic data for the period 1901 through 2009 and follows the same assessment procedures described earlier.

The upper ACT basin watersheds are shown in **Figure 6.50**. For five watersheds: Canton, Allatoona, Carter, Tilton, and Rome (Coosa), **Figure 6.51** presents the input and output sequences (normalized to their means). All watersheds are located very close to each other and they exhibit similar climate and hydrological characteristics. The results support several comments and observations:

- Watershed precipitation of the entire upper ACT watersheds shows a decreasing long-term trend (**Figure 6.51a; Table 6.4**) by approximately 2% - 6% of its early 20th century value.
- Watershed potential evapotranspiration shows a very mild decreasing long-term trend (**Figure 6. 51b; Table 6.4**). Over the 109-year assessment period, the decrease is about 1% - 4% of the early 20th century value. The PET in two downstream watersheds (Allatoona and Rome) decreases faster than in the three upstream watersheds (Canton, Carter, and Tilton).
- Soil moisture shows a very small decreasing trend of less than 1% for all upper ACT watersheds over the 109-year assessment period.

- Actual evapotranspiration generally follows the changes of soil moisture and PET trend and it decreases by 1% - 2% of the early 20th century value (**Figure 6. 51c; Table 6.4**).
- Total runoff of the upper ACT watersheds exhibit a decreasing trend of approximately 1% - 6% over the 109–year period (**Figure 6. 51e; Table 6.4**).
- The above historical analysis is also performed for the most recent 50 years (1960-2009). It can be seen from **Figure 6.52** and **Table 6.4** that during this period *(1)* precipitation exhibits a clear declining trend of about 11% - 15% for all upper ACT watersheds; *(2)* PET exhibits an increasing trend of about 3% -5% over 50 years; *(3)* soil moisture decreases by 4% - 5% of the early 1960s values; and *(4)* runoff decreases by about 20% - 23% of the early 1960s values.
- Comparing the historical response of the upper ACT basin over the most recent 50 years with that of the ACF, OOA, and SO basins, one can note the following observations: *(1)* All four basins show significant precipitation reductions; *(2)* all four basins experience PET increases (except for George in the ACF); and *(4)* all four basins show soil moisture and total runoff decreases.

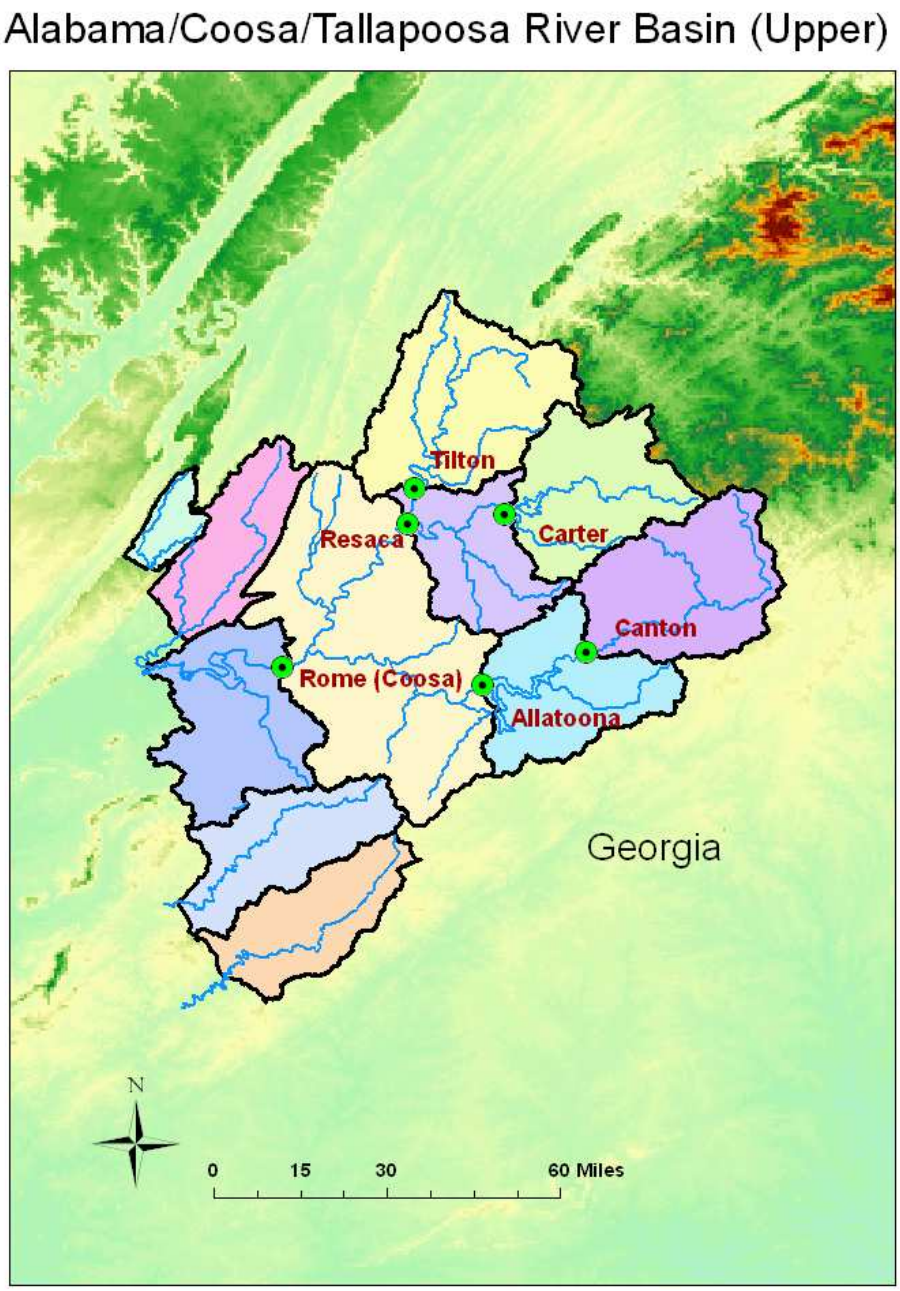

Figure 6.50: Map of Upper ACT Watersheds: Canton, Allatoona, Carter, Tilton, Resaca, and Rome.

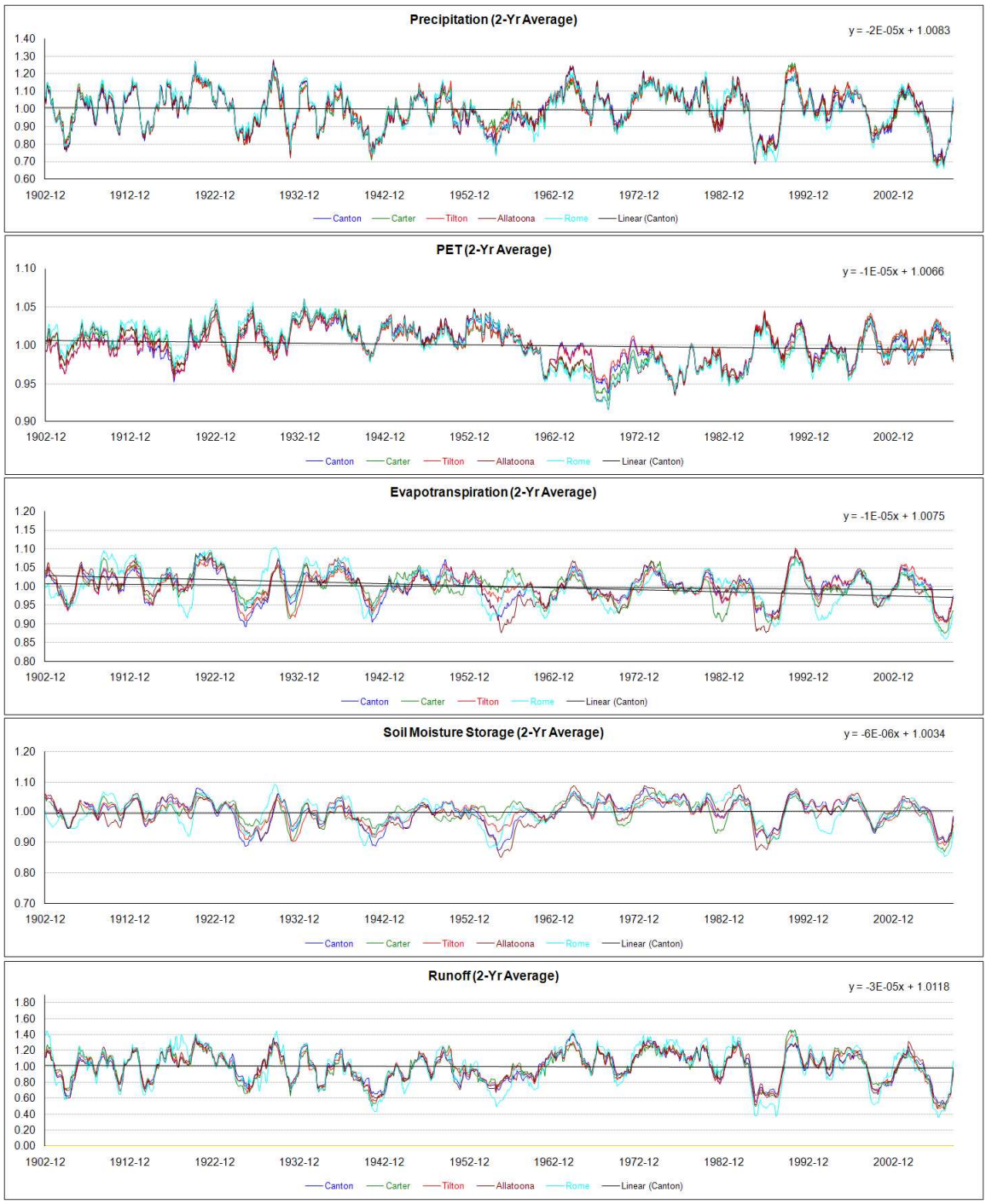

Figure 6.51: ACT Normalized, 2Yr Average Hydrologic Response (1901 - 2009).

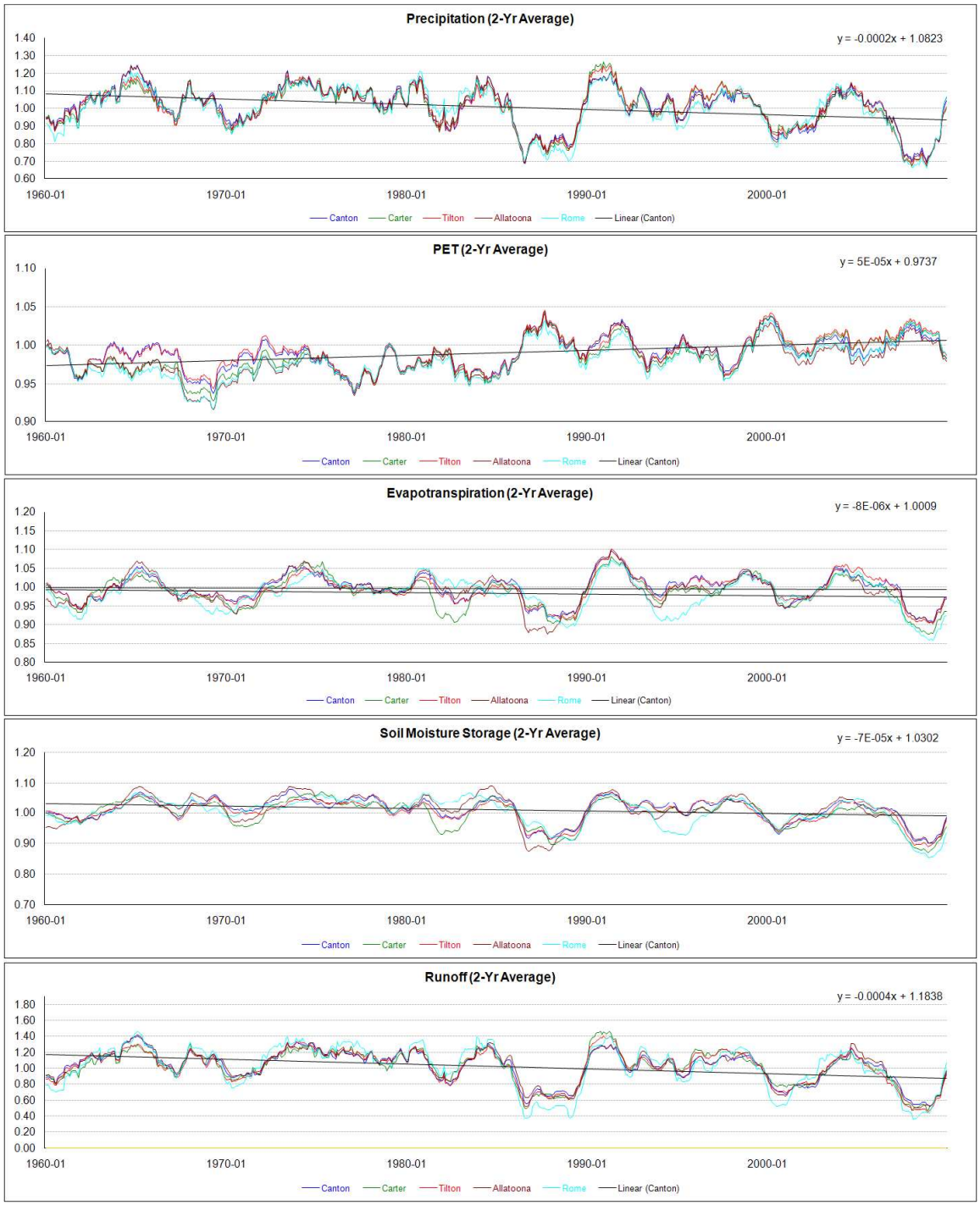

Figure 6.52: ACT Normalized, 2Yr Average Hydrologic Response (1960 - 2009).

Table 6.4 Slopes of Linear Trends for Normalized, 2Yr Average Hydrologic Variables in the upper ACT Basin.

	Canton	Carter	Tilton	Allatoona	Rome
	1901-2009 (unit: 10-4 of the mean per year)				
Precipitation	-2.04	-3.12	-2.40	-2.16	-5.64
PET	-1.20	-2.52	-0.84	-3.36	-4.08
Soil Moisture	-0.72	-1.08	-0.12	-0.48	-0.72
Runoff	-3.00	-2.28	-3.24	-0.72	-5.52
	1960-2009 (unit: 10-4 of the mean per year)				
Precipitation	-29.16	-23.76	-24.60	-27.84	-27.84
PET	6.48	10.68	7.44	8.40	9.72
Soil Moisture	-8.04	-9.96	-7.92	-9.12	-9.84
Runoff	-42.72	-43.32	-41.88	-43.92	-46.68
	Canton	Carter	Tilton	Allatoona	Rome
	1901-2009 (unit: percentage increase over 109 years)				
Precipitation	-2.224	-3.401	-2.616	-2.354	-6.148
PET	-1.308	-2.747	-0.916	-3.662	-4.447
Soil Moisture	-0.785	-1.177	-0.131	-0.523	-0.785
Runoff	-3.270	-2.485	-3.532	-0.785	-6.017
	1960-2009 (unit: percentage increase over 50 years)				
Precipitation	-14.580	-11.880	-12.300	-13.920	-13.920
PET	3.240	5.340	3.720	4.200	4.860
Soil Moisture	-4.020	-4.980	-3.960	-4.560	-4.920
Runoff	-21.360	-21.660	-20.940	-21.960	-23.340

6.4.2 Future Assessment

The future climate assessments consist of running the upper ACT watershed models under all A1B and A2 climate scenarios for the period from January 2000 through December 2099 (100 years) in monthly time steps. The future assessment also follows the same future assessment procedures described in previous sections.

Figures 6.53 and **6.54** show the assessment results in frequency curves and box plots of the Allatoona watershed. These figures lead to the following observations:

- On average (i.e., in the vicinity of the 50% percentile), precipitation is expected to decrease by 2% - 3% relative to the historical baseline for the upstream watersheds (Canton, Carter, and Tilton) but is not expected to change for the downstream watersheds (e.g., Rome). In addition, the precipitation distribution is expected to "stretch" becoming wetter and drier than that of the historical climate. This assertion holds for both the A1B and A2 scenarios, with the latter stretching the distribution farther.
- The median of the potential evapotranspiration is higher than the historical baseline for both A1B and A2 scenarios. In addition, the future PET is expected to increase faster for higher PET values than for lower PET values (similarly to other basins).
- The median of the soil moisture decreases for all watersheds under both A1B and A2 scenarios. The median of the runoff also decreases under both scenarios. The upstream watersheds (Canton, Carter, and Tilton) are expected to experience more soil moisture reductions than the downstream watershed (Rome). In addition, much like for precipitation, the future soil moisture distributions are also expected to "stretch" on both ends for all watersheds.

The box plots for the Allatoona watershed are shown on **Figures 6.55** and **6.56**. The following observations can be made:

- Mean watershed precipitation exhibits clear decreasing trends from April through September for both A1B *and* A2 scenarios by about 7% - 14%. It also shows mild increasing trends from December through March for A1B scenarios and from December to January for A2 scenarios.
- Future PET exhibits a higher mean and a wider range than historical PET from February to September, with the largest percentage changes observed in April and May. For these two months, the future mean PET is higher than the historical PET by up to 15% - 20%, while the quartile range of the future distribution exceeds that of the historical by nearly 10% - 20%.
- Future soil moisture is clearly lower than historical in almost all months. The change is more pronounced in August and September. Under the A1B scenario, the largest soil moisture reduction is up to 8%, while under the A2 scenario, up to 10%.
- Future runoff is drier under both A1B and A2 scenarios in most months. The change is more pronounced in August and September. Under the A1B scenario, the largest runoff reduction is 20%, while under the A2 scenario, up to 25%. Runoff increases only in December under the A1B scenario, by about 2%.
- Comparing the future response of the upper ACT basin with that of the ACF, OOA, and SO basins, one can conclude that (1) most watersheds in all four basins are expected to experience precipitation reduction during summer and early fall (June, July, August, and September); (2) all watersheds show significant PET increases; (3) summer PET increases are larger than those of winter in absolute value; (4) upstream watersheds

show higher PET increases in late spring (April and May); (5) runoff in all watersheds is expected to decrease for most months (especially in summer).

Results for all upper ACT watersheds are presented in **Appendix A**.

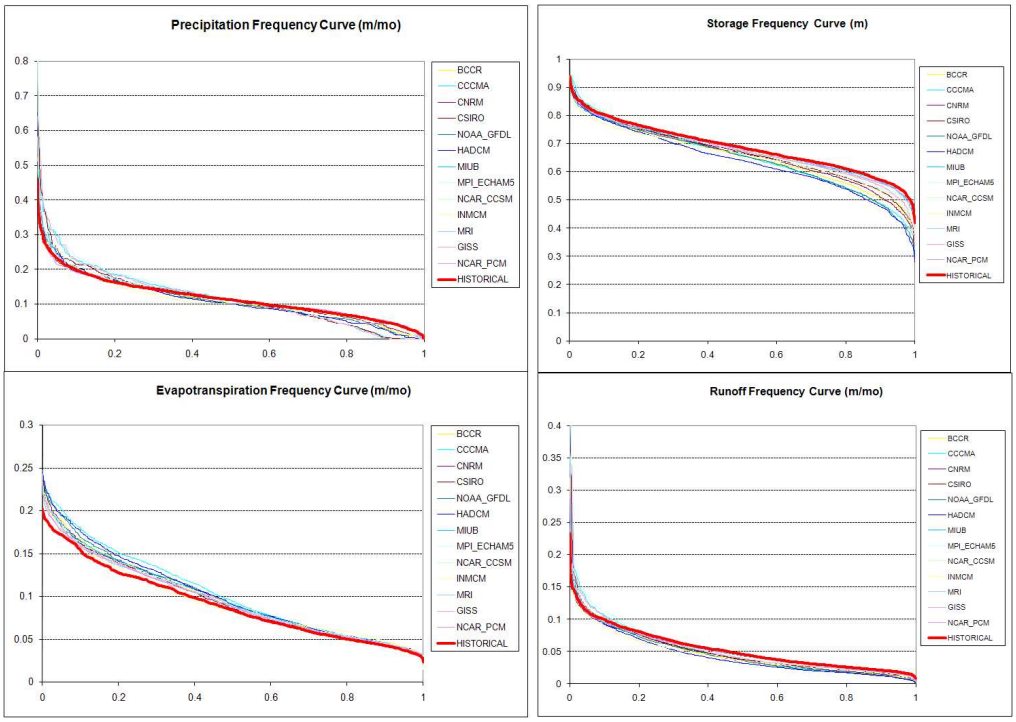

Figure 6.53: A1B Climate Scenarios (2000-2099), Allatoona, Frequency Curves.

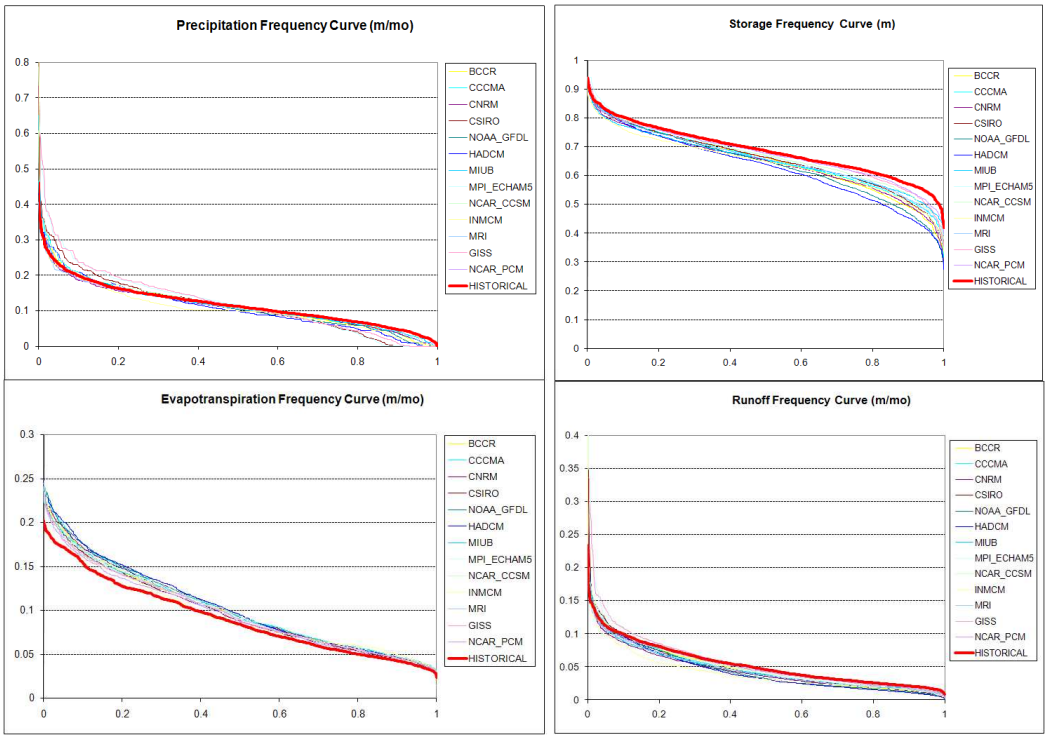

Figure 6.54: A2 Climate Scenarios (2000-2099), Allatoona, Frequency Curves.

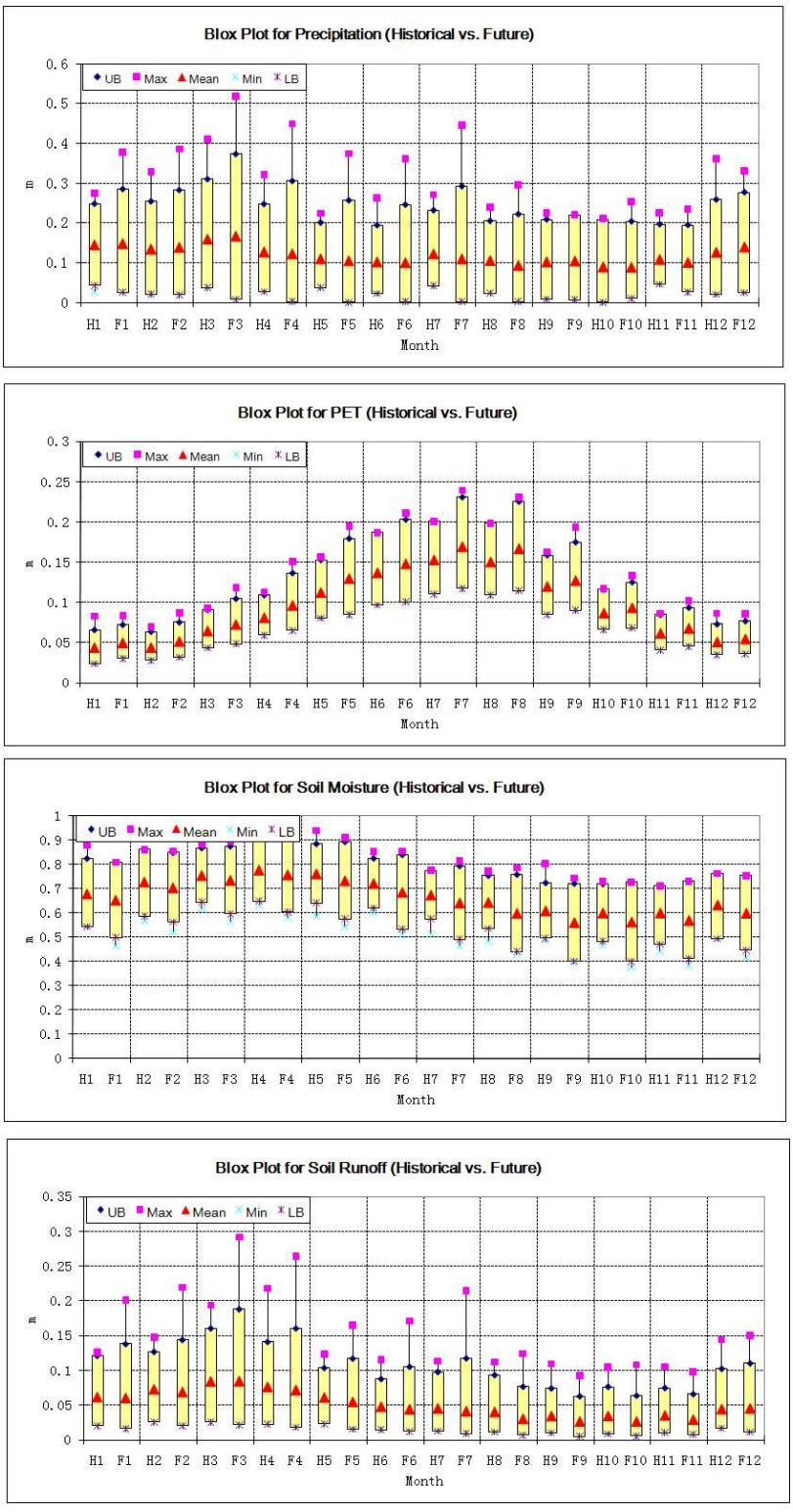

Figure 6.55: Monthly Historical vs. Future (A1B) Watershed Response, Allatoona. (Unit: Precipitation – m/mo; PET – m/mo; Soil Moisture – m; Runoff m/mo.)

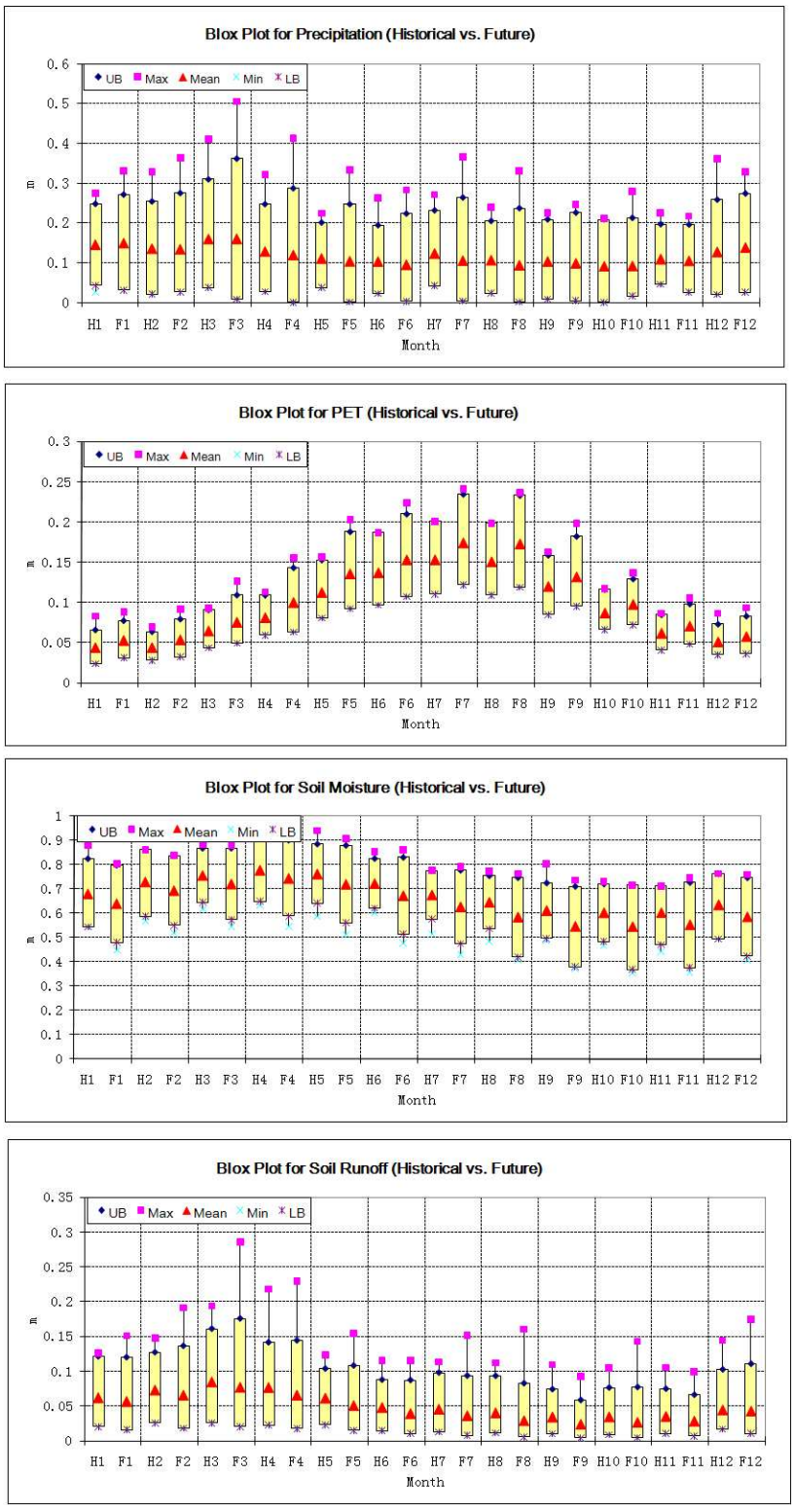

Figure 6.56: Monthly Historical vs. Future (A2) Watershed Response, Allatoona. (Unit: Precipitation – m/mo; PET – m/mo; Soil Moisture – m; Runoff m/mo.)

CHAPTER 7

CONCLUSIONS AND RECOMMENDATIONS

7.1 Scientific Contributions and Conclusions

This research used an integrative approach to assess the hydrologic impacts of climate change for four river basins in Georgia. The study combines *(1)* downscaling and assessment of future precipitation and temperature scenarios, and *(2)* hydrologic assessments for each sub-watershed. The study has made several important scientific contributions:

- Development and evaluation of a new statistical downscaling method (joint variable statistical downscaling) for downscaling GCM outputs (**Chapter 3**).
- Calibration of lumped conceptual watershed models developed by Georgakakos et al. (2010) in monthly time steps for all major Georgia basins where unimpaired flow observations have been developed (**Chapter 4**).
- Development modified Hamon PET equations to estimate the PET by using maximal month temperature and calibration of watershed model on weekly and daily time scales (**Chapter 4**).
- Development of model parameter regionalization procedures based on measurable watershed characteristics related to land cover, soil properties, and geomorphologic features (**Chapter 5**).
- Assessment of the hydrologic impacts of climate change on Georgia basins using A1B and A2 scenarios (**Chapter 6**).

The main findings of the assessment are summarized below:

- Historical precipitation of the 20th century and the early 21st century (1901-2009) in Georgia basins shows different long-term trends over the last 109 years. Some watersheds show a mild decreasing long-term trend (e.g., the upper ACT watersheds) and some show a mild increasing trend (e.g., the OOA watersheds). The precipitation increases are generally less than 5% of the early 20th century values; and precipitation decreases are generally less than 6% of the early 20th century values.
- Historical precipitation of the most recent 50 years (1960-2009) in Georgia shows a consistent decreasing long-term trend.
- Historical potential evapotranspiration of the 20th century and the early 21st century (1901-2009) shows a clearly decreasing long-term trend over Georgia basins, while PET decreases by about 1% - 5% of its early 20th century value.
- By contrast, historical potential evapotranspiration over the most recent 50 years (1960-2009) shows a consistent increasing trend. PET increases are about 1% - 5% of the early 1960 PET values.
- As a result of precipitation reductions and PET increases in the 50-year assessment period, runoff decreases by about 10% - 25% of its 1960 level.
- Assessments with 26 IPCC future climate scenarios (A1B and A2 scenarios; 2000-2099) generally do not indicate any long-term change in mean precipitation. Exceptions are few and include the watersheds at Harwell, Canton, Carter, Allatoona, and Tilton, where precipitation mildly decreases. In addition, the same IPCC scenarios indicate that all future precipitation distribution are expected to "stretch," showing wetter and drier conditions than those of the historical climate.

- Future potential evapotranspiration (with its strong dependence on daily maximum temperature) shows a consistently increasing future trend (see chapters for slope values of the trends for different basins) for all Georgia basins and under both A1B and A2 scenarios.
- As a result of increasing PET and decreasing precipitation, soil moisture exhibits a clear declining trend under future climates. Future soil moisture is expected to be lower than historical in almost all months (see chapters for slope values of the trends for different basins). The change is more pronounced for dry years and in the southern watersheds and is a foreboding indicator of adverse agricultural impacts.
- Future runoff generally decreases in summer months (June, July, and August) for most Georgia watersheds and under both A1B and A2 scenarios (see chapters for slope values of the trends for different basins).
- Generally, for all Georgia watersheds under A2 scenarios, future runoffs show greater reductions than those under the A1B scenarios.
- By comparison, for ACF and OOA basins, the southern watersheds are expected to have more summer runoff reductions than northern watersheds. However, for the SO basin, runoff reductions in downstream watersheds are less than upstream watersheds.
- In the southern watersheds of the OOA and ACF basins, a noticeable reduction in the mean runoff generally begins in January and extends through July (or through September for some watersheds) under A1B *and* A2 scenarios. This runoff reduction has implications for all water resources uses.

7.2 Recommendations for Future Research

General useful extensions of the current study include *(1)* assessment of groundwater resources impacts; *(2)* conjunctive assessment of surface water and groundwater resources; *(3)* assessments pertaining to daily time steps; and *(4)* assessments pertaining to water resources impacts such as water supply, hydropower, lake levels, and ecology.

More specific extensions are described below.

The JVSD downscaling method can be extended to include more climatic variables (e.g., solar radiation, wind speed, and air pressure) from future GCM outputs.

The issue of combined surface water - groundwater assessments is critical for Georgia and the southeast US because of the direct hydraulic linkage of these two systems. A follow-up study addressing the watershed model changes required at different temporal scales (from monthly to weekly to or daily) would enhance the simulation capability of the hydrologic model.

Hurricanes impact summer and early fall precipitation in the southeast United States, spawning tropical storms and destructive floods. Recent studies indicate that the frequency and severity of hurricanes will most likely intensify by warming sea temperatures (Bender et al., 2010). Future assessments would benefit by a more quantitative understanding of the impact of hurricanes on summer and early fall precipitation and increase the value of climate model precipitation scenarios in hurricane-prone areas.

Finally, daily and possibly sub-daily assessments that quantify the impact of climate change associated with flooding are needed. This effort would mainly require that hydrologic models be extended and re-calibrated to account for hydrologic processes that become important at finer time scales. This effort is currently on-going.

APPENDIX A

HISTORICAL (BASELINE) AND FUTURE HYDROLOGIC ASSESSMENTS RESULTS

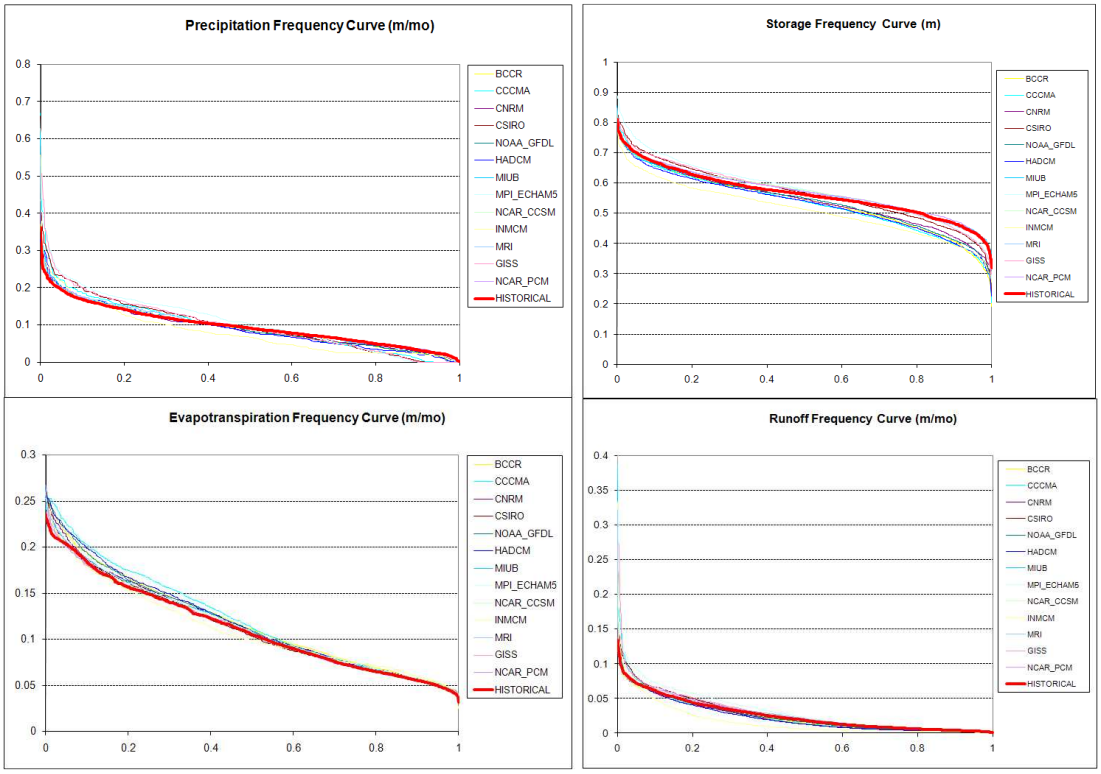

Figure A.1: A1B Climate Scenarios (2000-2099), OOA - Lower Oconee, Frequency Curves.

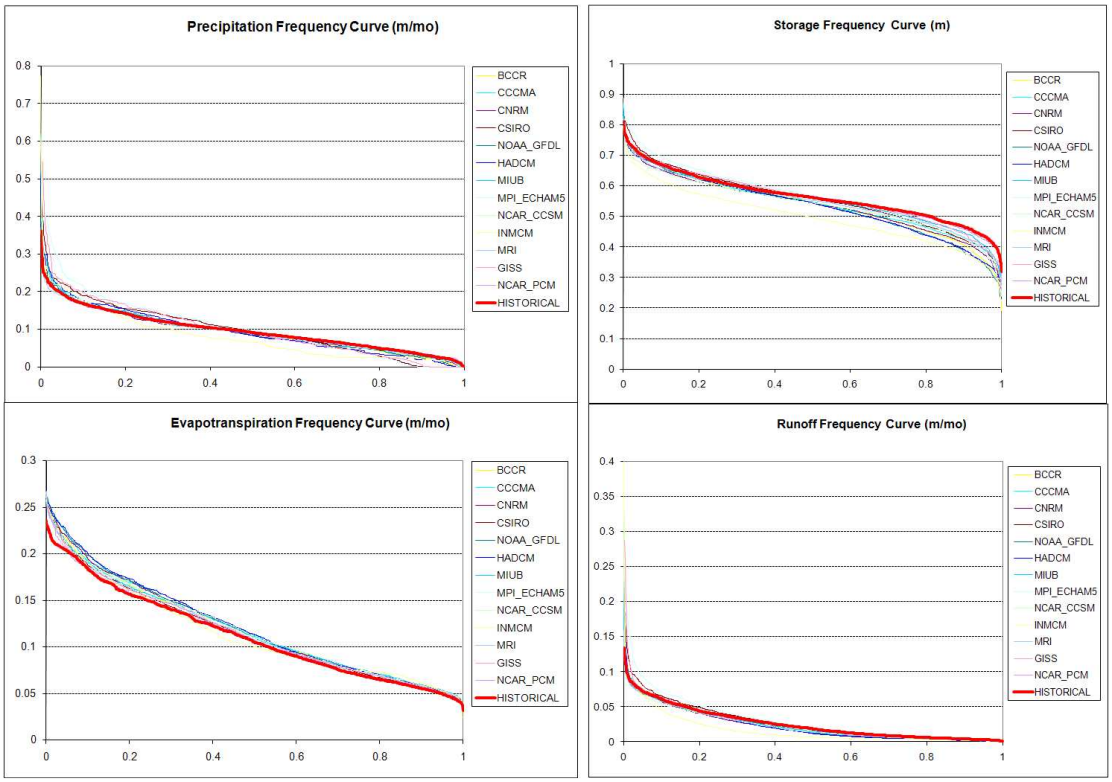

Figure A.2: A2 Climate Scenarios (2000-2099), OOA - Lower Oconee, Frequency Curves.

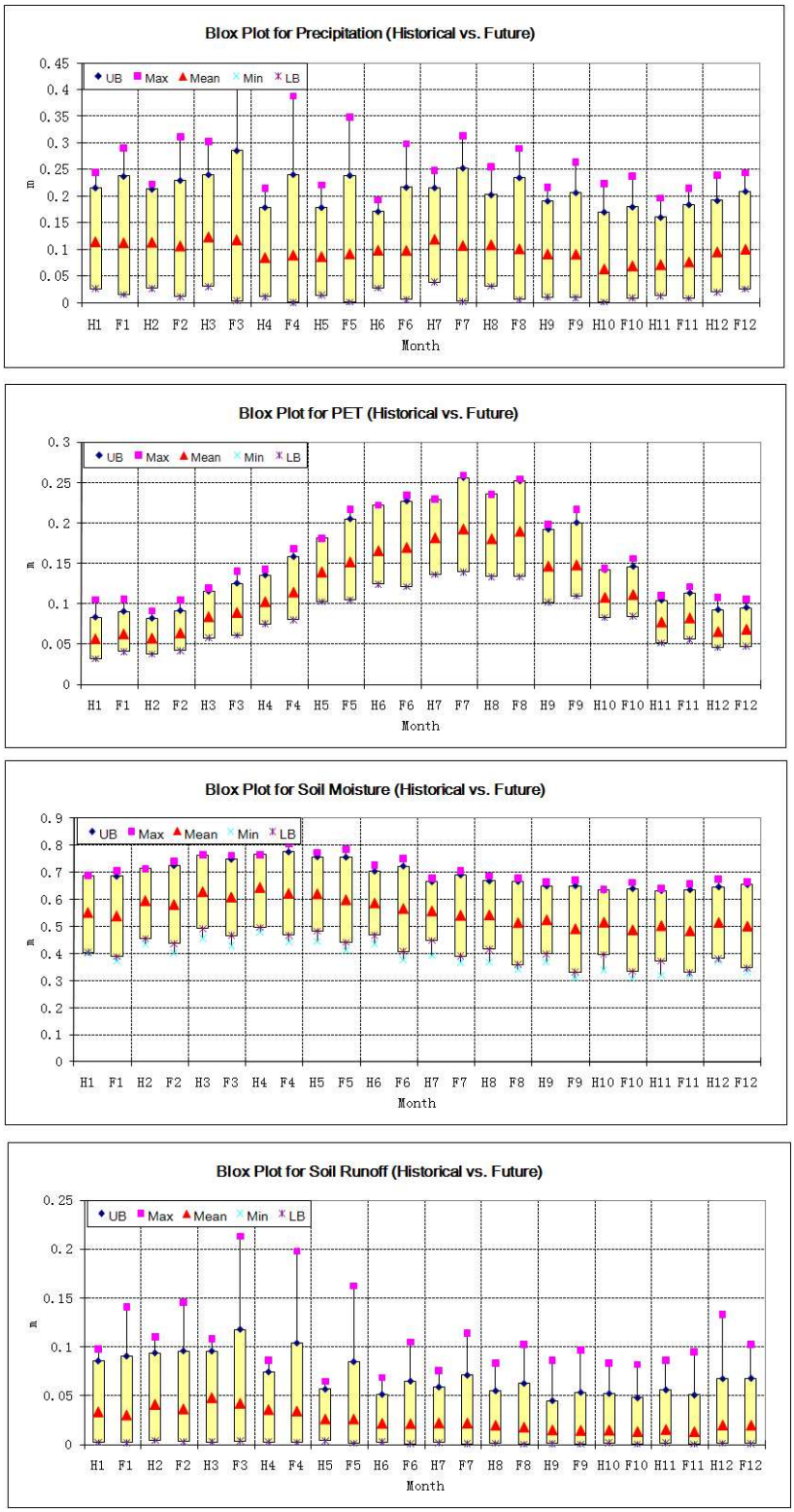

Figure A.3: Monthly Historical vs. Future (A1B) Watershed Response, OOA - Lower Oconee. (Unit: Precipitation – m/mo; PET – m/mo; Soil Moisture – m; Runoff m/mo.)

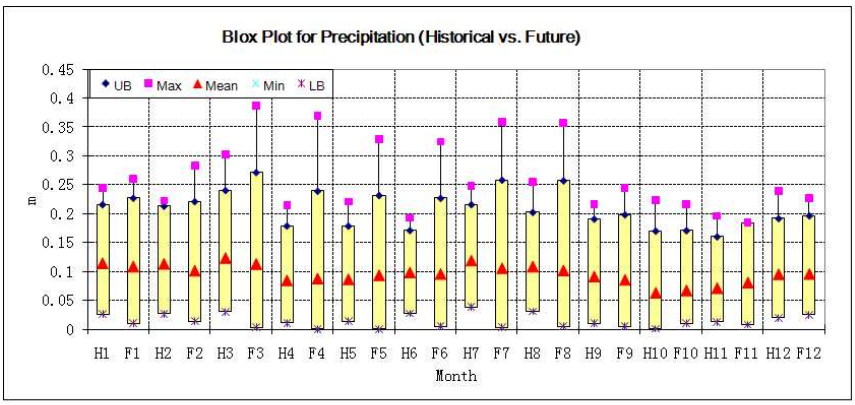

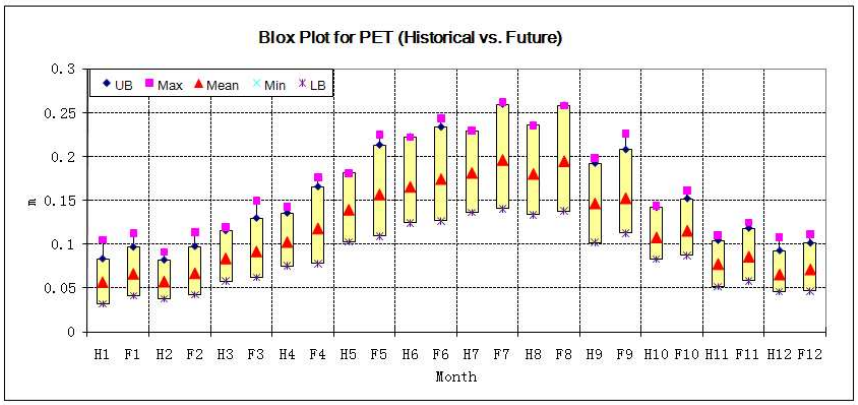

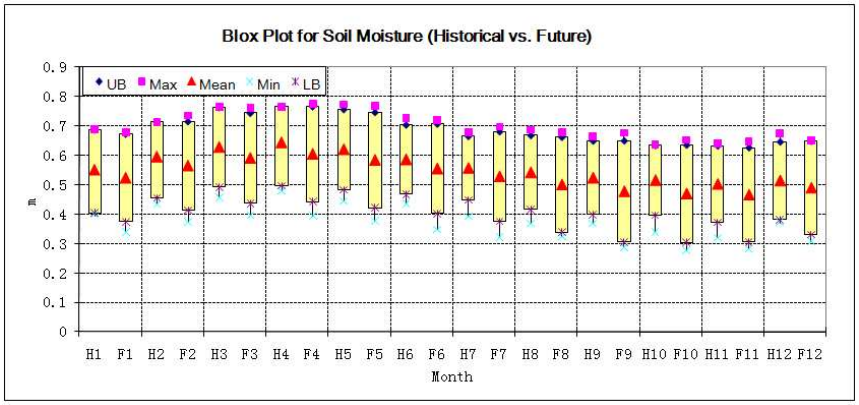

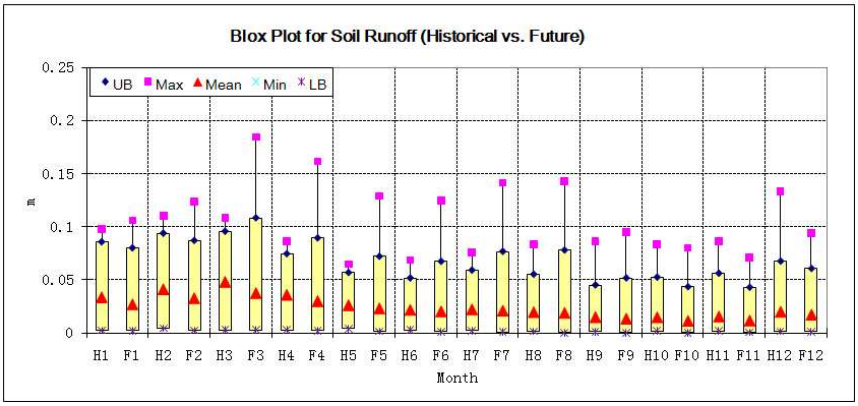

Figure A.4: Monthly Historical vs. Future (A2) Watershed Response, OOA - Lower Oconee. (Unit: Precipitation – m/mo; PET – m/mo; Soil Moisture – m; Runoff m/mo.)

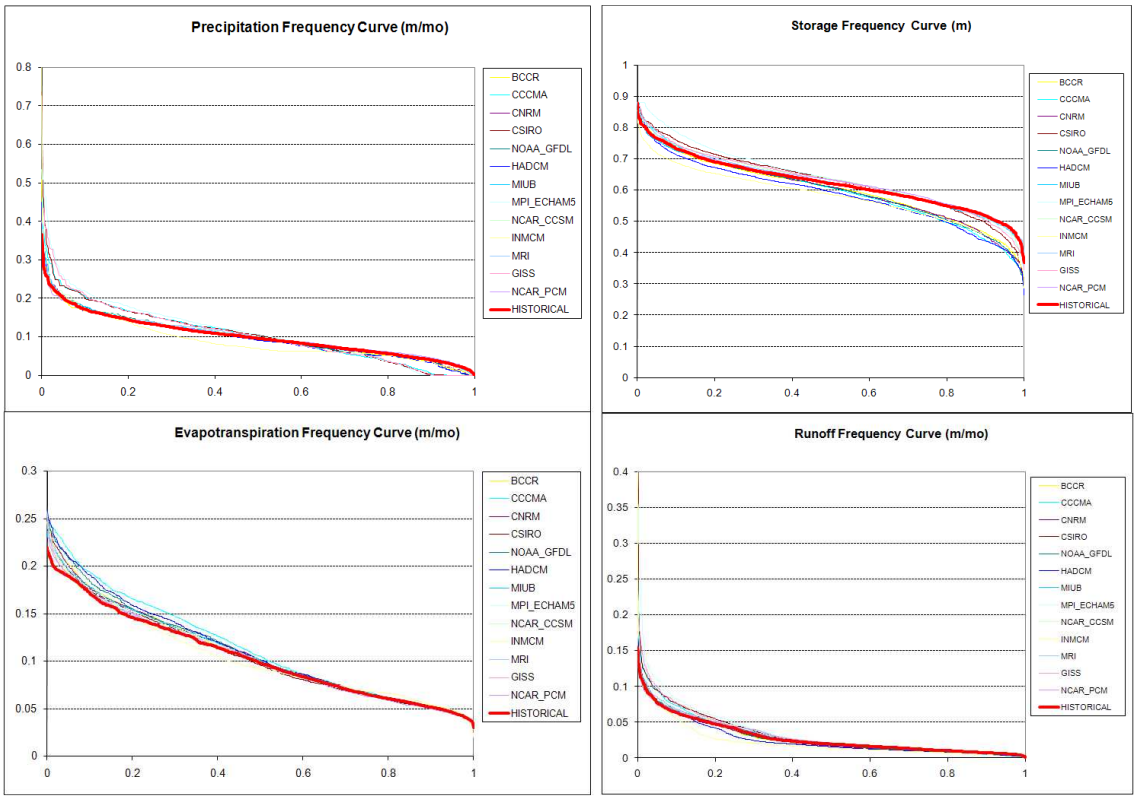

Figure A.5: A1B Climate Scenarios (2000-2099), OOA - Upper Ocmulgee, Frequency Curves.

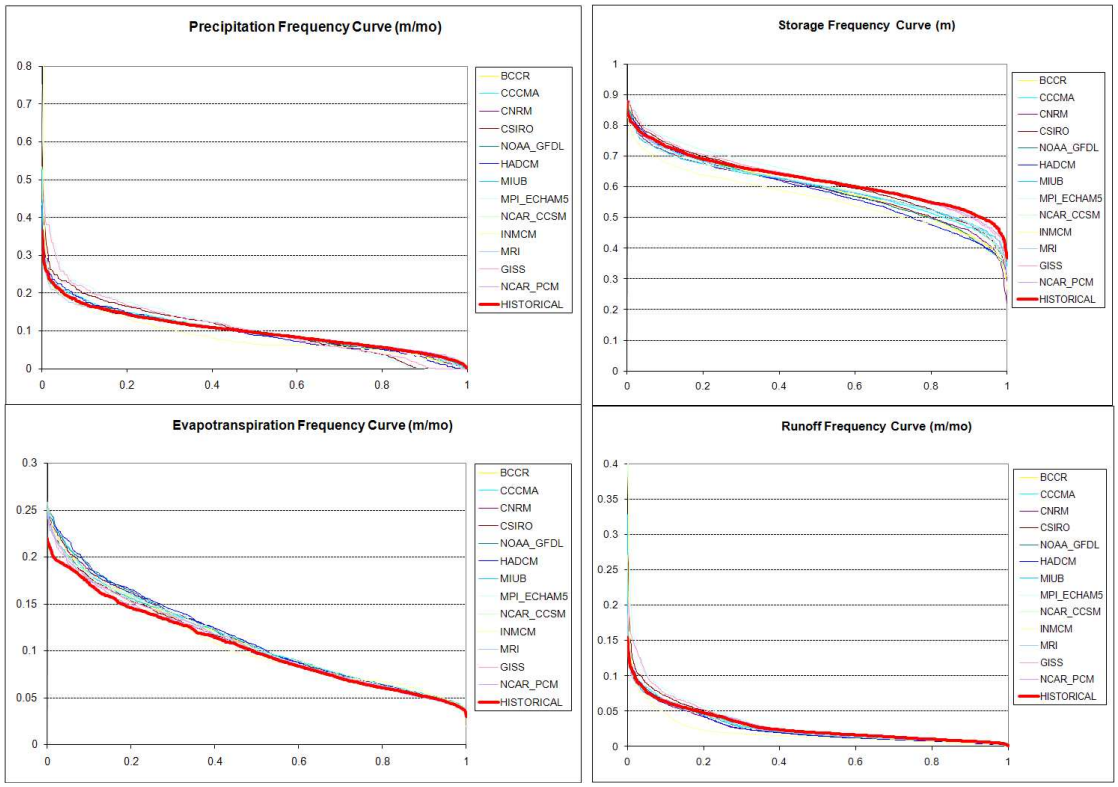

Figure A.6: A2 Climate Scenarios (2000-2099), OOA - Upper Ocmulgee, Frequency Curves.

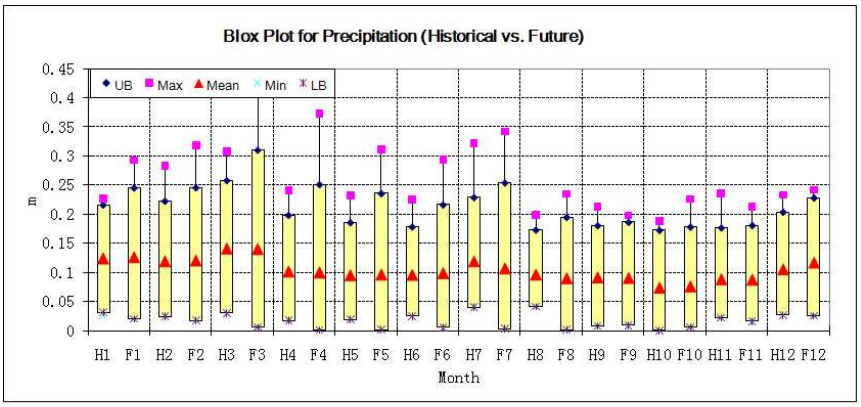

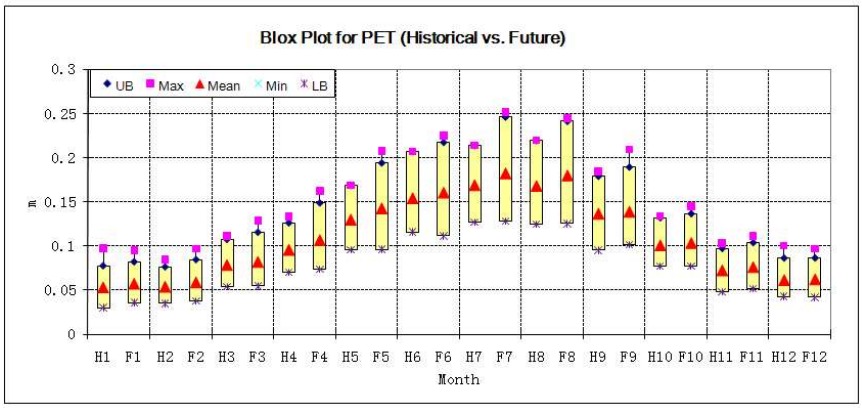

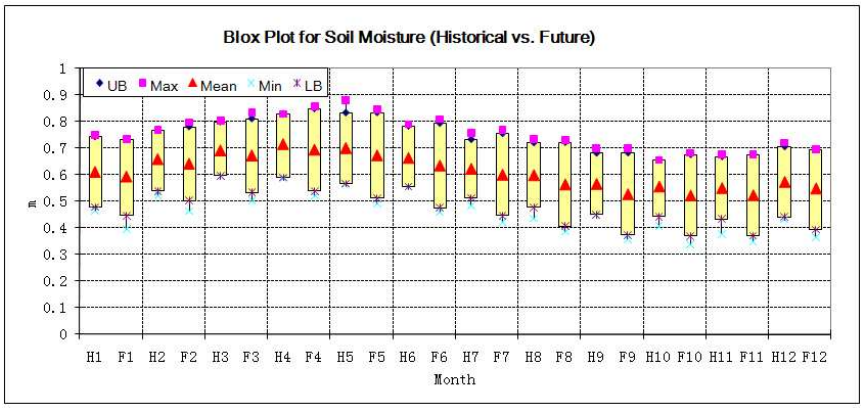

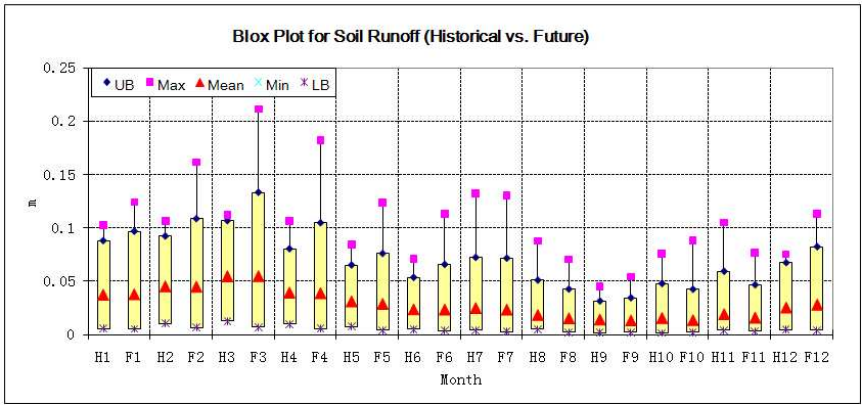

Figure A.7: Monthly Historical vs. Future (A1B) Watershed Response, OOA - Upper Ocmulgee. (Unit: Precipitation – m/mo; PET – m/mo; Soil Moisture – m; Runoff m/mo.)

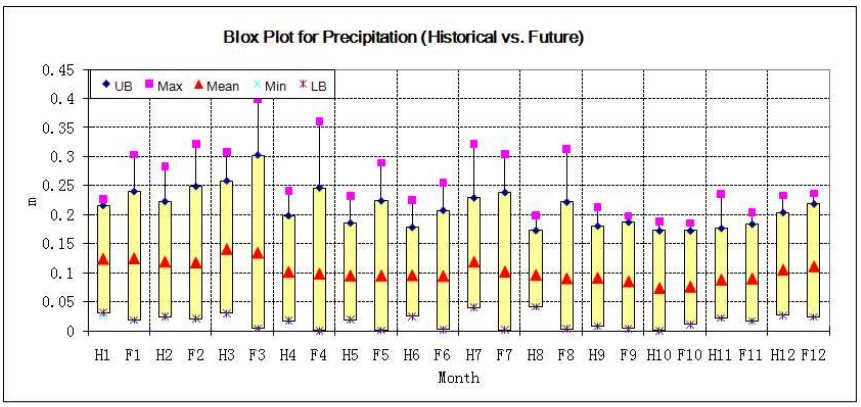

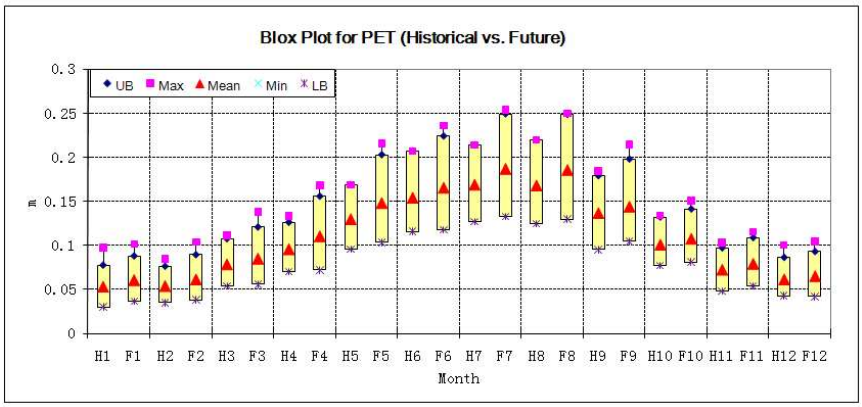

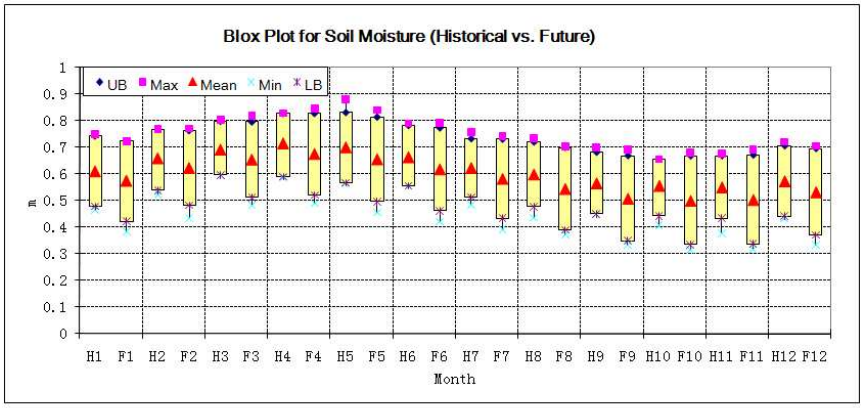

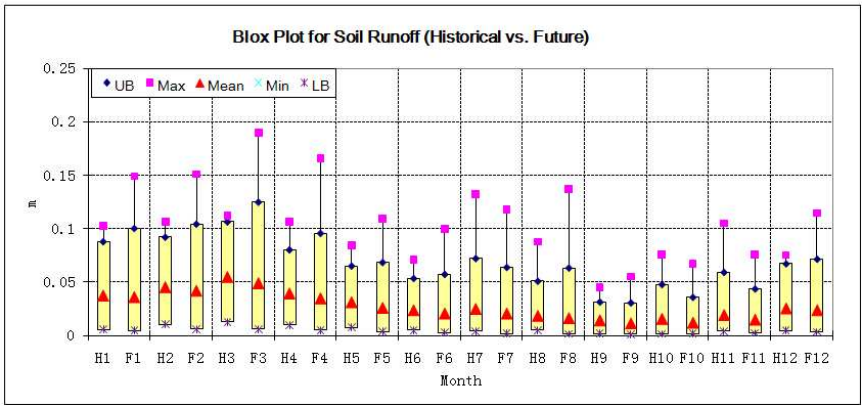

Figure A.8: Monthly Historical vs. Future (A2) Watershed Response, OOA - Upper Ocmulgee. (Unit: Precipitation – m/mo; PET – m/mo; Soil Moisture – m; Runoff m/mo.)

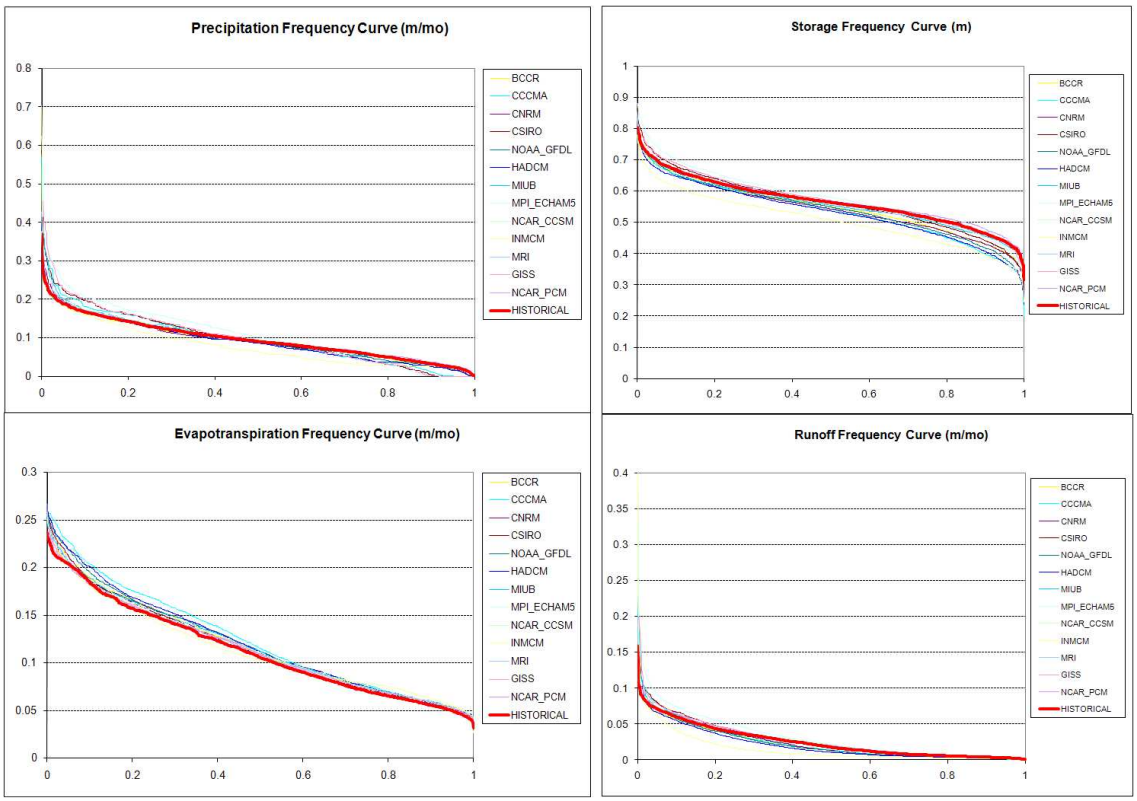

Figure A.9: A1B Climate Scenarios (2000-2099), OOA - Lower Ocmulgee, Frequency Curves.

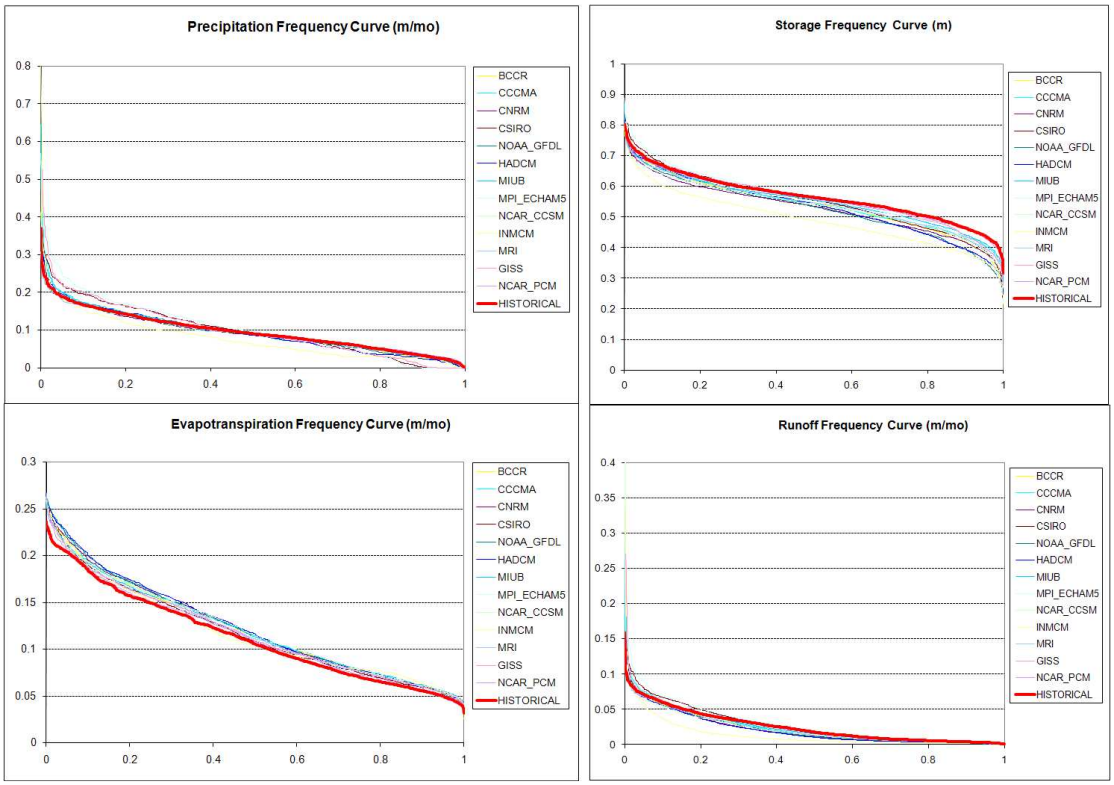

Figure A.10: A2 Climate Scenarios (2000-2099), OOA - Lower Ocmulgee, Frequency Curves.

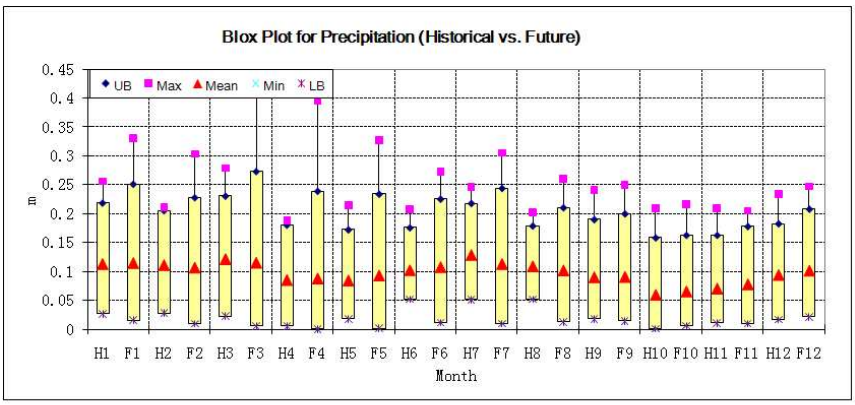

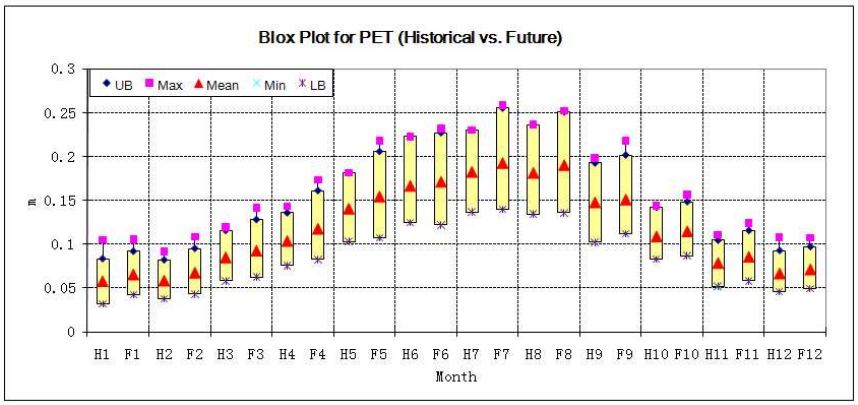

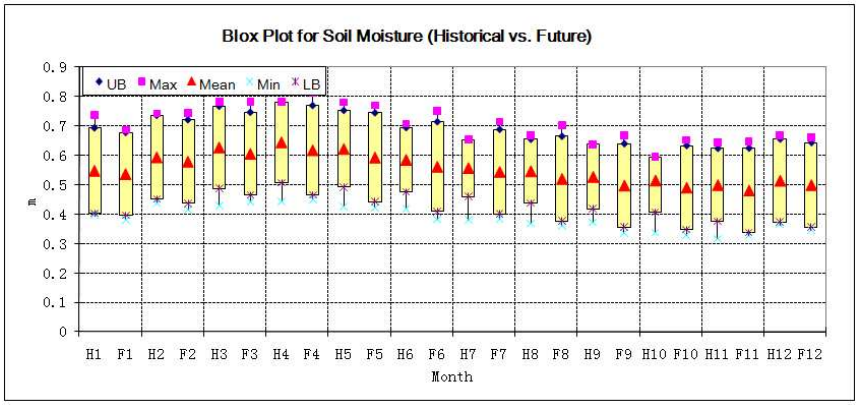

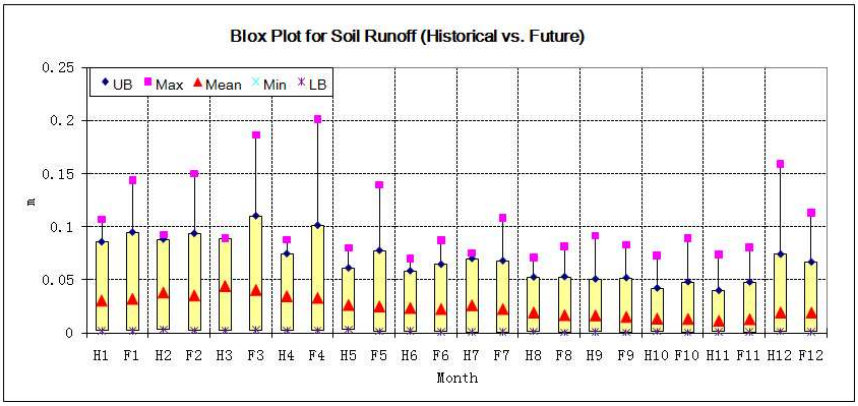

Figure A.11: Monthly Historical vs. Future (A1B) Watershed Response, OOA - Lower Ocmulgee. (Unit: Precipitation – m/mo; PET – m/mo; Soil Moisture – m; Runoff m/mo.)

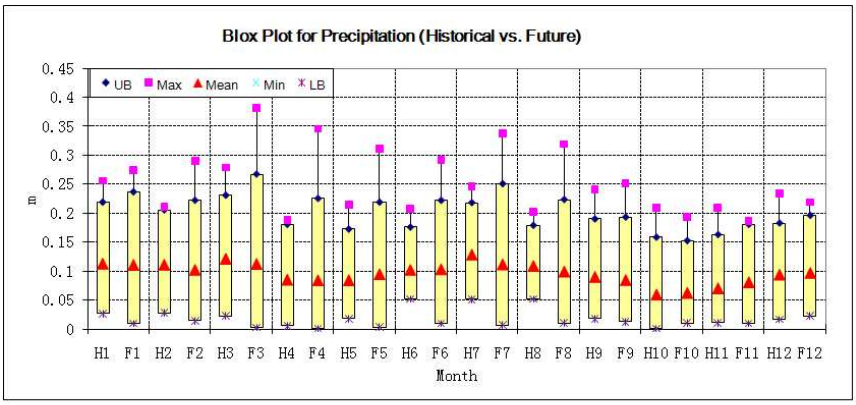

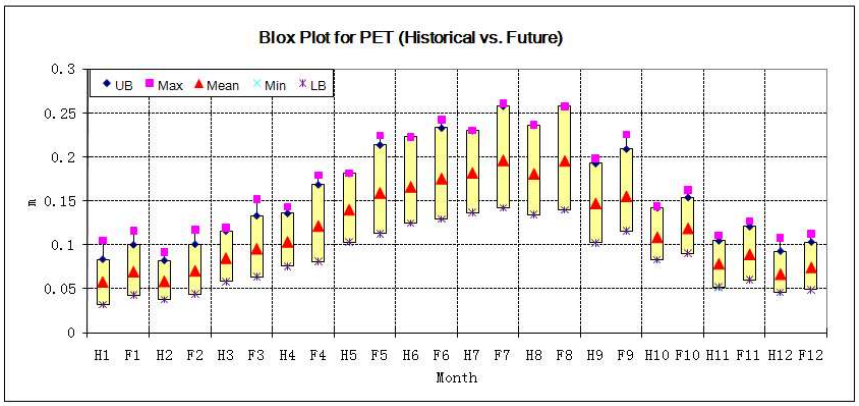

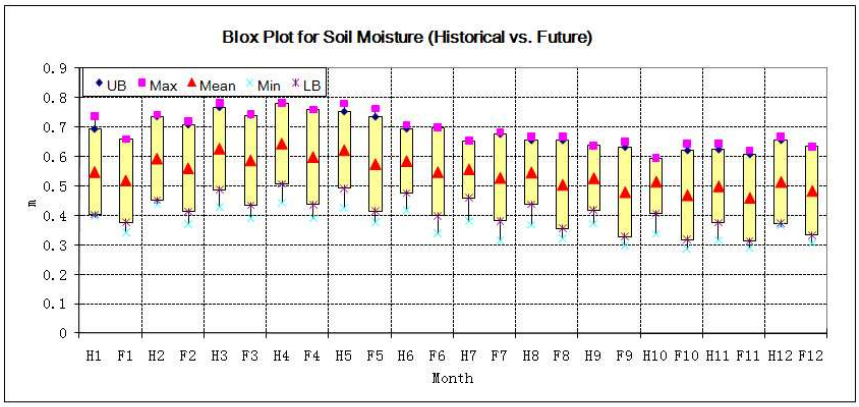

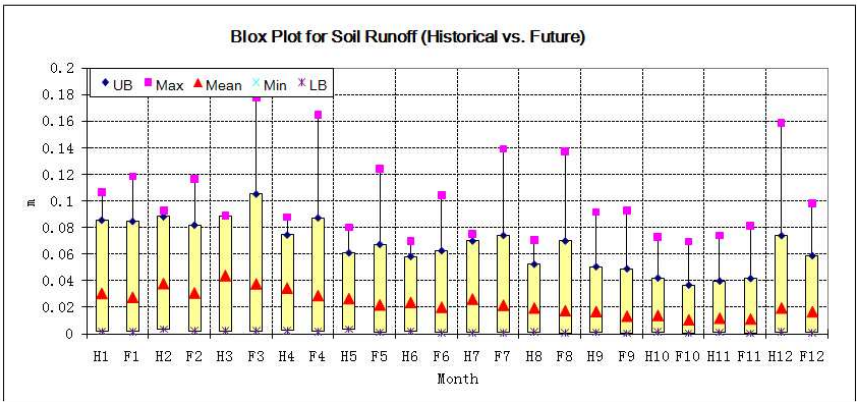

Figure A.12: Monthly Historical vs. Future (A2) Watershed Response, OOA - Lower Ocmulgee. (Unit: Precipitation – m/mo; PET – m/mo; Soil Moisture – m; Runoff m/mo.)

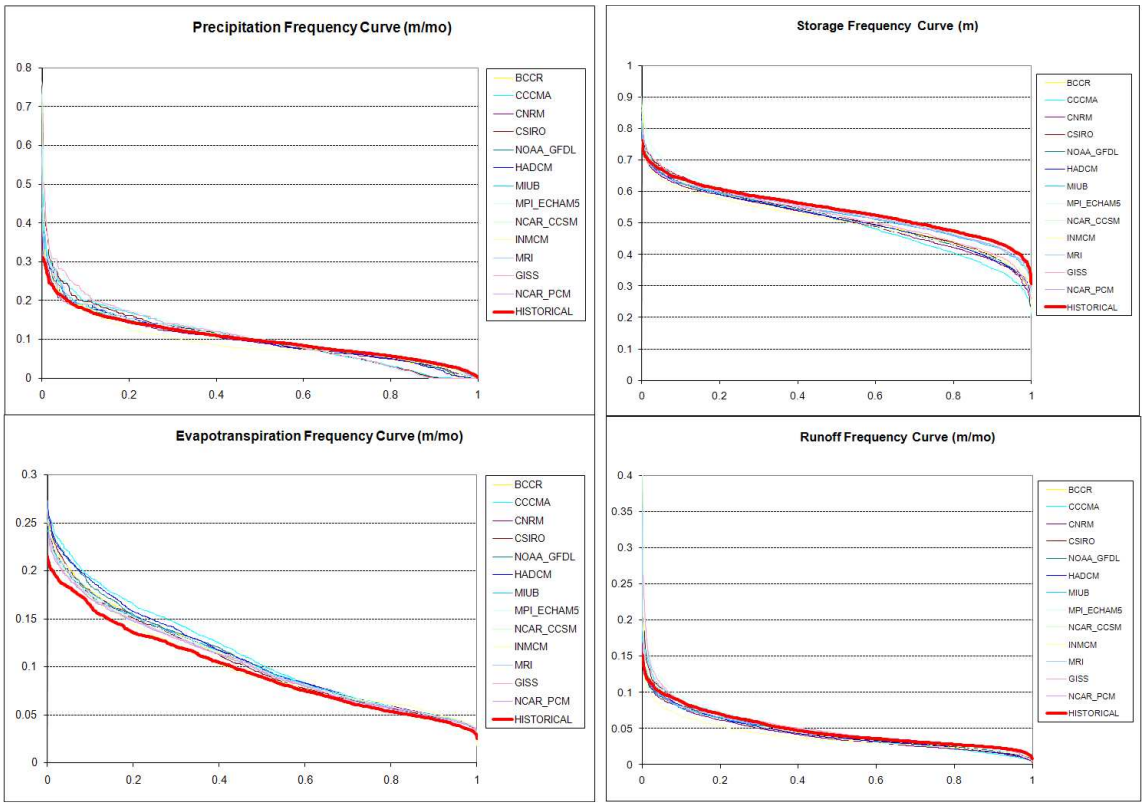

Figure A.13: A1B Climate Scenarios (2000-2099), SO - Russell, Frequency Curves.

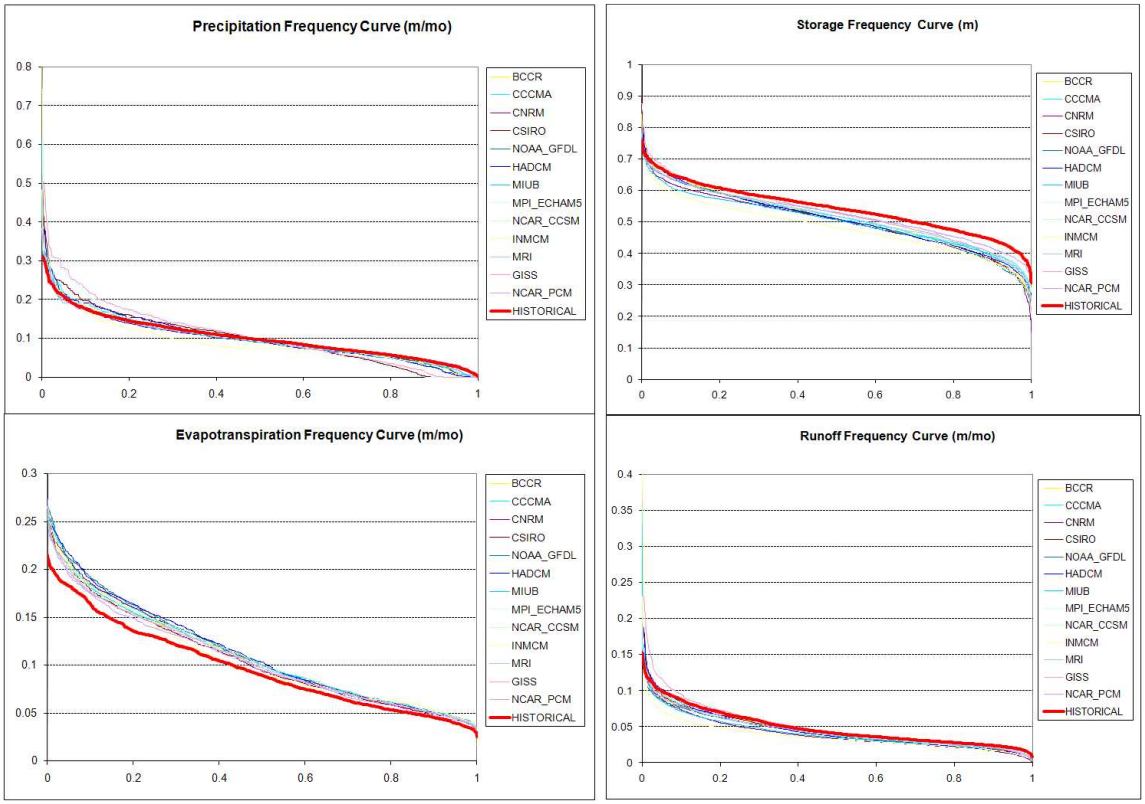

Figure A.14: A2 Climate Scenarios (2000-2099), SO - Russell, Frequency Curves.

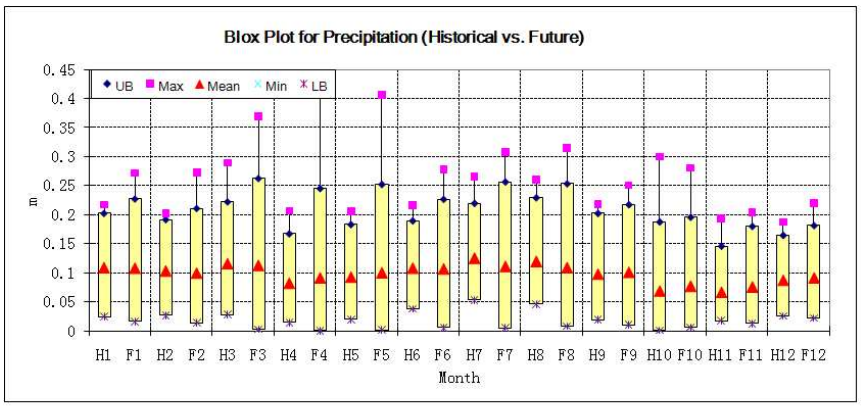

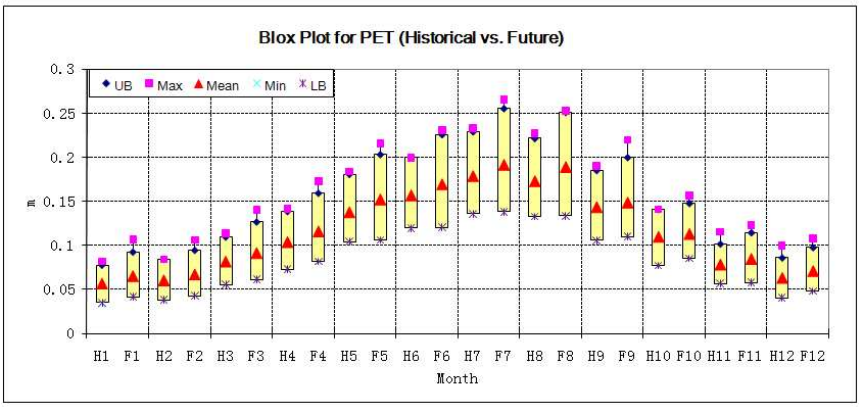

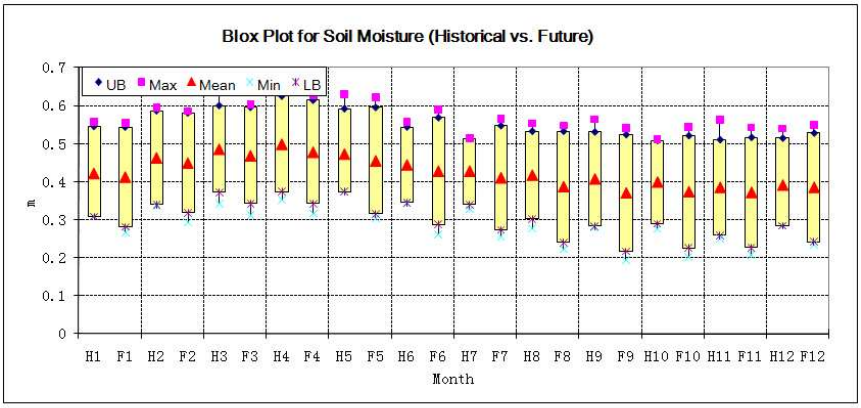

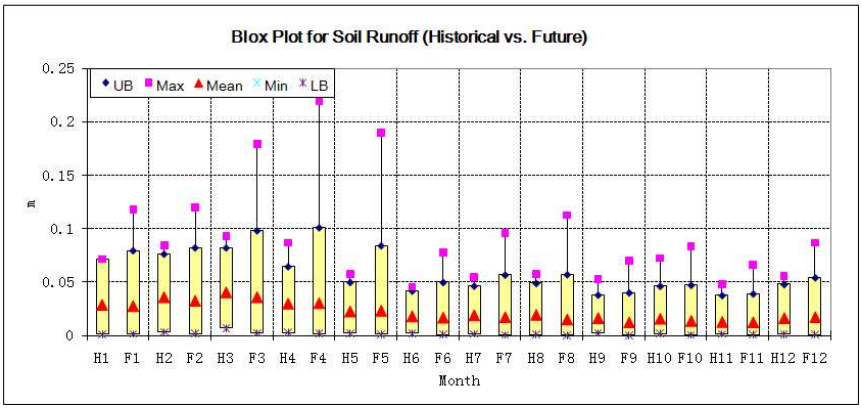

Figure A.15: Monthly Historical vs. Future (A1B) Watershed Response, SO - Russell. (Unit: Precipitation – m/mo; PET – m/mo; Soil Moisture – m; Runoff m/mo.)

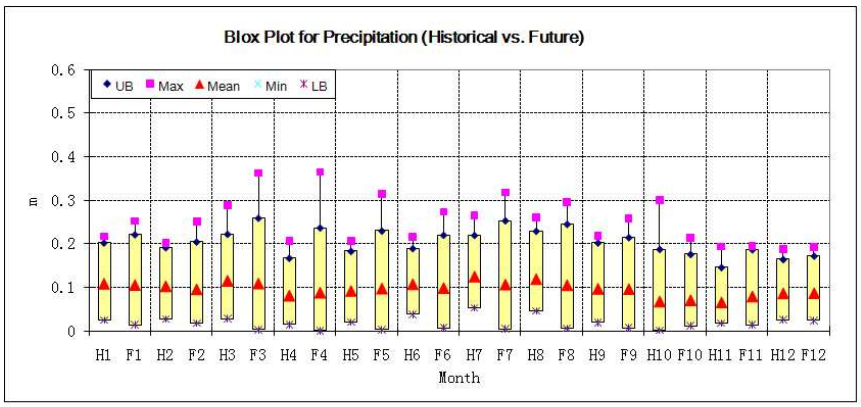

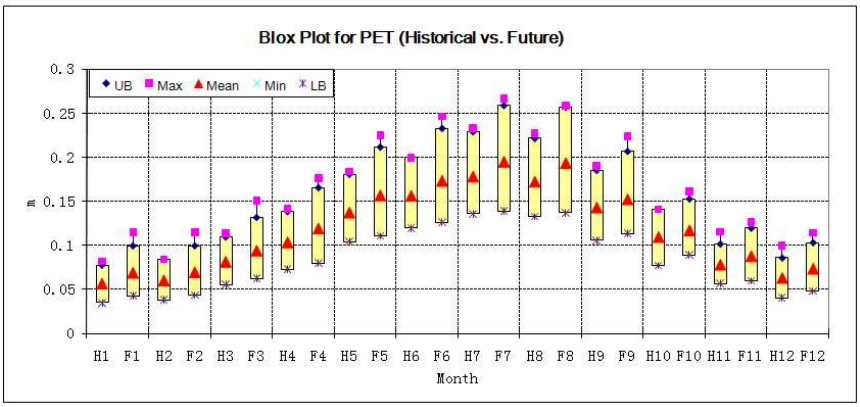

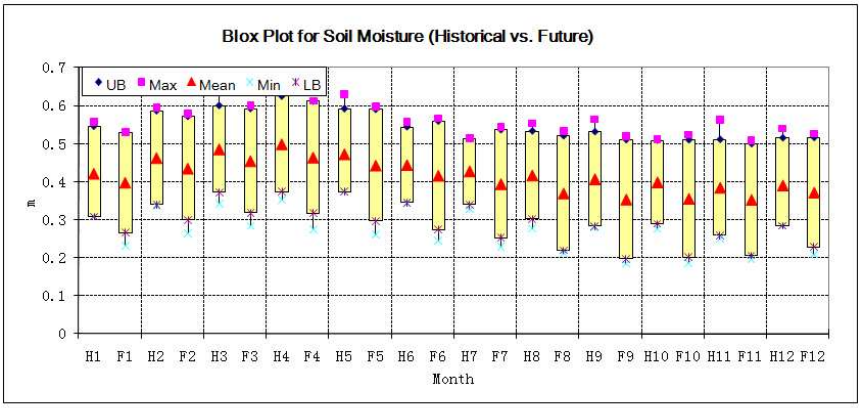

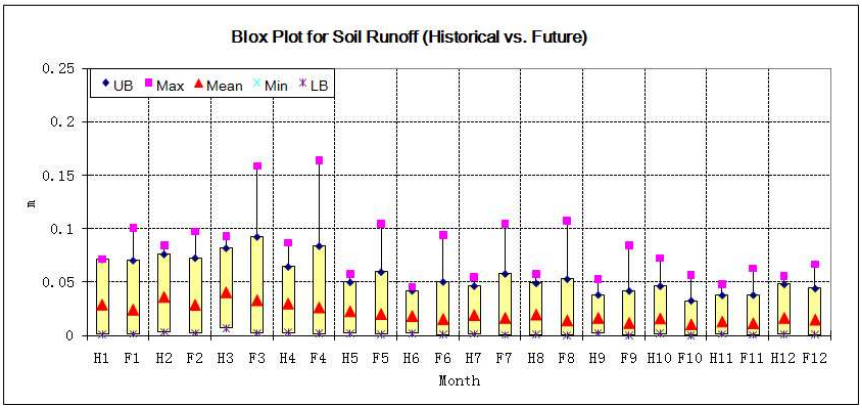

Figure A.16: Monthly Historical vs. Future (A2) Watershed Response, SO - Russell. (Unit: Precipitation – m/mo; PET – m/mo; Soil Moisture – m; Runoff m/mo.)

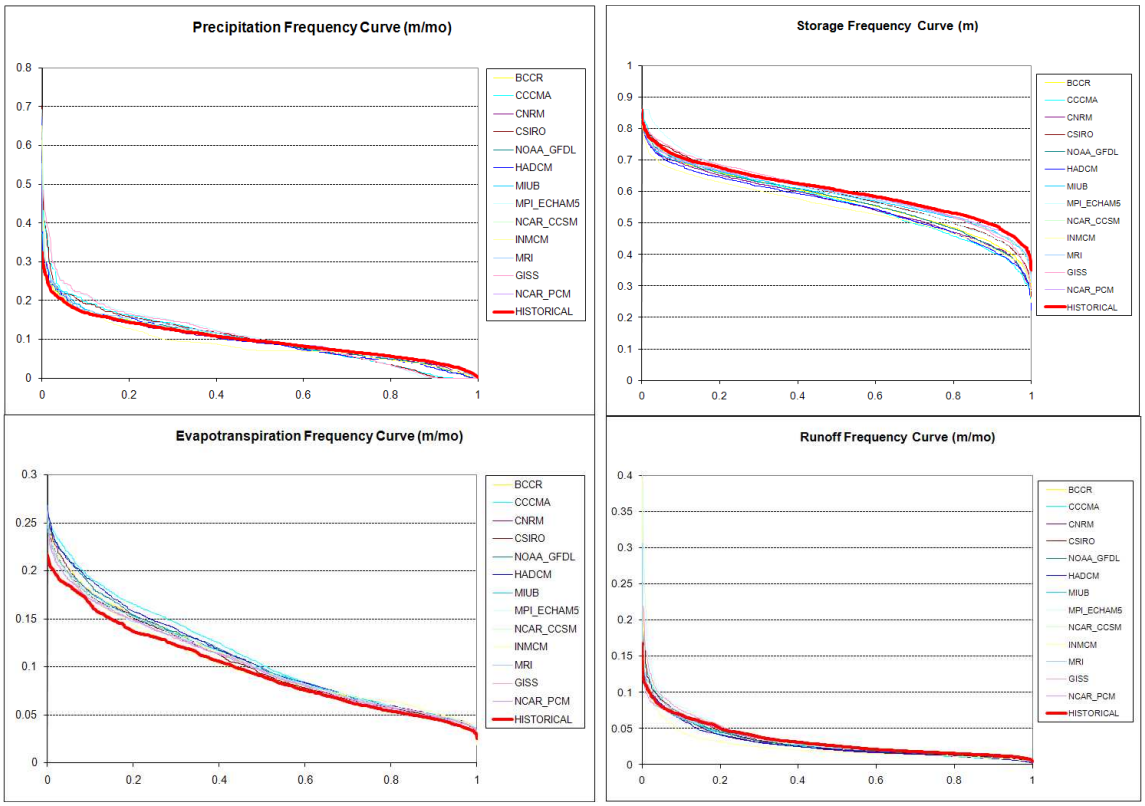

Figure A.17: A1B Climate Scenarios (2000-2099), SO - Thrmnd, Frequency Curves.

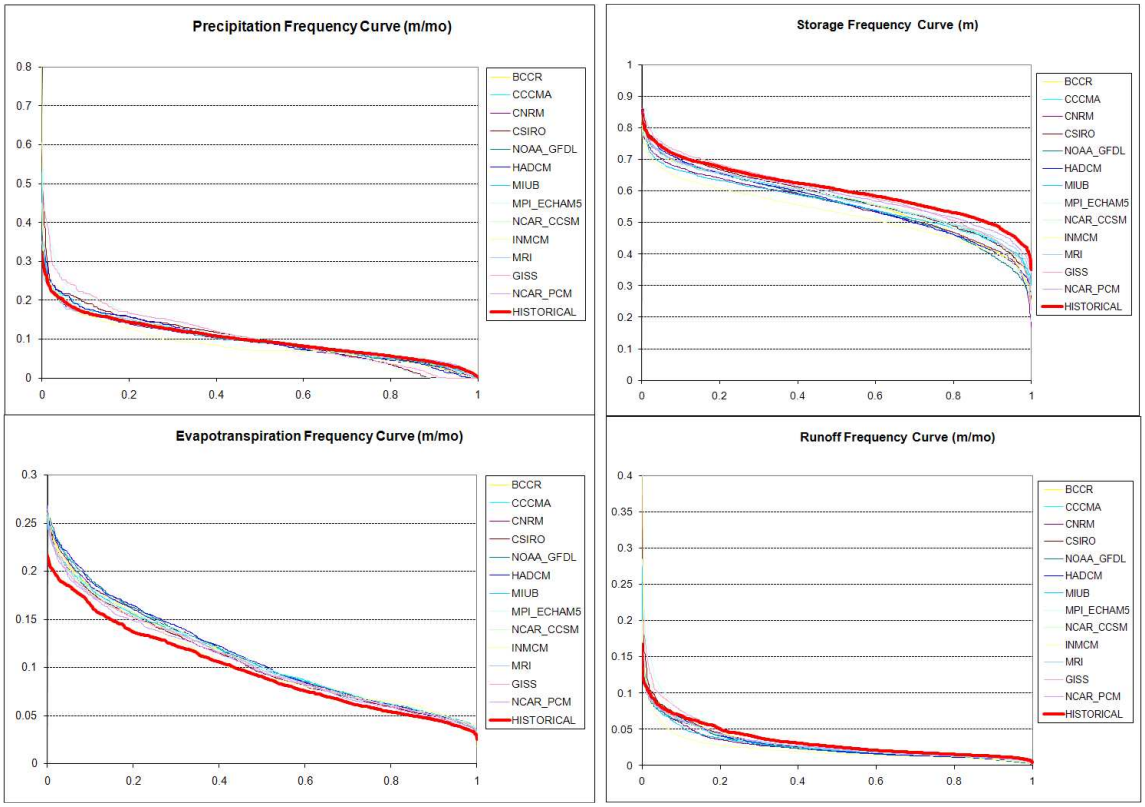

Figure A.18: A2 Climate Scenarios (2000-2099), SO - Thrmnd, Frequency Curves.

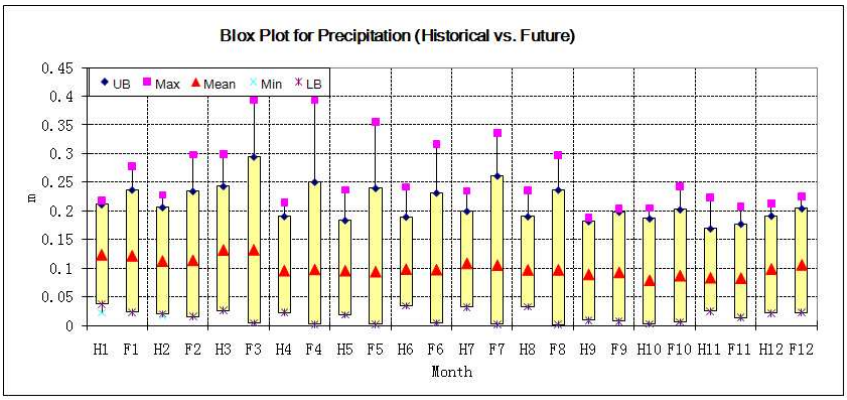

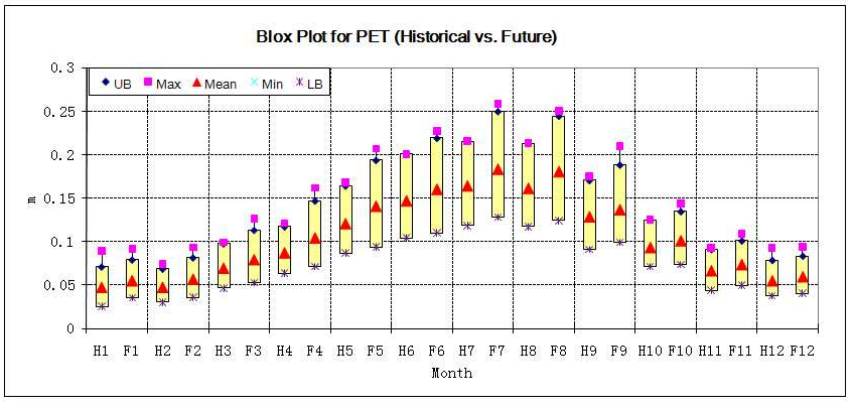

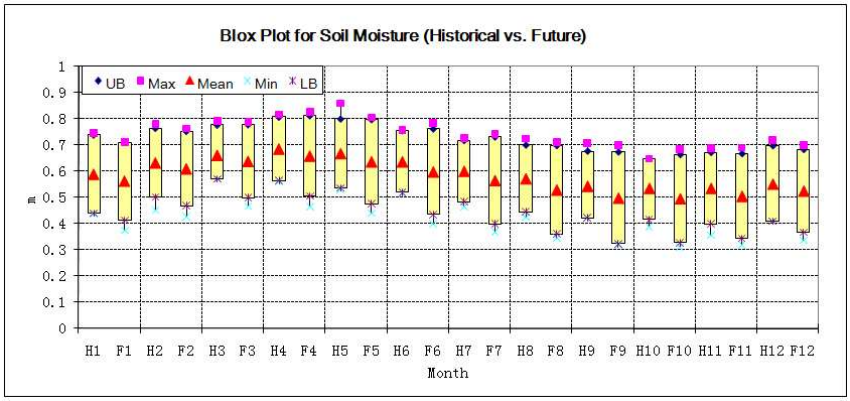

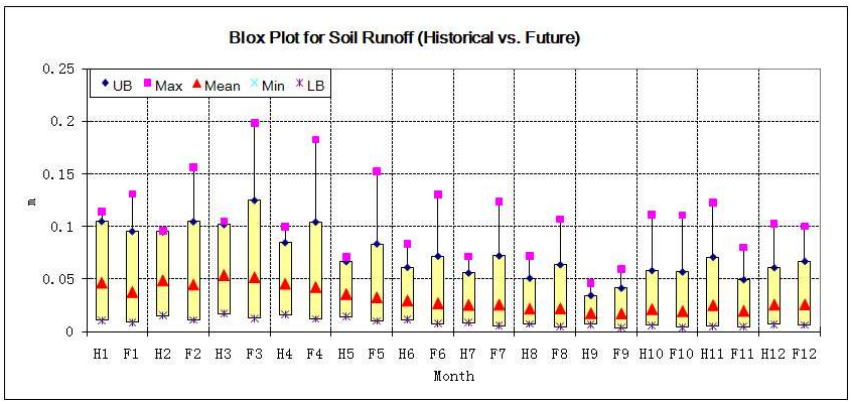

Figure A.19: Monthly Historical vs. Future (A1B) Watershed Response, SO - Thrmnd. (Unit: Precipitation – m/mo; PET – m/mo; Soil Moisture – m; Runoff m/mo.)

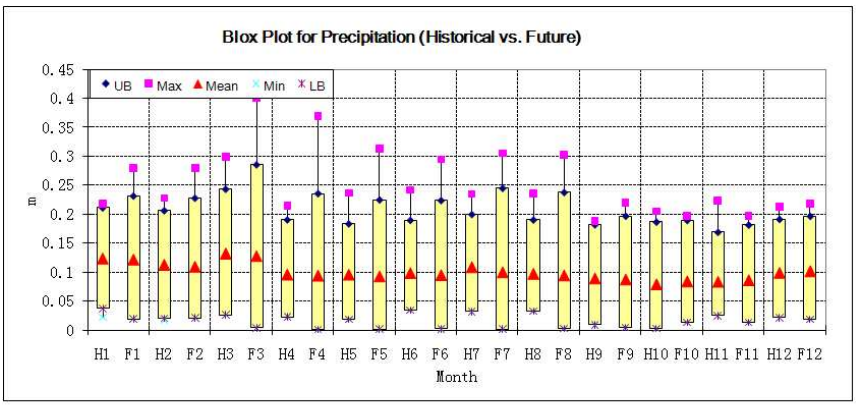

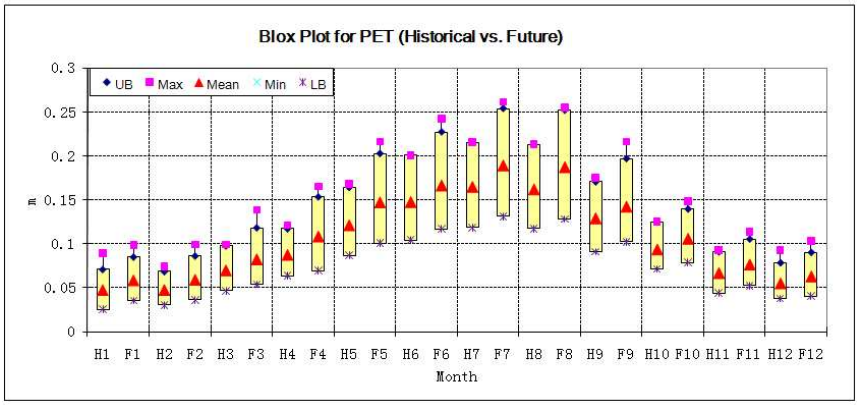

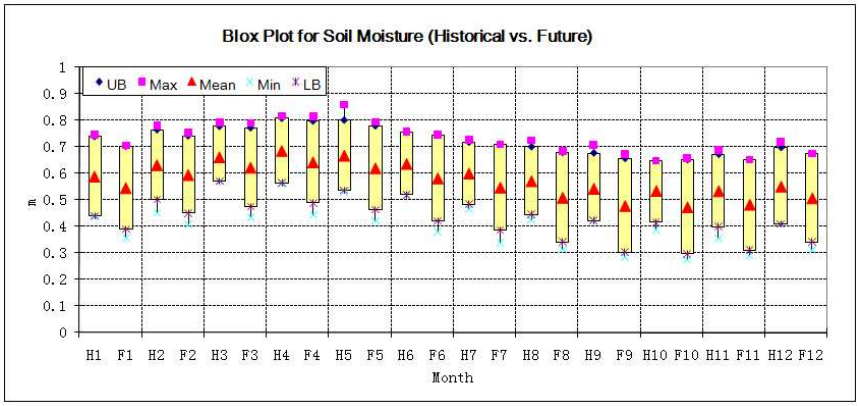

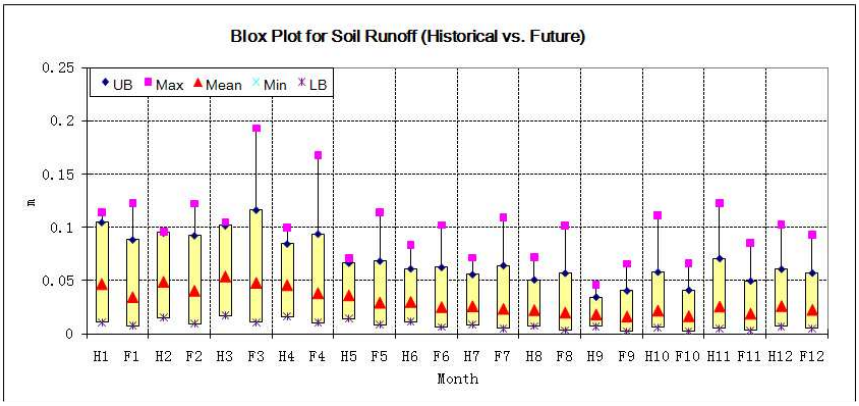

Figure A.20: Monthly Historical vs. Future (A2) Watershed Response, SO - Thrmnd. (Unit: Precipitation – m/mo; PET – m/mo; Soil Moisture – m; Runoff m/mo.)

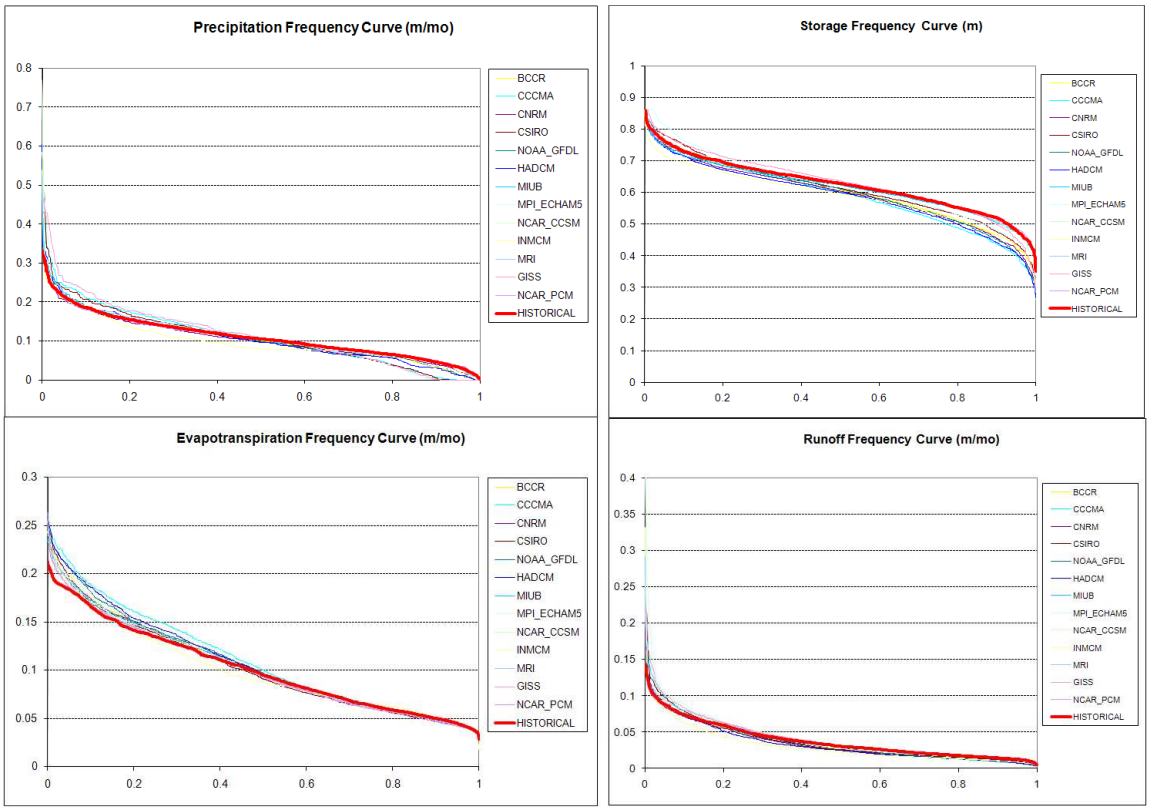

Figure A.21: A1B Climate Scenarios (2000-2099), SO - Augusta, Frequency Curves.

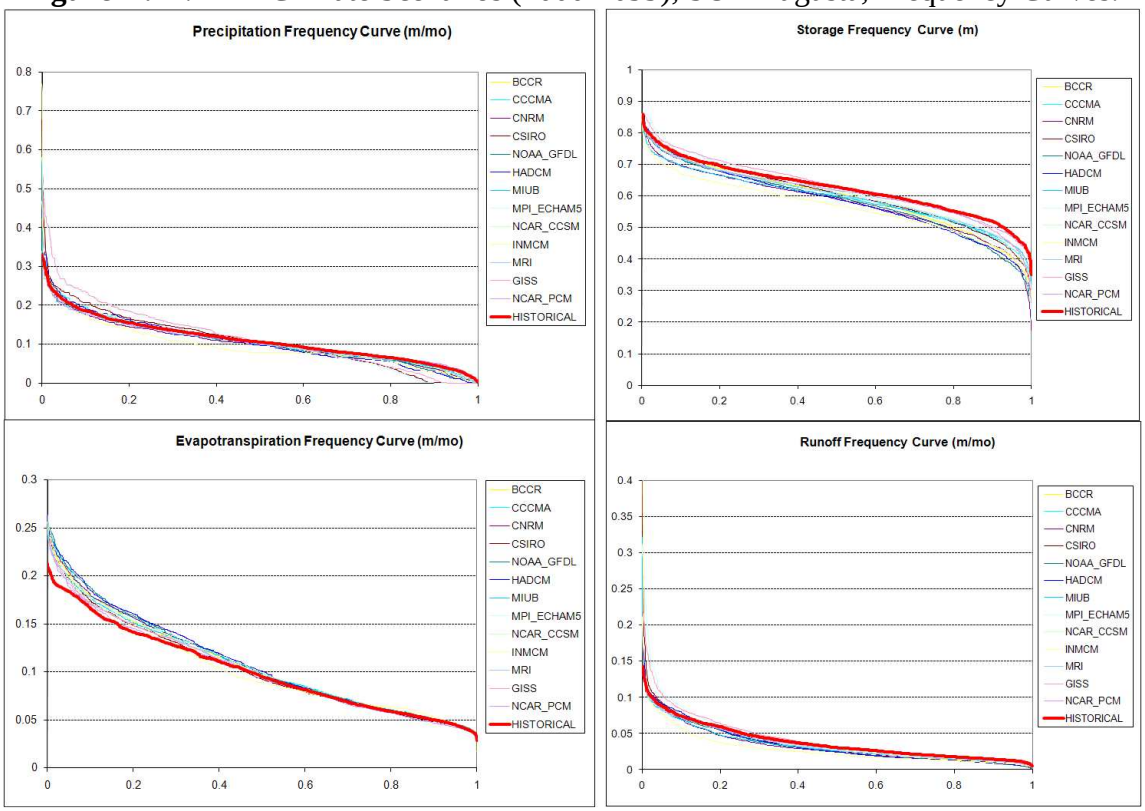

Figure A.22: A2 Climate Scenarios (2000-2099), SO - Augusta, Frequency Curves.

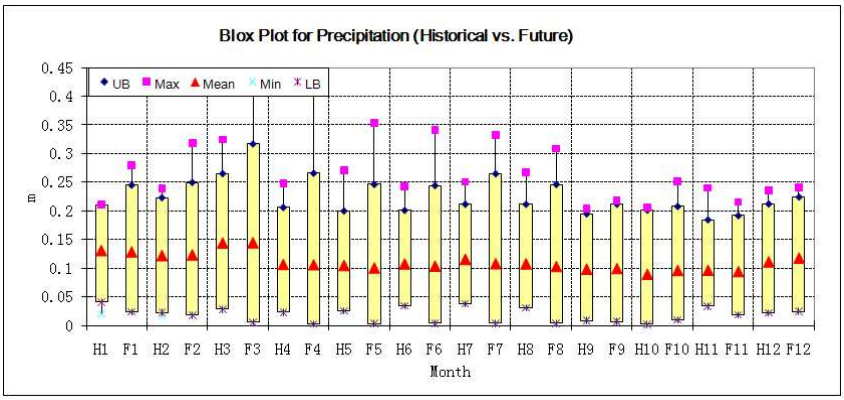

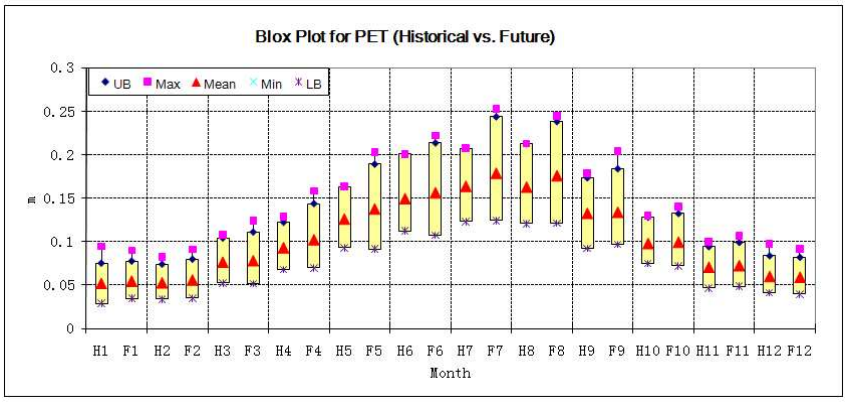

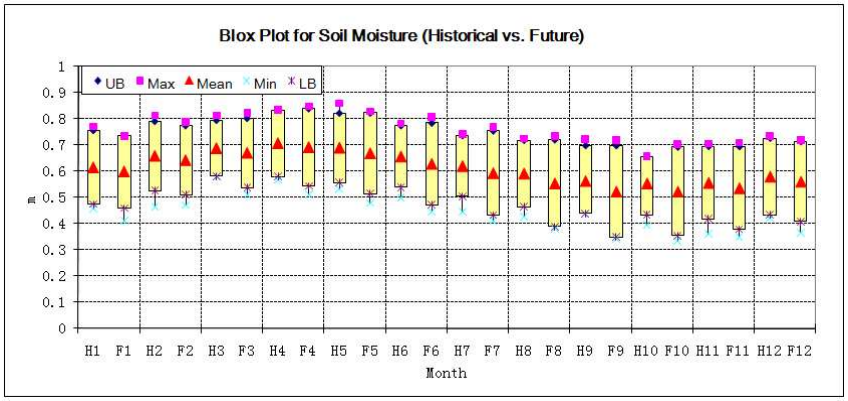

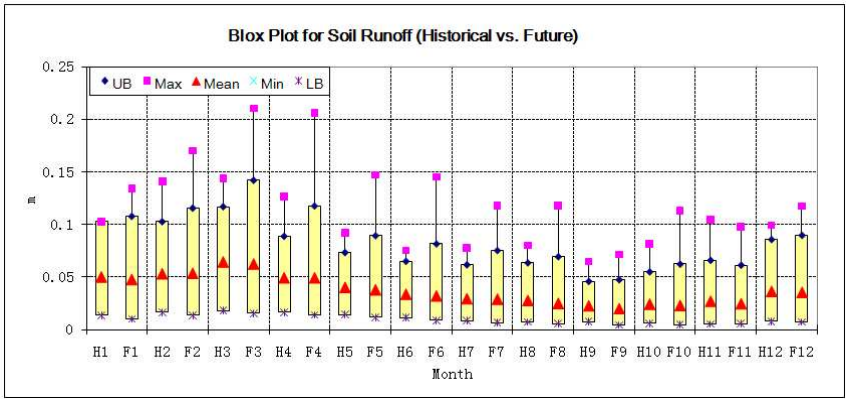

Figure A.23: Monthly Historical vs. Future (A1B) Watershed Response, SO - Augusta. (Unit: Precipitation – m/mo; PET – m/mo; Soil Moisture – m; Runoff m/mo.)

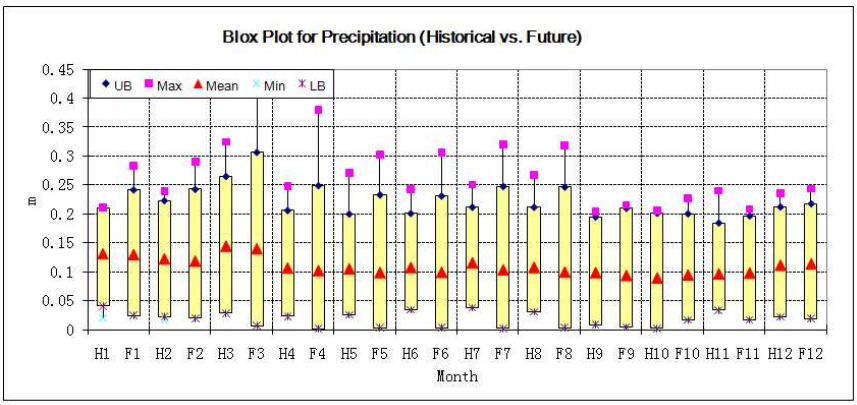

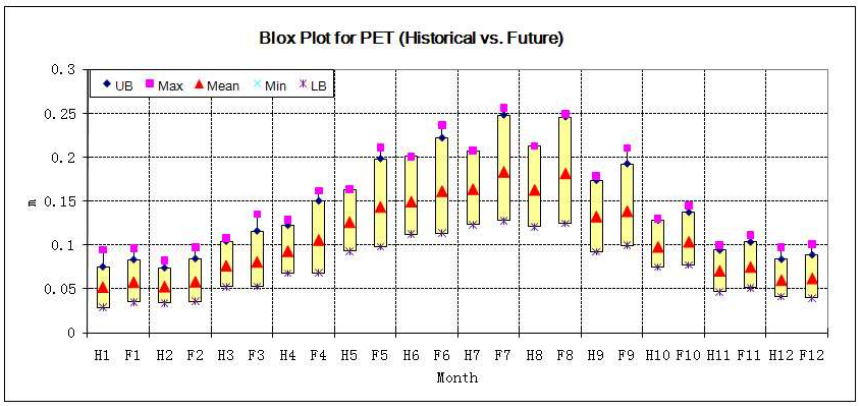

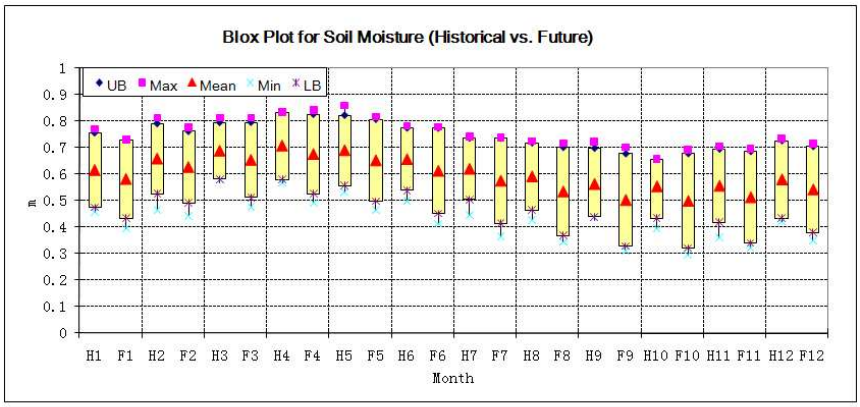

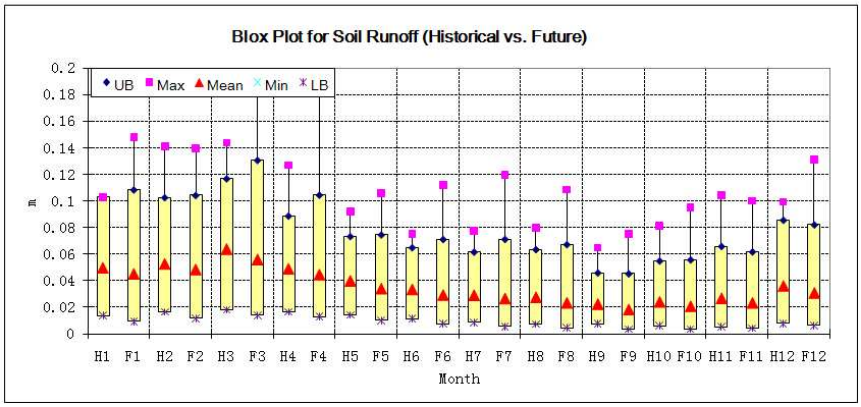

Figure A.24: Monthly Historical vs. Future (A2) Watershed Response, SO - Augusta. (Unit: Precipitation – m/mo; PET – m/mo; Soil Moisture – m; Runoff m/mo.)

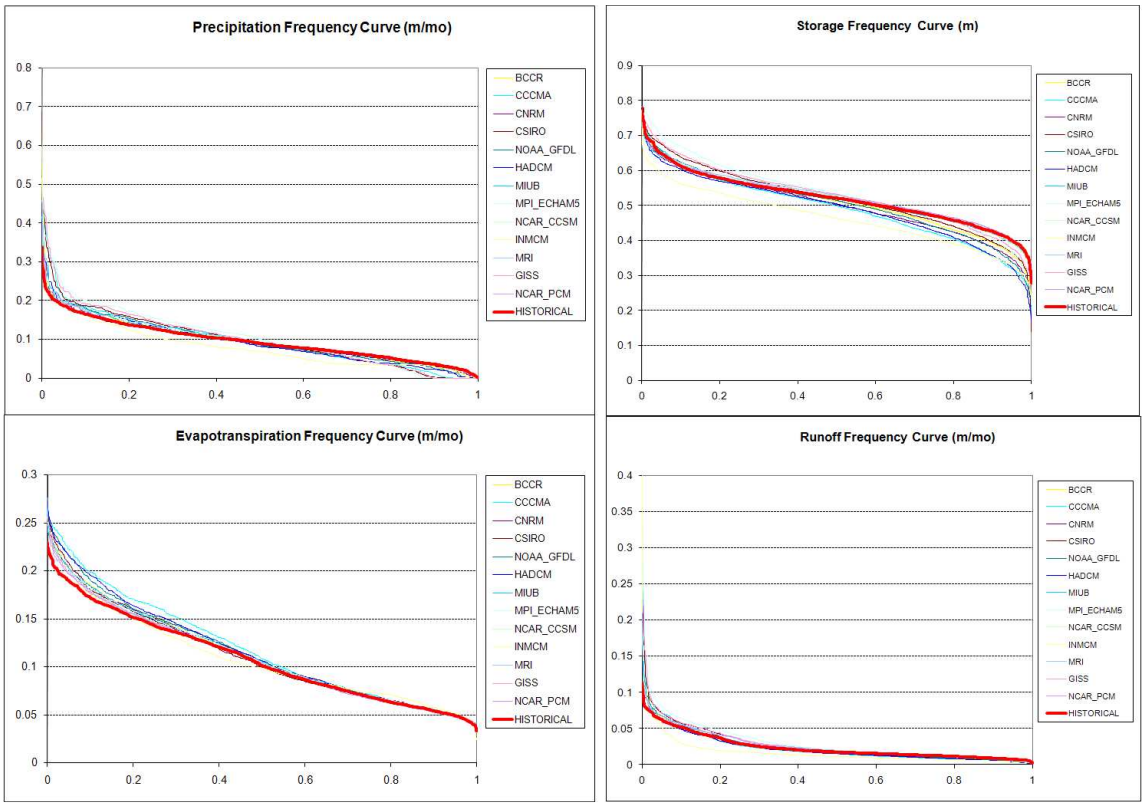

Figure A.25: A1B Climate Scenarios (2000-2099), SO - Lower Savannah, Frequency Curves.

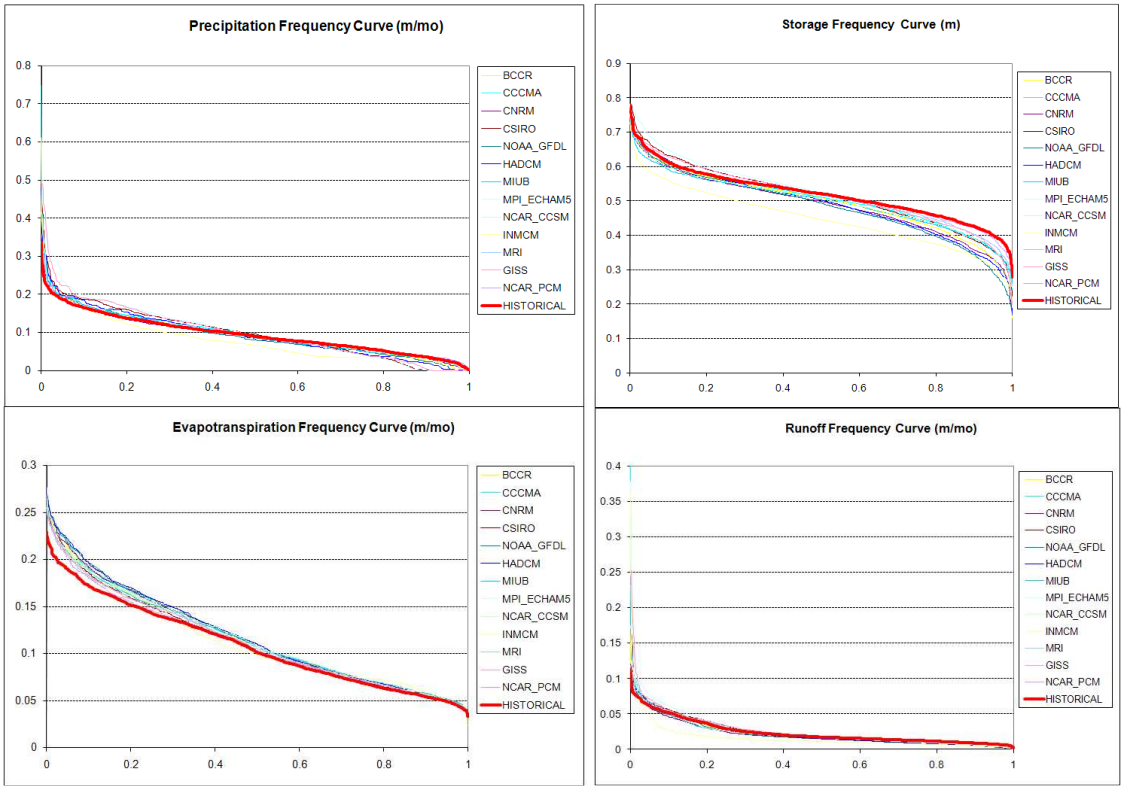

Figure A.26: A2 Climate Scenarios (2000-2099), SO - Lower Savannah, Frequency Curves.

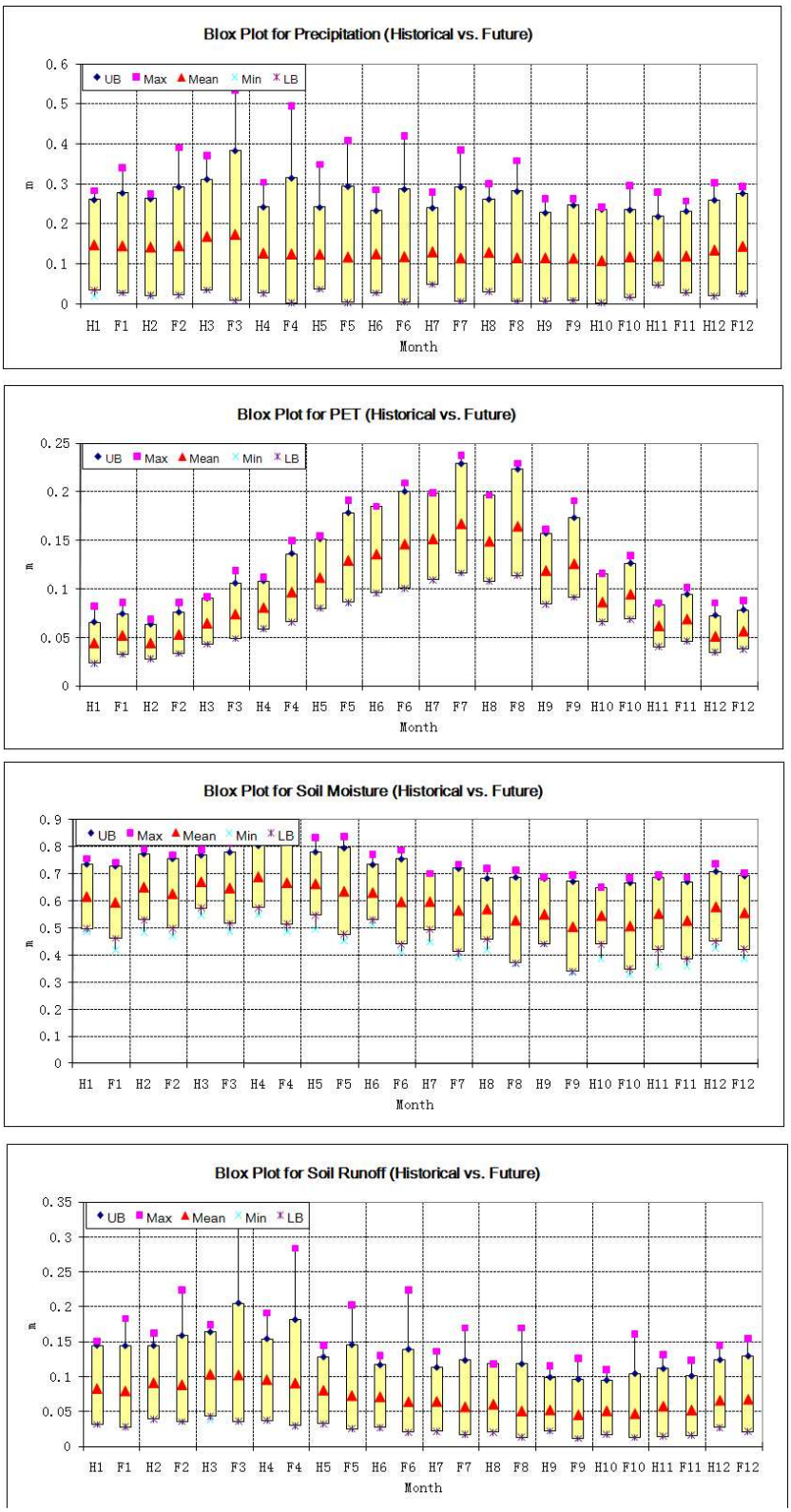

Figure A.27: Monthly Historical vs. Future (A1B) Watershed Response, SO - Lower Savannah. (Unit: Precipitation – m/mo; PET – m/mo; Soil Moisture – m; Runoff m/mo.)

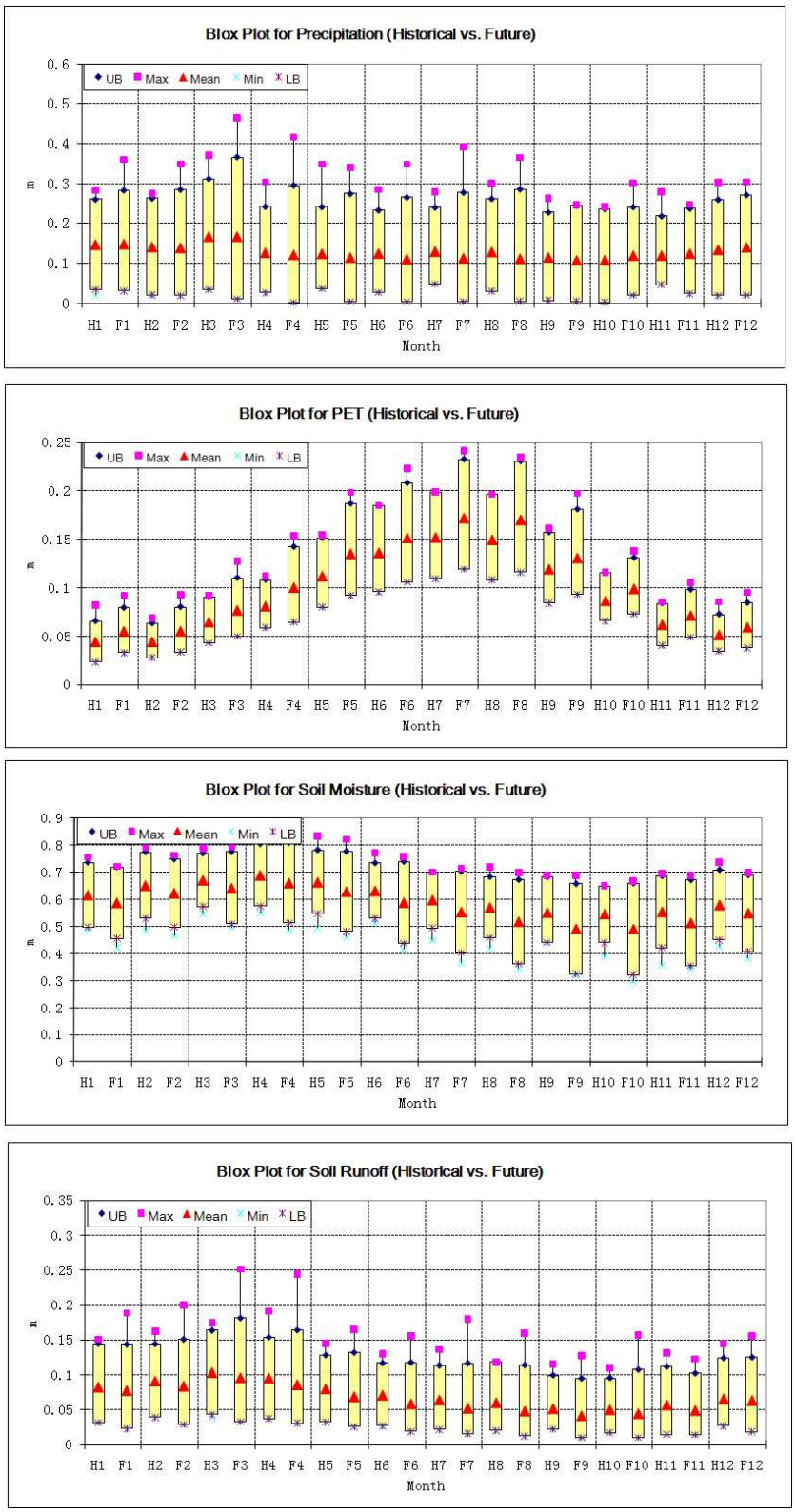

Figure A.28: Monthly Historical vs. Future (A2) Watershed Response, SO - Lower Savannah. (Unit: Precipitation – m/mo; PET – m/mo; Soil Moisture – m; Runoff m/mo.)

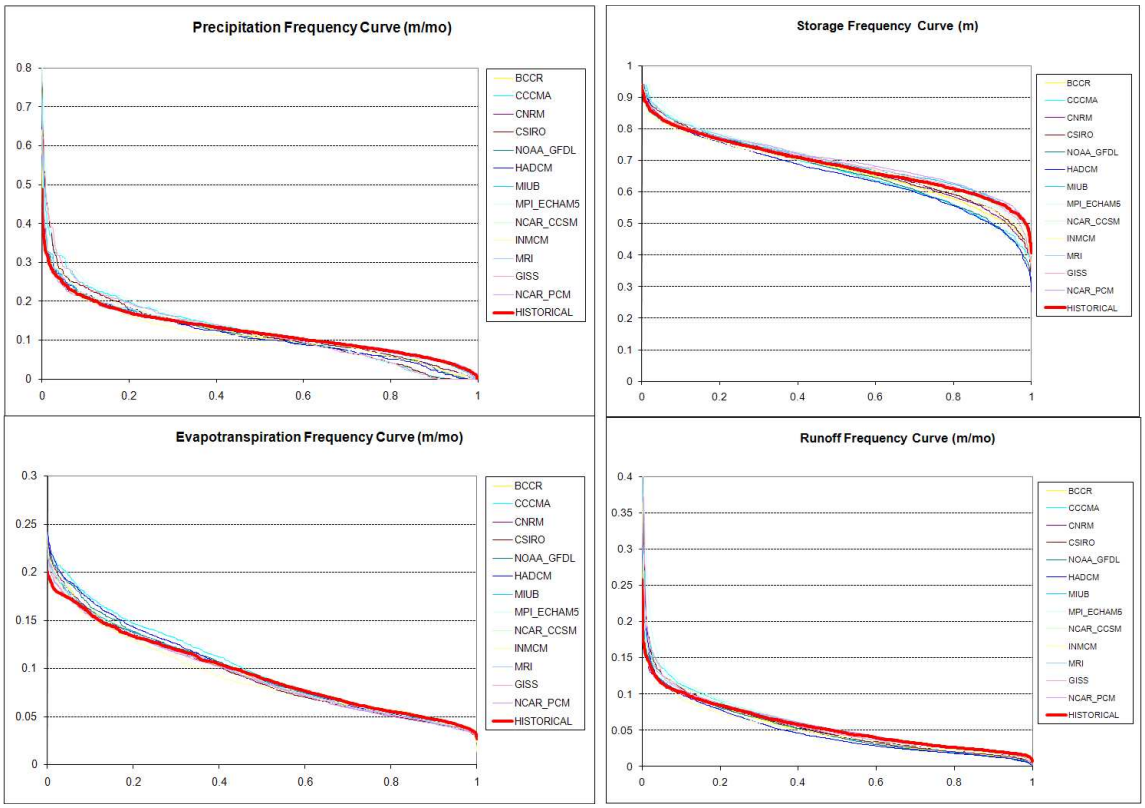

Figure A.29: A1B Climate Scenarios (2000-2099), ACT - Canton, Frequency Curves.

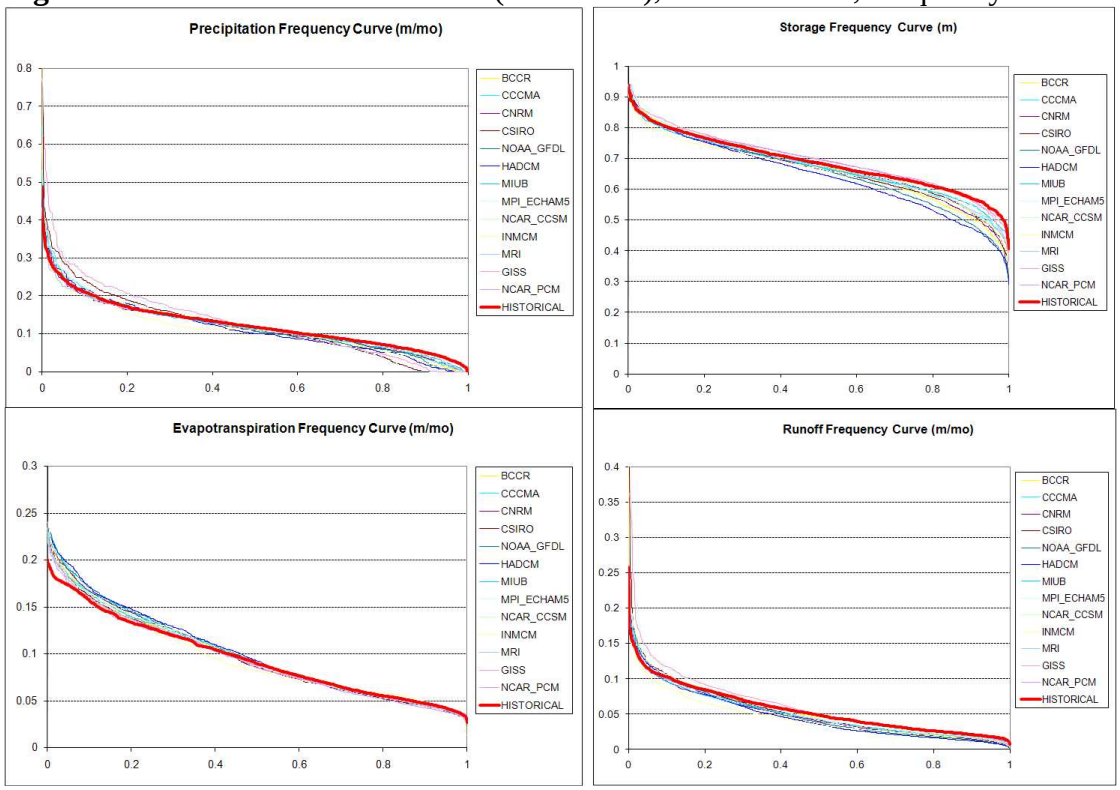

Figure A.30: A2 Climate Scenarios (2000-2099), ACT - Canton, Frequency Curves.

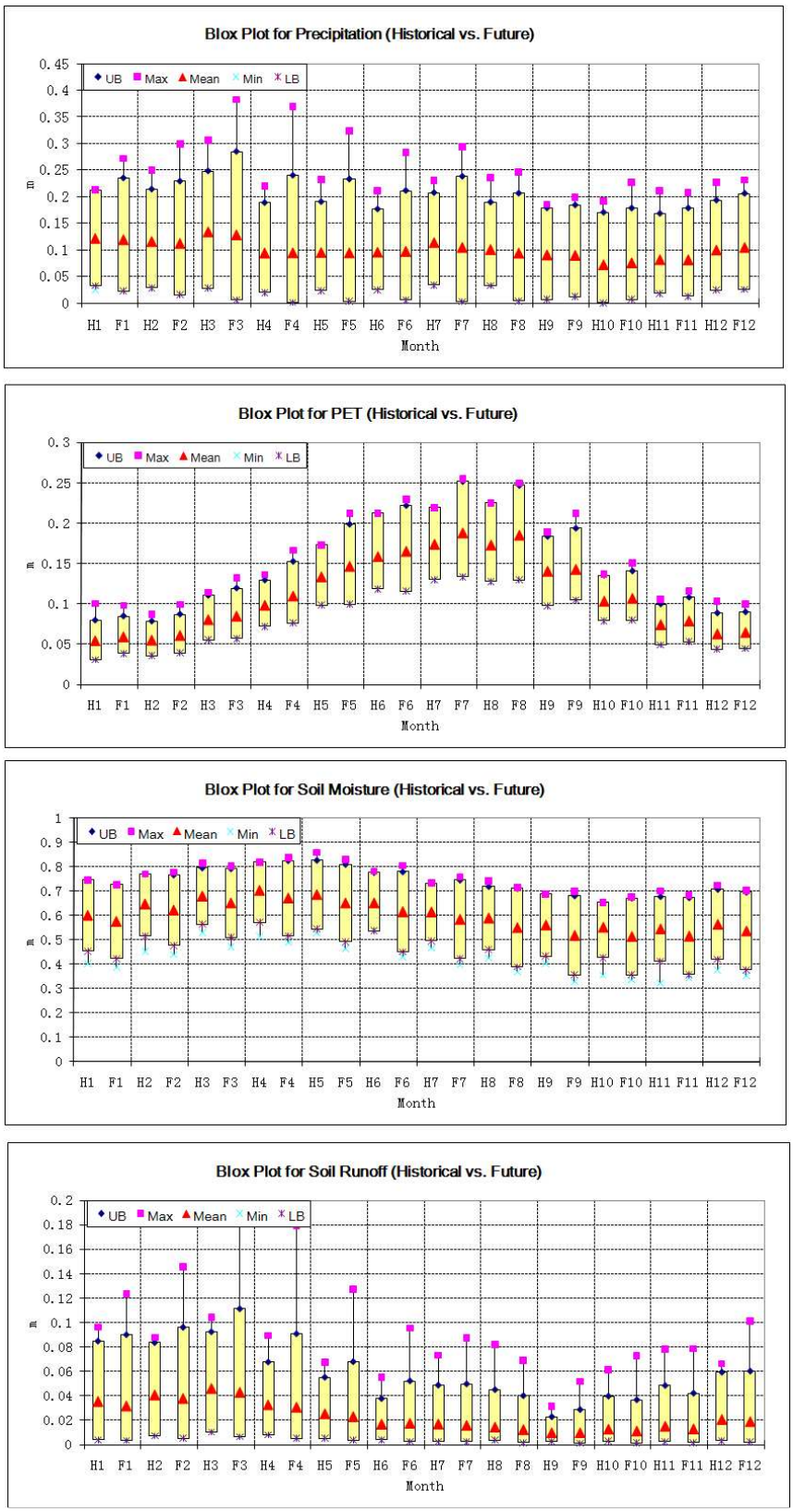

Figure A.31: Monthly Historical vs. Future (A1B) Watershed Response, ACT - Canton. (Unit: Precipitation – m/mo; PET – m/mo; Soil Moisture – m; Runoff m/mo.)

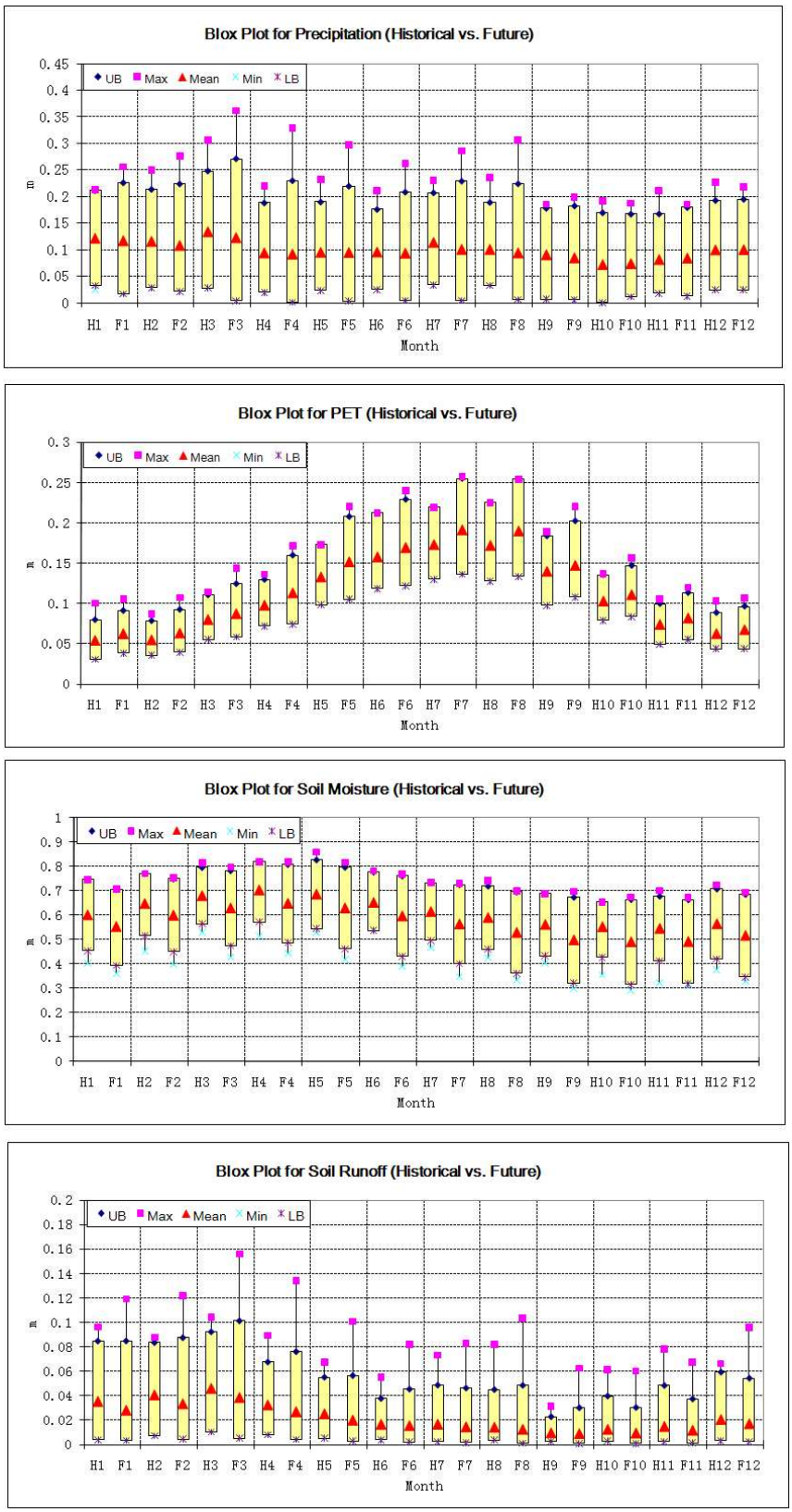

Figure A.32: Monthly Historical vs. Future (A2) Watershed Response, ACT - Canton. (Unit: Precipitation – m/mo; PET – m/mo; Soil Moisture – m; Runoff m/mo.)

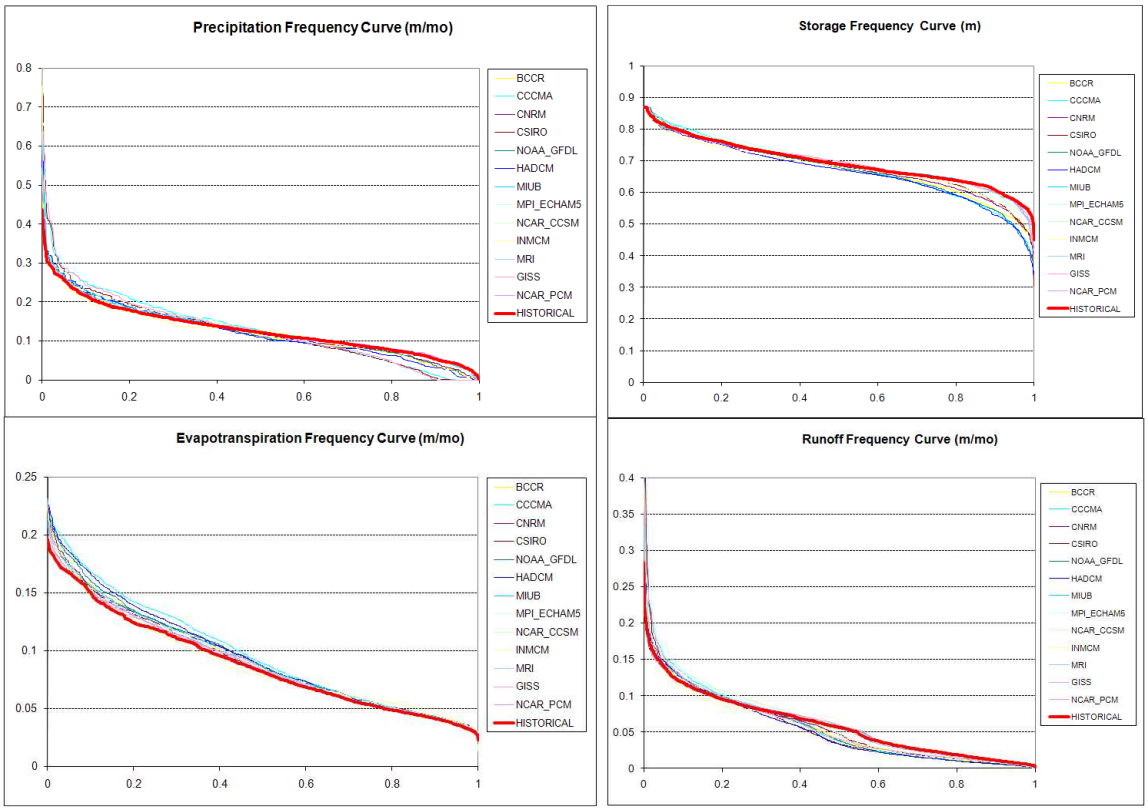

Figure A.33: A1B Climate Scenarios (2000-2099), ACT - Carter, Frequency Curves.

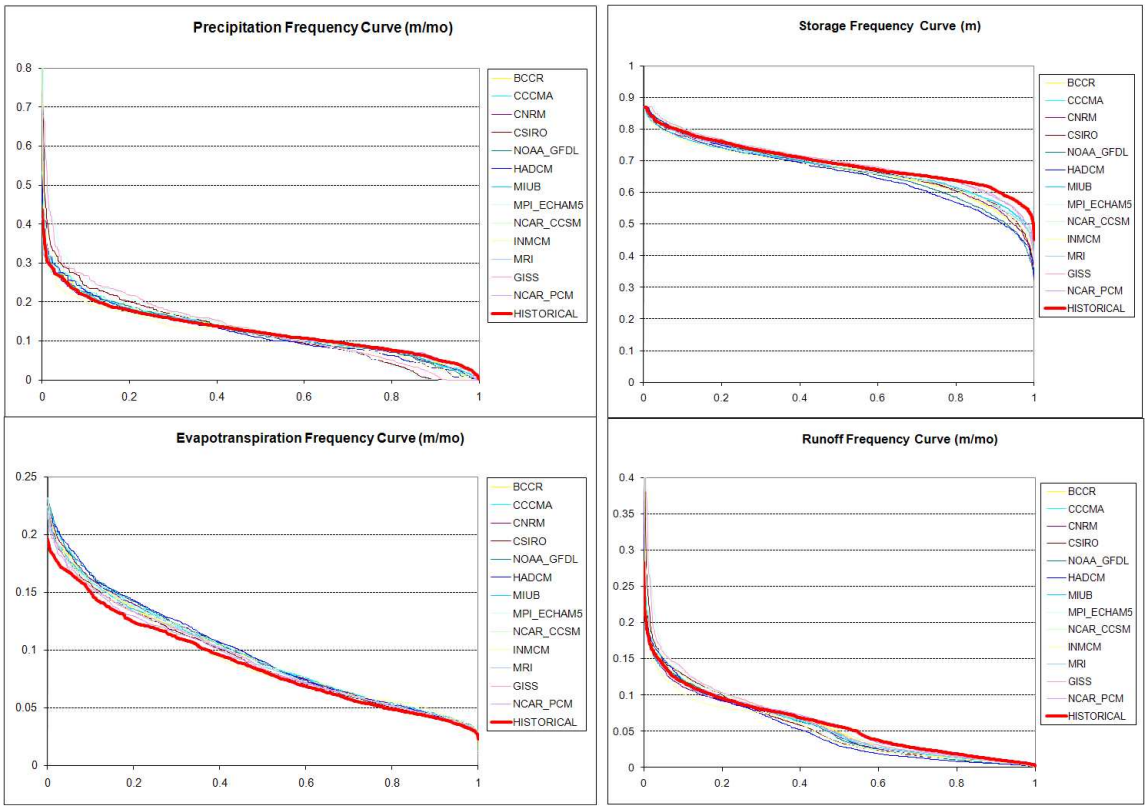

Figure A.34: A2 Climate Scenarios (2000-2099), ACT - Carter, Frequency Curves.

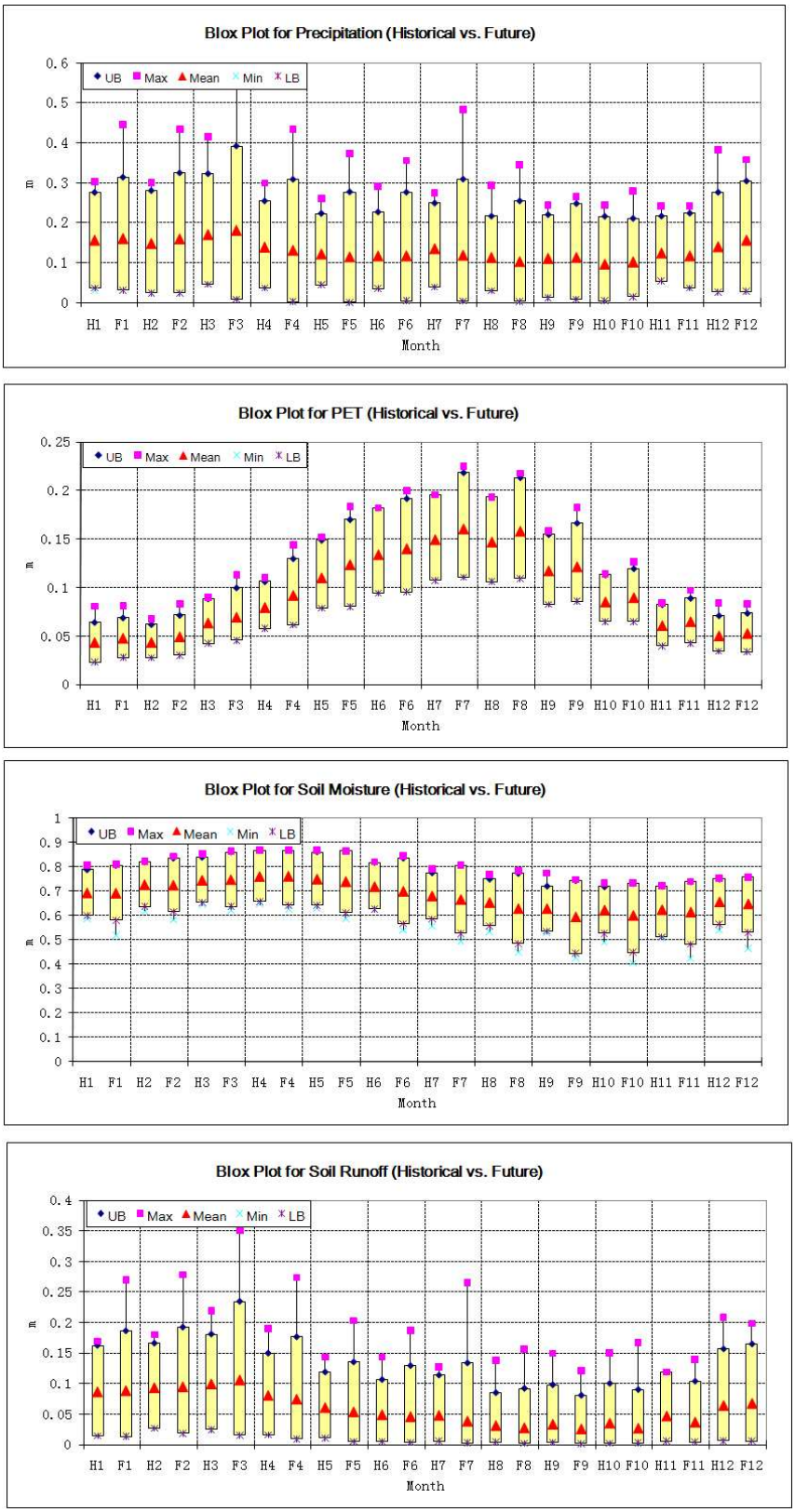

Figure A.35: Monthly Historical vs. Future (A1B) Watershed Response, ACT - Carter. (Unit: Precipitation – m/mo; PET – m/mo; Soil Moisture – m; Runoff m/mo.)

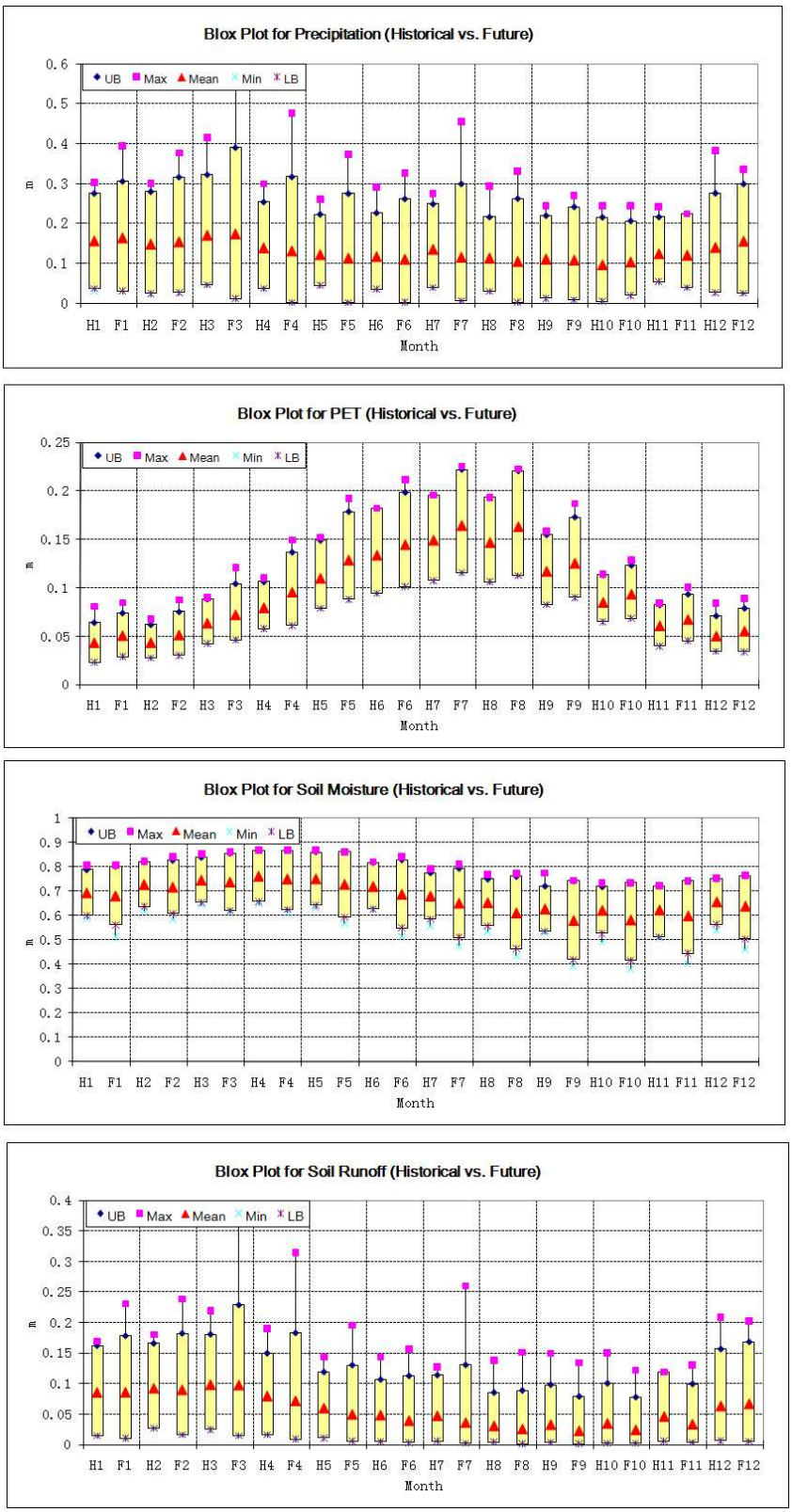

Figure A.36: Monthly Historical vs. Future (A2) Watershed Response, ACT - Carter. (Unit: Precipitation – m/mo; PET – m/mo; Soil Moisture – m; Runoff m/mo.)

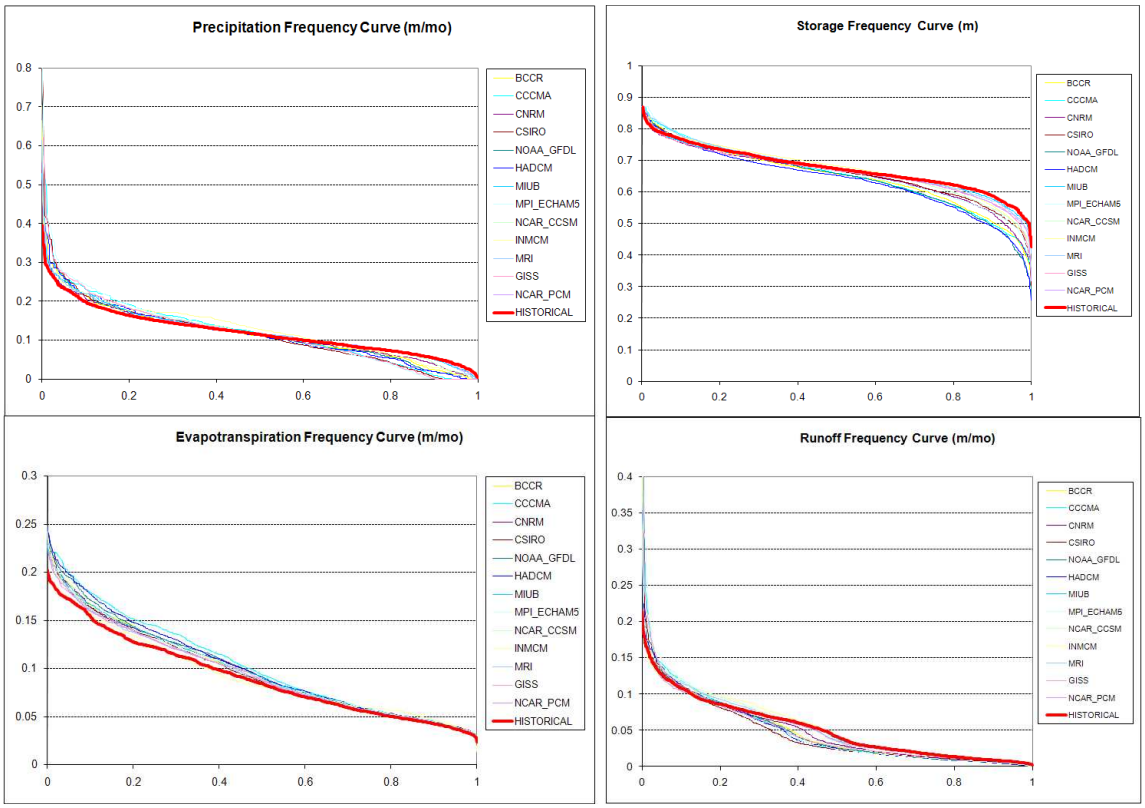

Figure A.37: A1B Climate Scenarios (2000-2099), ACT - Tilton, Frequency Curves.

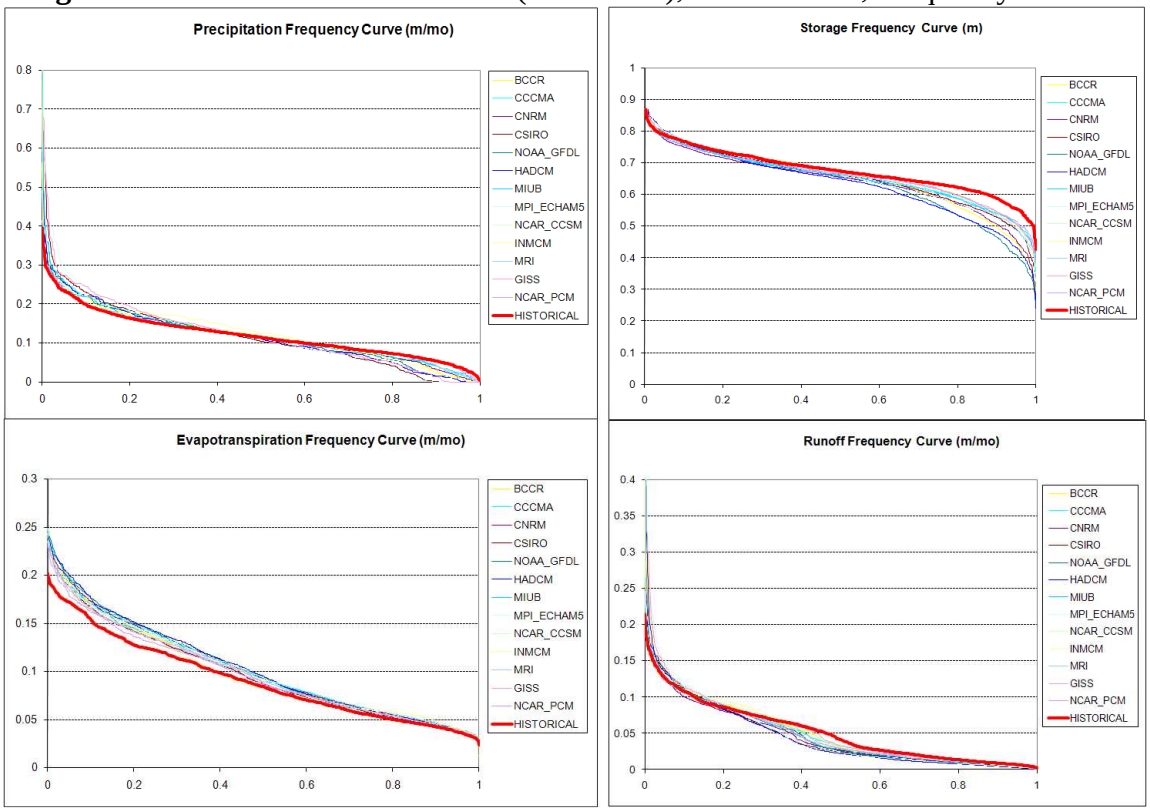

Figure A.38: A2 Climate Scenarios (2000-2099), ACT - Tilton, Frequency Curves.

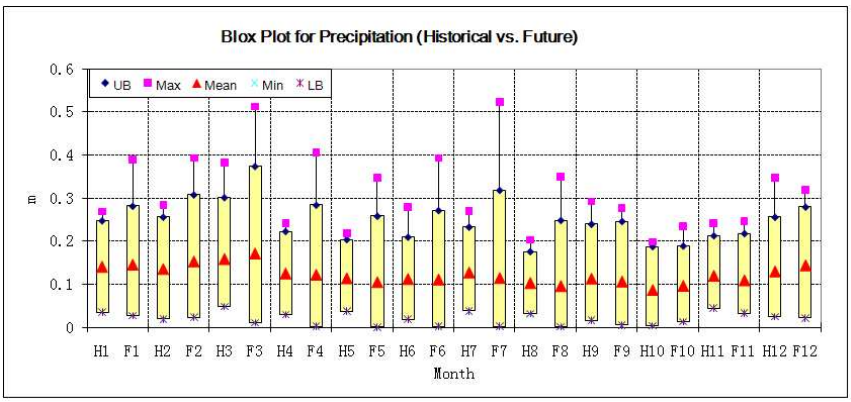

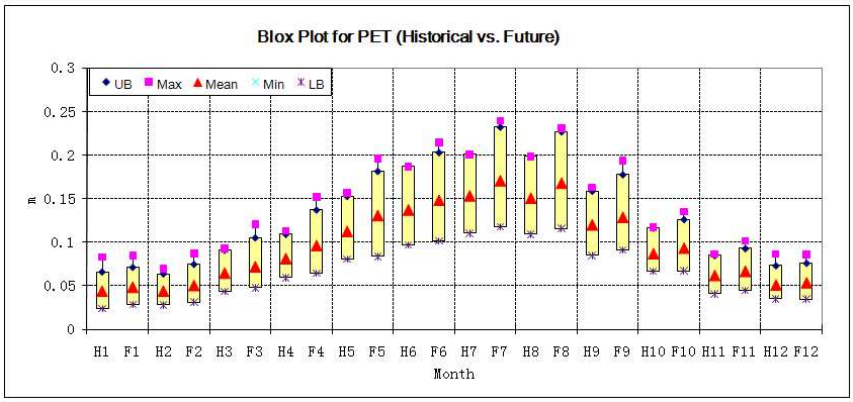

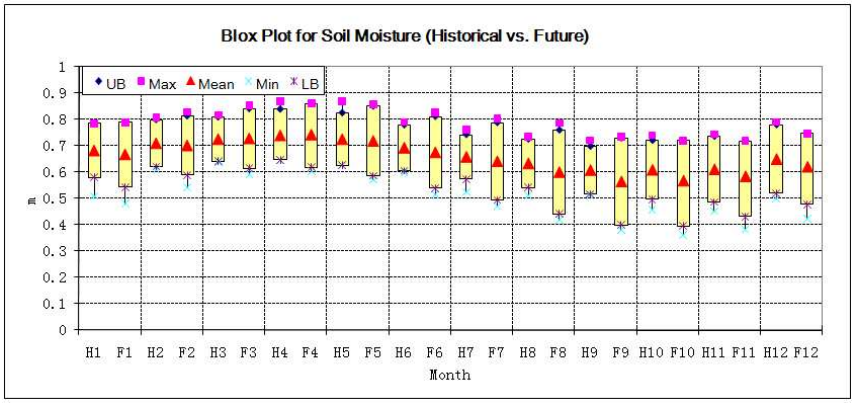

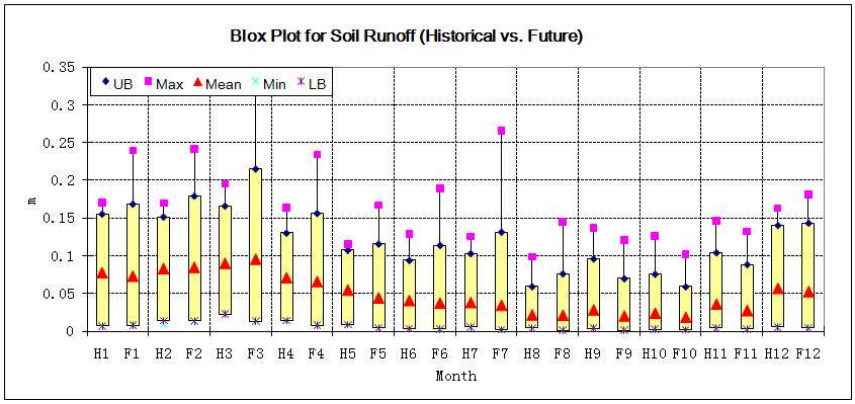

Figure A.39: Monthly Historical vs. Future (A1B) Watershed Response, ACT - Tilton. (Unit: Precipitation – m/mo; PET – m/mo; Soil Moisture – m; Runoff m/mo.)

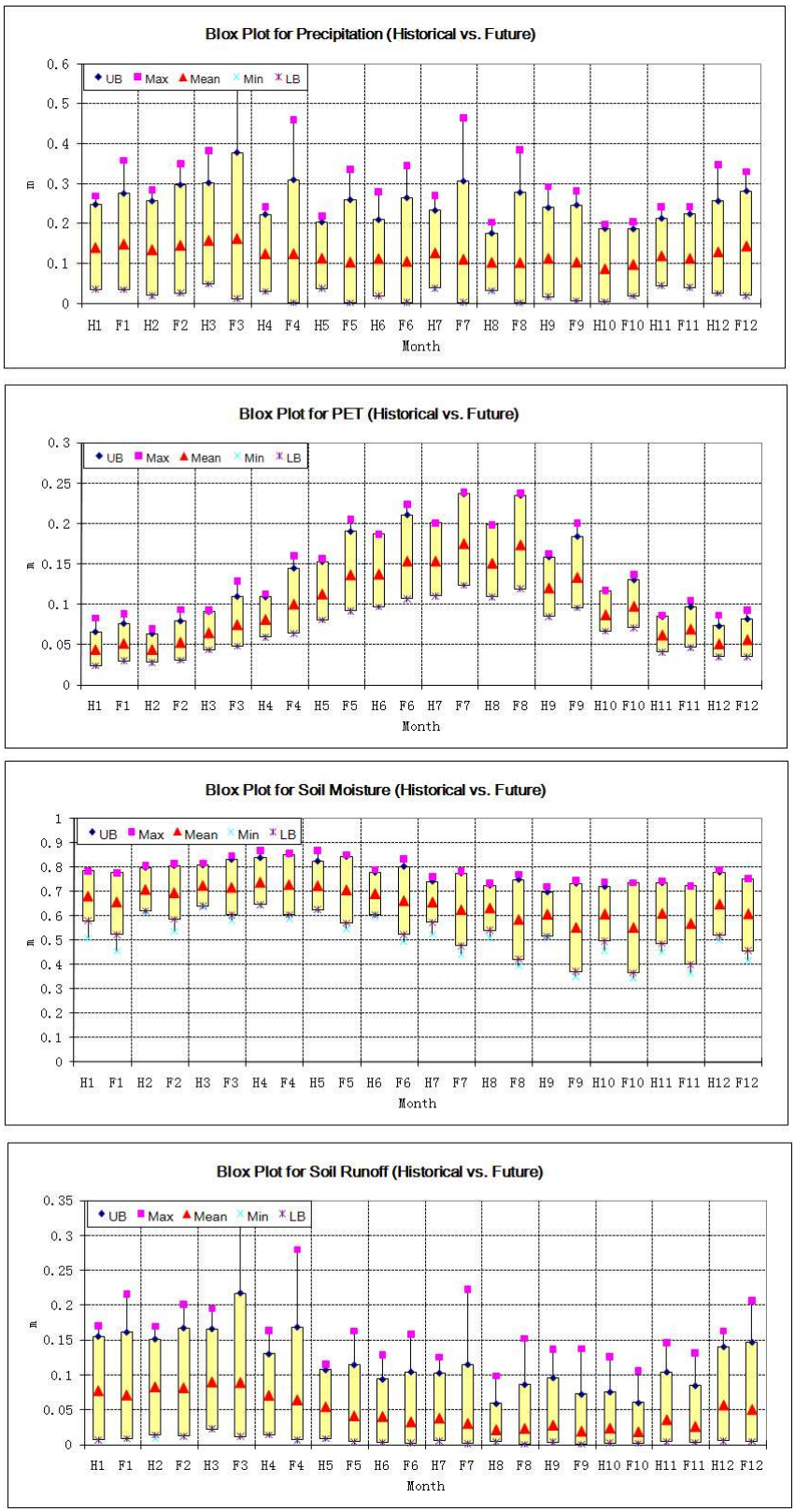

Figure A.40: Monthly Historical vs. Future (A2) Watershed Response, ACT - Tilton. (Unit: Precipitation – m/mo; PET – m/mo; Soil Moisture – m; Runoff m/mo.)

REFERENCES

Abdulla, F.A., Lettenmaier, D.P., (1997). Development of regional parameter estimation equations for a macroscale hydrologic model. Journal of Hydrology 197, 230–257.

Allen, R.G.; Pereira, L.S.; Raes, D.; Smith, M. (1998). Crop Evapotranspiration—Guidelines for Computing Crop Water Requirements. FAO Irrigation and drainage paper 56. Rome, Italy: Food and Agriculture Organization of the United Nations. ISBN 92-5-104219-4.

Amorocho, J., (1963). Measures of the linearity of hydrologic systems, J. Geophys. Res., 68(8), 2237–2249.

Amorocho, J., (1967). The nonlinear prediction problem in the study of the runoff cycle, Water Resour. Res., 3(3), 861–880.

Apostolopoulos, T. K., and K. P. Georgakakos, (1997). Parallel Computation for Streamflow Prediction with Distributed Hydrologic Models, Journal of Hydrology, 197(1-4), 1-24.

Arnold, J. G., and N. Fohrer, (2005). Swat2000: Current Capabilities and Research Opportunities in Applied Watershed Modelling, Hydrological Processes, 19(3), 563-72.

Bai, Y., T. Wagener, and P. Reed, (2009). A top-down framework forwatershed model evaluation and selection under uncertainty, Environ. Model Softw., doi:10.1016/j.envsoft.2008.12.012

Beven, K., (1996). A discussion of distributed hydrological modelling. In: Abbott, M.B., Refgaard, J.C. (Eds.), Distributed Hydrological Modelling. Kluwer Academic, pp. 255–278.

Bae, D.-H. and Georgakakos, K.P. (1992). Hydrologic modeling for flow forecasting and climate studies in large drainage basins. IIHR Pep. 360, Iowa Institute of Hydraulic Research and Department of Civil and Environmental Engineering, University of Iowa, Iowa City, 252 pp.

Bae, D.-H, and K.P. Georgakakos (1994). Climatic Variability of Soil Water in the American Midwest. Part 1. Hydrologic Modeling. Journal of Hydrology. 162, no. 3-4: 355.

Botter, G. , Porporato, A. , Rodriguez-Iturbe, I. , and Rinaldo, A., (2009). Nonlinear Storage-discharge Relations and Catchment Streamflow Regimes, Water Resources Research, 45.

Brutsaert, W., (2005). Hydrology: An Introduction, Cambridge Univ. Press, New York.

Brutsaert W. and J.P. Lopez (1998). Basin-scale geohydrologic drought for features of riparian aquifers in the southern Great Plains, Water Resources Research, 34, 233-240, doi:10.1029/97WR03068.

Brutsaert W. and J.L. Nieber (1977). Regionalized drought flow hydrographs form a mature glaciated plateau, Water Resources Research, 13, 637-643, doi:10.1029/WR013i003p00637.

Burn, D.H., Boorman, D.B., (1993). Estimation of hydrological parameters at ungauged catchments. Journal of Hydrology 143, 429–454.

Carpenter, T. M., and K. P. Georgakakos, (2004) Continuous Streamflow Simulation with the HRCDHM Distributed Hydrologic Model, Journal of Hydrology 298.1-4, 61-79.

Conway, D., (1998). Recent Climate Variability and Future Climate Change Scenarios for Great Britain, Progress in Physical Geography 22.3: 350-74.

Crawford, N.H. and R.K. Linsley, (1966). Digital Simulation in Hydrology: Stanford Watershed Model IV. Technical Report No. 39, Department of Civil Engineering, Stanford University, p. 210.

Drignei, D., (2009). A Kriging Approach to the Analysis of Climate Model Experiments, Journal of Agricultural Biological and Environmental Statistics 14.1: 99-114.

Duan, Q. Y., S. Sorooshian, and V. K. Gupta, (1994). Optimal Use of the Sce-Ua Global Optimization Method for Calibrating Watershed Models, Journal of Hydrology 158(3-4), 265-84.

Duan, Q. Y., et al., (2007). Multi-Model Ensemble Hydrologic Prediction Using Bayesian Model Averaging, Advances in Water Resources, 30(5), 1371-86.

Flato, G. M., Boer, G. J., Lee, W. G., McFarlane, N. A., Ramsden, D., Reader, M. C., and Weaver, A. J., (2000). The Canadian Centre for Climate Modelling and Analysis Global Coupled Model and Its Climate, Climate Dynamics 16.6: 451-67.

Fleming, G., and Franz, D.D., (2001). Flood Frequency Estimating Techniques. Journal of the Hydraulic Division, ASCE, 97 (HY9): 1441-1460.

Fowler, H. J., S. Blenkinsop, and C. Tebaldi, (2007). Linking Climate Change Modelling to Impacts Studies: Recent Advances in Downscaling Techniques for Hydrological Modelling, International Journal of Climatology 27.12: 1547-78.

Furey, P.R., Gupta, V.K. (2007). Diagnosing peak-discharge power laws observed in rainfall-runoff events in Goodwin Creek experimental watershed. Adv. Water Resour., 30 (11) 2387-2399

Georgakakos, A. P., Yao, H., Mullusky M. G., and Georgakakos, K. P., (1998). Impacts of Climate Variability on the Operational Forecast and Management of the Upper Des Moines River Basin. Water Resources Research 34.4: 799-821.

Georgakakos, A.P., H. Yao, M. Kistenmacher, K. P. Georgakakos, N. E. Graham, F.-Y. Cheng, C. Spencer, and E. Shamir (2011). Value of Adaptive Water Resources Management in Northern California under Climatic Variability and Change: Reservoir Management. Journal of Hydrology, online publication available at http://dx.doi.org/10.1016/j.jhydrol.2011.04.038.

Georgakakos, A., F. Zhang, and H. Yao, (2010). Climate Variability and Change Assessment for the ACF River Basin, Southeast US. Georgia Water Resources Institute (GWRI) Technical Report No. GWRI/2010-TR1, Georgia Institute of Technology, Atlanta, Georgia, 321 pp.

Georgakakos, K. P., and O. W. Baumer, (1996) Measurement and utilization of on-site soil moisture data, Journal of Hydrology, 184(1-2), 131-152.

Gissila, T., Black, E., Grimes, D. I. F., and Slingo, J. M., (2004). Seasonal Forecasting of the Ethiopian Summer Rains. International Journal of Climatology 24.11: 1345-58.

Gesch, D.B., (2007). The National Elevation Dataset, in Maune, D., ed., Digital Elevation Model Technologies and Applications: The DEM Users Manual, 2nd Edition: Bethesda, Maryland, American Society for Photogrammetry and Remote Sensing, p. 99-118.

Gesch, D., Oimoen, M., Greenlee, S., Nelson, C., Steuck, M., and Tyler, D., (2002). The National Elevation Dataset: Photogrammetric Engineering and Remote Sensing, v. 68, no. 1, p. 5-11.

Guo, S., Wang, J., Yang, J., (2001). A semi-distributed hydrological model and its application in a macroscale basin in China. In: Dolman, A.J., Hall, A.J., Kavvas, M.L., Oki, T., Pomeroy, J.W. (Eds.), Soil-Vegetation–Atmosphere Transfer Schemes and Large-Scale Hydrological Models. IAHS Publ. no. 270, pp. 167–174.

Gupta, H. V., S. Sorooshian, and P. O. Yapo, (1996). Toward Improved Calibration of Hydrologic Models: Multiple and Noncommensurable Measures of Information, Water Resources Research 34(4), 751-63.

Gupta, V.K., Castro S.L, and Over T.M. (1996). On scaling exponents of spatial peak flows from rainfall and river network geometry. J Hydrol 187:81–104.

Harald Kling and Hoshin Gupta, (2009). On the development of regionalization relationships for lumped watershed models: The impact of ignoring sub-basin scale variability. Journal of Hydrology 373, 337-351.

Heuvelmans, G., Muys, B., Feyen, J. (2004). Evaluation of hydrological model parameter transferability for simulating the impact of land use on catchment hydrology. Phys. Chem. Earth 29, 739–747.

Hidalgo, H. G., Dettinger, M. D., and Cayan, D. R. (2008). Downscaling with constructed analogues: daily precipitation and temperature fields over the United States, Report No. CEC-500-2007-123, California Energy Commission, Sacramento, CA, 48 pp.

Horton, R.E. (1941). Virtual channel-infow graphs, Eos Trans. AGU, 22, 811.

Horton, Robert E. (1941). The role of infiltration in the hydrologic cycle. Trans. AGU, 14th Ann. Mtg. pp. 446–460.

Huth, R., (1999). Statistical Downscaling in Central Europe: Evaluation of Methods and Potential Predictors. Climate Research 13.2: 91-101.

Huang, M., Liang, X., Liang, Y., (2003). A transferability study of model parameters for the variable infiltration capacity land surface scheme. Journal of Geophysical Research 108 (D22). doi:10.1029/2003JD003676.

Hundecha, Y., Ba´rdossy, A., (2004). Modeling the effect of land use changes on the runoff generation of a river basin through parameter regionalization of a watershed model. J. Hydrol. 292, 281–295.

IPCC, 2007: Climate Change (2007). The Physical Science Basis. Contribution of Working Group I to the Fourth Assessment Report of the Intergovernmental Panel on Climate Change [Solomon, S., D. Qin, M. Manning, Z. Chen, M. Marquis, K.B. Averyt, M. Tignor and H.L. Miller (eds.)]. Cambridge University Press, Cambridge, United Kingdom and New York, NY, USA, 996 pp.

Kirchner, J.W., (2009). Catchments as Simple Dynamical Systems: Catchment Characterization, Rainfall-runoff Modeling, and Doing Hydrology Backward, Water Resources Research, 45.

Kirchner, J.W., (2006). Getting the right answers for the right reasons: Linking measurements, analyses, and models to advance the science of hydrology, Water Resources Research, 42.

Klemes, V.,(1986). Operational testing of hydrological simulation. Hydrological Sciences Journal 31, 13–24.

Kokkonen, T.S., Jakeman, A.J., Young, P.C., Koivusalo, H.J., (2003). Predicting daily flows in ungauged catchments:model regionalisation from catchment descriptors at the Coweeta Hydrologic Laboratory, North Carolina.Hydrol. Process. 17 (11), 2219–2238.

Koren, V., Reed, S., Smith, M., Zhang, Z., Seo, D. J., (2004) Hydrology Laboratory Research Modeling System (Hl-Rms) of the Us National Weather Service, Journal of Hydrology, 291(3-4), 297-318.

Koren, V.I., Smith, M., Duan, Q., (2003). Use of a priori parameter estimates in the derivation of spatially consistent parameter sets of rainfall-runoff models. In: Duan, Q., Sorooshian, S., Gupta, H., Rosseau, H., Turcotte, H. (Eds.), Calibration

of Watershed Models, Water Science and Applications, vol. 6. AGU, pp. 239–254.

Liang, X., Lettennmaier, Dennis P., Wood, Eric F., Burges, and Stephen J., (1994). A simple hydrologically based model of land surface water and energy fluxes for general circulation models, Journal of Geophysical Research, 99(D7), 14415-14428.

Lettenmaier, D. P., and D. Rind, (1992). Hydrological Aspects of Global Climate Change – Preface, Journal of Geophysical Research-Atmospheres 97.D3: 2675-76.

Lyon, S.W. and P.A. Troch (2007). Hillslope subsurface flow similarity: Real-world tests of the hillslope Peclet number, Water Resources Research, 43, W07450, doi:10.1029/2006WR005323

Marechal, D. and Holman, I.P., (2005). Development and application of a soil classification-based conceptual catchment-scale hydrological model, J. Hydrol. 312, 277-293.

Maurer, E. P., (2007). Uncertainty in Hydrologic Impacts of Climate Change in the Sierra Nevada, California, under Two Emissions Scenarios, Climatic Change 82.3-4: 309-25.

Maurer, E. P., Wood, A. W., Adam, J. C., Lettenmaier, D. P., and Nijssen, B., (2002). A Long-Term Hydrologically Based Dataset of Land Surface Fluxes and States for the Conterminous United States, Journal of Climate 15.22: 3237-51.

Maurer, E.P. and H.G. Hidalgo (2008). Utility of daily vs. monthly large-scale climate data: an intercomparison of two statistical downscaling methods, Hydrology and Earth System Sciences Vol. 12, 551-563.

Mearns, L. O., F. Giorgi, P. Whetton, D. Pabon, M. Hulme, and M. Lal, (2003a). Guidelines for Use of Climate Scenarios Developed from Regional Climate Model Experiments, Data Distribution Center of the Intergovernmental Panel on Climate Change.

Mearns, L. O., F. Giorgi, L. McDaniel and C. Shields, (2003b). Climate Scenarios for the Southeastern US Based on Gcm and Regional Model Simulations, Climatic Change 60.1-2: 7-35.

Meehl, G. A., C. Covey, T. Delworth, M. Latif, B. McAvaney, J. F. B. Mitchell, R. J. Stouffer, and K. E. Taylor, (2007). The WCRP CMIP3 multi-model dataset: A new era in climate change research, Bulletin of the American Meteorological Society, 88, 1383-1394.

Miller, N. L., Jinwon Kim, and Robert K. HartmanJohn Farrara, (1999). Downscaled Climate and Streamflow Study of the Southwestern United States, Journal of the American Water Resources Association 35.6: 1525-37.

Mitchell, T. D., and M. Hulme, (1999). Predicting Regional Climate Change: Living with Uncertainty, Progress in Physical Geography 23.1 (1999): 57-78.

Mitchell, T. D., and P. D. Jones, (2005). An Improved Method of Constructing a Database of Monthly Climate Observations and Associated High-Resolution Grids, International Journal of Climatology 25.6: 693-712.

Mishra, A., H. Takeshi, W. Abdelhadi, A. Tada, and H. Tanakamaru, (2003). Recession flow analysis of the Blue Nile River, Hydrol. Processes, 17, 2825– 2835.

Mohseni, O., and H. G. Stefan, (1998). A monthly streamflow model, Water Resources Research, 34(5), 1287-1298.

Mosley, M.P., (1981). Delimitation of New Zealand hydrologic regions. Journal of Hydrology 49, 173–192.

Mujumdar, P. P., and S. Ghosh, (2008). Modeling Gcm and Scenario Uncertainty Using a Possibilistic Approach: Application to the Mahanadi River, India, Water Resources Research 44.6.

Nakicenovic N, Swart R (eds). (2000). Special Report on Emissions Scenarios. A Special Report of Working Group III of the Intergovernmental Panel on Climate Change. Cambridge University Press: Cambridge, UK and New York. 570 p.

Oberhuber, J. M., (1993). Simulation of the Atlantic Circulation with a Coupled Sea Ice-Mixed Layer-Isopycnic General-Circulation Model .2. Model Experiment, Journal of Physical Oceanography 23.5: 830-45.

Post, D. A., Jones, J. A, & Grant, G. E. (1998) An improved methodology for predicting the daily hydrologie response o!' ungauged catchments. Environ. Model. Softw. 13, 395-403.

Randel, D.A. and Wood, R. A., (2007). Climate models and their evaluation. In: Climate Change 2007: The Physical Basis. (Solomon et al., eds.) Cambridge University Press:Cambridge. pp. 589-662.

Richards, L.A. (1931). Capillary conduction of liquids through porous mediums, Physics 1 (5): 318–333. doi:10.1063/1.1745010.

Roeckner, E., J. M. Oberhuber, A. Bacher, M. Christoph and I. Kirchner, (1996). Enso Variability and Atmospheric Response in a Global Coupled Atmosphere-Ocean GCM, Climate Dynamics 12.11: 737-54.

Rupp, D.E. and R.A. Woods (2008). Increased flexibility in base flow modeling using a power law transmissivity profile, Hydrol. Processes, 22, 2667-2671, doi:10.1002/hyp.6863

Sefton, C.E.M., Howarth, S.M., (1998). Relationships between dynamic response characteristics and physical descriptors of catchments in England and Wales, J. Hydrol. 211, 1–16.

Seibert, P., (1999). Regionalization of parameters for a conceptual rainfall-runoff model, Agricultural and Forestry Meteorology 98–99, 279–293.

Singh, V.P., (1995). Computer Models of Watershed Hydrology, Water Resources Publications, Highlands Ranch, CO.

Shepard, D.S. (1984). Computer mapping: The SYMAP interpolation algorithm, in Spatial Statistics and Models, edited by G.L. Gaile and C.J. Willmott, pp. 133 145, D. Reidel, Norwell, Mass.

Stamm, J. F., E. F. Wood, and D. P. Lettenmaier, (1994). Sensitivity of a Gcm Simulation of Global Climate to the Representation of Land-Surface Hydrology, Journal of Climate 7.8 (1994): 1218-39.

Tebaldi, C., Smith, Richard L, Nychka, Doug, and Mearns, Linda O., (2005). Quantifying Uncertainty in Projections of Regional Climate Change: A Bayesian Approach to the Analysis of Multimodel Ensembles, Journal of Climate 18.10: 1524-40.

Teuling, A. J., I. Lehner, J. W. Kirchner, and S. I. Seneviratne (2010), Catchments as simple dynamical systems: Experience from a Swiss prealpine catchment, Water Resour. Res., 46, W10502, doi:10.1029/2009WR008777.

Thornthwaite, C.W., (1948) An approach toward a rational classification of climate,Geogr. Rev. 38(1),55–94.

Thornthwaite, C. W. and Mather, J. R., (1955) The water balance, Publ. Climatol. Lab. Climatol. Dresel Inst. Technol. 8(8), 1–104.

Vandewiele, G.L., Elias, A., (1995). Monthly water balance of ungauged catchments obtained by geographical regionalization. Journal of Hydrology 170, 277–291.

Vieux, B. E., (2001) Distributed hydrologic modeling using GIS, First Edition, Kluwer Academic Press, Water and Science Technology Series, 38.

Vrac, M., M. Stein, and K. Hayhoe, (2007). Statistical Downscaling of Precipitation through Nonhomogeneous Stochastic Weather Typing, Climate Research 34.3: 169-84.

Wagener, T., Wheater, H.S., (2006). Parameter estimation and regionalization for continuous rainfall–runoff models including uncertainty. Journal of Hydrology 310 (1–2), 132–154.

Wagener, T., et al., (2009). Multiobjective Sensitivity Analysis to Understand the Information Content in Streamflow Observations for Distributed Watershed Modeling, Water Resources Research, 45.

Walker, W.R., Skogerboe, G.V. (1987) Surface irrigation: Theory and practice. Prentice-Hall, Englewood Cliffs.

Wilby, R. L., and T. M. L. Wigley, (1997). Downscaling General Circulation Model Output: A Review of Methods and Limitations, Progress in Physical Geography 21.4: 530-48.

Wilby, R. L., Charles, S.P., Zorita, E., Timbal, B., Whetton, P., and Mearns, L.O. (2004). Guidelines for use of climate scenarios developed from statistical downscaling methods, Data Distribution Center of the Intergovernmental Panel on Climate Change.

Wilks, D. S., and R. L. Wilby, (1999). The Weather Generation Game: A Review of Stochastic Weather Models, Progress in Physical Geography 23.3: 329-57.

Wittenberg, H., (1999) Baseflow recession and recharge as nonlinear storage processes, Hydrol. Processes, 13, 715– 726.

Wood, A. W., L. R. Leung, V. Sridhar and D. P. Lettenmaier, (2004). Hydrologic Implications of Dynamical and Statistical Approaches to Downscaling Climate Model Outputs, Climatic Change 62.1-3: 189-216.

Wood, A. W., et al., (2004). Hydrologic Implications of Dynamical and Statistical Approaches to Downscaling Climate Model Outputs, Climatic Change 62(1-3), 189-216.

Wood, E. F., Lettenmaier, D. P., and Zartarian, V. G., (1992). A land-surface hydrology parameterization with subgrid variability for general circulation models, J. Geophys. Res., 97, 2717-2728.

Xie, Z., Yuan, F., Duan Q., Zheng, J., Liang, M., Chen, F., (2007). Regional Parameter Estimation of the VIC Land Surface Model: Methodology and Application to River Basins in China. Journal of Hydrometeorology. Vol.8, 447-468

Xu, C. Y., (1999). From Gcms to River Flow: A Review of Downscaling Methods and Hydrologic Modelling Approaches, Progress in Physical Geography 23.2: 229-49.

Xu, C.Y. and Vandewiele, G. L., (1995). Parsimonious monthly rainfallrunoff models for humid basins with different input requirements, Adv. Water Resour. 18, 39–48.

Xue, Y. K., Vasic, Ratko, Janjic, Zavisa, Mesinger, Fedor, and Mitchell, Kenneth E, (2007). Assessment of Dynamic Downscaling of the Continental Us Regional Climate Using the Eta/Ssib Regional Climate Model, Journal of Climate 20.16: 4172-93.

Yapo, P. O., H. V. Gupta, and S. Sorooshian, (1998). Multi-Objective Global Optimization for Hydrologic Models, Journal of Hydrology, 204(1-4), 83-97.

Young P.C., (1993). Time variable and state dependent modelling of nonstationary and nonlinear time series, In Developments in Time Series Analysis, Subba Rao T (ed.). Chapman and Hall: 374–413.

Young P.C., (1998). Data-based mechanistic modelling of environmental, ecological, economic and engineering systems, Environmental Modelling and Software 13: 105–122.

Young P.C. (1999). Data-based mechanistic modelling, generalised sensitivity and dominant mode analysis, Computer Physics Communications 115: 1–17.

Young, P.C., (2003). Top-down and data-based mechanistic modelling of rainfall-flow dynamics at the catchment scale, Hydrol. Processes, 17, 2195– 2217.

Zhang, F. and Georgakakos, A. (2011a). Climate and Hydrologic Change Assessment for Georgia, 2011 Georgia Water Resources Conference, April 11-13, 2011, Athens, GA.

Zhang, F., and Georgakakos, A. (2011b). Comparing Joint Variable Spatial Downscaling Results with NARCCAP Datasets, The 3rd North American Regional Climate Change Assessment Program Users' Workshop, April 7-8, 2011, Boulder, CO.

Zhang, F. and Georgakakos, A. (2011c). Joint Variable Spatial Downscaling, Climatic Change, in press.

VITA

FENG ZHANG

Feng Zhang was born in Tanghe in the Henan Province of China. He attended high school in Wuhan, China, and college at the Huazong University of Science and Technology, where he received his B.S. degree in *Automobile Engineering* in 2000 and M.S. in *Power System and Its Automation* in 2003. After graduation, he worked as a research associate for the Engineering Computation and Simulation Institute in Wuhan for two years before coming to the United States to attend North Carolina State University, where he was a research and teaching assistant. In 2007, he came to Georgia Tech to pursue his doctorate in *Civil Engineering*. When he is not working on his research, Feng enjoys music, movies, tennis, and traveling with his friends.